

# Modelling Cometary X-rays

---

A THESIS SUBMITTED TO THE DEPARTMENT OF PHYSICS

OF THE UNIVERSITY OF STRATHCLYDE

FOR THE DEGREE OF DOCTOR OF PHILOSOPHY.

Martin Torney

March 2007

# © Copyright 2007

The copyright of this thesis belongs to the author under the terms of the United Kingdom Copyright Acts as qualified by University of Strathclyde Regulation 3.49. Due acknowledgement must always be made of the use of any material contained in, or derived from, this thesis.

## Abstract

The emission mechanism responsible for cometary x-ray emission is still unresolved. The two most probable models are driven by a charge exchange capture-cascade system and energetic electron collisions with ions. A modification of the energetic electron model is presented. Both this model and the charge exchange emission model are advanced by describing the resultant emission in a collisional radiative framework, and by using the most sophisticated atomic data available.

A catalogue of cometary x-ray observations by the *Chandra X-ray Observatory* is collated, with most of the data being previously unpublished. Theoretical spectra from the charge exchange and energetic electron models are compared to the emission spectra from *Chandra*, and the validity of each model is tested.

From the *Chandra* observations, it is not possible to determine which of the models is dominant. Several suggestions that will maximise the scientific yield of future observations with current satellites are made, and the distinguishable features of each emission mechanism are highlighted so as to demonstrate the capability of future observatories to resolve primary emission the mechanism. The diagnostic potential of each of the above models, with a view to remote sensing of both the cometary constituents and the local solar wind plasma, is discussed.

# Contents

<b>Contents</b>	<b>i</b>
<b>List of Figures</b>	<b>iv</b>
<b>List of Tables</b>	<b>xi</b>
<b>Acknowledgements</b>	<b>xii</b>
<b>1 Introduction</b>	<b>1</b>
<b>2 Previous Work</b>	<b>9</b>
2.1 X-ray Satellite Observations . . . . .	9
2.1.1 <i>Einstein Observatory</i> – Comet C/1979 l (Bradfield) – Feb 1980	9
2.1.2 <i>ROSAT</i> – Comet C/1996 B2 (Hyakutake) – Mar 1996 . . . . .	10
2.1.3 <i>ROSAT</i> – Comet C/1996 T1 (Tabur) – Sep 1996 . . . . .	12
2.1.4 The <i>ROSAT</i> All-Sky Survey – Comets C/1990 K1 (Levy), C/1990 N1 (Tsuchiya-Kiuchi), 45/P Honda-Mrkos- Pajdušáková and C/1991 A2 (Arai) . . . . .	12
2.1.5 <i>EUVE</i> – Comets 6P/D’Arrest, C/1995 Q1 (Bradfield), C/1996 B2 (Hyakutake), C/1995 O1 (Hale-Bopp) . . . . .	14
2.1.6 Comet C/1995 O1 (Hale-Bopp) . . . . .	15
2.1.7 <i>ROSAT</i> and <i>EUVE</i> – Comet 2P/Encke – July 1997 . . . . .	18
2.1.8 <i>EUVE</i> – Comet C/1996 B2 (Hyakutake) – Mar 1996 . . . . .	20
2.1.9 <i>CXO</i> – Comet C/1999 S4 (LINEAR) – July 2000 . . . . .	21
2.1.10 <i>CXO</i> – Comet C/1999 T1 (McNaught-Hartley) – Jan 2001 . .	22
2.1.11 <i>XMM-Newton</i> – Comet C/2000 WM1 (LINEAR) – Dec 2001	24
2.1.12 <i>CXO</i> – Comet 2P/Encke – Nov 2003 . . . . .	25
2.1.13 Collective Results . . . . .	26
2.2 <i>In Situ</i> Results from Comet 1P/Halley . . . . .	29
2.2.1 Neutral Particle Measurements . . . . .	30
2.2.2 Solar Wind Ion Measurements . . . . .	31

2.2.3	Electron Measurements . . . . .	32
2.2.4	Electric Field Measurements . . . . .	34
2.3	Emission Models . . . . .	35
2.3.1	Discounted Theories . . . . .	35
2.3.2	Charge-Exchange Driven Emission . . . . .	36
2.3.3	Electron-Ion Collision Driven Emission . . . . .	39
2.4	The Comet-Solar Wind Atmosphere . . . . .	40
2.5	Conclusions . . . . .	41
<b>3</b>	<b>Observations</b>	<b>42</b>
3.1	Solar Wind Measurements by the <i>Advanced Composition Explorer</i> . .	42
3.2	The <i>AXAF CCD Imaging Spectrometer – ACIS</i> . . . . .	44
3.3	Data Processing . . . . .	46
3.3.1	Data Reduction . . . . .	46
3.3.2	Grouping Observations . . . . .	49
3.3.3	Analysis of Background Counts . . . . .	49
3.4	<i>Chandra</i> Observations of Comets . . . . .	51
3.4.1	Comet C/1999 S4 (LINEAR) . . . . .	53
3.4.2	Comet C/1999 S4 (LINEAR) — After Breakup . . . . .	61
3.4.3	Comet C/1999 T1 (McNaught-Hartley) . . . . .	63
3.4.4	Comet C/2002 C1 (Ikeya-Zhang) . . . . .	72
3.4.5	Comet 2P/Encke (2003) . . . . .	79
3.4.6	Comet C/2001 Q4 (NEAT) . . . . .	83
3.4.7	Comet 9P/Tempel 1 . . . . .	88
3.4.8	Comet 73P/Schwassmann-Wachmann 3B . . . . .	96
3.4.9	High Resolution Spectroscopy . . . . .	101
3.4.10	Collective Results . . . . .	102
3.5	Future Missions and Observations . . . . .	104
3.5.1	<i>ASTRO-E2 (Suzaku)</i> . . . . .	104
3.5.2	Sounding Rockets . . . . .	104
3.5.3	<i>Constellation X</i> . . . . .	105
<b>4</b>	<b>Modelling the X-ray Emission from Cometary Atmospheres</b>	<b>107</b>
4.1	Electron Energisation . . . . .	108
4.1.1	The Modified Two-Stream Instability . . . . .	108
4.1.2	Landau Damping of Electrostatic Waves . . . . .	110
4.1.3	Emission from Energetic Electrons . . . . .	111
4.2	Atomic Data . . . . .	113
4.2.1	Atomic Structure . . . . .	113

4.2.2	Excitation/De-excitation Processes . . . . .	115
4.2.3	Recombination Processes . . . . .	123
4.2.4	Ionisation . . . . .	130
4.2.5	Bremsstrahlung . . . . .	131
4.2.6	Summary . . . . .	132
4.3	Collisional Radiative Modelling . . . . .	133
4.4	Application of Collisional Radiative Modelling . . . . .	137
4.4.1	The Solar Wind . . . . .	137
4.4.2	Modelling Emission Spectra . . . . .	139
<b>5</b>	<b>Fitting</b>	<b>146</b>
5.1	Convolving Theoretical Spectra . . . . .	146
5.1.1	Verification of Convolution Process . . . . .	147
5.2	Fitting Algorithm . . . . .	149
5.3	Background Signals . . . . .	150
5.3.1	Comet C/1999 S4 (LINEAR) . . . . .	151
5.3.2	Comet C/1999 T1 (McNaught-Hartley) (January 8) . . . . .	152
5.3.3	Comet C/2002 C1 (Ikeya-Zhang) . . . . .	152
5.3.4	Comet 2P/Encke . . . . .	153
5.3.5	Comet C/2001 Q4 (NEAT) . . . . .	154
5.3.6	Comet 9P/Tempel 1 (July 8) . . . . .	155
5.3.7	Comet 73P/Schwassmann-Wachmann 3B . . . . .	156
5.4	Source Data . . . . .	157
5.5	Fitting <i>Chandra</i> Data . . . . .	158
5.5.1	Arbitrary Line Emission . . . . .	158
5.5.2	Arbitrary Bremsstrahlung Emission . . . . .	168
5.5.3	Arbitrary Line + Bremsstrahlung Emission . . . . .	169
5.5.4	Charge Exchange Between Solar Wind Ions and Cometary Neutrals . . . . .	177
5.5.5	Energetic Electrons – Excitation of Solar Wind Ions and Bremsstrahlung . . . . .	186
5.6	Conclusions . . . . .	196
<b>6</b>	<b>Conclusions</b>	<b>197</b>
	<b>Bibliography</b>	<b>I</b>
	<b>Appendix</b>	<b>VI</b>

# List of Figures

1.1	<i>Giotto</i> image of comet 1P/Halley . . . . .	4
1.2	<i>Deep Space 1</i> image of Comet 19P/Borrelly . . . . .	5
1.3	Comet 9P/Tempel 1 shortly after the <i>Deep Impact</i> collision . . . . .	6
1.4	Comet 9P/Tempel 1 as observed by the <i>Deep Impact</i> impactor . . . . .	7
2.1	The first successful x-ray observation . . . . .	11
2.2	The x-ray spectrum of comet C/1990 K1 (Levy) . . . . .	13
2.3	EUV image of comet 6P/D'Arrest . . . . .	14
2.4	EUV image of comet C/1995 O1 (Hale-Bopp) . . . . .	15
2.5	X-ray image of comet C/1995 O1 (Hale-Bopp) . . . . .	17
2.6	X-ray spectrum of comet C/1995 O1 (Hale-Bopp) . . . . .	17
2.7	Cometary and Solar Wind parameters for comet 2P/Encke . . . . .	19
2.8	<i>EUVE</i> spectrum from comet C/1996 B2 (Hyakutake) . . . . .	20
2.9	The <i>Chandra</i> spectrum of comet C/1999 S4 (LINEAR) . . . . .	21
2.10	The <i>Chandra</i> spectrum of comet C/1999 T1 (McNaught-Hartley) . . . . .	23
2.11	The <i>XMM</i> spectrum of comet C/2000 WM1 (LINEAR) . . . . .	24
2.12	The <i>Chandra</i> spectrum of comet 2P/Encke . . . . .	25
2.13	X-ray luminosity vs. optical luminosity from the <i>ROSAT</i> survey . . . . .	27
2.14	<i>VEGA</i> and <i>Giotto</i> trajectories . . . . .	29
2.15	The derived neutral density in comet 1P/Halley's atmosphere . . . . .	30
2.16	Measured solar wind ion density at comet 1P/Halley . . . . .	31
2.17	Electron distribution in comet 1P/Halley's atmosphere . . . . .	32
2.18	<i>In situ</i> wave activity in the atmosphere of comet 1P/Halley . . . . .	34
2.19	<i>EBIT</i> charge exchange spectrum . . . . .	38
3.1	A schematic of <i>Chandra's</i> <i>ACIS</i> array of CCDs from the <i>Chandra</i> Proposers' Observatory Guide. . . . .	44
3.2	Typical effective area functions for <i>ACIS</i> chips. . . . .	45
3.3	CCD image of comet C/1999 s4 (LINEAR) . . . . .	46
3.4	Graded CCD image of comet C/1999 S4 (LINEAR) . . . . .	47
3.5	Filtered CCD image of comet C/1999 S4 (LINEAR) . . . . .	48

3.6	Filtered CCD image of comet C/1999 T1 (McNaught-Hartley) . . . . .	48
3.7	Destreaked CCD image of comet C/1999 T1 (McNaught-Hartley) . .	49
3.8	X-ray data from comet C/1999 S4 (LINEAR) . . . . .	53
3.9	X-ray data from <i>ACIS-S3</i> for comet C/1999 S4 (LINEAR) . . . . .	54
3.10	X-ray data from <i>ACIS-S1</i> for comet C/1999 S4 (LINEAR) . . . . .	55
3.11	X-ray data from a circular region for comet C/1999 S4 (LINEAR) . .	55
3.12	X-ray data from an annular region for comet C/1999 S4 (LINEAR) . .	56
3.13	X-ray data from the chip edge for comet C/1999 S4 (LINEAR) . . . . .	56
3.14	Low and high energy x-ray data for comet C/1999 S4 (LINEAR) . . . .	57
3.15	Low energy source x-ray data for comet C/1999 S4 (LINEAR) . . . . .	57
3.16	X-ray light curve for comet C/1999 S4 (LINEAR) . . . . .	58
3.17	<i>ACE-SWEPAM</i> measurements corresponding to comet C/1999 S4 (LINEAR) . . . . .	59
3.18	<i>ACE-MAG</i> measurements corresponding to comet C/1999 S4 (LINEAR)	59
3.19	<i>ACE-SWICS</i> measurements corresponding to comet C/1999 S4 (LIN- EAR) . . . . .	60
3.20	<i>ACE-SWICS</i> measurements corresponding to comet C/1999 S4 (LIN- EAR) . . . . .	60
3.21	X-ray data for comet C/1999 S4 (LINEAR) . . . . .	61
3.22	X-ray data from <i>ACIS-S3</i> for comet C/1999 S4 (LINEAR) . . . . .	62
3.23	X-ray data for comet C/1999 T1 (McNaught-Hartley) . . . . .	63
3.24	X-ray data from <i>ACIS-S1</i> for comet C/1999 T1 (McNaught-Hartley) .	64
3.25	X-ray spectra from <i>ACIS-S1</i> and <i>ACIS-S3</i> for comet C/1999 T1 (McNaught-Hartley) . . . . .	64
3.26	X-ray morphologies for comet C/1999 T1 (McNaught-Hartley) . . . . .	65
3.27	X-ray spectra for comet C/1999 T1 (McNaught-Hartley) . . . . .	66
3.28	Narrowband x-ray data for comet C/1999 T1 (McNaught-Hartley) . .	67
3.29	X-ray light curves for comet C/1999 T1 (McNaught-Hartley) . . . . .	68
3.30	<i>ACE-SWEPAM</i> measurements corresponding to comet C/1999 T1 (McNaught-Hartley) . . . . .	69
3.31	<i>ACE-MAG</i> measurements corresponding to comet C/1999 T1 (McNaught-Hartley) . . . . .	70
3.32	<i>ACE-SWICS</i> measurements corresponding to comet C/1999 T1 (McNaught-Hartley) . . . . .	70
3.33	<i>ACE-SWICS</i> measurements corresponding to comet C/1999 T1 (McNaught-Hartley) . . . . .	71
3.34	X-ray data for comet C/2002 C1 (Ikeya-Zhang) . . . . .	72
3.35	X-ray data from <i>ACIS-I</i> for comet C/2002 C1 (Ikeya-Zhang) . . . . .	73
3.36	X-ray data from <i>ACIS-S1</i> for comet C/2002 C1 (Ikeya-Zhang) . . . . .	74

3.37	X-ray data from <i>ACIS-S2</i> for comet C/2002 C1 (Ikeya-Zhang) . . . . .	74
3.38	X-ray data from <i>ACIS-S3</i> for comet C/2002 C1 (Ikeya-Zhang) . . . . .	75
3.39	X-ray data from <i>ACIS-S4</i> for comet C/2002 C1 (Ikeya-Zhang) . . . . .	76
3.40	<i>ACE-SWEPAM</i> measurements corresponding to comet C/2002 C1 (Ikeya-Zhang) . . . . .	77
3.41	<i>ACE-MAG</i> measurements corresponding to comet C/2002 C1 (Ikeya-Zhang) . . . . .	77
3.42	<i>ACE-SWICS</i> measurements corresponding to comet C/2002 C1 (Ikeya-Zhang) . . . . .	78
3.43	<i>ACE-SWICS</i> measurements corresponding to comet C/2002 C1 (Ikeya-Zhang) . . . . .	78
3.44	X-ray data for comet 2P/Encke . . . . .	79
3.45	X-ray data from <i>ACIS-S3</i> for comet 2P/Encke . . . . .	80
3.46	X-ray light curve for comet 2P/Encke . . . . .	80
3.47	<i>ACE-SWEPAM</i> measurements corresponding to comet 2P/Encke . . . . .	81
3.48	<i>ACE-MAG</i> measurements corresponding to comet 2P/Encke . . . . .	81
3.49	<i>ACE-SWICS</i> measurements corresponding to comet 2P/Encke . . . . .	82
3.50	<i>ACE-SWICS</i> measurements corresponding to comet 2P/Encke . . . . .	82
3.51	X-ray data for comet C/2001 Q4 (NEAT) . . . . .	83
3.52	X-ray data from <i>ACIS-S3</i> for comet C/2001 Q4 (NEAT) . . . . .	84
3.53	X-ray data from <i>ACIS-S1</i> for comet C/2001 Q4 (NEAT) . . . . .	84
3.54	X-ray light curve for comet C/2001 Q4 (NEAT) . . . . .	85
3.55	<i>ACE-SWEPAM</i> measurements corresponding to comet C/2001 Q4 (NEAT) . . . . .	85
3.56	<i>ACE-MAG</i> measurements corresponding to comet C/2001 Q4 (NEAT) . . . . .	86
3.57	<i>ACE-SWICS</i> measurements corresponding to comet C/2001 Q4 (NEAT) . . . . .	86
3.58	<i>ACE-SWICS</i> measurements corresponding to comet C/2001 Q4 (NEAT) . . . . .	87
3.59	X-ray morphologies of comet 9P/Tempel 1 . . . . .	89
3.60	X-ray spectra of comet 9P/Tempel 1 . . . . .	90
3.61	X-ray light curves of comet 9P/Tempel 1 . . . . .	91
3.62	X-ray light curves of comet 9P/Tempel 1 . . . . .	92
3.63	<i>ACE-SWEPAM</i> measurements corresponding to comet 9P/Tempel 1 . . . . .	93
3.64	<i>ACE-MAG</i> measurements corresponding to comet 9P/Tempel 1 . . . . .	94
3.65	<i>ACE-SWICS</i> measurements corresponding to comet 9P/Tempel 1 . . . . .	94
3.66	<i>ACE-SWICS</i> measurements corresponding to comet 9P/Tempel 1 . . . . .	95
3.67	X-ray data for comet 73P/Schwassmann-Wachmann 3B . . . . .	96
3.68	X-ray data from <i>ACIS-S3</i> for comet 73P/Schwassmann-Wachmann 3B . . . . .	97
3.69	X-ray data from <i>ACIS-S1</i> for comet 73P/Schwassmann-Wachmann 3B . . . . .	97
3.70	X-ray light curve for comet 73P/Schwassmann-Wachmann 3B . . . . .	98

3.71	<i>ACE-SWEPAM</i> measurements corresponding to comet 73P/Schwassmann-Wachmann 3B . . . . .	98
3.72	<i>ACE-MAG</i> measurements corresponding to comet 73P/Schwassmann- Wachmann 3B . . . . .	99
3.73	<i>ACE-SWICS</i> measurements corresponding to comet 73P/Schwassmann-Wachmann 3B . . . . .	99
3.74	<i>ACE-SWICS</i> measurements corresponding to comet 73P/Schwassmann-Wachmann 3B . . . . .	100
3.75	Comparison of <i>ACIS-S3</i> effective areas . . . . .	102
3.76	Comparison of various satellite effective areas . . . . .	105
3.77	Simulation of the resolving power of <i>Constellation X</i> . . . . .	106
4.1	Evolution of the electron distribution under Landau damping . . . . .	110
4.2	Evolution of the distribution function in the direction of the magnetic field . . . . .	111
4.3	Example of two-photon emission continuum . . . . .	114
4.4	Maxwell-averaged collision strengths for $1s^2\ ^1S$ and $1s2s\ ^3S$ in $O^{6+}$ .	116
4.5	Maxwell-averaged collisions strengths for $1s^2\ ^1S$ and $1s2s\ ^1S$ in $O^{6+}$ .	117
4.6	Maxwell-averaged collision strengths for $1s^2\ ^1S$ and $1s2p\ ^1P$ in $O^{6+}$ .	118
4.7	The effective density for transitions from $1s2s\ ^3S\ O^{6+}$ . . . . .	119
4.8	The energy density of the solar radiation field at a distance of 1 AU from the Sun. . . . .	122
4.9	Total radiative recombination rates to $O^{6+}$ . . . . .	124
4.10	Radiative and dielectronic recombination rates to $O^{6+}\ 1s2p\ ^1P$ from $O^{7+}\ 1s$ . . . . .	126
4.11	Oxygen fractional abundances as a function of temperature . . . . .	137
4.12	Iron fractional abundances as a function of temperature . . . . .	138
4.13	O VII excitation driven spectrum . . . . .	140
4.14	Temperature dependence of $\mathcal{P}\mathcal{E}\mathcal{C}^{\text{exc}}$ transitions in O VII . . . . .	141
4.15	O VII charge exchange driven spectrum . . . . .	143
4.16	Collision speed dependence of $\mathcal{P}\mathcal{E}\mathcal{C}^{\text{CX}}$ in O VII . . . . .	144
5.1	Comparison of fitting routine with XSPEC . . . . .	148
5.2	The background signal for comet C/1999 S4 (LINEAR) . . . . .	151
5.3	The background signal for comet C/1999 T1 (McNaught-Hartley) . .	152
5.4	The background signal for comet 2P/Encke . . . . .	153
5.5	The background signal for comet C/2001 Q4 (NEAT) . . . . .	154
5.6	The background signal for comet 9P/Tempel 1 . . . . .	155
5.7	The background signal for comet 73P/Schwassmann-Wachmann 3B .	156

5.8	8 line fit of comet C/1999 S4 (LINEAR) . . . . .	159
5.9	8 line for of comet C/1999 T1 McNaught-Hartley) . . . . .	159
5.10	12 line fit of comet C/2002 C1 (Ikeya-Zhang) (ACIS-S1) (first obser- vation) on the ACIS-S1 chip. . . . .	160
5.11	12 line fit of comet C/2002 C1 (Ikeya-Zhang) (ACIS-S2) (first obser- vation) on the ACIS-S2 chip. . . . .	160
5.12	12 line fit of comet C/2002 C1 (Ikeya-Zhang) (ACIS-S3) (first obser- vation) on the ACIS-S3 chip. . . . .	161
5.13	12 line fit of comet C/2002 C1 (Ikeya-Zhang) (ACIS-S4) (first obser- vation) on the ACIS-S4 chip. . . . .	161
5.14	12 line fit of comet C/2002 C1 (Ikeya-Zhang) (ACIS-S1) (second ob- servation) on the ACIS-S1 chip. . . . .	162
5.15	12 line fit of comet C/2002 C1 (Ikeya-Zhang) (ACIS-S2) (second ob- servation) on the ACIS-S2 chip. . . . .	162
5.16	12 line fit of comet C/2002 C1 (Ikeya-Zhang) (ACIS-S3) (second ob- servation) on the ACIS-S3 chip. . . . .	163
5.17	12 line fit of comet C/2002 C1 (Ikeya-Zhang) (ACIS-S4) (second ob- servation) on the ACIS-S4 chip. . . . .	163
5.18	7 line fit of comet 2P/Encke . . . . .	164
5.19	7 line fit of comet C/2001 Q4 (NEAT) . . . . .	164
5.20	7 line fit of comet 9P/Tempel 1 with background . . . . .	165
5.21	8 line fit of comet 9P/Tempel 1 without background . . . . .	165
5.22	5 line fit of comet 73P/Schwassmann-Wachmann 3B with background	166
5.23	6 line fit of comet 73P/Schwassmann-Wachmann 3B without background	166
5.24	A bremsstrahlung fit of comet C/1999 S4 (LINEAR) . . . . .	168
5.25	A bremsstrahlung plus 5 lines fit of comet C/1999 S4 (LINEAR) . . .	169
5.26	A bremsstrahlung plus 6 lines fit of comet C/1999 T1 (McNaught- Hartley) . . . . .	169
5.27	A Bremsstrahlung + 8 lines fit of comet C/2002 C1 (Ikeya-Zhang) (ACIS-S1) (first observation) . . . . .	170
5.28	A Bremsstrahlung + 8 lines fit of comet C/2002 C1 (Ikeya-Zhang) (ACIS-S2) (first observation) . . . . .	170
5.29	A Bremsstrahlung + 8 lines fit of comet C/2002 C1 (Ikeya-Zhang) (ACIS-S3) (first observation) . . . . .	171
5.30	A Bremsstrahlung + 8 lines fit of comet C/2002 C1 (Ikeya-Zhang) (ACIS-S4) (first observation) . . . . .	171
5.31	A Bremsstrahlung + 7 lines fit of comet C/2002 C1 (Ikeya-Zhang) (ACIS-S1) (second observation) . . . . .	172

5.32 A Bremsstrahlung + 8 lines fit of comet C/2002 C1 (Ikeya-Zhang) (ACIS-S2) (second observation) . . . . .	172
5.33 A Bremsstrahlung + 8 lines fit of comet C/2002 C1 (Ikeya-Zhang) (ACIS-S3) (second observation) . . . . .	173
5.34 A Bremsstrahlung + 8 lines fit of comet C/2002 C1 (Ikeya-Zhang) (ACIS-S4) (second observation) . . . . .	173
5.35 A bremsstrahlung plus 6 lines fit of comet 2P/Encke . . . . .	174
5.36 A bremsstrahlung plus 5 lines fit of comet C/2001 Q4 (NEAT) . . . . .	174
5.37 A bremsstrahlung plus 5 lines fit of comet 9P/Tempel 1 with modelled background . . . . .	175
5.38 A bremsstrahlung plus 4 lines fit of comet 9P/Tempel 1 with no background treatment . . . . .	175
5.39 A bremsstrahlung plus 5 lines fit of comet 73P/Schwassmann-Wachmann with modelled background . . . . .	176
5.40 A bremsstrahlung plus 5 lines fit of comet 73P/Schwassmann-Wachmann with no background treatment . . . . .	176
5.41 Charge exchange fit of comet C/1999 S4 (LINEAR) . . . . .	178
5.42 Charge exchange fit of comet C/1999 T1 (McNaught-Hartley) . . . . .	178
5.43 Charge exchange fit of comet C/2002 C1 (Ikeya-Zhang) (ACIS-S1) (first observation) . . . . .	179
5.44 Charge exchange fit of comet C/2002 C1 (Ikeya-Zhang) (ACIS-S2) (first observation) . . . . .	179
5.45 Charge exchange fit of comet C/2002 C1 (Ikeya-Zhang) (ACIS-S3) (first observation) . . . . .	180
5.46 Charge exchange fit of comet C/2002 C1 (Ikeya-Zhang) (ACIS-S4) (first observation) . . . . .	180
5.47 Charge exchange fit of comet C/2002 C1 (Ikeya-Zhang) (ACIS-S1) (second observation) . . . . .	181
5.48 Charge exchange fit of comet C/2002 C1 (Ikeya-Zhang) (ACIS-S2) (second observation) . . . . .	181
5.49 Charge exchange fit of comet C/2002 C1 (Ikeya-Zhang) (ACIS-S3) (second observation) . . . . .	182
5.50 Charge exchange fit of comet C/2002 C1 (Ikeya-Zhang) (ACIS-S4) (second observation) . . . . .	182
5.51 Charge exchange fit of comet 2P/Encke . . . . .	183
5.52 Charge exchange fit of comet C/2001 Q4 (NEAT) . . . . .	183
5.53 Charge exchange fit of comet 9P/Tempel 1 with modelled background . . . . .	184
5.54 Charge exchange fit of comet 9P/Tempel 1 with no background treatment . . . . .	184

5.55	Charge exchange fit of comet 73P/Schwassmann-Wachmann with modelled background . . . . .	185
5.56	Charge exchange fit of comet 73P/Schwassmann-Wachmann with no background treatment . . . . .	185
5.57	Energetic electron fit of comet C/1999 S4 (LINEAR) . . . . .	187
5.58	Energetic electron fit of comet C/1999 T1 (McNaught-Hartley) . . . .	187
5.59	Energetic electron fit of comet C/2002 C1 (Ikeya-Zhang) (ACIS-S1) (first observation) . . . . .	188
5.60	Energetic electron fit of comet C/2002 C1 (Ikeya-Zhang) (ACIS-S2) (first observation) . . . . .	188
5.61	Energetic electron fit of comet C/2002 C1 (Ikeya-Zhang) (ACIS-S3) (first observation) . . . . .	189
5.62	Energetic electron fit of comet C/2002 C1 (Ikeya-Zhang) (ACIS-S4) (first observation) . . . . .	189
5.63	Energetic electron fit of comet C/2002 C1 (Ikeya-Zhang) (ACIS-S1) (second observation) . . . . .	190
5.64	Energetic electron fit of comet C/2002 C1 (Ikeya-Zhang) (ACIS-S2) (second observation) . . . . .	190
5.65	Energetic electron fit of comet C/2002 C1 (Ikeya-Zhang) (ACIS-S3) (second observation) . . . . .	191
5.66	Energetic electron fit of comet C/2002 C1 (Ikeya-Zhang) (ACIS-S4) (second observation) . . . . .	191
5.67	Energetic electron fit of comet 2P/Encke . . . . .	192
5.68	Energetic electron fit of comet C/2001 Q4 (NEAT) . . . . .	192
5.69	Energetic electron fit of comet 9P/Tempel with modelled background .	193
5.70	Energetic electron fit of comet 9P/Tempel with no background treatment	193
5.71	Energetic electron fit of comet 73P/Schwassmann-Wachmann with modelled background . . . . .	194
5.72	Energetic electron fit of comet 73P/Schwassmann-Wachmann with no background treatment . . . . .	194

# List of Tables

2.1	Overview of observations . . . . .	26
3.1	<i>ACE</i> Solar Wind measurements . . . . .	43
3.2	Details of comets observed by <i>Chandra</i> . . . . .	51
4.1	Radiative rates between the lowest terms in the He-like oxygen system	118
4.2	Charge exchange data sources . . . . .	129
4.3	Electron collision driven lines . . . . .	141
4.4	Prominent electron collision driven transitions in the soft x-ray regime. Emission lines from each ion species are arranged by photon emissiv- ity coefficient for an electron temperature of 300 eV. . . . .	142
4.5	Charge exchange driven lines . . . . .	143
5.1	Data sources for modelling . . . . .	157
5.2	$\chi^2$ results for each fit . . . . .	196

## Acknowledgements

I would like to take this opportunity to thank some of the people who have helped me in the last few years. Firstly, the support and patience of my supervisors Prof. Bob Bingham and Prof. Hugh Summers have been invaluable. The breadth of Bob's expertise is incredible, and he has contributed many ideas and a great deal of enthusiasm to this study. I'm also grateful to his kind family, who put a roof over my head for several weeks during a visit to RAL. I acknowledge Hugh's financial support through ADAS, and thank him for all of his guidance and input, and the use of ADAS routines and data.

Throughout my doctorate, I have been fortunate enough to be surrounded by some excellent colleagues and I'm proud to call them friends. Dr Allan Whiteford provided an inspirational wealth of knowledge on atomic physics and programming, and he contributed a huge effort in proof-reading this thesis, even during his Christmas holidays. It was a pleasure to share a lab/office/pub with Allan, Dr Iain Paton and Dr Paul Bryans. They were a terrific sounding board, and it was during a chat with Iain that the idea for the modified energetic electron model came about. I'm grateful that Iain and Paul also took the time to read through several versions of this thesis, and they made many implemented suggestions despite Iain's busy schedule in the real world and Paul's distance from the source. Also within the university department, Cynthia Nam always provided some respite at coffee breaks, Prof. Nigel Badnell gave patient assistance with his structure codes, Dr Stuart Loch convinced me that a PhD was the correct career path and helped me get to grips with several incomprehensible Fortran routines, and Prof. Alan Phelps contributed a lot of advice and spent a fair portion of his time in helping to organise the viva.

I made several visits to RAL, usually with Allan, Iain, Paul and Adam Foster as travel companions. Despite often finding ourselves in questionable accommodation, they made Oxfordshire feel like home, and I enjoyed each of the trips that we made there. At RAL, I'm indebted to Dr Jim Lang, Jeff Payne, Dr Peter Young and especially Barry Kellett, who introduced me to the details of cometary x-rays. Barry's enthusiasm for this subject quickly captured my imagination, and his flair for presenting results is something that I try to emulate. At the nearby JET and Culham laboratories, Dr Martin O'Mullane has always provided assistance with ADAS, Dr Terry Martin kindly allowed the use of his ZERINT code, and Dr Martin O'Brien provided access to and assistance with the late Brian Harvey's Fokker-Planck routines.

During this period of study, I've had the opportunity to travel to several overseas institutions. At the Ruhr-Universität in Bochum, Germany, I was lucky enough to work with Prof. Padma Shukla, Dr Mohammad Salimullah and Dr Ingmar Sandberg in dusty plasma research. The rate at which Padma can produce papers is extraordinary, and it

was a pleasure to learn from him for three months. I continued to study dusty plasma during a nine month visit to the Università di Napoli Federico II. My experience there was one of the greatest of my life, and I'm eternally grateful to Bob and Prof. Umberto de Angelis for the opportunity, and to Umberto for opening my eyes to planet Napoli. My thanks also go to Dr. Ciro Marmolino, who guided me through the maze of algebra created by Umberto, and to Prof. Antonio Forlani.

I've also visited Dr. Scott Porter and Dr. Tim Kallman at NASA Goddard, and even though he couldn't be there during my stay, I must thank Dr. Randall Scott, who organised the trip, for inducting me in the black art of Chandra data analysis. Although I've never met them, I'd also like to thank Dr. Andrea Prestwich at the Chandra Helpdesk for hours of assistance, and Dr. Paul Pluckinsky for keeping me updated on the latest Chandra calibration.

Most recently, Dennis Bodewits welcomed me in Groningen, where I also met Dr. Damian Christian and Prof. Ronnie Hoekstra. I'd also like to acknowledge the other cometary x-ray scientists out there, especially Dr. Carey Lisse and Dr. Konrad Dennerl. Although we're working on different models, we have all been open to possibilities, and we are all pulling in the same direction. I believe that our continued collaboration will solve the problem of cometary x-rays.

Thanks also go to my examiners, Dr. Alex Cunningham and Dr. Dave Riley. They took a lot of time and effort to read the thesis in detail, and their feedback and the interest that they showed are greatly appreciated.

Closer to home, I'd like to thank all the friends who kept me sane through these years, especially Mick, Dave, Jenny, Richie, Kirsty, Julie, Craig and everyone else that I owe a pint. I thank my old physics teachers, Mr. Malkin and Mr. Ross, who showed me the wonder of physics and gave me a direction in life. Finally, my family: my parents, Jim and Dee, and my sister Marysia have supported me in every way possible, and I wouldn't have completed this work, or even started it, without them. Thank you.

Martin Torney  
March 2007

# Chapter 1

## Introduction

X-rays were generated and first detected by Wilhelm Röntgen (Röntgen 1895, 1898) during experiments with cathode rays. While ensuring that a glass enclosure for the rays was opaque when covered with cardboard, he observed a shimmering from a nearby barium platinocyanide screen. Note however, that the discovery was not serendipitous: Röntgen planned on using the barium platinocyanide screen in his experiments (hence its presence in the laboratory), and through the nature of his work, the discovery would have been made imminently by Röntgen or one of his colleagues. Röntgen immediately proposed that a form of radiation was responsible for the glowing effect he observed on the screen, and labelled the emission “x-rays”. The results were published 50 days after the observation (Röntgen, 1895)<sup>1</sup>, and Röntgen concluded that there was a relation between x-rays and other known forms of electromagnetic waves, but noted that many of the properties of ultraviolet radiation were not associated with x-rays. Although the term Röntgen rays is now common, the discoverer always preferred the title of x-rays.

X-rays, as Röntgen first concluded, are a form of electromagnetic radiation. Usually, x-rays are labelled as either hard or soft, with hard x-rays having energies greater than 10 keV, and soft x-rays falling in the range of 0.1 keV to 10 keV. In contradiction with perceived common knowledge, x-rays are visible to the naked eye when it has adjusted to dark conditions (Brandes and Dorn, 1896). However, given the harmful effects of x-rays on living tissue, perhaps propagation of this myth, rather than correction, is appropriate.

Soft x-rays are absorbed in a few metres of air, so extraterrestrial x-ray sources can't be detected by ground based telescopes. Detectors must be positioned 100 km or more above sea-level. The technology to achieve this was developed during the Second World War, in the shape of the V2 rocket. Shortly after the war, it was discovered that

---

<sup>1</sup>A translation of Röntgen's papers can be found at <http://www.mindfully.org/Nucs/Roetgen-X-Rays28dec1895.htm>

the Sun was a bright x-ray emitter (Burnight, 1949); however, its brightness was due to its proximity, and a similar star at a distance of several parsecs was too faint to be detected by early instruments. As a result, early x-ray sounding rocket missions (each with an observing period of 5 or 6 minutes) were almost exclusively dedicated to solar research.

One of the exceptions to this rule, a search for fluorescent emission from the surface of the moon (Giacconi *et al*, 1962), resulted in a surprising find. The detector constantly scanned the sky, and the analysis did reveal a bright x-ray source. However, the source was  $25^\circ$  from the moon, and the lunar signal was negligible. The object was so bright that the x-ray flux at Earth was only a factor of 10 to 100 times fainter than that of solar x-rays (Giacconi and Gursky, 1964). After careful analysis, it was verified that the source was real, and was located in the Scorpius constellation. Dubbed Sco X-1, a corresponding object in the visible part of the spectrum was found; although rather than clarify the nature of the object, this initially caused more confusion. In visible light, Sco X-1 was a faint blue speck, dimmer than the faintest star visible to the naked eye; in x-rays, the energy emitted was one hundred million times greater than that from the Sun.

This incredible discovery signalled the birth of cosmic x-ray astronomy. In the following years, further rocket- and balloon-borne missions with ever advancing detectors found more bright sources, but their nature remained mysterious. This was partly due to the incredible detected intensities (Giacconi and Gursky, 1964) and the large variability of the flux in a matter of minutes (Lewin *et al*, 1968).

The launch of the *Uhuru* satellite in 1970 allowed the first all-sky survey, and over 1000 x-ray sources were discovered. An *Uhuru* observation of Cen X-3, an object similar to Sco X-1, revealed the nature of these sources. Cen X-3 emitted x-ray bursts with an average period of 4.84 seconds, that varied as the object orbited another body every 2.09 days (Giacconi *et al*, 1971). Also, the emission disappeared for 11 hours as the source was eclipsed. The object was a binary system, comprising of a star and a neutron star. Stellar material is accreted onto the neutron star, and reaches energies sufficient to produce x-ray emission. These objects are the most powerful x-ray emitters in our galaxy, with luminosities as high as  $10^{38}$  erg s<sup>-1</sup>.

The other x-ray sources detected by early instruments were all very energetic objects: supernova remnants, bright stellar coronae (10,000 times solar luminosity), galaxies, clusters of galaxies.

Considering the colossal nature of the list of x-ray emitters, the recent addition of the comet appears quite out of place, and some justification is required.

Comets are frequent visitors to the inner solar system, where their spectacular light shows have amazed (and often terrified!) observers throughout human history. Ori-

nating in the Oort Cloud<sup>2</sup> or the Kuiper Belt<sup>3</sup> where they are undetectable from Earth, comets are continuously dislodged from these regions into the inner solar system. Whipple famously described comets as “Dirty Snowballs”; that is, large agglomerates of various ices mixed together with dust contaminants. The ratio of ice to dust is thought to vary to the extent that “Icy Dirtballs” may be more apt in some cases.

Comets orbit the Sun with periods that generally depend on their origin: short period comets are from the Kuiper Belt; long period comets are from the Oort Cloud. As one of these small bodies, typically a few kilometres in diameter, approaches the Sun its surface is irradiated, and particles sublimate from the surface. The ejected particles – gaseous molecules and large dust particles – gradually form an almost spherically symmetrical atmosphere, the coma, which can extend for millions of kilometres.

Under the influence of radiation pressure, the dust particles form one of the comet tails. As the liberated dust is orbiting the Sun independently of the comet, the white dust tail curves and points back along the direction of the comet’s trajectory. Gas particles in the coma are photo-ionised, at which point they feel the influence of the solar magnetic field (which is altered due to the presence of the comet). Trapped by the field, the ions are transported from the coma, forming the blue tail which points back in the direction of the Sun-comet vector.

Visible emission from the coma is caused by scattering of sunlight by dust particles. The dust scatters light over a broad wavelength range, and so the coma and dust tail appear white. The ion tail is characterised by  $\text{CO}^+$  ions, which give the tail a blue tint.

Cometary nuclei were formed in the early years of the solar system while the planets were still coalescing, and as such may be considered as pristine samples of the early solar system. It is postulated that the chemical composition of a comet is similar to the initial composition of the Earth, and it is speculated that the building blocks of life may be found on comets. For this reason and others, vast amounts of money have been spent on several high profile cometary missions in the last two decades, and more missions are planned.

In 1985, the first comet interception was made by NASA’s *International Cometary Explorer (ICE)*<sup>4</sup>. The aim of the encounter with comet Giacobini-Zinner was to examine the interaction of the cometary atmosphere with the solar wind. Following this successful mission, *ICE* joined the armada of spacecraft heading toward comet 1P/Halley. In March 1986, *ICE* was the first of six craft to successfully intercept comet 1P/Halley,

---

<sup>2</sup>A postulated spherical region surrounding the solar system, ranging from 50,000 to 100,000 AU, believed to contain billions of comets

<sup>3</sup>A region between 30 and 50 AU in the solar system plane

<sup>4</sup>See <http://heasarc.gsfc.nasa.gov/docs/heasarc/missions/isee3.html>

followed by the Soviet Union's *Vega 1*<sup>5</sup> and *Vega 2*<sup>6</sup> craft, the Japanese *Sakigake*<sup>7</sup> and *Suisei*<sup>8</sup> devices, and Europe's *Giotto*<sup>9</sup> spacecraft.

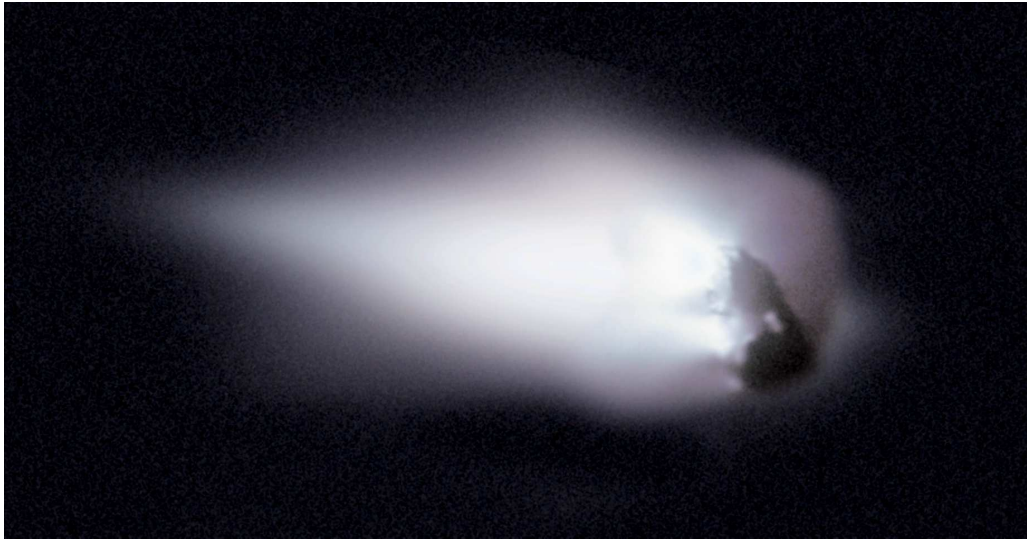


Figure 1.1: A *Giotto* image of comet 1P/Halley, showing large plumes of dust being ejected from the dayside of the nucleus.

The missions measured properties of the plasma, such as electron temperature, density and distribution, neutral density, dust composition, ion density, velocity and composition, electrostatic waves and magnetic fields amongst other things. Results from these missions are detailed in special issues of *Astronomy and Astrophysics* (vol. 187) and *Nature* (vol. 321). The missions also returned the first detailed images of a cometary nucleus, such as that from *Giotto* shown in figure 1.1. A large dust plume can be seen extending on the day-side of the nucleus, and small jets from the surface are also visible.

---

<sup>5</sup>See [http://sse.jpl.nasa.gov/missions/profile.cfm?Sort=Target&Target=Comets&MCode=Vega\\_01&Display=ReadMore](http://sse.jpl.nasa.gov/missions/profile.cfm?Sort=Target&Target=Comets&MCode=Vega_01&Display=ReadMore)

<sup>6</sup>See [http://sse.jpl.nasa.gov/missions/profile.cfm?Sort=Target&Target=Comets&MCode=Vega\\_02&Display=ReadMore](http://sse.jpl.nasa.gov/missions/profile.cfm?Sort=Target&Target=Comets&MCode=Vega_02&Display=ReadMore)

<sup>7</sup>See <http://www.isas.ac.jp/e/enterp/missions/complate/sakigake.shtml>

<sup>8</sup>See <http://www.isas.ac.jp/e/enterp/missions/complate/suise.shtml>

<sup>9</sup>See <http://sci.esa.int/science-e/www/area/index.cfm?fareaid=15>

The next cometary encounter was *Deep Space 1*<sup>10</sup>, a NASA project. The primary aim of this mission was to test twelve new high-risk technologies, such as an ion drive propulsion system and integrated ion and electron spectrometers (Rayman *et al*, 2000). After an encounter with an asteroid, the spacecraft was redirected to approach comet 19P/Borrelly. The spacecraft passed within 200 km of the nucleus, producing the photograph of the nucleus shown in figure 1.2 (Rayman, 2003).



Figure 1.2: Photograph of the nucleus of Comet 19P/Borrelly taken by *Deep Space 1* (Rayman, 2003).

In the summer of 2005, NASA's *Deep Impact*<sup>11</sup> mission successfully crashed an impactor probe into the surface of comet 9P/Tempel 1, causing a large plume of material to be thrown into the atmosphere (A'Hearn *et al*, 2005). The flash from the impact, as seen by the launcher, is shown in figure 1.3.

As the impactor travelled toward its target, it continued to record images of the surface of the comet. Images were captured up to a few seconds before the point of impact, and the image shown in figure 1.4 shows the comet in extraordinary detail. Figure 1.4 is composed of a number of consecutive images taken as the impactor approached the target, with each image showing a smaller region in more detail. A crater speckled surface can be clearly resolved, as can thin ice ridges.

In the same period, NASA's *Stardust*<sup>12</sup> mission was active (Brownlee *et al*, 1994). During a close approach of comet 89P/Wild in January 2004, dust and gas particles from the coma were collected by the spacecraft, which then returned to Earth with its

<sup>10</sup>See <http://nmp.nasa.gov/ds1/>

<sup>11</sup>See <http://deepimpact.jpl.nasa.gov/home/index.html>

<sup>12</sup>See [stardust.jpl.nasa.gov/home/index.html](http://stardust.jpl.nasa.gov/home/index.html)

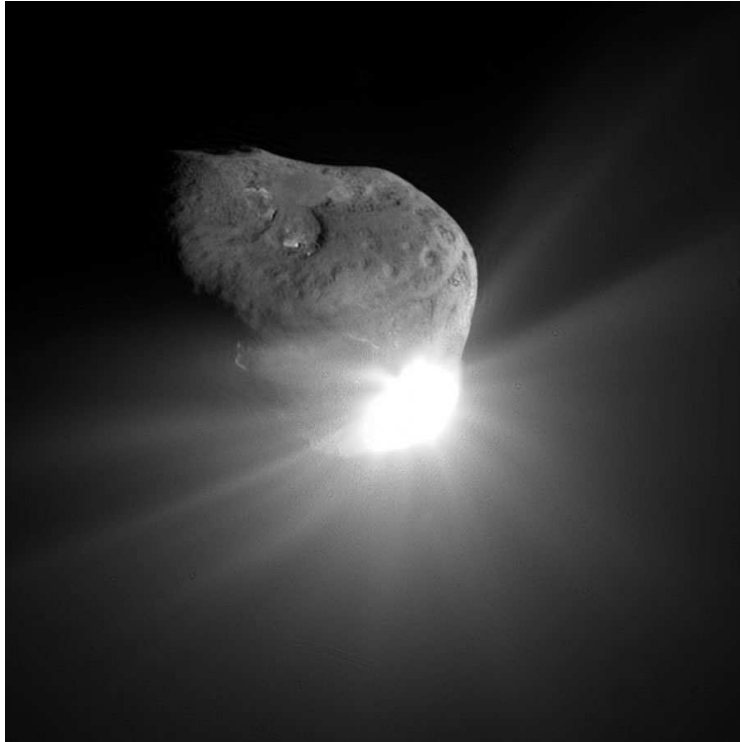


Figure 1.3: Photograph of Comet 9P/Tempel 1 shortly after the moment of the collision in the Deep Impact mission.

cometary cargo in January 2006.

ESA have launched the *Rosetta*<sup>13</sup> spacecraft which will visit comet 67P/Churyumov-Gerasimenko in 2014. Upon reaching its destination, it will deploy a landing module, which will touch down onto the comet's surface, allowing direct measurement of the conditions on the surface of the nucleus.

The discovery of x-ray emission from comet Hyakutake by Lisse *et al* (1996) was surprising, in that the observed radiation was two orders of magnitude brighter than even the most optimistic predictions. In the following months it was found that x-ray emission was a general property of comets, and in the intervening years almost every attempted observation has been successful.

The emission mechanism is still not clear. Several mechanisms have been suggested in the literature, and the two most likely candidates are driven by charge exchange and energetic electrons. In charge exchange, minor species ions in the solar wind such as  $O^{7+}$  capture an electron from the neutral atoms and molecules in the cometary atmosphere. The captured electron is in an excited state, and x-rays are emitted as the electron radiatively cascades to the ground state. The resultant spectrum is composed of emission lines.

The energetic electron model has evolved in recent years. Initially, it was thought

---

<sup>13</sup>See <http://www.esa.int/SPECIALS/Rosetta/index.html>



Figure 1.4: A composite image of comet 9P/Tempel 1 recorded by the impactor probe as it approached the surface. The image resolution increases closer to the point of the collision in the lower-right quadrant.

that the electrons could lead to x-rays by bremsstrahlung and following inner-shell excitation of cometary neutrals, such as carbon, nitrogen and oxygen. The first spectrum from *Chandra* showed that the strongest emission lines are from  $O^{6+}$  and  $O^{7+}$  (Lisse *et al*, 2001), and as a result the model was modified such that the electrons caused ionisation of the cometary atoms to the required ionisation stage, and the emission was caused by bremsstrahlung and emission from the collisionally excited cometary ions. The required timescales for these ionisation states to be reached suggest that this scenario is unlikely.

A new incarnation of the energetic electron model has been developed in this study. It is proposed that the energised electrons may excite the minor species in the solar wind, and also radiate through bremsstrahlung collisions with solar wind protons, cometary photo-ions and neutrals.

A review of the previous work in the field of cometary x-rays is presented in chapter 2. This includes published observations (and attempted observations) of x-rays from comets and the various models that have been proposed to explain the emission. Also, the relevant *in situ* results from comet 1P/Halley are shown, and there is a brief description of the comet-solar wind atmosphere.

Data from two spacecraft are shown in chapter 3. Measurements of the solar wind by the *Advanced Composition Explorer (ACE)* and a complete analysis of the cometary data collected by *Chandra* are presented. Most of the observations have not been published to date, and where data have been published, restrictions in journalistic styles have dictated that a detailed analysis of the emission cannot be presented. Here, a description of the analysis techniques employed is given, and each observation is catalogued in detail.

The modelling techniques used in this thesis are detailed in chapter 4. Firstly, the plasma instability believed to generate energetic electrons is presented in general terms. The focus of this thesis is the modelling of emission from the ions in the cometary atmosphere from both the charge exchange and energetic electron models. The atomic data, the modelling framework, and the application of the model are presented in chapter 4.

In chapter 5, the emission models are compared to the *Chandra* catalogue from chapter 3. Results from non-physical models — arbitrary line emission, bremsstrahlung, and a combination of both — are presented. This mirrors the level of sophistication in recent publications (see the modelling presented by Lisse *et al.*, 2001, 2005; Krasnopolsky, 2006). Results from modelling the emission from charge exchange and energetic electrons models, as discussed in chapter 4, are also presented in chapter 5.

Finally, the conclusions of the study and recommendations for future work are presented in chapter 6.

# Chapter 2

## Previous Work

A review of previous studies is presented in this chapter, with the work being partitioned into several categories: x-ray observations, *in situ* measurements from comet 1P/Halley, proposed emission models and, briefly, cometary atmosphere models.

### 2.1 X-ray Satellite Observations

Previous x-ray observations from the literature are presented here, with spectra and images being shown where they are available. The details are presented in chronological order with respect to the date of publication.

A detailed independent study of observations by the *Chandra X-ray Observatory* is presented in chapter 3.

#### 2.1.1 *Einstein Observatory* – Comet C/1979 l (Bradfield) – Feb 1980

The first intentional attempt to observe cometary x-rays was by Hudson *et al* (1981), who proposed that x-rays could be produced by a mechanism analogous to a process observed in the Earth's aurora (Anderson, 1965).

The *High Energy Astrophysics Observatory 2 (Einstein)* was pointed at comet C/1979 l (Bradfield) in February 1980. While the comet was 1.13 AU<sup>1</sup> from the Sun and 0.47 AU from the Earth, it was observed for a continuous period of 2.6 ks, in which time no x-rays were detected at a  $3\sigma$  level in the energy range 0.2 – 4 keV.

As the emission was believed to be a consequence of substorms in the cometary atmosphere, it was reasoned that the emission would be sporadic in nature. The authors estimated that the probability of an observation similar to theirs coinciding with such an event was only a few percent. Further study was urged, with the suggestion that simultaneous ultraviolet and optical observations could provide some insight into the

---

<sup>1</sup>1 Astronomical Unit  $\simeq 1.5 \times 10^8$  km

cometary weather. Despite these suggestions and the apparent enthusiasm for further study, 15 years passed before the next attempted observation.

### 2.1.2 *ROSAT* – Comet C/1996 B2 (Hyakutake) – Mar 1996

The first successful, intentional<sup>2</sup> cometary x-ray detections were the simultaneous observations of comet C/1996 B2 (Hyakutake) in 1996 by the *Röntgen X-ray Satellite (ROSAT)*<sup>3</sup> and the *Rossi X-ray Timing Explorer*<sup>4</sup> (Lisse *et al.*, 1996). Motivation for these missions came from the *in situ* measurements of energetic electrons in comet 1P/Halley (Gringauz *et al.*, 1986a, 1986b, and 1987; see section 2.2), and from Ibadov (1990), who suggested that collisions between cometary dust and interplanetary dust could release sufficient energy to produce x-rays. The total *ROSAT* observing time was 20 ks, spread over 9 intervals on the 26th and 27th of March 1996. At this time, the heliocentric and geocentric distances of the comet were 1.00 and 0.12 AU respectively. X-rays were observed in each of the observing periods, effectively ruling out the sporadic substorm model suggested by Hudson *et al.* (1981). In eight of the observations the emission was offset toward the Sun on the Sun-comet vector. The exception was the observation of shortest duration and, consequently, lowest signal to noise ratio and lowest statistical significance. In six of the observations the emission region was a semi-sphere around the Sun-comet vector, centred near the nucleus and extending to  $\sim 10^5$  km, which is the approximate position of the bow shock. No emission was observed from the tail. One of the x-ray images obtained is shown in figure 2.1 (Lisse *et al.*, 1996).

Over the course of the observation, the point of peak x-ray brightness was fixed near  $1.8 \times 10^4$  km from the nucleus on the sunward side, offset from the Sun-comet line by a few thousand km. The total x-ray power was calculated to be  $4 \times 10^{15}$  erg  $s^{-1}$ . The emission flux was variable over a period of 1 to 2 hours, which is shorter than the period of rotation of the nucleus (6.2 hours) and the minimum coma crossing time of an out-gassing particle ( $\sim 7$  hours if the out-gassing speed is  $0.8$  km  $s^{-1}$ , as was the case for comet 1P/Halley at a heliocentric distance of 1 AU, Combi, 1989). The morphology and the lack of correlation with the rotation of the nucleus suggested that the phenomenon was due to the interaction of the cometary atmosphere with the solar wind. As broadband photometry was employed, a detailed, energy resolved x-ray spectrum is not available.

---

<sup>2</sup>The detection of cometary x-rays in the *ROSAT* All-Sky Survey preceded this, but the survey was not scanned for comets until after the Hyakutake observation

<sup>3</sup>See <http://www.ssl.berkeley.edu/euve/>

<sup>4</sup>See <http://xte.mit.edu/>

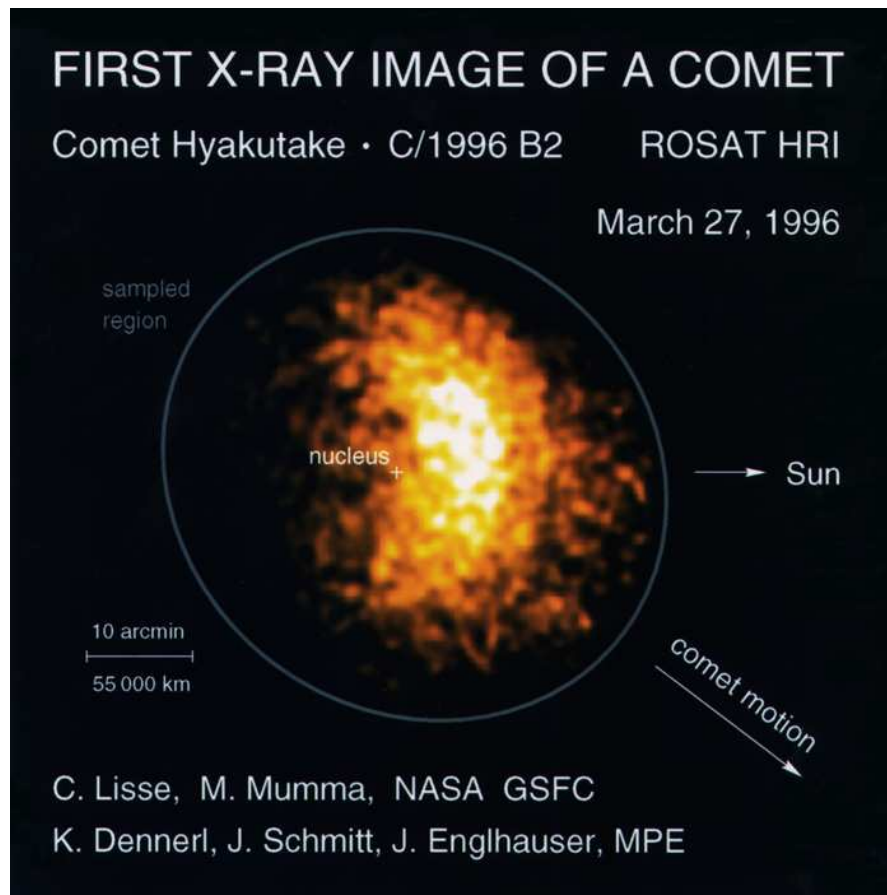


Figure 2.1: The first successful x-ray observation (Lisse *et al.*, 1996). The emission region extends to  $\sim 10^5$  km, and appears symmetrical around the Sun-comet axis.

### **2.1.3 ROSAT – Comet C/1996 T1 (Tabur) – Sep 1996**

Following the Hyakutake observations, *ROSAT* was again used to observe comet C/1996 Q1 (Tabur) (Dennerl *et al.*, 1996) in September and October 1996, when the comet was situated 1.09 AU from the Sun and 0.51 AU from the Earth. As with the Hyakutake observation, the emission was variable in intensity over a period of hours, as was the observed morphology. Considerable deviation from the crescent-like structure of Hyakutake was observed, with the emission resembling more a jet shape (Dennerl *et al.*, 1997). The brightest parts of the emission had a typical extent of  $9 \times 10^4$  km, and were centred  $3 \times 10^4$  km from the nucleus. The peak x-ray brightness was similar to that of Hyakutake. No further details have been published.

### **2.1.4 The ROSAT All-Sky Survey – Comets C/1990 K1 (Levy), C/1990 N1 (Tsuchiya-Kiuchi), 45/P Honda-Mrkos-Pajdušáková and C/1991 A2 (Arai)**

After the *ROSAT* discovery of x-rays from Hyakutake (Lisse *et al.*, 1996), a detailed examination of the *ROSAT* All-Sky Survey revealed seven previous x-ray observations from 4 different comets (Dennerl *et al.*, 1997). The exposure with the most detections was the first observation of C/1990 K1 (Levy), with 175 cometary photons and 11 background counts in an exposure of 77 s. The number of x-ray photons detected in the other exposures is not stated. Most of the morphologies were similar to that of Hyakutake, with the emission forming a crescent-shaped region between the comet and the Sun. The emission was independent of the velocity vectors of the comets. Typically the peak x-ray brightness was of the order  $10^4$  km from the nucleus in the nucleus-Sun direction, and the emitting regions extended to between  $10^5$  and  $10^6$  km. In every case the x-rays observed were soft, with about 95% of the photons having an energy of less than 0.4 keV. In one of the observations (the least significant statistically) the emission region formed a jet-like structure, similar to that observed from comet C/1996 T1 (Tabur) (Dennerl *et al.*, 1996). The survey found that any comet that passed closer than 2 A.U. to the Sun and was optically brighter than 12<sup>th</sup> magnitude was detected in the x-ray region of the spectrum. The comets left x-ray trails as they travelled through the field of view of the satellite, which again demonstrated that the emission process is continuous.

A detailed comparison of the observations (including the previous *ROSAT* observations of comets C/1996 B2 (Hyakutake) and C/1999 T1 (Tabur)) was presented by Dennerl *et al.*(1997). In general, the x-ray luminosity scaled well with the optical brightness, although the Hyakutake observation did not follow this trend. The ratio of the x-ray brightness to the optical brightness was independent of the heliocentric

distance of the comet, the distance from the ecliptic plane, and the solar wind speed. It was also noted that the x-ray brightness was dependent on the gas production rate rather than the dust production rate. This comparison is expanded to include more recent observations in section 2.1.13.

Unlike the Hyakutake observation, coarse x-ray spectra were obtained from the survey, although the counting statistics are poor. The spectrum from comet C/1990 K1 (Levy) is shown in figure 2.2.

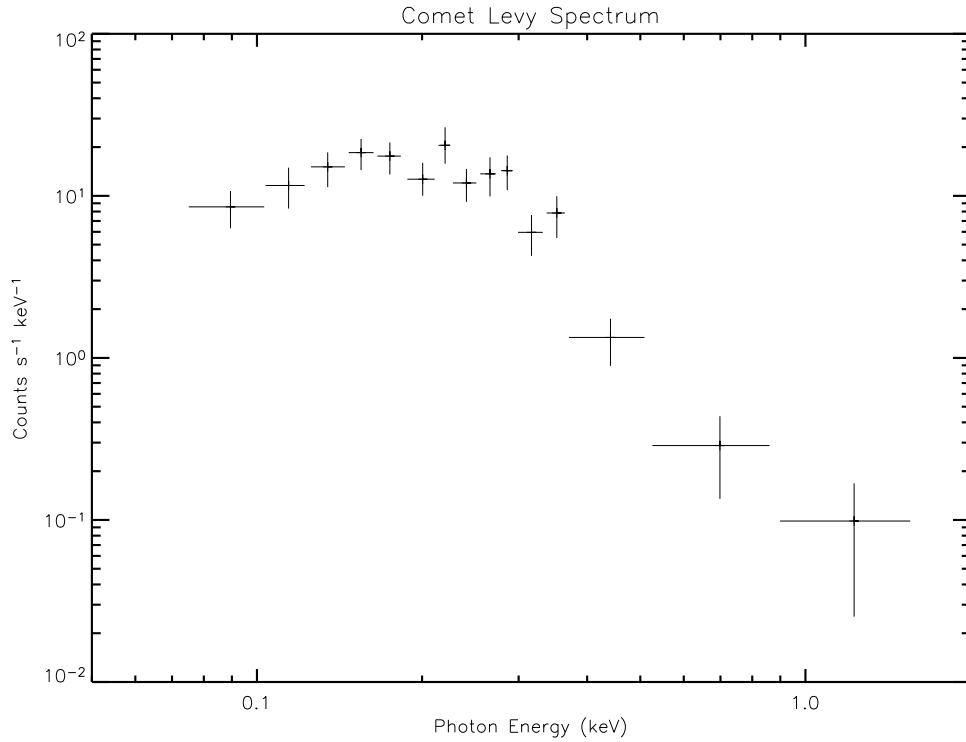


Figure 2.2: The x-ray spectrum of comet C/1990 K1 (Levy) in the *ROSAT* All-Sky Survey (Dennerl *et al*, 1997) with  $1\sigma$  error bars. The emission can be fitted by a thermal bremsstrahlung curve with  $kT_e = 0.23$  keV.

It was found that the data could be represented by a thermal bremsstrahlung with an electron temperature of 0.23 keV, although it was suggested that a charge exchange capture-cascade mechanism could yield similar results at such low resolving powers (Wegmann *et al*, 1998).

Dennerl *et al*(1997) established that x-ray emission was a standard feature of comets, which encouraged further observations. The general similarities between the emission morphologies seen in the survey, and with that of comet C/1996 B2 (Hyakutake), suggested that the same emission mechanism could be acting in each case.

### 2.1.5 *EUVE* – Comets 6P/D’Arrest, C/1995 Q1 (Bradfield), C/1996 B2 (Hyakutake), C/1995 O1 (Hale-Bopp)

Results from the *Extreme UltraViolet Explorer (EUVE)*<sup>5</sup> observations of four comets were published by Mumma *et al* (1997). The observations took place between September 1995 and September 1996, and spanned the energy range 100 to 165 eV.

One of the comets, comet C/1995 Q1 (Bradfield), was not detected within a  $2\sigma$  limit. The Hyakutake observation coincided with the *ROSAT* and *Rossi* observations (Lisse *et al*, 1996), and the reported morphology is consistent with the *ROSAT* results. The morphology of comet 6P/D’Arrest is shown in figure 2.3, and is similar in nature to that of Hyakutake, although due to the small phase angle the emission region appeared to be more spherically symmetrical from the brightest point.

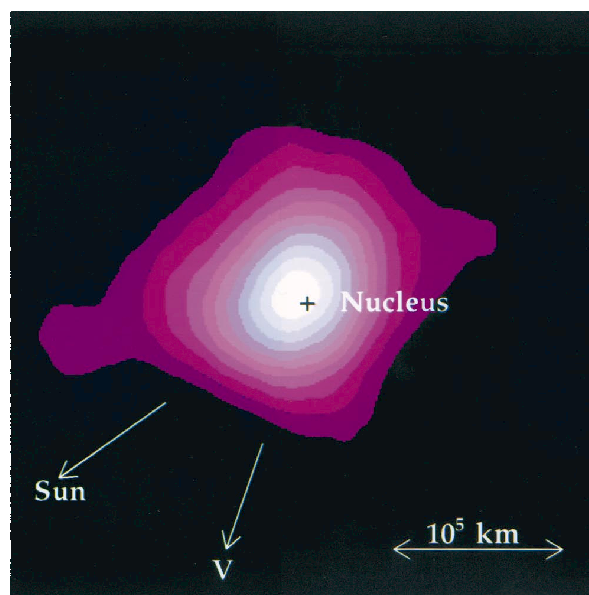


Figure 2.3: The EUV image of comet 6P/D’Arrest as observed by the *Extreme Ultraviolet Explorer* (Mumma *et al*, 1997).

Two mechanisms were considered to explain the emission: 1) charge exchange and 2) scattering by attogram dust particles, both of which are discussed further in section 2.3. By comparing the x-ray emission power to the gas and dust production rates, and by considering the position of the peak x-ray brightness, the conclusion of Mumma *et al* (1997) was that charge exchange was a more probable explanation.

---

<sup>5</sup>See <http://www.ssl.berkeley.edu/euve/>

### 2.1.6 Comet C/1995 O1 (Hale-Bopp)

Comet C/1995 O1 (Hale-Bopp) was one of the the largest and optically brightest comets of the twentieth century, with a nuclear mass estimated to be 40 times greater than that of comet C/1996 B2 (Hyakutake). Over a period of more than a year a number of observations were attempted. Contradictory results were obtained, with one device failing to detect x-rays from the comet on several occasions, and another showing that Hale-Bopp was the brightest x-ray comet observed to date. Details of these observations are given below.

#### *EUVE*

The first reported observation of Hale-Bopp was by Krasnopolsky *et al* (1997b). The detection with *EUVE* in September 1996 was over the energy range 70 to 180 eV. The effective (reduced due to filtering) duration of the observation was 90 ks.

The x-ray image obtained was rather different to that of previous images. Although the emission was again on the sunward side of the comet, it was largely displaced from the Sun-comet vector.

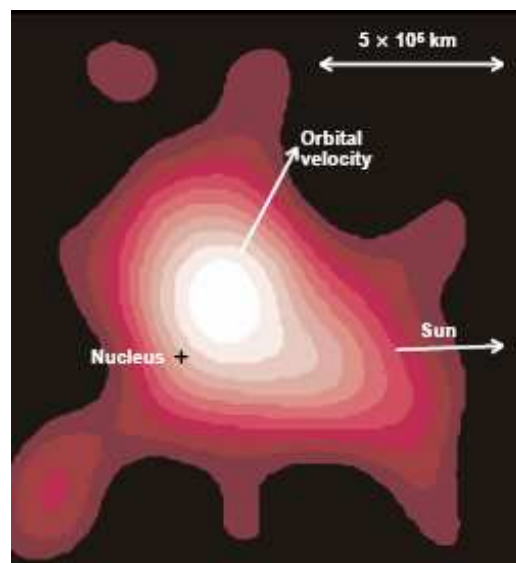


Figure 2.4: The EUV image of comet C/1995 O1 (Hale-Bopp) as observed by the *Extreme Ultraviolet Explorer* (Krasnopolsky *et al*, 1997b).

There is no correlation with an optical image from the same time. The optical emission is driven by scattering of sunlight by dust, and therefore the optical picture mapped the location of dust emanating from the comet and occupying a region of space that was radiating in x-rays. The maximum brightness was located  $(2.7 \pm 1.2) \times 10^5$  km from the nucleus, again on the sunward side and displaced from the Sun-comet

vector. The brightness was reduced by a factor of 3 from the peak at a distance of  $2 \times 10^5$  km. It was reasoned that the larger heliocentric distance of Hale-Bopp would result in a much lower x-ray flux if the emission were dust driven, due to the factor 2 difference in the dust temperatures; if the emission were driven by the gas production rate, then the larger heliocentric distance would reduce the emission by a factor of 1.5. The observed x-ray emission rate was  $\sim 80\%$  of the Hyakutake rate, suggesting that the emission was gas driven. The lack of correlation between the x-ray and optical images strengthened this theory.

### ***BeppoSAX***

An independent observation was carried out slightly before the *EUVE* mission by Owens *et al* (1998) using *BeppoSAX*<sup>6</sup>. During the observation on 10th September 1996, the comet's geocentric and heliocentric distances were 2.87 and 3.13 AU respectively.

Primarily, the *Low-Energy Concentrator Spectrometer (LECS)*, with an energy range of 0.1-10.0 keV, was used to image the comet and record a low resolution spectrum. From the 11.5 ks exposure, a weak source (with a total energy flux of  $(2.1 \pm 0.3) \times 10^{-12}$  erg cm<sup>-2</sup> s<sup>-1</sup> below 2 keV) was detected in the vicinity of the cometary nucleus. The x-ray image and spectrum from this exposure are shown in figures 2.5 and 2.6 respectively.

The brightest point in figure 2.5 is  $(2.1 \pm 1.3) \times 10^5$  km from the nucleus, which is comparable to the value suggested in the *EUVE* observation (Krasnopolsky, 1997b). A total of 246 x-rays were collected, compared to the 113 detections made with a background exposure of the same region. The average luminosity is reported as  $4.8 \times 10^{16}$  erg s<sup>-1</sup>, making Hale-Bopp the brightest x-ray comet in the literature, despite having the largest heliocentric distance.

It was claimed that the spectrum is inconsistent with models involving emission from gas, as there is no significant feature at 0.57 keV (corresponding to emission from O<sup>6+</sup>). From the low statistics of the spectrum, it is difficult to draw any conclusions about which spectral features may or may not be present. It was noted that the best fit was a thermal bremsstrahlung continuum, with  $kT_e = 0.29$  keV, which is similar to the best fit to the C/1990 K1 (Levy) spectrum.

The *Medium-Energy Concentrator Spectrometer (MECS)* on *BeppoSAX* was also used to observe Hale-Bopp. The energy range of *MECS* is 1.3–10 keV, and a low signal was detected below 2 keV with similar to the *LECS* exposure in the same energy range. If this emission were from the comet, Hale-Bopp would be the only comet in the literature to exhibit any x-ray emission at an energy greater than 1 keV.

---

<sup>6</sup>See <http://www.asdc.asi.it/bepposax/>

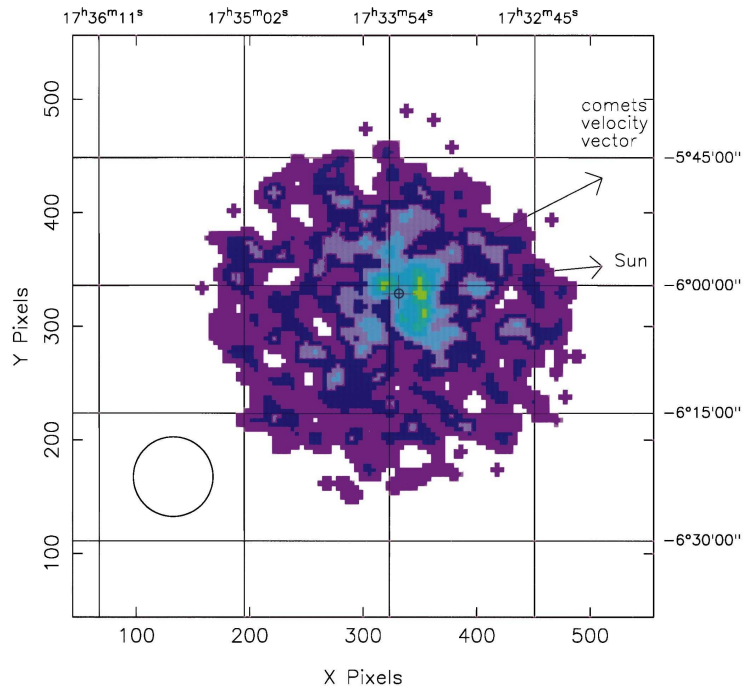


Figure 2.5: The x-ray image of comet C/1995 O1 (Hale-Bopp) as observed by the *LECS* on *BeppoSAX* (Owens *et al.*, 1998).

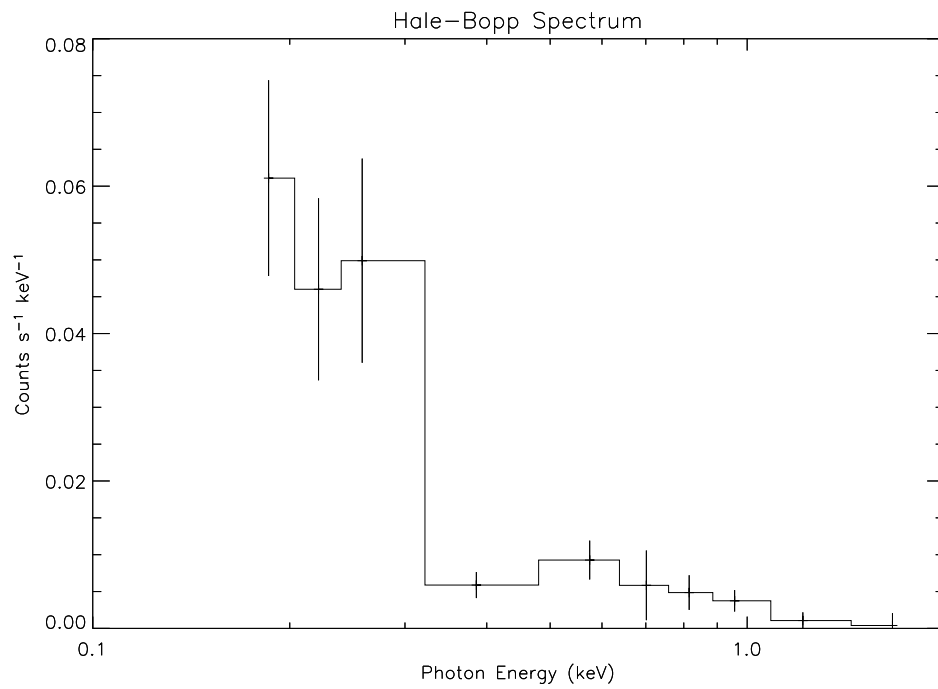


Figure 2.6: The x-ray spectrum of comet C/1995 O1 (Hale-Bopp) as observed by the *LECS* on *BeppoSAX* (Owens *et al.*, 1998).

Comparisons with optical images show an apparent correlation with the ejection of a dust plume. Coupled with the fact that Hale-Bopp was a particularly dusty comet, the large x-ray flux and the lack of symmetry around the Sun-comet vector, Owens *et al* (1998) suggest that the x-ray emission from this observation and from comets in general is driven by dust.

## ***ROSAT***

At this point, *ROSAT* had been the most popular and successful satellite for cometary x-ray observations: the first six observations utilised this satellite. Several *ROSAT* observations of Hale-Bopp were attempted: two in September 1996 (coinciding with attempts using *EUVE* and *BeppoSAX*) and one observation in September, October and December 1997 (Lisse *et al*, 1999a). All of the exposures were of comparable length to the total Hyakutake observation. None of the *ROSAT* missions detected the comet in x-rays.

This result, together with results from the *ROSAT* All-Sky Survey (Dennerl *et al*, 1997), indicated that the emission was not driven by dust, and it was suggested that a high dust-to-gas ratio could even stifle the x-ray emission process.

### **2.1.7 *ROSAT* and *EUVE* – Comet 2P/Encke – July 1997**

*ROSAT* and *EUVE* were used simultaneously to observe comet 2P/Encke (Lisse *et al*, 1999b) during its close approach to Earth in July 1997. The total observing time with *ROSAT* was 62 ks, and the *EUVE* exposure was 103 ks. During the period of the *ROSAT* observations, the heliocentric and geocentric distances of the comet ranged from 0.988 to 1.07 AU and 0.191 to 0.204 AU (with the closest approach distance being 0.190 AU). The total x-ray emission power was  $4 \times 10^{14}$  erg s<sup>-1</sup>.

The morphology was similar to Hyakutake, with 90% of the x-ray emission confined to  $5 \times 10^4$  km and the peak x-ray brightness located  $5 \times 10^3$  km from the nucleus, at an angle of 60° from the Sun-comet line. For Hyakutake this angle was  $\sim 10^\circ$  (Lisse *et al*, 1996). Extreme ultraviolet emission was detected up to  $1.1 \times 10^5$  km from the nucleus.

The x-ray signal was highly variable over a matter of hours, as is shown in the light curve in figure 2.7. Figure 2.7 also shows the quiescent solar wind magnetic field strength, the solar x-ray flux, and the solar proton flux (Lisse *et al*, 1999b).

The lack of any correlation with the solar x-ray flux is evidence to rule out any scattering mechanisms, especially considering the strong correlation between the magnetic field strength and the proton flux.

A simple model of the propagation of broad solar wind characteristics was used to

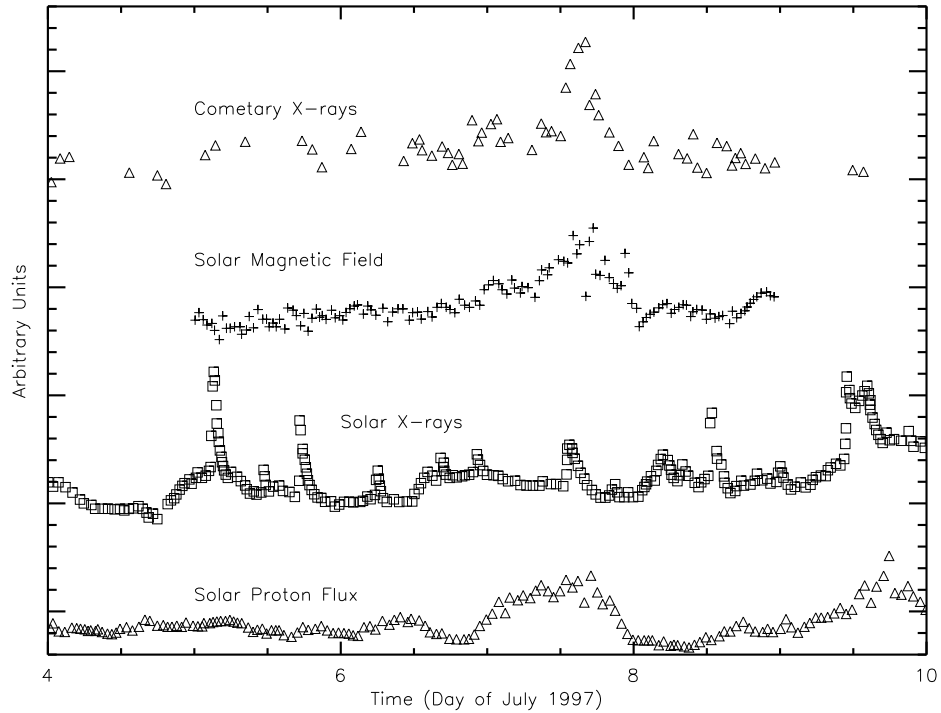


Figure 2.7: Simultaneous measurements of the cometary x-ray signal, the solar magnetic field strength, the solar x-ray signal and the solar proton flux. The lack of correlation with solar x-rays disqualifies solar x-ray scattering as the primary source, and the strong correlation with the magnetic field strength and proton flux suggest that the emission is driven by the solar wind.

derive a delay of 0.17 days between the conditions at the comet being measured near the Earth, which appears to agree well with figure 2.7.

A spectrum was obtained, although with low spectral resolution due to the use of broadband photometry. The spectrum was similar to those from comets C/1996 B2 (Hyakutake), C/1990 K1 (Levy) and C/1995 O1 (Hale-Bopp) again suggesting that there is a common emission mechanism in each case.

Analysis of the images suggested that the EUV and x-ray emission was from the same approximate volume, and that the average x-ray energy was roughly constant with cometocentric distance. The large offset angle of the brightest point was too large to be due to perturbation of the solar wind by the comet's trajectory, and is so far unexplained. Possible explanations were offered: anti-correlation with a dust-jet, as appears to be the case with Hale-Bopp (Krasnopolsky *et al*, 1997b); or, if the emission were caused by bremsstrahlung, acceleration of the emitting electrons by a streaming instability (which would depend on the magnetic field strength). Despite the acknowledgement that emission driven by energetic electrons could explain the light curve and morphology, and provided the best spectral fit, it was concluded that the most likely emission mechanism was charge exchange.

### 2.1.8 EUVE – Comet C/1996 B2 (Hyakutake) – Mar 1996

Extreme ultraviolet spectra from comet C/1996 B1 (Hyakutake) were published by Krasnopolsky and Mumma (2001). *EUVE* was used, and the results were over the range 80–700 Å (155–17 eV). The resolution of the spectra is low, and it is difficult to explain many of the features with any confidence. An example spectrum is shown in figure 2.8.

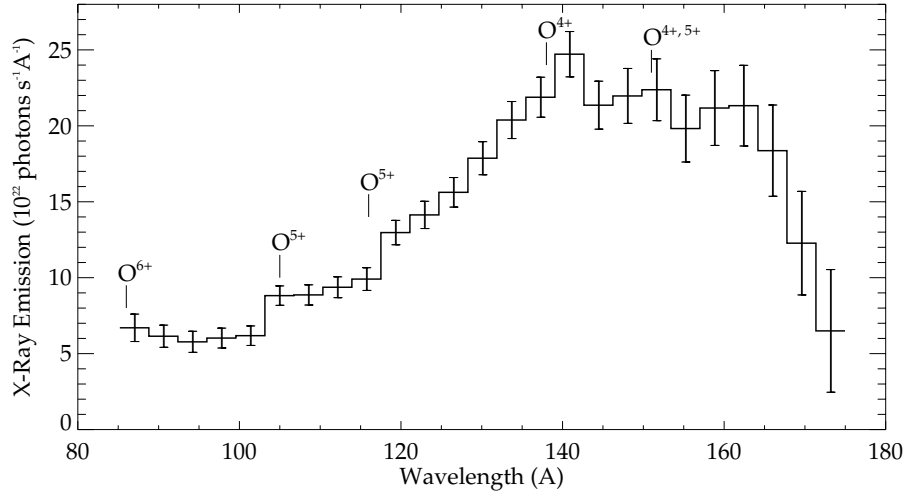


Figure 2.8: One of the *EUVE* spectra of comet C/1996 B2 (Hyakutake) published by Krasnopolsky and Mumma (2001).

It was also noted that the background signal exceeded the signal from the comet. Part of the subtracted background count included the helium 584Å (21.2 eV) line. As a result of this removal, the line is not present at all (in fact the final signal is large and negative). This contrasts with the *EUVE* observation of comet C/1995 O1 (Hale-Bopp), which detected strong emission from this line (Krasnopolsky *et al*, 1997b). The apparent absence of this line could be explained by the variation of the charge-exchange cross-section with collision speed (Bodewits *et al*, 2004). The other feature observed in Hale-Bopp (Owens *et al*, 1998), at energies attributable to both helium and oxygen, is detected in Hyakutake, but is attributed solely to oxygen. Emission from He<sup>+</sup> at 304Å (40.8 eV) was also observed.

It was stated that lines were observed from oxygen ions of several charge states, indicating that the plasma was collisionally thick to charge exchange. Unlike the previously published x-ray spectra, the data could not be represented by a thermal bremsstrahlung. As a result, it was claimed that “convincing proof that charge transfer ... is the main source of X-ray and extreme ultraviolet photons in comets” was demonstrated.

### 2.1.9 CXO – Comet C/1999 S4 (LINEAR) – July 2000

The following generation of x-ray satellites allowed more detailed observations to be performed. The first cometary x-ray observation by the *Chandra X-ray Observatory* was that of comet C/1999 S4 (LINEAR) (Lisse *et al*, 2001). Two separate observations were performed, before and after the comet broke-up into several smaller pieces, with the x-ray signal decreasing substantially after the break up of the nucleus.

An independent analysis of this observation (and observations of other comets by *Chandra*) is presented in chapter 3.

The pre-breakup observation, when the comet was 0.801 AU and 0.530 from the Sun and Earth respectively, lasted for 9.39 ks, in which time 13, 500 cometary photons were collected. The emission was again from a crescent region on the comet's day-side, with a peak x-ray brightness at  $\sim 2 \times 10^4$  km, and extending to  $10^5$  km ( $3 \times 10^5$  km in the EUV).

The position of the bow shock was estimated to be, by comparison with Halley,  $1.1 \times 10^4$  km, so most of the emission was from outside the bow shock (Lisse *et al*, 2001).

The published x-ray spectrum from the first observation is shown in figure 2.9.

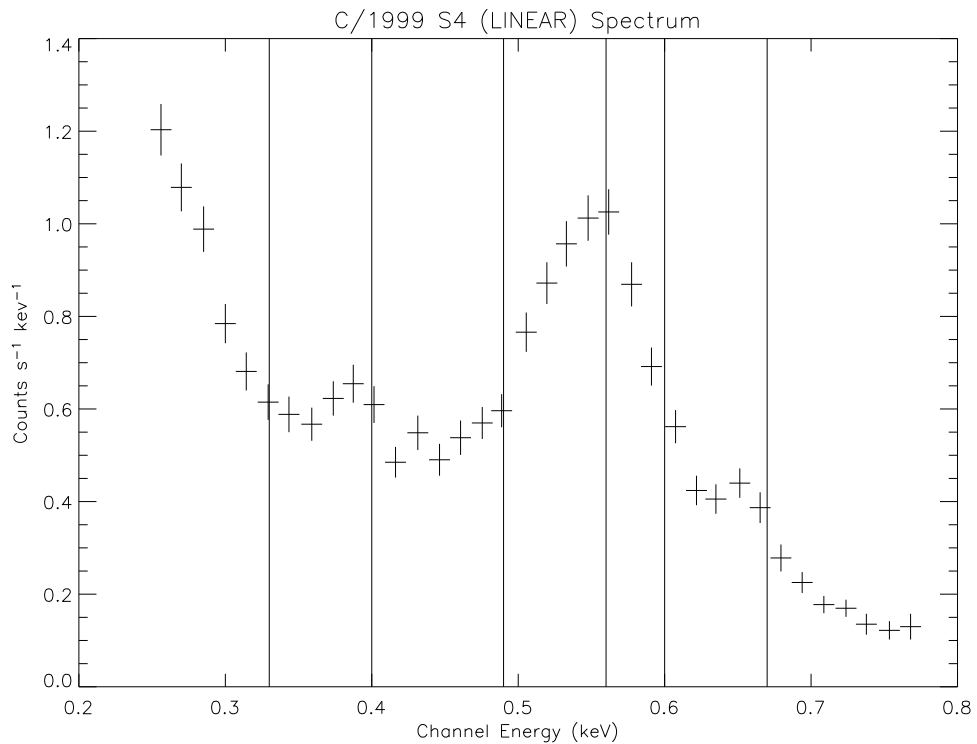


Figure 2.9: The x-ray spectrum of comet C/1999 S4 (LINEAR) from the *Chandra X-ray Observatory* (Lisse *et al*, 2001) with  $1\sigma$  error bars. The position of lines from the best fit are shown. The fit also includes a bremsstrahlung continuum with a temperature of 0.39 keV.

The spectrum provided the first clear evidence that x-ray lines contributed a signif-

icant part of the emission, as a thermal bremsstrahlung continuum was insufficient to completely explain the spectrum. The best fit to the data was found to be a superposition of x-ray lines at 0.33, 0.40, 0.49, 0.56, 0.60 and 0.67 keV, and a bremsstrahlung continuum with  $kT_e = 0.39$  keV.

### **2.1.10 CXO – Comet C/1999 T1 (McNaught-Hartley) – Jan 2001**

*Chandra* was also used to observe comet C/1999 T1 (McNaught-Hartley) (Krasnopolsky *et al.*, 2002). The observation was conducted over 6 days in January 2001, and was composed of five hour-long exposures.

The morphology was similar to that of the previously observed comets. In this case, the source emission appeared to extend to less than half of the CCD area. By assuming that a uniform background signal was present over the entire chip, the signal from an annulus with a minor radius of 353 pixels was subtracted from the signal from a circular region with radius 353 pixels. This approach is incorrect, as the effective area of the CCD varies over the chip area.

After removal of the background signal using the above technique, a total of 16,720 counts were detected.

The x-ray power emitted for photons with energy greater than 150 eV in an aperture of  $1.5 \times 10^5$  km was  $7.8 \times 10^{15}$  erg s<sup>-1</sup>. The intensity of the emission varied by a factor of 5 over the course of the observation period.

The published spectra (both before and after removal of a background signal) are shown in figure 2.10.

The intensity of the emission varied by up to a factor of 5 over the course of the observing period. The morphology formed the familiar crescent shape.

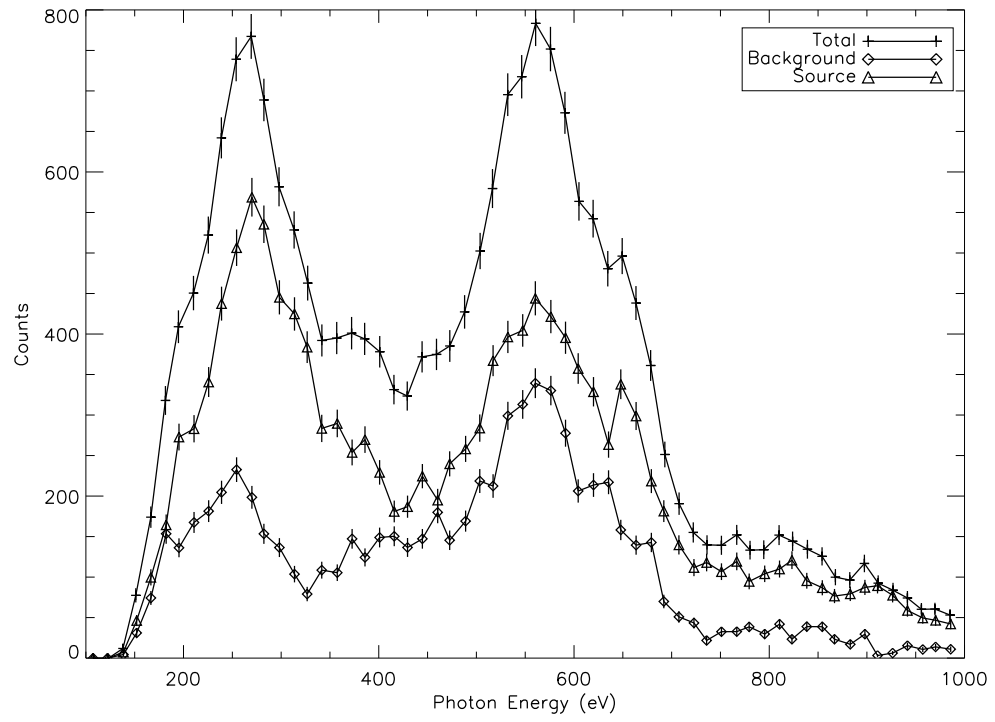


Figure 2.10: The x-ray spectrum of comet C/1999 T1 (McNaught-Hartley) from the *Chandra X-ray Observatory*, taken from Krasnopolsky *et al.*, (2002).

### 2.1.11 XMM-Newton – Comet C/2000 WM1 (LINEAR) – Dec 2001

The longest observation to date was of comet C/2000 WM1 (LINEAR) using *XMM-Newton* (Dennerl *et al*, 2003). The observation was almost uninterrupted over 17 hours, and more than  $10^6$  photons were collected. The overall morphology was similar to previous observations, with the peak x-ray brightness located 15,000 km from the nucleus on the Sun-nucleus vector. The emission was traced out to 250,000 km from the nucleus due to the sensitivity of the observation. The morphology was discussed further by Wegmann *et al* (2004), who gives the x-ray luminosity as  $2.14 \times 10^{16}$  erg  $s^{-1}$ , and Wegmann and Dennerl (2005). The x-ray spectrum from the inner coma is shown in figure 2.11.

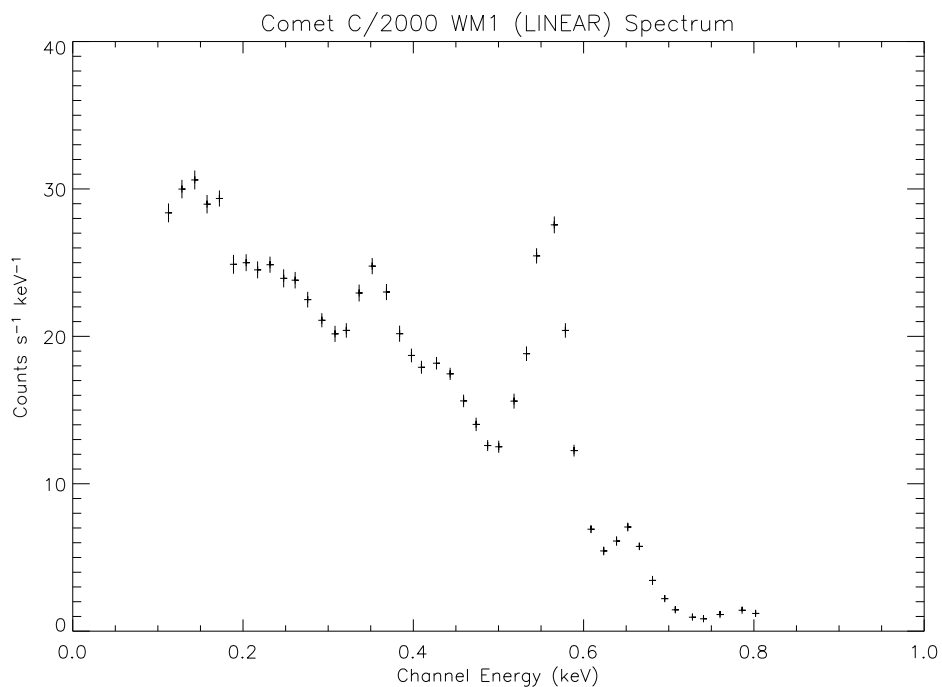


Figure 2.11: The x-ray spectrum of comet C/2000 WM1 (LINEAR) from *XMM-Newton* (Dennerl *et al*, 2003).

The article by Dennerl *et al*, (2003) gives few details of the observation, and seems to indicate that a more extensive paper on the observation will follow. No further articles on the observation have been published.

The paper states that “the results so far clearly demonstrate that the X-ray emission is caused by charge exchange”.

### 2.1.12 CXO – Comet 2P/Encke – Nov 2003

In November 2003, comet 2P/Encke became the first comet to be observed in two separate orbits (Lisse *et al*, 2005). For the second observing period, *Chandra* was used, and so data from the observation are included in the *Chandra* catalogue presented in chapter 3.

At the time of the *Chandra* observation, Encke was 0.27 AU from the Earth and 0.88 from the Sun. The total exposure lasted 44 s. The background corrected spectrum is shown in figure 2.12 (Lisse *et al*, 2005).

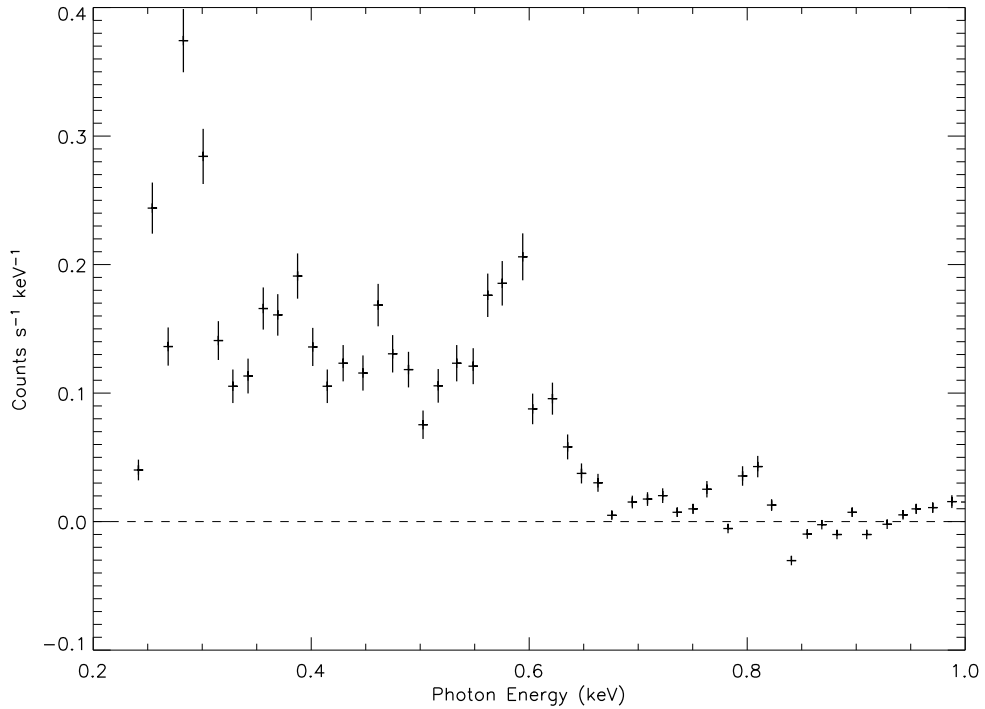


Figure 2.12: The x-ray spectrum of comet 2P/Encke from the *Chandra X-ray Observatory*, taken from Lisse *et al* (2005).

It was found that the best fits to the data were obtained using a six line model with lines at 0.283, 0.279, 0.464, 0.553, 0.600, 0.795 eV, and a combination of a thermal bremsstrahlung continuum with temperature 0.270 keV and 4 emission lines with energies 0.285, 0.377, 0.463 and 0.570 keV.

## 2.1.13 Collective Results

General results from these observations are given in table 2.1.

Comet	Satellite	Date	$R_{90\%}$	$R_{x-max}$	$R_H$	$\Delta$	$P_x$	$P_{opt}$	$Q_{gas}$
Bradfield	<i>Einstein</i>	2/80	—	—	1.13	0.47	—	—	—
Hyakutake	<i>ROSAT</i>	3/96	$10^5$	$1.8 \times 10^4$	1.07	0.12	$4 \times 10^{15}$	$3 \times 10^{20}$	$2 \times 10^{29}$
Hyakutake	<i>EUVE</i>	3/96	—	$6 \times 10^4$	1.07	0.12	—	—	—
Tabur	<i>ROSAT</i>	9/96	$9 \times 10^5$	$3 \times 10^5$	1.09	0.51	$4 \times 10^{15}$	$3 \times 10^{19}$	—
Levy	<i>ROSAT</i>	9/90	—	$10^4$	1.25	0.57	$1.16 \times 10^{16}$	$10^{20}$	—
T-K	<i>ROSAT</i>	11/90	—	—	1.37	1.08	$3 \times 10^{15}$	$10^{19}$	—
H-M-P	<i>ROSAT</i>	7/90	—	—	1.00	0.29	$4 \times 10^{13}$	$10^{17}$	—
Aria	<i>ROSAT</i>	11/90	—	—	1.47	1.20	$3 \times 10^{14}$	$10^{18}$	—
D'Arrest	<i>EUVE</i>	9/95	—	—	1.42	0.47	—	—	$1.2 \times 10^{28}$
Bradfield	<i>EUVE</i>	11/95	—	—	1.50	1.26	—	—	$4 \times 10^{27}$
Hale-Bopp	<i>EUVE</i>	9/96	$10^5$	$2.7 \times 10^5$	3.07	2.91	$2 \times 10^{15}$	$5 \times 10^{21}$	$6 \times 10^{29}$
Hale-Bopp	<i>BeppoSAX</i>	9/96	$8 \times 10^5$	$2 \times 10^4$	3.13	2.87	$4.8 \times 10^{16}$	—	—
Hale-Bopp	<i>ROSAT</i>	9/96	—	—	3.0	2.9	—	$5 \times 10^{21}$	$2 \times 10^{29}$
Encke	<i>ROSAT</i>	7/97	$5 \times 10^5$	$5 \times 10^3$	1.00	0.190	$4 \times 10^{14}$	$8 \times 10^{17}$	$2 \times 10^{27}$
1999 S4	<i>Chandra</i>	7/00	$10^5$	$2 \times 10^4$	0.801	0.530	$2 \times 10^{15}$	—	$3 \times 10^{28}$
McN-H	<i>Chandra</i>	1/01	$1.5 \times 10^5$	$2.2 \times 10^4$	1.39	1.24	$7.8 \times 10^{15}$	—	$10^{29}$
2000 WM1	<i>XMM</i>	12/01	$2 \times 10^5$	$1.5 \times 10^4$	1.02	0.41	$2.14 \times 10^{16}$	—	$5 \times 10^{28}$
Encke	<i>Chandra</i>	11/03	$4 \times 10^4$	—	0.88	0.27	$3.8 \times 10^{14}$	$2 \times 10^{19}$	$8 \times 10^{27}$

Table 2.1: Overview of Observations.  $R_{90\%}$  is the radius encapsulating 90% of the x-ray emission in km,  $R_{x-max}$  is the position of the peak x-ray brightness in km,  $R_H$  is the heliocentric distance of the comet in A.U.,  $\Delta$  is the geocentric distance of the comet in A.U.,  $P_x$  is the x-ray power over the aperture  $R_{90\%}$  in  $\text{erg s}^{-1}$ ,  $P_{opt}$  is the optical power over the same aperture, and  $Q_{gas}$  is the outgassing rate in  $\text{mol s}^{-1}$ .

From the observations, some general features of the x-ray emission can be described.

It is important that each observation is not given equal weight in this analysis. Observations with *CXO* and *XMM-Newton* are more valuable than those with older instruments due to the increase in the effective area and spectral resolution of their detectors. Also, it is possible that the processes driving extreme ultraviolet emission may subtly differ from the cause of x-rays in the comet, so results from *EUVE* should be regarded with some trepidation.

### X-ray Emission Morphology

The emission morphology is similar in almost every case, suggesting that a common emission mechanism may be acting in each comet. The emission regions forms a large crescent on the day side of the comet, almost symmetrical around the Sun-comet axis. The exceptions to this are the dimmest (and statistically least significant) comets Tabur and Tsuchiya-Kiuchi, and comet Hale-Bopp. In the case of Hale-Bopp, the emission appears to anti-correlate with a large dust plume, suggesting that a large dust production rate is detrimental to x-ray production.

The emission tends to extend to between  $10^5$  and  $10^6$  km. Lisse *et al* (2004) demonstrated that the radial extent of the emission roughly scaled linearly with the outgassing rate  $Q_{\text{gas}}$ . No x-ray emission has been detected from cometary tails in any of the observations to date. The morphology of several comets is modelled by Wegmann *et al* (2004).

### X-ray Power

In general, the x-ray emission power varies with  $Q_{\text{gas}}^{1/2}$  (Dennerl *et al*, 1997; Lisse *et al*, 1999b). A comparison between the x-ray and optical luminosities is shown in figure 2.13.

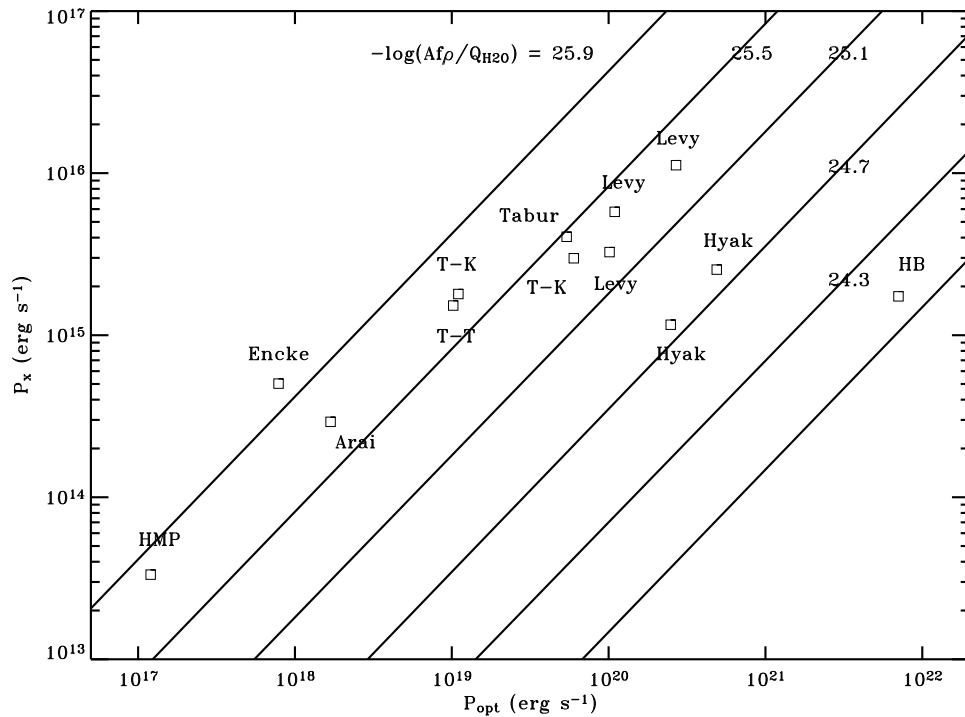


Figure 2.13: The x-ray luminosity vs. optical luminosity for comets in the *ROSAT* All-Sky Survey. The solid lines show contours of the ratio of  $Af\rho$  to the outgassing rate, such that the lower right corner would represent a particularly dusty comet and the upper left corner would represent a very dust poor comet. Comets with high dust production rates had lower x-ray to optical luminosity ratios (Dennerl *et al*, 1997; Lisse *et al*, 1999b)

The term  $Af\rho$  in figure 2.13 is the product of the dust albedo,  $A$  (the ratio of reflected sunlight to incident sunlight for a dust grain), the filling factor,  $f$  (the total cross section of dust grains in the field of view) and the radius of the field of view,  $\rho$  (A'Hearn *et al*, 1984). This term provides an aperture independent measure of the amount of dust present in a comet. This demonstrates that dust-poor comets are more efficient x-ray emitters.

## X-ray Spectra

The early x-ray observations of comet with *ROSAT* (Dennerl *et al*, 1997) and *Bep-poSAX* (Owens *et al*, 1998) have produced low resolution energy spectra. These spectra are best fitted with thermal bremsstrahlung models, although these results carry little weight. Observations by *Chandra* (Lisse *et al*, 2001, 2005; Krasnopolsky *et al*, 2002), and subsequently *XMM-Newton* (Dennerl *et al*, 2003) have demonstrated that at least some of the measured x-ray flux is from line emission. From these observation, it appears that the emitting ions include  $O^{6+}$  and  $O^{7+}$ , although it is difficult specify any other ions with any certainty.

## 2.2 *In Situ* Results from Comet 1P/Halley

In March 1986, a total of six spacecraft were sent to intercept comet 1P/Halley. In order of closest approach, they were *Giotto*, *Vega-1*, *Vega-2*, *Suisei*, *Sakigake* and the *International Cometary Explorer*. A large proportion of the data are archived by the Small Bodies Node<sup>7</sup>. Schematics of the trajectories of the *VEGA* and *Giotto* missions are shown in figure 2.14.

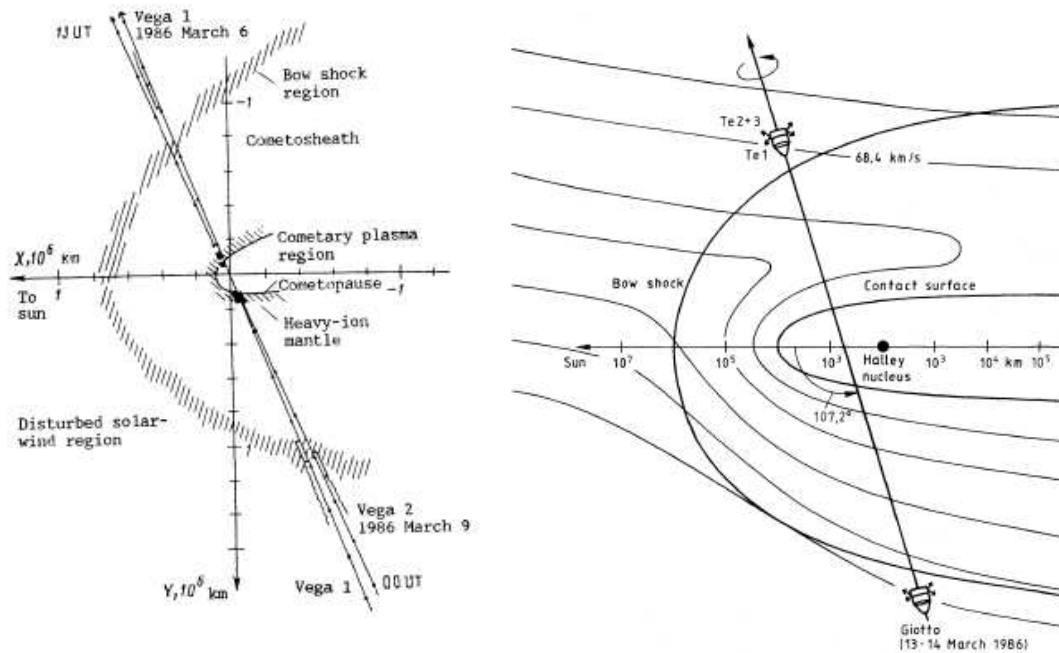


Figure 2.14: The trajectories of the *VEGA* (left) and *Giotto* (right) spacecraft through the atmosphere of comet 1P/Halley

Measurements relevant to cometary x-rays from *VEGA* and *Giotto* are presented here. This includes observations of neutral particles, solar wind ions, free electrons and electrostatic waves.

<sup>7</sup><http://pdssbn.astro.umd.edu/sbnhtml/comets/IHW/>

## 2.2.1 Neutral Particle Measurements

The neutral particle density was measured by the *Neutral Gas Experiment* on *Vega-1* (Keppler *et al*, 1986, Gringauz *et al*, 1986a, 1986b, Curtis *et al*, 1987) and by *Giotto's Neutral Mass Spectrometer* (Krankowsky *et al*, 1986). *Vega-1* results from both the inbound and outbound periods are shown in figure 2.15 (Gringauz *et al*, 1986b, Curtis *et al*, 1987).

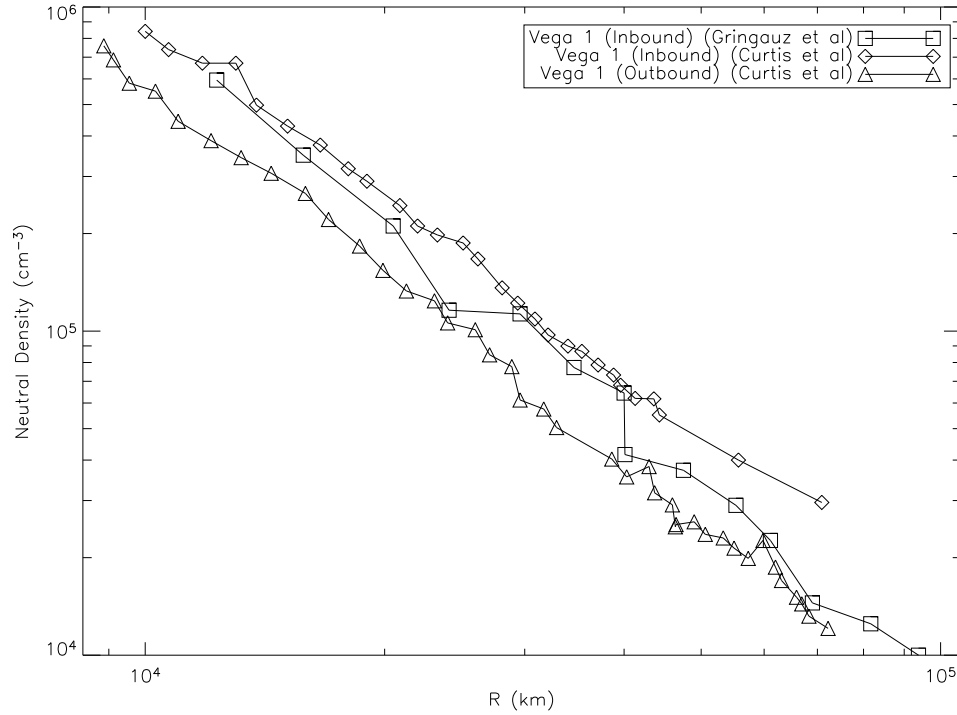


Figure 2.15: The neutral density profile through the atmosphere of comet 1P/Halley. The values are derived from the *Neutral Gas Experiment* (Curtis *et al*, 1987) and the *Ram Faraday Cup* (Gringauz *et al*, 1986b) on *Vega-1*.

The best fits to the data show an inverse square dependence on cometocentric distance with a corrective exponential decay factor, in accordance with the Haser formula (Haser, 1957). From this, the total outgassing rate for 1P/Halley was  $Q_{\text{gas}} = 1.3 \times 10^{30}$  molecules  $\text{s}^{-1}$  (Gringauz *et al*, 1987) or  $Q_{\text{gas}} = 1 \times 10^{30}$  molecules  $\text{s}^{-1}$  (Curtis *et al*, 1987).

The data from *Giotto's Neutral Mass Spectrometer (NMS)* indicated an outgassing rate of  $Q_{\text{gas}} = 6.9 \times 10^{29}$  molecules/s (Krankowsky *et al*, 1986).

The *Infrared Spectrometer (IKS)* on *Vega-1* was used to estimate production rates of several parent molecules (Moroz *et al*, 1987):  $Q_{\text{H}_2\text{O}} = 10^{30}$  molecules  $\text{s}^{-1}$ ,  $Q_{\text{CO}_2} = 2 \times 10^{28}$  molecules  $\text{s}^{-1}$ , and the production rate for various hydrocarbons is  $7 \times 10^{28}$  molecules  $\text{s}^{-1}$ . An upper limit for the production rate of CO is  $2 \times 10^{29}$  molecules  $\text{s}^{-1}$ . Profiles of neutral and ionic components are presented by Umbach *et al* (1998).

Note that the outgassing rates for 1P/Halley are higher than those for comets observed by x-ray satellites (see tables 2.1 and 3.2).

## 2.2.2 Solar Wind Ion Measurements

Measurements of solar wind ions in the atmosphere of 1P/Halley by the *Giotto Ion Mass Spectrometer/High Energy Range Spectrometer (IMS/HERS)* are presented by Shelley *et al* (1987) and Fuselier *et al* (1991). Results from Shelley *et al* (1987) are shown in figure 2.16.

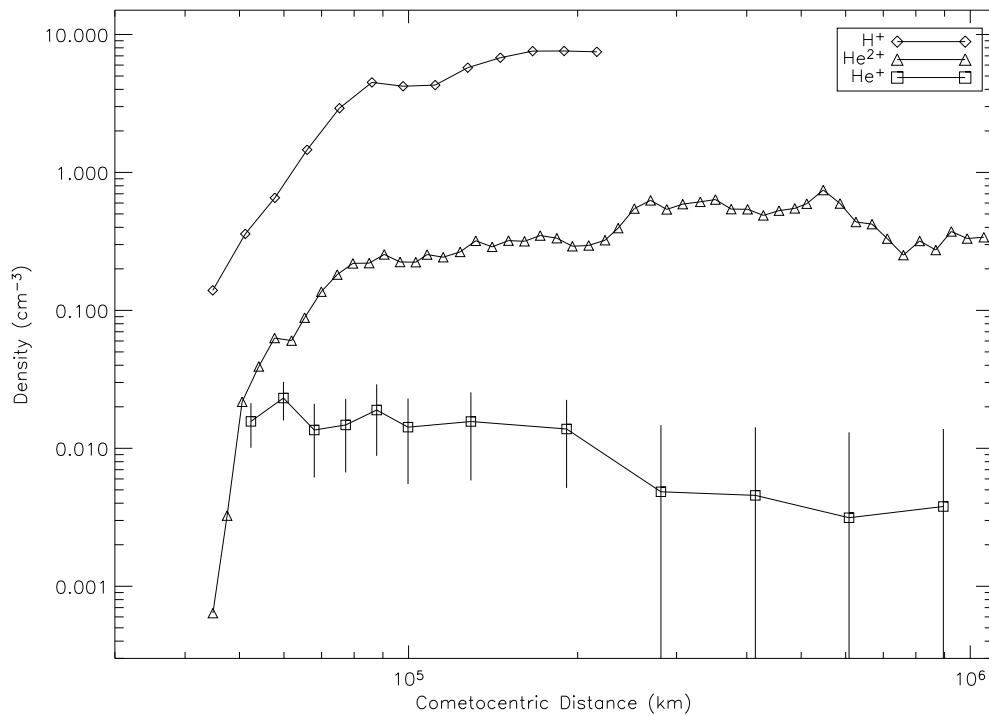


Figure 2.16: The density of solar wind ions in the atmosphere of 1P/Halley as measured by *Giotto IMS/HERS* (Shelley *et al*, 1987).

As helium is not present in the comet, all of the helium ions originate in the solar wind, where they are generally fully ionised. Figure 2.16 shows that the fractional abundance of He<sup>+</sup> increased as *Giotto* approached the nucleus, indicating that helium recombination has taken place. Balsiger *et al* (1986) reported detecting He<sup>2+</sup> as close as 5000 km from the nucleus.

## 2.2.3 Electron Measurements

### Vega-2 Measurements

The *PLASMAG-1* devices on the *Vega* spacecraft were capable of measuring the free electron distribution between 3 eV and 10 keV. Results from *VEGA-2* are published by Gringauz *et al* (1987). Approaching the cometopause, from a distance of  $8 \times 10^5$  km to  $1.6 \times 10^5$  km, the electron temperature decreases by a factor of two, from 40 eV to 20 eV.

Near the closest approach, from a distance of  $3 \times 10^4$  km to  $1.5 \times 10^4$  km, a significant population of 1 keV electrons is observed. The change in the distribution functions is illustrated in figure 2.17.

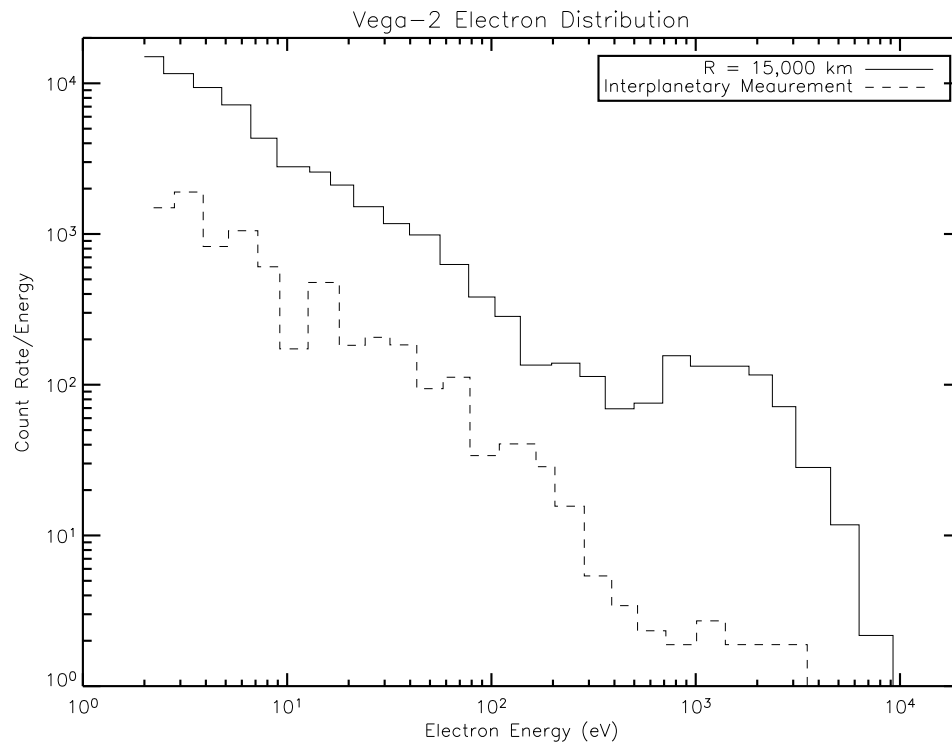


Figure 2.17: A comparison of electron distributions outside the cometary atmosphere (lower curve) and closer to the nucleus (upper curve).

After the craft reached  $1.5 \times 10^4$  km, the detector malfunctioned temporarily, and no data were returned until the outbound leg of the transit.

*VEGA-1* had an identical device, but unfortunately it was not operational by the time the spacecraft reached comet Halley.

### Giotto Measurements

The *Rème Plasma Analyzer* on *Giotto* included the *Electron ElectroStatic Analyzer* (*EESA*), which was capable of measuring the free electron distribution in three dimen-

sions. The results, presented by Rème *et al* (1986, 1993), are in excellent agreement with the *Vega-2* measurements outside the cometopause (at  $1.6 \times 10^5$  km). Within the cometopause, *EESA* did not detect any significant high energy ( $\sim 1$  keV) electrons.

### **Indirect *Giotto* Measurements**

Eberhardt and Krankowsky (1995) calculated electron temperatures from the measured ratio of the ions  $\text{CH}_3\text{OH}_2^+$  and  $\text{H}_3\text{O}^+$ . One of their models predicts an electron temperature of the order 100 eV at a distance of  $10^4$  km from the nucleus. Their other calculations produced lower temperatures in the same region, around 3 eV.

### **Conclusions**

The contradiction between the *Giotto* and *Vega* results is puzzling, and as yet unexplained. It has been suggested that the *Vega* detection of energetic electrons was due to an instrument effect, although Gringauz *et al* (1987) have shown this is not the case. Given that each observation is accurate, it was reasoned that the generation of energetic electrons is a sporadic phenomenon. It was suggested by Gringauz *et al* (1987) that the electrons were energised in a substorm, as suggested by Ip and Mendis (1976). However, Hudson *et al* (1981) predicted that the probability of an observation of one hour coinciding with a substorm was only a few percent. The transit period of *Vega-2* through the region featuring energetic electrons was less than 3 minutes. If the *Vega-2* transit did observe the effect of a substorm, it was a very fortunate observation.

A more plausible suggestion for the discrepancy is that the energetic electrons are present in a region corresponding to x-ray emission from comets: a semi-sphere with the brightest point  $\sim 10^4$  km from the nucleus on the sunward side. The closest approach for *Vega-2* was 9,000 km. The closest approach for *Giotto* was 600 km. Figure 2.14 shows that *Giotto* passed between the nucleus and the (assumed) x-ray emitting region. If x-ray emission is driven by energetic electrons, the contradiction between the *Giotto* and *Vega* results is explained by the morphology of x-ray observations.

## 2.2.4 Electric Field Measurements

The *Vega* probes were fitted with a *Low-Frequency Plasma Wave Detector (APV-N)* (Russian initials). Measurements are presented by Klimov *et al* (1986). The wave spectra before, during and after a measured sharp increase in the plasma density in the cometopause are shown in figure 2.18.

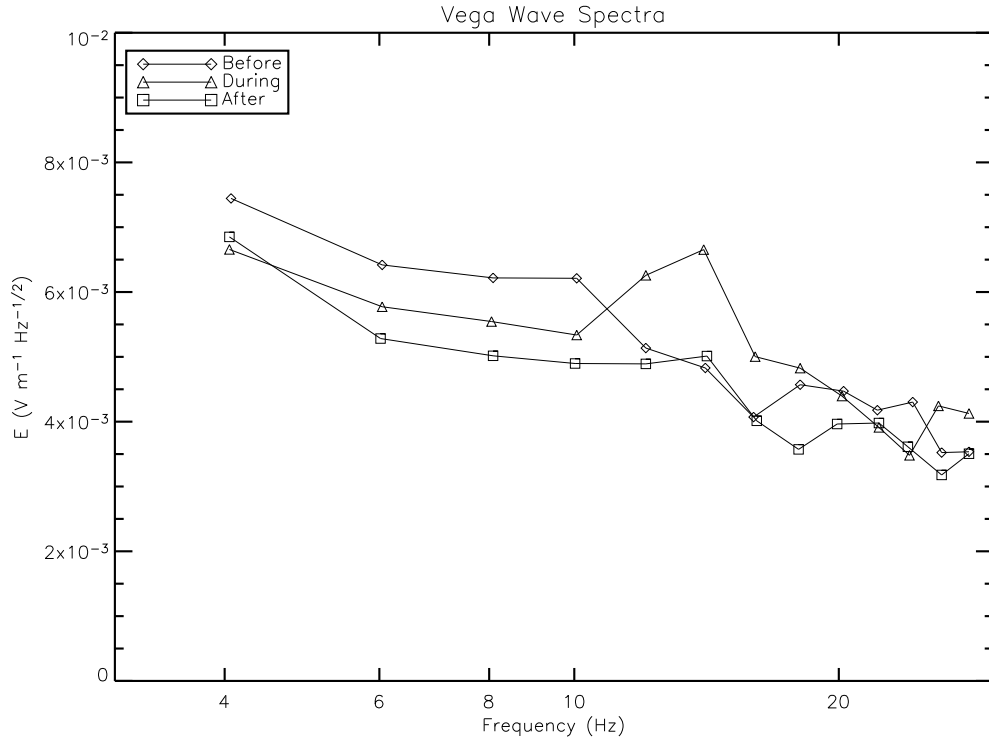


Figure 2.18: Wave activity before ( $\diamond$ ), during ( $\triangle$ ) and after ( $\square$ ) an abrupt increase in plasma density at  $R = 4.13 \times 10^4$  km. The peak at 14 Hz corresponds to the lower-hybrid frequency.

The increase in plasma density (detected by the *PLASMAG-1* device) and the corresponding increase in wave activity at 15 Hz occurred at a distance of  $\sim 4 \times 10^4$  km from the nucleus. The region of the wave activity is adjacent to a significant increase in the density of energetic  $\sim 1$  keV electrons from  $2.4 \times 10^4$  km (Gringauz *et al*, 1987). The peak in frequency is of the order of the lower-hybrid frequency for a magnetic field of 50 nT (Riedler *et al*, 1986), which is the geometric mean of the electron and ion gyrofrequencies. From this, it is possible that the electrons were accelerated through a resonant energy transfer from the electrostatic waves. This is discussed in section 4.1.2.

## 2.3 Emission Models

Previously suggested emission models are listed here, and brief details are given for the methods that are still considered plausible.

### 2.3.1 Discounted Theories

Krasnopolsky (1997a) examined the potential of several x-ray emission models. The conclusion was that the following models could not match the x-ray flux of models that involve the interaction of the solar wind and the outgassing cometary atmosphere. Further reasons to discount the models are given here.

#### Atmospheric Substorms

Atmospheric substorms, analogous to those observed in the Earth's aurora, were suggested by Ip and Mendis (1976). Hudson *et al* (1981) used this mechanism as motivation for an attempted detection of x-rays from comet Bradfield (see section 2.1.1). This theory gained some credence through the apparent sporadic nature of the energetic electrons detected in comet Halley (Gringauz *et al*, 1987). However, as explained in section 2.2.3, the contradiction between *Giotto* and *Vega* results could be due to the spacecraft passing through different regions of the cometary atmosphere. In addition to this, the x-ray light curves from comets, although variable, have been significantly larger than the x-ray background in almost every observation. This indicates that the emission mechanism behind cometary x-rays is more stable than the substorm model.

#### Scattering of Solar X-rays

The lack of correlation between the solar x-ray flux and cometary x-ray light curves, as demonstrated by Lisse *et al* (1999) (see figure 2.7) sufficiently shows that the x-ray emission is not scattering of solar x-rays.

#### Dust-Driven Mechanisms

Dennerl *et al* (1997) demonstrated a general trend of dusty comets being less efficient x-ray emitters. This is supported by an anti-correlation between the x-ray morphology of comet Hale-Bopp and an ejected dust jet (Krasnopolsky *et al*, 1997). Therefore, x-ray emission from comets is not driven by dust, and may even be quenched by the presence of dust.

### 2.3.2 Charge-Exchange Driven Emission

Currently, the most widely accepted explanation of cometary x-rays is charge exchange between highly ionised minor species in the solar wind and neutral particles emanating from the nucleus of the comet. The development of the charge exchange model is presented here, again in chronological order in respect of publication date.

Cravens (1997) first suggested a charge exchange model to explain cometary x-ray emission. Highly ionised minor species in the solar wind, such as  $O^{8+}$ ,  $O^{7+}$  and  $C^{6+}$ , capture bound electrons from neutral atoms and molecules in the cometary atmosphere. After the charge transfer, the recombined ions are in an excited state. This excited ion will radiatively cascade to the ground system by one or more transitions, some of which will produce x-ray photons. The emission spectrum described by Cravens (1997) was composed of dozens of emission features, most of which have energies less than a few hundred eV.

The model proposed by Cravens (1997) was partly based on the observed charge exchange products in the coma of comet 1P/Halley (Shelley *et al*, 1987). Ip (1989) explored the role of charge exchange reactions in the formation of the cometopause at  $\sim 1.4 \times 10^4$  km in comet 1P/Halley (Gringauz *et al*, 1986a, 1986b) and found that charge exchange did not contribute. Ip (1989) did note that charge transfer could significantly deplete solar wind ions within the range  $\sim 6 - 8 \times 10^4$  km from the nucleus.

The preliminary picture of cometary charge exchange developed by Cravens (1997) demonstrated that the process was plausible near the range suggested by Ip (1989).

Häberli *et al* (1997) considered emission driven by charge exchange within a 3D magnetohydrodynamic fluid model of the comet-solar wind atmosphere. They found that their models agreed well with the morphology and luminosity of comet C/1996 B2 (Hyakutake).

Wegmann *et al* (1998) synthesised spectra from charge exchange reactions as would be observed by a device similar to *ROSAT*. They found that *ROSAT* would not be able to distinguish between their charge exchange emission spectrum and a thermal bremsstrahlung with  $kT_e = 0.2$  keV. Wegmann *et al* (1998) also considered the emission in the context of a simple hydromagnetic representation of the comet-solar wind atmosphere, and found an agreement between their model and the observed morphologies. Wegmann *et al* (1998) concluded that the results of Häberli *et al* (1997) were incompatible with the observation of comet C/1996 B2 (Hyakutake). In addition to considering a charge exchange model, Wegmann *et al* (1998) also considered bremsstrahlung by electrons, as is discussed in the following section.

Beiersdorfer *et al* (2003) have compared laboratory charge-exchange results with the x-ray spectrum of comet C/1999 S4 (LINEAR) (Lisse *et al*, 2001). They used

the spare *X-Ray Spectrometer* microcalorimeter detector from *ASTRO-E2*, which has a resolution of 10 eV. They installed the *XRS* on the Lawrence Livermore *Electron Beam Ion Trap (EBIT)*, and measured charge exchange emission lines from ions of carbon, nitrogen and oxygen following collisions with selected gases.

They observed that the spectrum of helium-like oxygen is dominated by the forbidden  $1s2s\ ^3S_1 \rightarrow 1s^2\ ^1S_0$  transition, though to a smaller degree than they predicted. Beiersdorfer *et al* (2003) noted that this contradicts earlier studies: Häberli *et al* (1997), Wegmann *et al* (1998) and Schwadron and Cravens (2000) predicted that the  $1s2p\ ^1P_1 \rightarrow 1s^2\ ^1S_0$  resonance transition would be the strongest; and Kharchenko and Dalgarno (2001) who used the  $1s2p\ ^3P_1 \rightarrow 1s^2\ ^1S_0$  intercombination transition. As is demonstrated in section 4.4.2, the ratio of these lines is a strong indicator of the emission mechanism.

In the hydrogen-like case, the Lyman- $\alpha$  lines dominated, but the other Lyman series lines (up to and including  $\epsilon$ ) were also prominent.

Strong emission from  $n = 3, 4$  is explained by double capture reactions (the significance of which in cometary atmospheres is discussed by Ali *et al*, 2005), and the magnitude of lines from these levels compared to the magnitude of emission from  $n_c$  (the preferred capture level) shows that double capture reactions are about as likely as the single capture case.

From their results they have build a spectrum using He- and H-like C, N and O, and have compared the result to the spectrum observed from LINEAR 1999 S4 (Lisse *et al*, 2001). The spectrum contains 24 lines, and is convolved with the instrumental response function of *Chandra's ACIS-S* device, with a spectral resolution of 100 eV. Their results are shown in figure 2.19.

Bodewits *et al* (2004, 2006) used an experimental method developed by Lubinski *et al* (2001) to synthesis cometary x-ray spectra. The experimental method allows the measurement of state selective charge exchange cross sections at velocities between 30 and 1500 km s<sup>-1</sup>, so both slow and fast solar wind conditions can be represented. Experiments to date have included He<sup>+,2+</sup>, O<sup>6+,7+</sup>, C<sup>5+,6+</sup> and N<sup>5+,6+</sup> as receiver species, and donors have included neutral H, H<sub>2</sub>, He and CO.

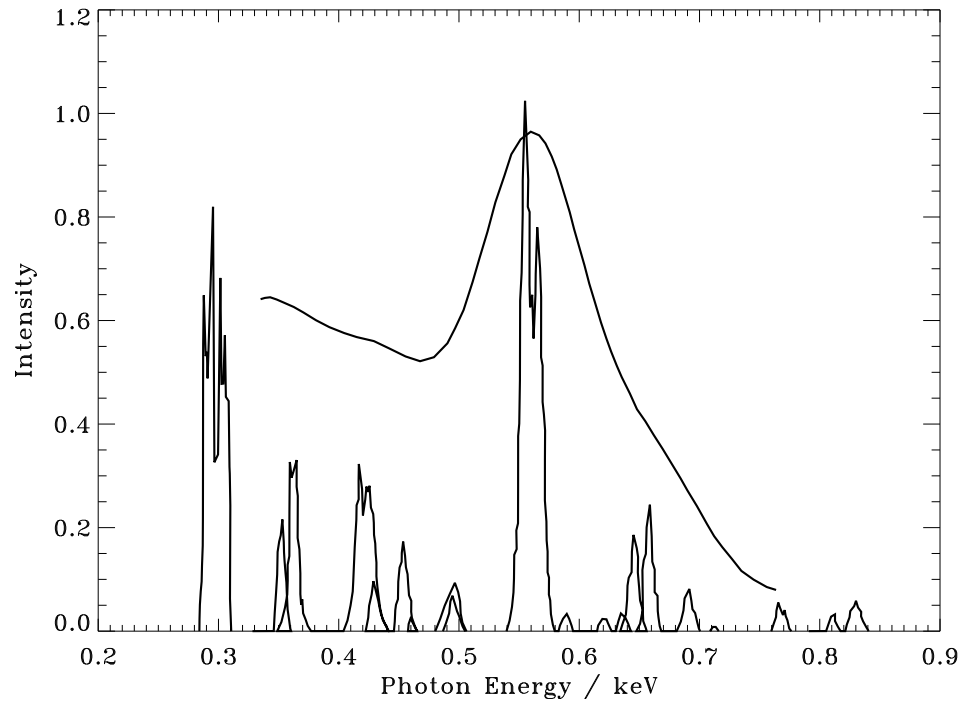


Figure 2.19: The x-ray spectrum from collisions of neutral  $\text{CO}_2$  with hydrogen- and helium-like oxygen, nitrogen and carbon, observed with the *ASTRO-E* microcalorimeter on the Livermore *EBIT*. The solid line shows the spectrum after convolution with the *ACIS-S* detector aboard *Chandra*, with a spectral resolution of 100 eV.

### 2.3.3 Electron-Ion Collision Driven Emission

Competing models suggests that the emission is driven by electron collisions rather than charge exchange collisions.

#### Emission from Thermal Solar Wind Electrons

Wegmann *et al* (1998) considered the bremsstrahlung emission by solar wind electrons passing through the neutral cometary atmosphere. The electrons were heated by the cometary bow shock in an unspecified manner. Their calculations show that the emission due to bremsstrahlung from adiabatically heated electrons is 4000 times smaller than that observed from comet C/1996 B2 (Hyakutake), although it is stated that a more efficient heating process could boost the effect. The shape of the emission region from this mechanism is similar to the morphology of comet Hyakutake, although there is closer agreement with their charge exchange model.

#### Energised Electrons

A similar model, with a more effective heating process, suggested by Bingham *et al* (1997), Northrop *et al* (1997), Northrop (1997), Milikh and Sharma (1997), and Uchida *et al* (1998), and developed by Shapiro *et al* (1998, 1999) is as follows: cometary ions are created by photoionisation and charge exchange ionisation of the out-gassing cometary neutrals. In the solar wind reference frame, the photo-ions form a beam distribution parallel to the magnetic field and a ring distribution transverse to the field. The relative streaming of the cometary and solar wind particles leads to the growth of electrostatic waves, almost perpendicular to the magnetic field. These waves may transfer their energy to the free electrons in the system, propelling them along the field lines at energies of the order of 1 keV. A more detailed description of the process is given in section 4.1.

Uchida *et al* (1998) and Shapiro *et al* (1999) assumed that the energetic electrons would drive x-ray emission through bremsstrahlung and excitation of cometary neutrals. The resulting emission lines would have energies of 277 eV, 392 eV and 525 eV, corresponding to neutral carbon, nitrogen and oxygen respectively. The observation of comet C/1999 S4 (LINEAR) by *Chandra* (Lisse *et al*, 2001) demonstrated that this was not the case, and that the clearest emission line is from He-like oxygen.

As a result, a modification to the model is suggested in this thesis: the energetic electrons drive the emission by exciting the minor species in the solar wind, and through bremsstrahlung collisions with solar wind protons and cometary photoions. This new approach is detailed in section 4.1.3.

## 2.4 The Comet-Solar Wind Atmosphere

When approaching the Sun, a cometary atmosphere is formed by the sublimation of molecules and dust particles from the surface. Detailed descriptions of the formation of the atmosphere over a wide range of cometocentric distances can be found in, for example, Festou (1981) and Divine *et al* (1986). Beyond a distance of approximately  $10r_n$ , where  $r_n$  is the radius of the nucleus, a simple model is sufficient to describe the environment. Beyond this distance, gas molecules can be treated ballistically: flowing radially from a point source nucleus with a uniform speed  $v_{\text{gas}}$ . The neutral particles are not affected by the solar magnetic field  $\mathbf{B}$  until they are ionised, either by a solar photon, an electron collision or a charge transfer reaction. A comprehensive list of photodissociation and photoionisation timescales of neutral molecules and a photoionisation timescales of ions is given by Huebner *et al* (1992).

For a given atomic or molecular species  $x$ , the neutral density at a distance  $r$  from the nucleus is given by the Haser equation (Haser, 1957)

$$N_x(r) = \frac{Q_x}{4\pi v_{\text{gas}} r^2} \exp\left(-\frac{r}{v_{\text{gas}} \tau_x}\right), \quad (2.1)$$

where  $Q_x$  is the outgassing rate of  $x$  and  $\tau_x$  is the ionisation timescale for  $x$ . This model is close to the *in situ* results from comet 1P/Halley (see section 2.2.1). Detailed study of the neutral atmosphere are presented by Combi and Delsemme (1980a, 1980b), Combi (1980) and Delsemme and Combi (1983). The density of the daughter ions  $i$  created from  $x$  is

$$N_i = \frac{Q_x}{4\pi v_{\text{gas}} r^2} \exp\left(1 - \frac{r}{v_{\text{gas}} \tau_x}\right) \simeq \frac{Q_x}{4\pi \tau_x v_{\text{gas}}^2 r}. \quad (2.2)$$

Inaccuracies in this approach occur as a spread in velocities is introduced by collisions near the nucleus and by the release of energy as daughter molecules are created (Festou, 1981).

Once ionised, the particles are influenced by the magnetic field and the  $\mathbf{v} \times \mathbf{B}$  electric field. As the ions gyrate around the magnetic field, they are incorporated into the solar wind flow. As this occurs, the solar wind is slowed as momentum is conserved. This process is known as mass loading, and a review of the physics of mass loading plasmas, including comets, is given by Szegö *et al* (2000).

Magnetohydrodynamic models of the interaction of the outgassing, ionising cometary particles with the flowing solar wind and magnetic field have been performed by several authors (for example, see Gombosi *et al*, 1994, 1996; Häberli, 1996; Wegmann, 2002). The resulting profiles of the atmosphere and tails are in close agreement to observations. A kinetic approach is used by Lipatov *et al* (2002), although the

electrons are still treated as a fluid. In the above cases, energisation of electrons (as observed by *VEGA-2*; see section 2.2.3) and the effect of energetic electrons is not considered.

## 2.5 Conclusions

The published cometary x-ray data to date have been presented. It has also been demonstrated that currently, there is no conclusive explanation for cometary x-rays. From the literature it has been shown that only two of the contemporary emission mechanisms are plausible.

There is clear evidence that charge exchange reactions take place in the cometary environment. The products of charge exchange reactions (e.g.  $\text{He}^+$ ) have been detected in the atmosphere of comet 1P/Halley within the cometopause (Shelley *et al*, 1987). Although charge exchange emission models, when combined with MHD models, can represent the observed morphologies (Häberli, 1997; Wegmann *et al*, 1998), the emission spectra from *Chandra* and *XMM-Newton* are not satisfactorily modelled.

There is also evidence to support the energetic electrons model. Both lower-hybrid waves (Klimov *et al*, 1986, Savin *et al*, 1987) and energetic electrons (Gringauz *et al*, 1986a, 1986b, 1987) have been observed *in situ* in comet 1P/Halley at a position corresponding to the position of peak brightness in x-ray observations. It has been demonstrated that the detection of energetic electrons at comet 1P/Halley by *VEGA-2* and the non-detection of energetic electrons by *Giotto* may be explained by the difference in the spacecrafts' trajectories. Finally, a new modification of the energetic electron model has been presented, whereby the electrons cause emission by collisions with solar wind minor species, resulting in x-ray line emission, and by collisions with solar wind protons and cometary photoions, causing bremsstrahlung.

# Chapter 3

## Observations

In this chapter, the available observational data is presented. The focus of the chapter is the collection of cometary observations performed with the *Chandra X-ray Observatory*. Data from these observations are presented along with contemporary measurements of the solar wind by the *Advanced Composition Explorer (ACE)*.

General properties of the solar wind from *ACE* measurements are given in section 3.1. The *AXAF CCD Imaging Spectrometer (ACIS)* on *Chandra*, the device used in observations of comets, is described in section 3.1. The processing steps that must be applied to datasets before a scientific analysis is possible are demonstrated in section 3.3. Data from *Chandra* observations of seven comets are presented section 3.4. This section also includes *ACE* data from the corresponding periods. The potential of future x-ray missions with regard to cometary x-ray analysis is discussed in section 3.5.

### 3.1 Solar Wind Measurements by the *Advanced Composition Explorer*

The emission from the comet-solar wind plasma is characterised by minor species ions in the solar wind. Solar wind conditions are continually monitored by the *Advanced Composition Explorer (ACE)*, and averages of measured parameters since 1999 are shown in table 3.1. The average speed of solar wind protons in this period is  $v_p = (451 \pm 106) \text{ km s}^{-1}$ . The “fast” and “slow” values in table 3.1 refer to periods when the proton speed was above or below this average.

Some elemental data is not included in the *ACE* data archive; values for these abundances are taken from Wimmer-Schweingruber (2002).

Several models are used to predict the solar wind conditions throughout the ecliptic plane based on near-Earth measurements (see Fry *et al* (2003) for a comparison of models). From these models, Bodewits *et al* (2007) estimate the delay between condi-

Parameter	Slow	Fast
$N_p$	$(7.84 \pm 6.06) \text{ cm}^{-3}$	$(4.86 \pm 3.99) \text{ cm}^{-3}$
$T_p$	$(6.45 \pm 2.65) \times 10^4 \text{ K}$	$(1.55 \pm 0.93) \text{ cm}^{-3}$
$N_{\text{He}}/N_p$	$0.0361 \pm 0.0236$	$0.0322 \pm 0.0224$
$ \mathbf{B} $	$(6.45 \pm 2.93) \text{ nT}$	$(7.35 \pm 3.99) \text{ nT}$
$N_{\text{He}}/N_{\text{O}}$	$80.2 \pm 34.1$	$93.5 \pm 41.4$
$N_{\text{C}}/N_{\text{O}}$	$0.676 \pm 0.182$	$0.695 \pm 0.129$
$N_{\text{N}}/N_{\text{O}}^*$	$0.0079 \pm 0.037$	$0.114 \pm 0.022$
$N_{\text{Ne}}/N_{\text{O}}$	$0.241 \pm 0.101$	$0.129 \pm 0.103$
$N_{\text{Na}}/N_{\text{O}}^*$	$0.00791 \pm 0.00304$	$0.00378 \pm 0.00118$
$N_{\text{Mg}}/N_{\text{O}}$	$0.158 \pm 0.087$	$0.154 \pm 0.109$
$N_{\text{Al}}/N_{\text{O}}^*$	$0.0175 \pm 0.00657$	$0.00806 \pm 0.0021$
$N_{\text{Si}}/N_{\text{O}}$	$0.139 \pm 0.045$	$0.149 \pm 0.066$
$N_{\text{S}}/N_{\text{O}}^*$	$0.050 \pm 0.018$	$0.053 \pm 0.013$
$N_{\text{Ca}}/N_{\text{O}}^*$	$0.0085 \pm 0.0002$	$0.0186 \pm 0.0042$
$N_{\text{Cr}}/N_{\text{O}}^*$	$0.0019 \pm 0.0008$	$0.0017 \pm 0.0004$
$N_{\text{Fe}}/N_{\text{O}}$	$0.131 \pm 0.070$	$0.102 \pm 0.073$

Table 3.1: Statistics from *ACE* Solar Wind measurements from 1999 to 2005. Values marked by (\*) are from Wimmer-Schweingruber (2002). “Fast” and “slow” refer to periods when the solar wind proton speed was above or below the average value.

tions measured by *ACE* being representative of the solar wind at the position of each comet observed by *Chandra*.

Data contemporary to *Chandra* observations are presented alongside the cometary x-ray data in section 3.4. The quality of data returned by *ACE* varies, and each data point is assigned a quality grade. Data with low grades are not included here. This results in sporadic gaps in the data plots – see, for example, the lack of data between days 194.7 and 194.8 in figure 3.17.

### 3.2 The AXAF CCD Imaging Spectrometer – ACIS

*Chandra* consists of two x-ray detecting devices: the *High Resolution Camera (HRC)* and the *AXAF CCD Imaging Spectrometer (ACIS)*. The instruments can be used with or without high or low energy gratings. The only practical configuration for observing comets is *ACIS* with no grating. This device is described here.

There are two sets of CCDs on the device: 4 imaging chips (*ACIS-I*) and 6 spectrometer chips (*ACIS-S*). The configuration of the detector is shown in figure 3.1.

## ACIS FLIGHT FOCAL PLANE

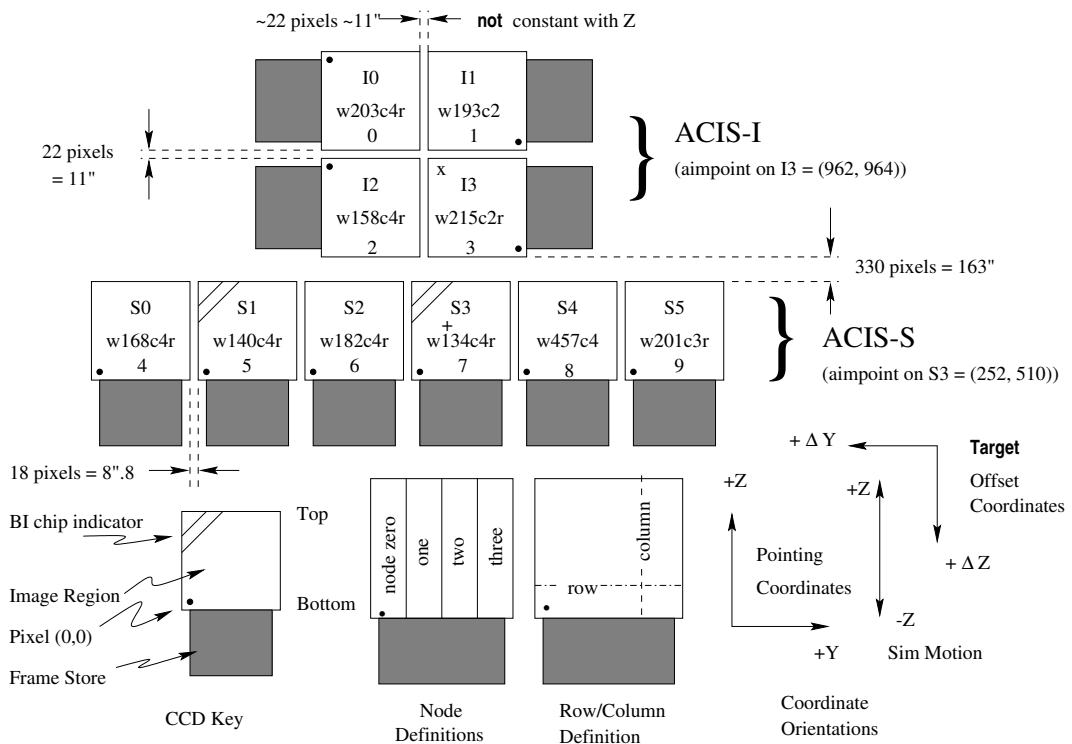


Figure 3.1: A schematic of *Chandra*'s *ACIS* array of CCDs from the *Chandra* Proposers' Observatory Guide.

*ACIS-I* is used for capturing x-ray images over a large field of view. *ACIS-S* can be used in the same manner (as is the case here), although it is designed to be used with diffraction gratings to record high resolution spectra. Another important feature is that there are two categories of CCD in the *ACIS-S* array. Four of the chips are front illuminated (as are all of the *ACIS-I* CCDs), which is the normal mode of CCD operation. In these chips, there is a silicon window between the mirror array and the CCD surface. The remaining CCDs (*S1* and *S3*) are similar to the others, but they are inverted in the array such that they are back illuminated. That is, the sensing volume at

the back of the device is exposed to incident x-rays. In this case, photons do not have to pass through a silicon window, and as a result the chips are an order of magnitude more sensitive to x-rays below 1 keV (in the energy range of interest in this study). However, energy resolution is approximately 60% of the front illuminated chips.

The sensitivity of the CCDs is reflected by their effective areas. Typical effective areas for front and back illuminated chips are shown in figure 3.2.

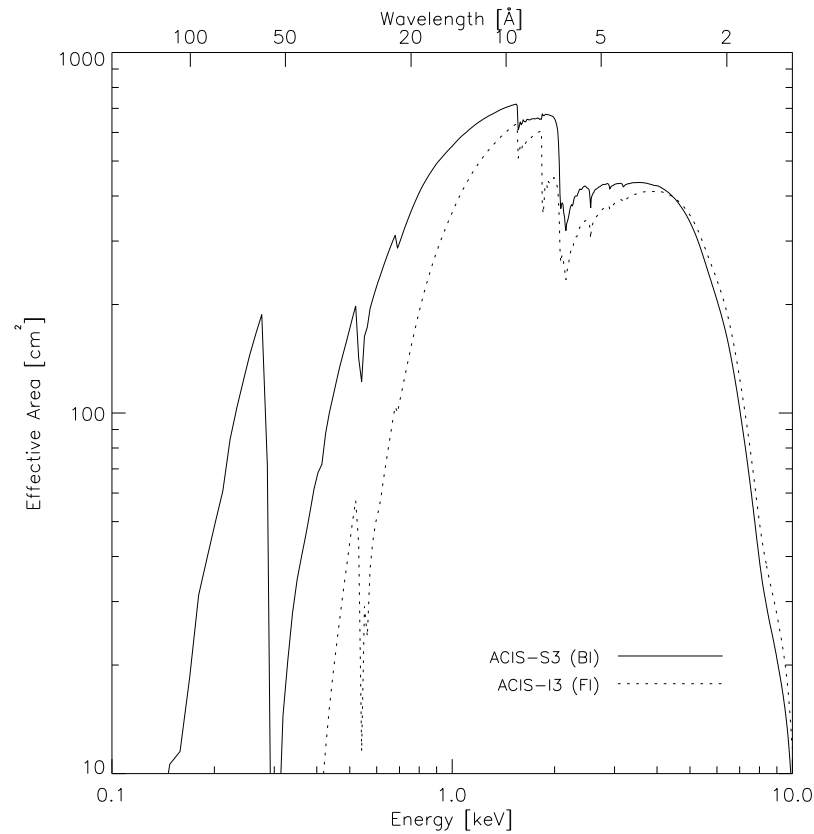


Figure 3.2: Typical effective area functions for *ACIS* chips.

More detailed descriptions of *ACIS* are given in the *ACIS Handbook* (Nousek, 1997), and “The *Chandra* Proposers’ Observatory Guide”<sup>1</sup>.

For cometary observations, the aimpoint of the *S3* CCD (marked by a cross in figure 3.1) is usually pointed (and periodically redirected) at the nucleus of the comet.

<sup>1</sup><http://cxc.harvard.edu/proposer/POG/html/>

## 3.3 Data Processing

### 3.3.1 Data Reduction

The *Chandra* data archive can be accessed online, and after a period of one year, observation data is in the public domain and may be accessed through the *WebCHASER*<sup>2</sup> service.

Two levels of data are available. Level 2 data are created by processing of level 1 datafiles. For most scientific analysis, a new set of level 2 data should be prepared by processing the level 1 data with the most recent calibration database *CALDB*<sup>3</sup> for the period of the observation.

The data from *ACIS* is arranged such that information about every detection is tabulated. The raw signal from the CCD array is full of contamination from effects such as cosmic rays, and defects on individual CCDs. These have to be removed using the latest version of the *Chandra Interactive Analysis of Observations (CIAO)*<sup>4</sup> package<sup>5</sup>.

The CCD false colour image of an observation of comet C/1999 S4 (LINEAR) is shown in figure 3.3. The resolution of the image is 32 times lower than the actual CCD array.

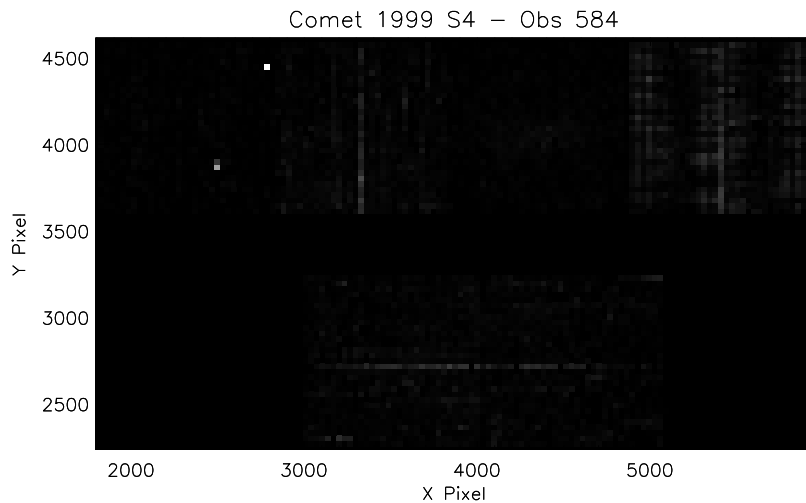


Figure 3.3: A raw *ACIS* CCD image of observation 584 of comet C/1999 S4 (LINEAR).

The first step is to create a list of all of the known bad pixels on the device from the period of this observation and to remove these data from the event file. The resultant image is only slightly different, and is not shown.

Next, each pixel for each event is graded. That is, the signal on each pixel is

---

<sup>2</sup><http://cda.harvard.edu/chaser/mainEntry.do>

<sup>3</sup>*CALDB* version 3.3.0 was used here

<sup>4</sup><http://cxc.harvard.edu/ciao/>

<sup>5</sup>*CIAO* version 3.4 was used here.

compared to an event threshold value, and if the signal is greater than that on each of the 8 neighbouring pixels, the pixel is graded. The signals on neighbouring pixels are compared to a split-event threshold value, and the pixels with values greater than the threshold are assigned a value of 1. The grade of the central pixel is determined by the binary pattern formed on the neighbouring pixels. The grading distinguishes between true counts and background detections from cosmic rays. Events with an unfavourable grading are removed from the datafile.

Events with certain grades are removed from the data file, in this case leaving only 13% of the events. The CCD image is shown in figure 3.4

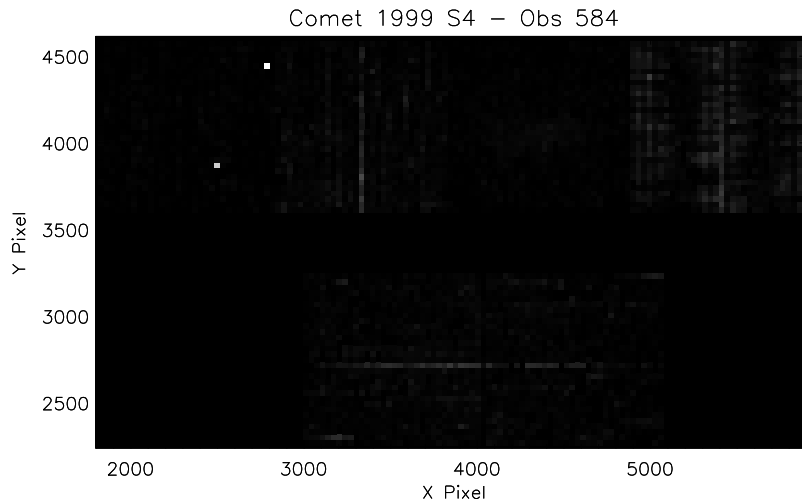


Figure 3.4: The graded *ACIS* CCD image of observation 584 of comet C/1999 S4 (LINEAR).

The final filtering step leaves data collected within Good Time Intervals (GTI). A GTI is a period with low background and a stable aspect (which can be thought of as a projecting a constant field of view after corrections for the natural dither of the satellite). When re-pointing the satellite, the aspect becomes unstable, and any detections from transition periods are not included in the GTI list. This is important in the analysis of comets, as the satellite is periodically re-pointed to track the path of the comet. The list of GTIs can be determined for each observation, allowing corresponding x-ray detections to be extracted, and the resultant data file is now a level 2 file. The GTI corrected data for observation 584 is shown in figure 3.5.

A common problem at this stage is a streaking effect in the horizontal on the *S4* CCD. This is caused by a flaw in the output system of the chip, which results in a random charge being distributed along the pixel row. All of the *ACIS* CCDs suffer from this problem to a small extent. The problem is well known, and the CIAO data package includes algorithms to destreak the data. In general, destreaking the *S4* CCD is not necessary as data from the chip are not analysed. The exception is the observation of comet C/2002 C1 (Ikeya-Zhang). Despite this, destreaking algorithm is applied to each observation for completeness. The destreaked level 2 file is shown in figure 3.7.

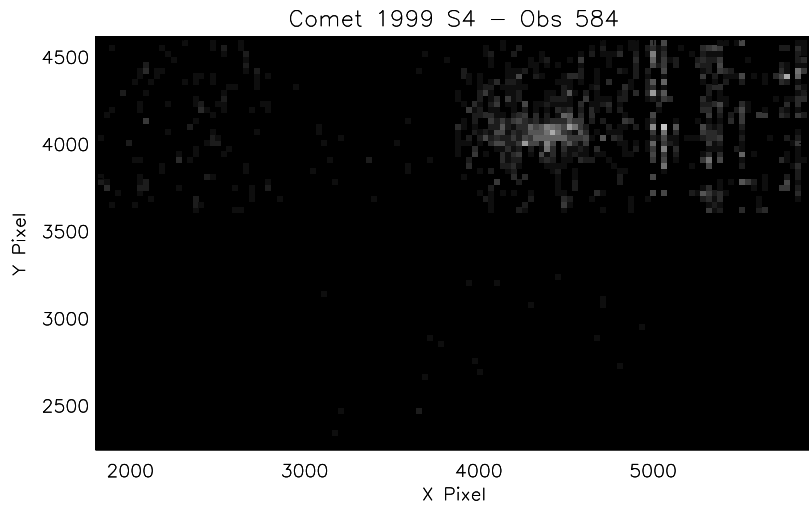


Figure 3.5: The GTI *ACIS* CCD image of observation 584 of comet *C/1999 S4* (LINEAR).

This effect is not obvious in this case, as there appears to be a stronger noise signal in the vertical direction. To demonstrate, a GTI filtered image of observation 1863 of comet *C/1999 T1* (McNaught-Hartley) is shown in figure 3.6. Compare this to the destreaked image shown in figure 3.7.

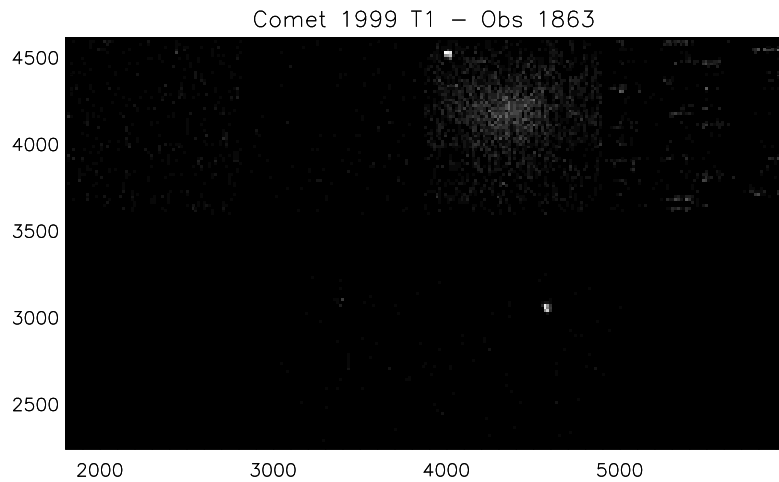


Figure 3.6: The GTI *ACIS* CCD image of observation 1863 of comet *C/1999 T1* (McNaught-Hartley).

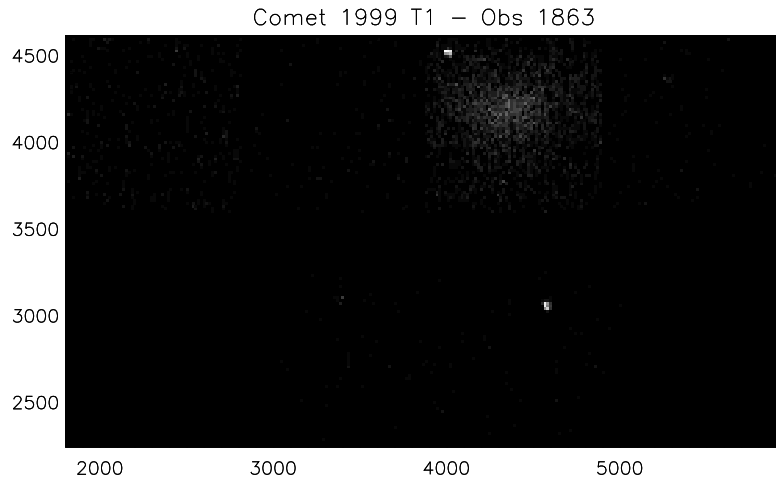


Figure 3.7: The destreaked *ACIS* CCD image of observation 1863 of comet *C/1999 T1* (McNaught-Hartley).

The final stage in preparing the level 2 event file is to remove background point sources, such as those visible in figure 3.7.

### 3.3.2 Grouping Observations

In many observations, the total observing period is divided into several observation IDs. Between each ID, the satellite is re-pointed to track the motion of the comet (the exception to this is the observation of comet *C/2002 C1* (Ikeya-Zhang), where the comet passed through the field of view). In order to combine each observation ID, a common coordinate system must be introduced. Using the comet ephemeris data (which is archived in the *Chandra* archives), a comet-centred coordinate system may be introduced. After this, sequential (in time, though not necessarily in observation ID number) observations can be combined.

### 3.3.3 Analysis of Background Counts

The treatment of background counts is rarely simple, and is particularly tricky in the case of comets. The ideal scenario for cometary x-rays is to observe the comet's projected position shortly before or after the actual observation. This has not been attempted to date. The best available scenario is that the *SI* chip is also active during the observation, and that x-ray emitting region of the comet does not extend far enough to fall into the projected view of the *SI* CCD. This allows the entire chip to be used as a background source.

Failing this, if the source covers only a small part of the *S3* chip leaving a large area empty, distinct source and background regions can be assigned. It will be shown later that the x-ray emitting cometary plasma may extend far enough to fill the *S3* CCD or even the entire *ACIS* array. Therefore, following this approach could result in a significant amount of source data being neglected, although the method has been used in previous analyses (for example Krasnopolsky *et al*, 2002; Lisse *et al*, 2005).

If neither of these options are available, there is no way to derive a reliable background from the observation. It is possible to use a blank-sky datafile, although application of this method is complex, and relies on the assumption that the x-ray background is uniform, which is not the case. Also, it is crucial to ensure that the background datafile has been processed with the same calibration data as the source. At the moment it is not possible to reprocess the blank-sky files to ensure that this is the case.

If a contemporary sample of the background can be extracted by one of the above methods, it is important that it is utilised properly. It is not acceptable to simply subtract a background signal from the source (with appropriate scaling of the solid angles). To do so assumes that the responses does not vary over the CCD area (which it does), or in the case of using the blank-sky data, that the response for each observation is identical, which is also false. The correct approach is to model the background emission using an response function derived from the background sample. The model that is used to fit the data is not significant. The background model must be superimposed onto any model of the source emission. This method has not been employed in previously published analyses on cometary x-rays.

Further details of the background signals used in this study are discussed in section 5.3.

### 3.4 *Chandra* Observations of Comets

At the moment, the *Chandra X-ray Observatory* is the most powerful satellite for examining cometary x-ray emission. The spectral resolution is high enough to demonstrate that the emission is composed, at least in part, of emission lines. Although the spectral resolution of *XMM-Newton* is slightly higher, *Chandra* is supported by a comprehensive selection of software packages that allow easy access to the data and thorough analysis. As a result, *Chandra* is the most commonly used active instrument in cometary x-ray research, with 9 observations to date.

For two of the *Chandra* observations, gratings were used in unsuccessful attempts to obtain high resolution results. In the other cases, CCD images and spectra were recorded. Details of the observations are listed in table 3.2.

Comet	Instrument	Grating	Date	$\Delta$	$R$	Lat	$\Delta t$	$Q_{\text{gas}}$	Duration	Counts	$P_x$
C/1999 S4	ACIS-S	None	14/7/2000	0.530	0.801	24°	-1.09	$3 \times 10^{28}$	9.34	16300	$2.6 \times 10^{15}$
C/1999 S4	ACIS-S	None	1/8/2000	0.552	0.774	24°	—	—	18.6	15538	—
C/1999 T1	ACIS-S	None	8/1/2001	1.399	1.239	15°	-6.63	$10^{28}$	3.3	5500	$2.5 \times 10^{16}$
C/1999 T1	ACIS-S	None	10/1/2001	1.384	1.250	15°	—	$10^{28}$	3.6	5400	—
C/1999 T1	ACIS-S	None	12/1/2001	1.370	1.261	15°	—	$10^{28}$	3.3	5000	—
C/1999 T1	ACIS-S	None	13/1/2001	1.363	1.267	15°	—	$10^{28}$	3.3	1400	—
C/1999 T1	ACIS-S	None	14/1/2001	1.356	1.273	15°	—	$10^{28}$	3.1	2300	—
C/2001 A2	HRC-S	LETG	8/7/2001	0.267	1.141	—	—	—	43.7	—	—
C/2001 A2	HRS-I	None	9/7/2001	0.273	1.153	—	—	—	23.8	—	—
C/2000 WM1	ACIS-S	LETG	31/12/2001	0.676	0.753	—	—	$5 \times 10^{28}$	33.9	—	—
C/2002 C1	ACIS-S	None	15/4/2002	0.457	0.799	26°	-0.73	$2 \times 10^{29}$	23.4	428000	$2.8 \times 10^{16}$
2P/Encke	ACIS-S	None	24/11/2003	0.275	0.891	-10°	-1.09	$7.3 \times 10^{27}$	44.1	11400	$1 \times 10^{14}$
C/2001 Q4	ACIS-S	None	12/5/2004	0.362	0.964	-3°	-1.80	$1.3 \times 10^{29}$	10.4	9510	$5 \times 10^{15}$
9P/Tempel	ACIS-S	None	30/6/2005	0.872	1.507	0.8°	—	$4.73 \times 10^{27}$	50.1	9700	—
9P/Tempel	ACIS-S	None	4/7/2005	0.892	1.506	0.8°	—	$5.01 \times 10^{27}$	61.3	8700	—
9P/Tempel	ACIS-S	None	5/7/2005	0.898	1.506	0.8°	—	$8.18 \times 10^{27}$	47.9	6900	—
9P/Tempel	ACIS-S	None	8/7/2005	0.914	1.506	0.8°	-0.38	$6.31 \times 10^{27}$	33.1	8600	$1.7 \times 10^{16}$
9P/Tempel	ACIS-S	None	10/7/2005	0.925	1.507	0.8°	—	$5.01 \times 10^{27}$	33.5	6200	—
9P/Tempel	ACIS-S	None	13/7/2005	0.942	1.508	0.8°	—	$5.6 \times 10^{27}$	33.4	4800	—
9P/Tempel	ACIS-S	None	24/7/2005	1.01	1.518	0.8°	—	$5.6 \times 10^{27}$	33.4	5900	—
73P/SW 3B	ACIS-S	None	24/5/2006	0.106	0.965	0.5°	0.2	$2 \times 10^{28}$	20.6	8470	$3.6 \times 10^{14}$

Table 3.2: Details of comets observed by *Chandra*.  $\Delta$  and  $R$  are the geocentric and heliocentric distances of the comet in AU, Lat is the ecliptic latitude of the comet,  $\Delta t$  is the delay between equivalent solar wind flows being present in the vicinity of the comet and the Earth  $Q_{\text{gas}}$  is the outgassing rate in molecules  $\text{s}^{-1}$ , the duration of each observation is in ks, and  $P_x$  is the x-ray luminosity in  $\text{erg s}^{-1}$ . The luminosities are estimated by comparing the source signals to the background. 73P/SW 3B is comet 73P/Schwassmann-Wachmann 3B.

In the literature, there are details of the observations of comets C/1999 S4 (LINEAR) (Lisse *et al*, 2001), C/1999 T1 (McNaught-Hartley) (Krasnopolsky, 2004) and comet 2P/Encke (Lisse *et al*, 2005). Publications are in preparation for the observation C/2002 C1 (Ikeya-Zhang) (Dennerl, private communication 2005), and a review of all of the *Chandra* cometary data (Bodewits *et al*, 2007). The review paper will include some of work presented here.

The aim of this section is to collect and catalogue all of the available data from *Chandra* observations of comets and to process the data using the most up-to-date calibration and techniques to allow full spectroscopic analysis. Aspects of the data presented here are morphology, spectra and light curves, where possible. Although

previous studies have presented these facets of the data, more detailed results are given here. No interpretation of the emitting plasmas is made in this chapter: this is done in chapter 5.

An important caveat of the analysis of *Chandra* spectra regards the instrument response. The response function comprises two components: the effective area and the redistribution matrix. The effective area dictates how sensitive the device is as a function of energy. The calculation of the effective area considers physical obstructions by the structure of the device, the reflectivity of the mirrors, and the quantum efficiency of the CCD. Also, the effect of incident photons transmitting through an optical blocking filter must be considered. This is complicated by the buildup of contaminants on one side of the filter, which have the effect of degrading the effective area over time, especially in the energy range of interest for comets. Calibration observations indicate that the thickness of this contaminating layer is increasing linearly with time. The effective area varies spatially over the CCD. The spatial and temporal variations are included in the calibration data.

The redistribution matrix indicates the probability of a photon of energy  $E$  resulting in the incrementation of counts in the bin  $I$ . This is the manifestation of the energy resolution of the device. The redistribution matrix, like the effective area, varies in time, and spatially over the chip. However, only the most recent response is included in the calibration data.

Both aspects of the response also depend on the device temperature, although this is automatically treated in the analysis.

As a result of variation of the response, weighted effective areas and redistribution matrices must be calculated separately for every observation.

### 3.4.1 Comet C/1999 S4 (LINEAR)

Comet C/1999 S4 (LINEAR) was the first comet to be observed by *Chandra* (Lisse *et al.*, 1999c). The comet disintegrated as it approached the Sun, and observations were made both before (July 14th 2000) and after (August 1st 2000) the initial breakup of the nucleus. The first observation is discussed in this section (the post-disintegration observation is detailed in section 3.4.2).

The heliocentric radius of the comet was  $R = 0.801$  AU, and its distance from the Earth was  $\Delta = 0.530$  AU. The observation was split into 8 sequential periods, with the device being re-pointed toward the comet nucleus for the start of each period. The total observing time was 10.6 ks, but this includes data collected while the satellite was being re-pointed. Removing these data gives a total “good time interval” of 9.39 ks. The CCD image (translated into a comet-centred coordinate system) and aggregate spectrum of the comet pre-breakup are shown in figure 3.8. In this figure, there has been no treatment of background counts other than the removal of cosmic ray detections and point-sources (as described in section 3.3).

Comet C/1999 S4 (LINEAR)

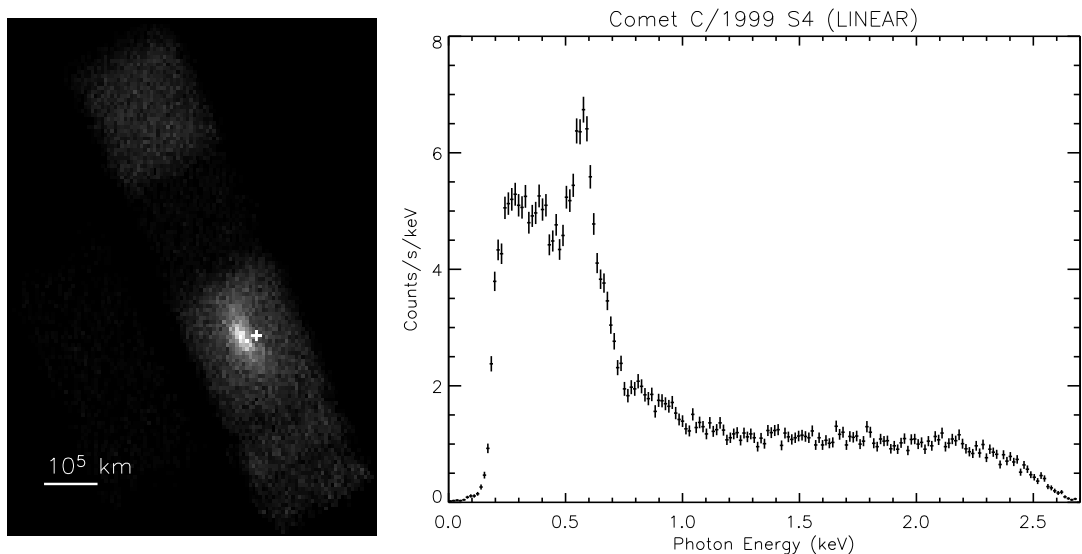


Figure 3.8: The total x-ray image and spectrum from the first *ACIS* observation of comet C/1999 S4 (LINEAR).

The spatial extent and the energy range of emission from the comet (rather than from the x-ray background) must be evaluated. First, consider the emission on the *S3* (where the nucleus was centred) and *S1* CCDs. Images and spectra from *S3* and *S1* are shown in figures 3.9 and 3.10 respectively.

The x-ray image in figure 3.9 is with a resolution of 16 pixels, equating to 3075 km. In this case, the photon energy is limited to only include the range 0.2–1.0 keV.

The nucleus is marked by a white cross. A distinct crescent shape can be seen, with the x-ray brightness peak at 24,300 km from the nucleus, near the Sun-comet line. Clear emission features are visible in the spectrum.

Comet C/1999 S4 (LINEAR)

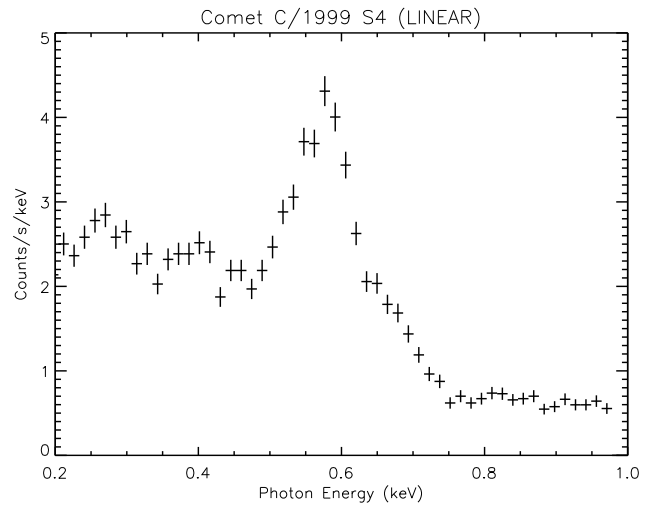
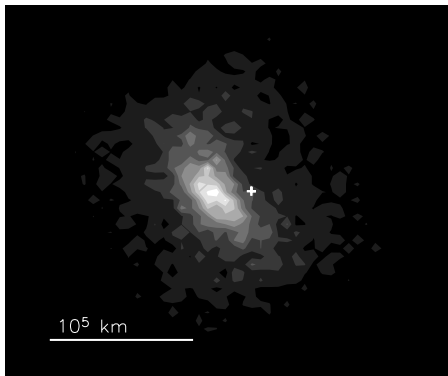


Figure 3.9: The x-ray morphology and spectrum of comet C/1999 S4 (LINEAR) from the *ACIS-S3* chip in the energy range 0.2–1 keV.

The x-ray luminosity incident on the *S3* CCD, assuming that all of the emission is from the comet, is  $P_x = 4.4 \times 10^{15}$  erg s<sup>-1</sup>.

Data from the *S1* CCD however, do not form a structured morphology, and the spectrum lacks detailed features. From this, one may conclude that the x-ray emission does not extend to the *S1* CCD, and that data from this chip may be used to represent a contemporary local x-ray background. The luminosity on *S1* is  $P_x = 1.8 \times 10^{15}$  erg s<sup>-1</sup>.

The extent to which the source emission fills the *S3* CCD should also be checked. To achieve this, define three regions of interest on the CCD: 1) a circle centred at the brightest point; 2) an annulus, such that the minor radius is equal to the radius of the first region, and with an area equal to that of the first region; and 3) the remainder of the chip. The radii are chosen such that the major radius of the annulus is close to the width of the CCD. The circular and annular regions each represent 37% of the CCD area.

The x-ray image and spectrum of the circular region are shown in figure 3.11

Comet C/1999 S4 (LINEAR)

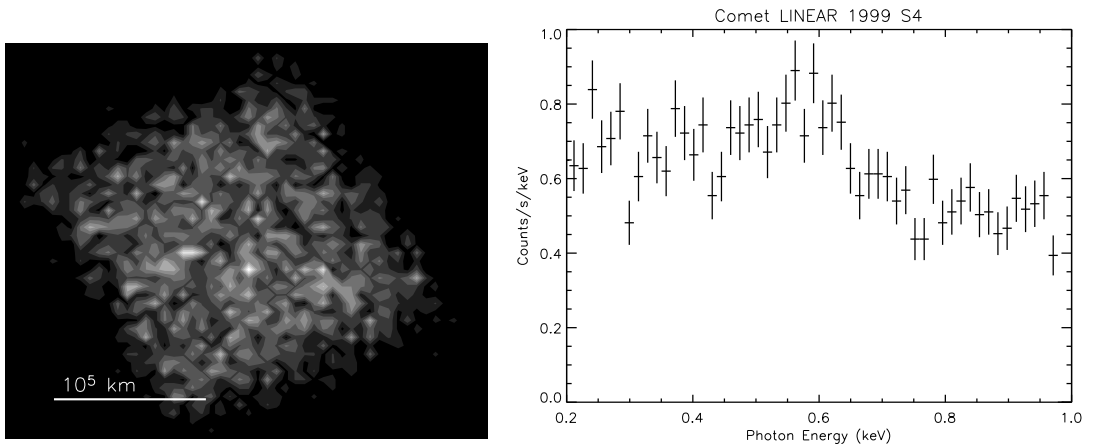


Figure 3.10: The x-ray morphology and spectrum of comet C/1999 S4 (LINEAR) from the *ACIS-S1* chip.

Comet C/1999 S4 (LINEAR)

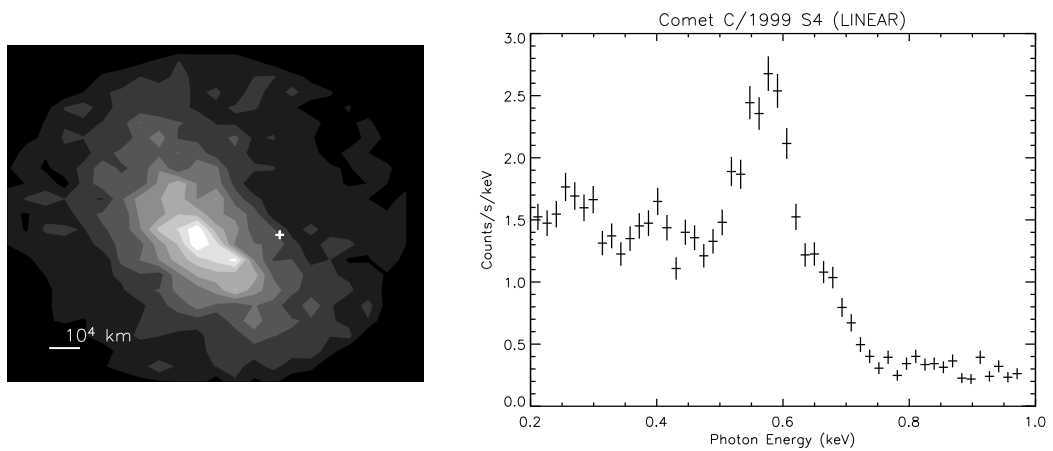


Figure 3.11: The x-ray morphology and spectrum of comet C/1999 S4 (LINEAR) from a circular region on the *ACIS-S3* chip. The region is centred at the brightest point.

As one would expect, the spectrum is similar in nature to that of the total *S3* CCD. The same plots are shown for the annular region in figure 3.12.

Comet C/1999 S4 (LINEAR)

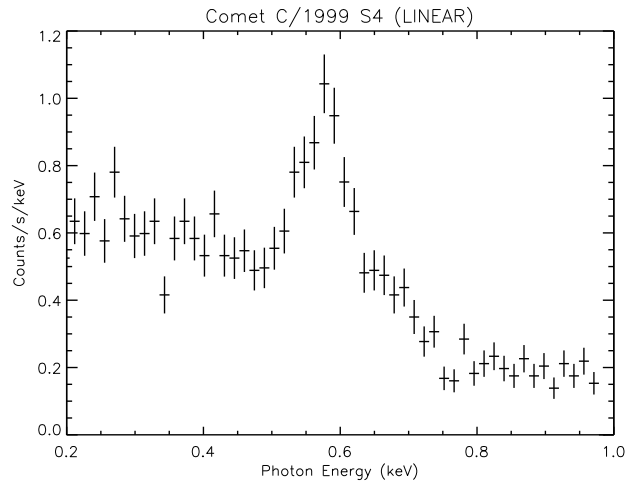
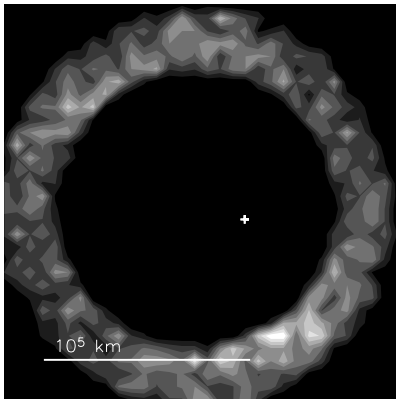


Figure 3.12: The x-ray morphology and spectrum of comet C/1999 S4 (LINEAR) from an annular region on the ACIS-S3 chip. This minor radius of the annulus is the radius of the circle in figure 3.11, and both regions are of equal area.

Again, the spectrum appears to be representative of the total S3 spectrum. This indicates that treating this region as a background source would only serve to remove source counts from the data.

The data from the remaining portion of the CCD are shown in figure 3.13.

Comet C/1999 S4 (LINEAR)

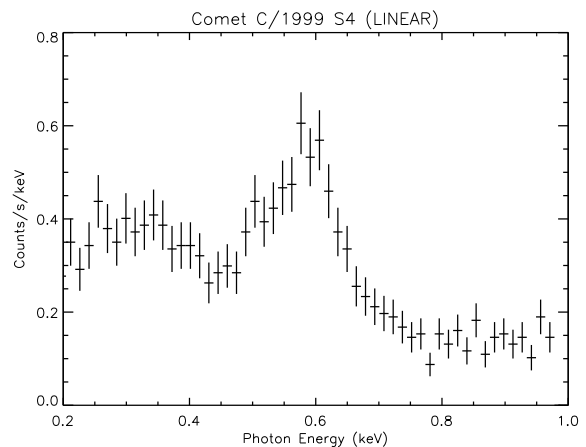
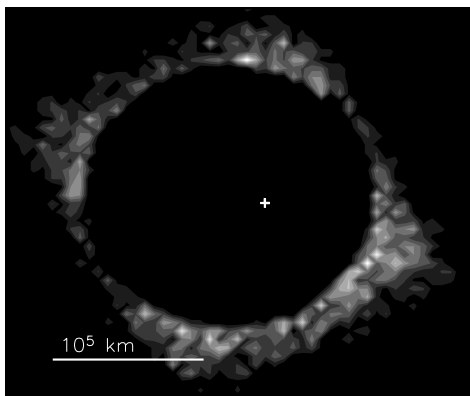


Figure 3.13: The x-ray morphology and spectrum of comet C/1999 S4 (LINEAR) from the ACIS-S3 chip without the regions in figures 3.11 and 3.12.

Once again, the spectrum retains the main features of the complete S3 data, demonstrating that a source signal can be found even at the edge of the chip. As a result, using any part of the S3 CCD as a background signal will remove source counts, and should be avoided.

Recall that figure 3.9 only featured photons in the range 0.2–1 keV. Compare the morphology of this figure to those shown in figure 3.14, which shows data from below and above this energy range.

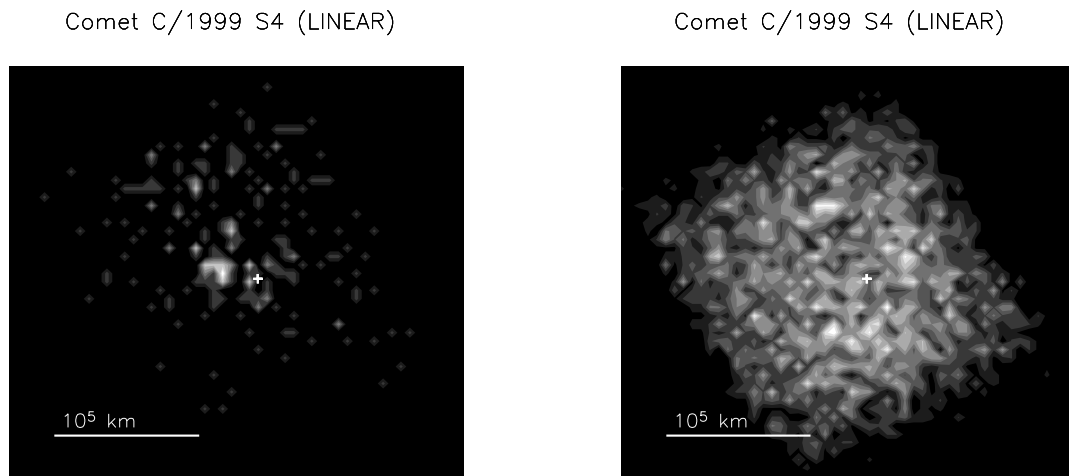


Figure 3.14: The x-ray morphology of comet C/1999 S4 (LINEAR) from the *ACIS-S3* chip in the energy ranges 0–0.2 keV (left) and 1–3 keV (right).

The lack of correlation between these morphologies and that for the energy range 0.2–1 keV suggests that photons outside of this energy range are from the background rather than the cometary atmosphere.

To confirm that detections in this range close to the lower limit are from the cometary atmosphere, the morphology of counts in the range 0.2–0.25 keV is shown in figure 3.15.

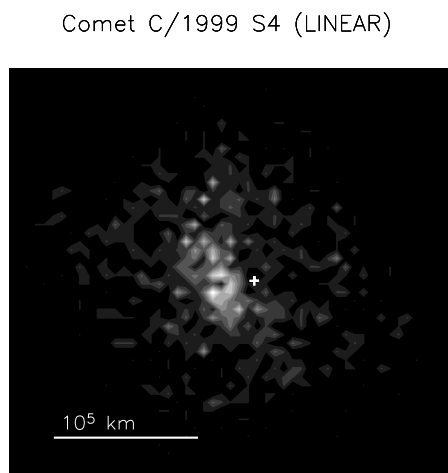


Figure 3.15: The x-ray morphology of comet C/1999 S4 (LINEAR) from the *ACIS-S3* chip in the energy ranges 0.2–0.25 keV.

The similarity of figure 3.15 and figure 3.9 demonstrate that these data should be attributed to the cometary atmosphere.

The light curve from the *S3* chip is shown in figure 3.16. Only photons in the range 0.2–1.0 keV are included, and the complete CCD area is sampled.

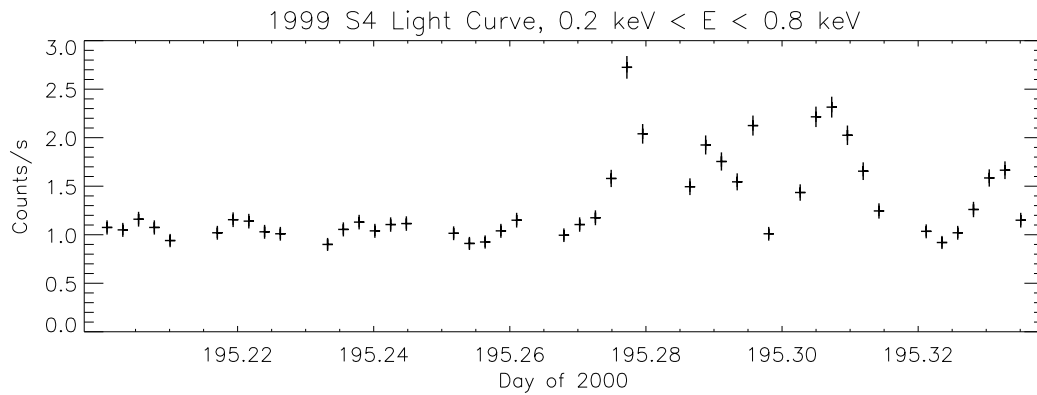


Figure 3.16: The *ACIS-S3* light curve from comet C/1999 S4 (LINEAR) for photon energies in the range 0.2–1 keV. The short periods of no counts represent the time taken to re-point the satellite in order to track the movement of the comet.

Compare this to the measured solar wind parameters from the same time. Figure 3.17 shows parameters measured by *ACE-SWEPAM* around the period of the *Chandra* observation. In the following plots, the line-shaded region shows the period of the observation, while the dot-shaded region shows this period minus a shift of 1.15 days, representing the time difference between the solar wind conditions travelling from the *ACE* to the region of the comet. This compares well to the value of 1.09 suggested by Bodewits *et al* (2007).

An increase in the x-ray flux by a factor of two coincides with an increase in the solar wind H flux, and a sharp increase in the solar wind He density (and the He flux). The solar magnetic field strength, measured by *ACE-MAG*, is plotted in figure 3.18. Again, there appears to be a correlation between an increase in the magnetic field and the x-ray flux.

The densities of some of the other minor species are shown in figure 3.19. The average ion charge for each species is plotted in figure 3.20. Due to the long sampling time (one hour), sharp changes in these parameters are not resolved.

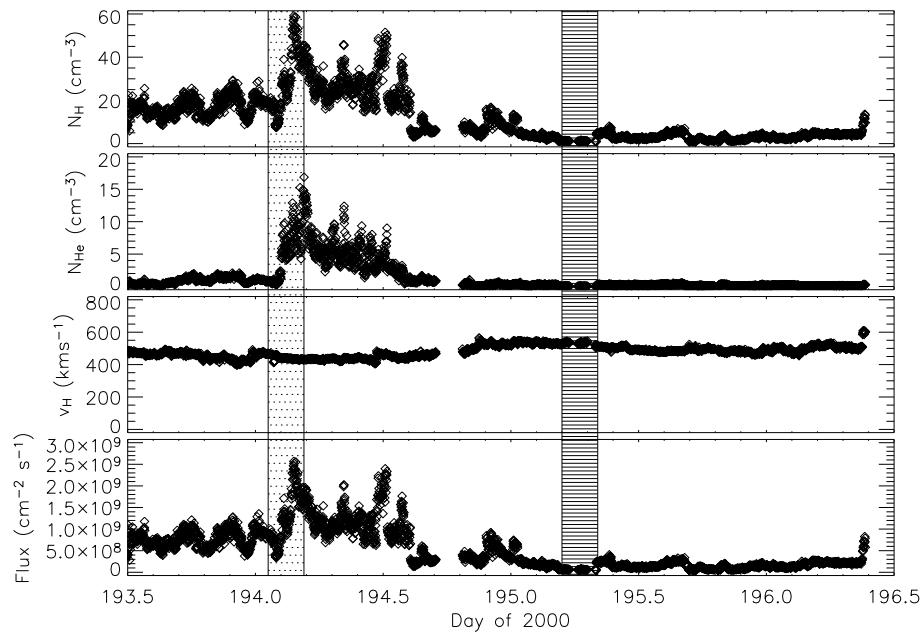


Figure 3.17: *ACE-SWEPAM* measurements of the solar wind parameters around the observation of comet C/1999 S4 (LINEAR). The *Chandra* observation took place during day 195 of the year 2000.

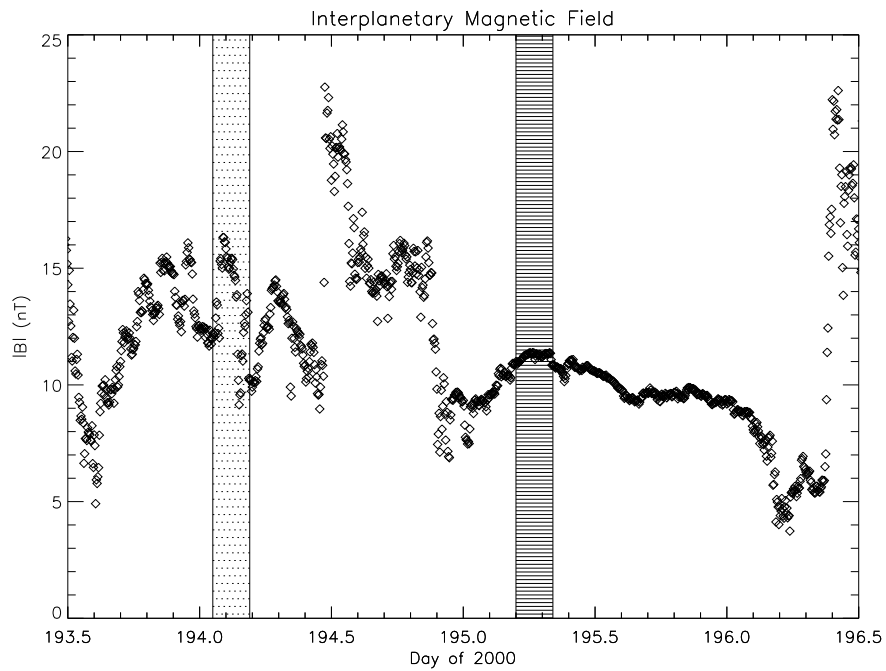


Figure 3.18: *ACE-MAG* measurements of the interstellar magnetic field around the observation of comet C/1999 S4 (LINEAR). The *Chandra* observation took place during day 195 of the year 2000.

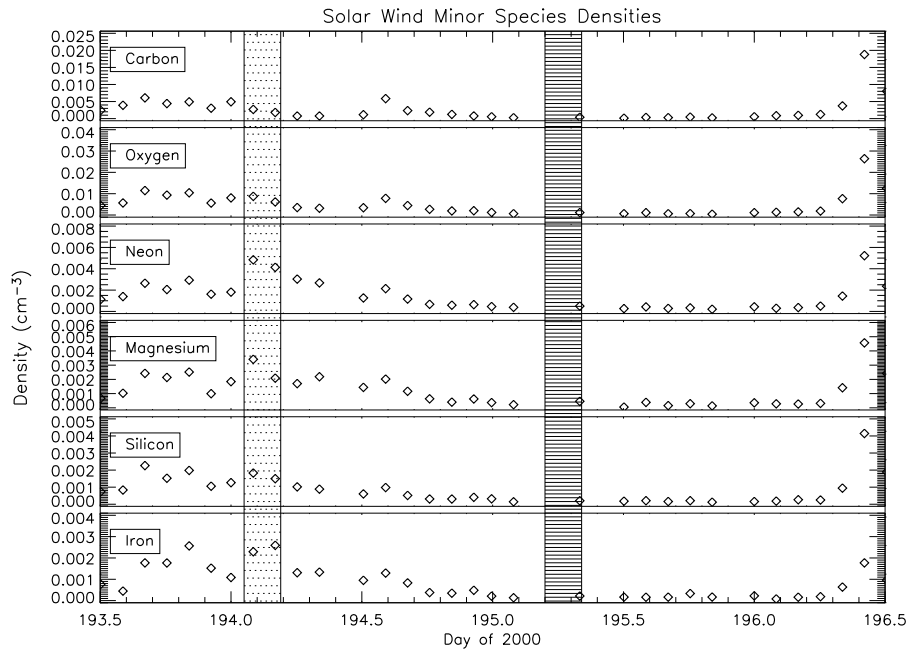


Figure 3.19: *ACE-SWICS* measurements of the solar wind minor species densities in the period of the observation of comet C/1999 S4 (LINEAR). The *Chandra* observation took place during day 195 of the year 2000.

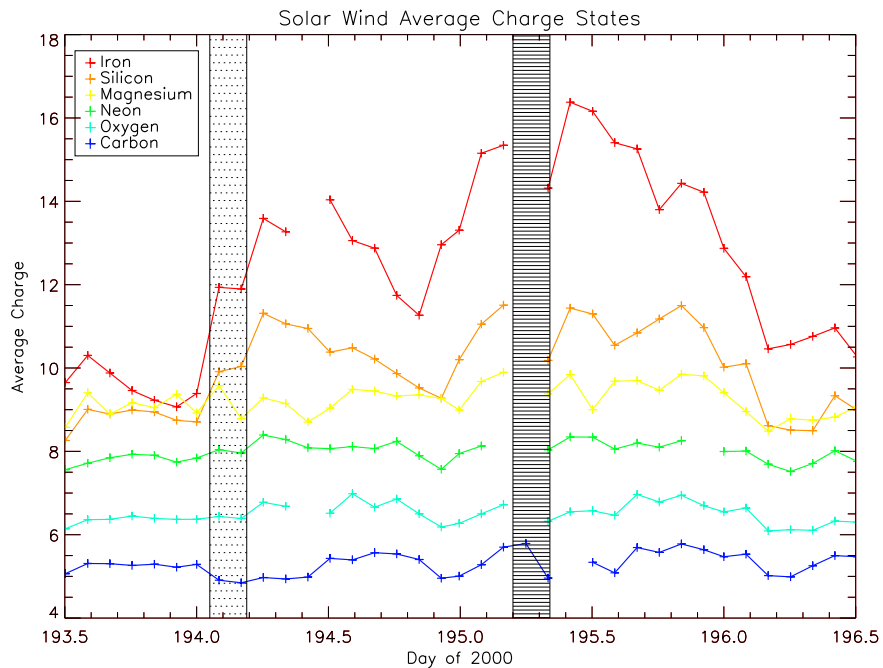


Figure 3.20: *ACE-SWICS* measurements of the average charge of the solar wind minor species in the period of the observation of comet C/1999 S4 (LINEAR). The *Chandra* observation took place during day 195 of the year 2000.

### 3.4.2 Comet C/1999 S4 (LINEAR) — After Breakup

In the days following the original observation, the comet started to disintegrate, and a secondary observation was performed on August 1st 2000. At this time, the comet was 0.552 AU from the Earth, and 0.774 AU from the Sun. The good time interval was 18.6 ks, a factor of two greater than the initial observation. The full comet-centred *ACIS* image and combined spectrum are shown in figure 3.21.

Comet C/1999 S4 (LINEAR)

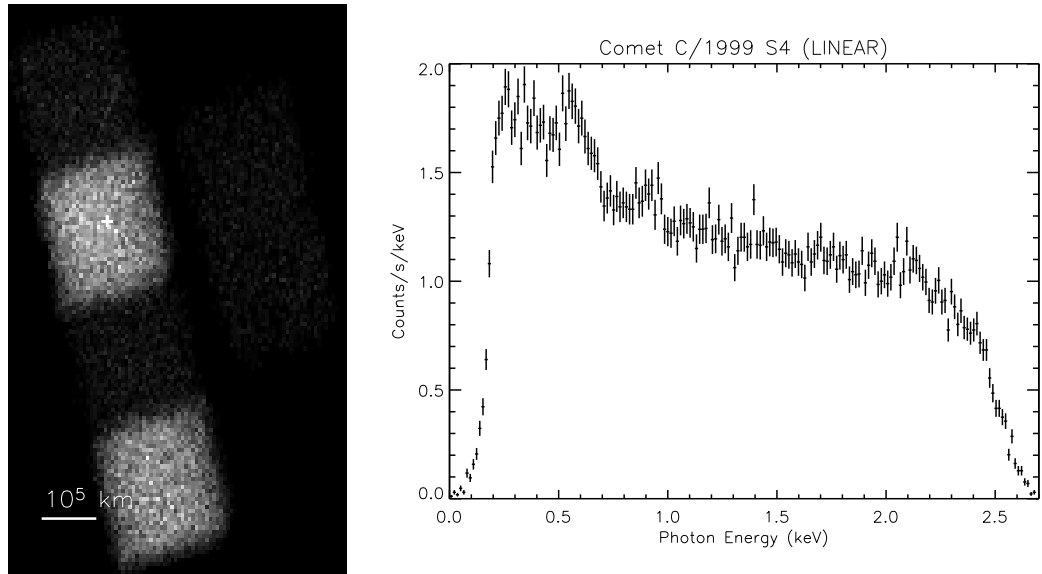


Figure 3.21: The total x-ray image and spectrum of comet C/1999 S4 (LINEAR) after the breakup of the nucleus.

The data from the *S3* chip are shown in figure 3.22. The resolution of the image is 128 pixels or 25,600 km. Note that at this resolution, a morphology peaking at the centre of the chip is naturally present, and the presence of a weak cometary signal is exaggerated. A total of 10,601 photons were collected between 0.2 and 1.0 keV. The point of maximum brightness is 42,800 km from the nucleus. The x-ray flux decreased below 1 keV, and clear emission lines are not as prominent (compare with figure 3.9).

Note that the emission above 1 keV is similar before and after the breakup of the nucleus (compare figures 3.8 and 3.21). This, along with the lack of structure of the high energy morphology in the first observation (see figure 3.14), suggests that the emission above 1 keV is background noise. This observation is not analysed further here.

Comet C/1999 S4 (LINEAR)

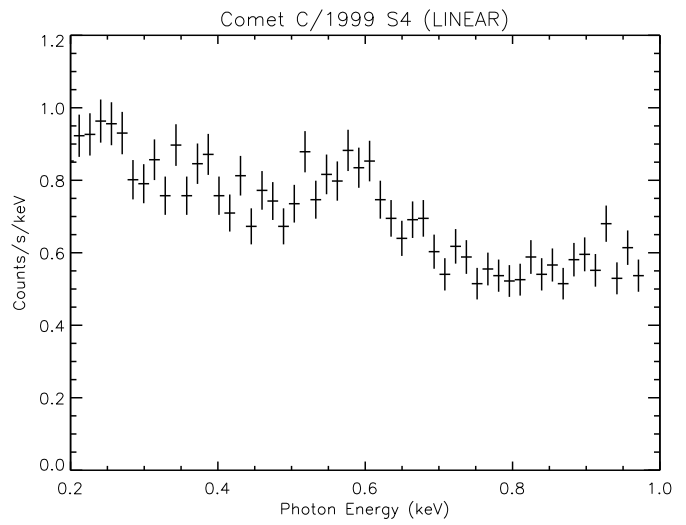
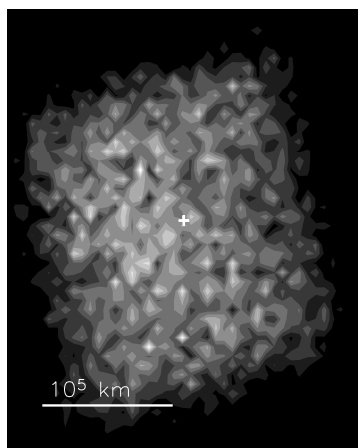


Figure 3.22: The total x-ray image and spectrum of comet C/1999 S4 (LINEAR) after the breakup of the nucleus. Only data from the ACIS-S3 chip are shown.

### 3.4.3 Comet C/1999 T1 (McNaught-Hartley)

Comet C/1999 T1 (McNaught-Hartley) was observed by both *Chandra* and *XMM*. The *Chandra* observation, by Krasnopolsky (2000), was conducted over seven days between January 8th and January 14th 2001. In this period, five separate exposures of around one hour were made. Between the first and last observations, the comet's heliocentric distance had changed from  $R = 0.124$  and  $R = 0.127$  AU, with the geocentric distance going from  $\Delta = 1.40$  to  $\Delta = 1.36$  AU. The combined *ACIS* image (in comet centred coordinates) and spectrum are shown in figures 3.23.

Comet C/1999 T1 (McNaught-Hartley)

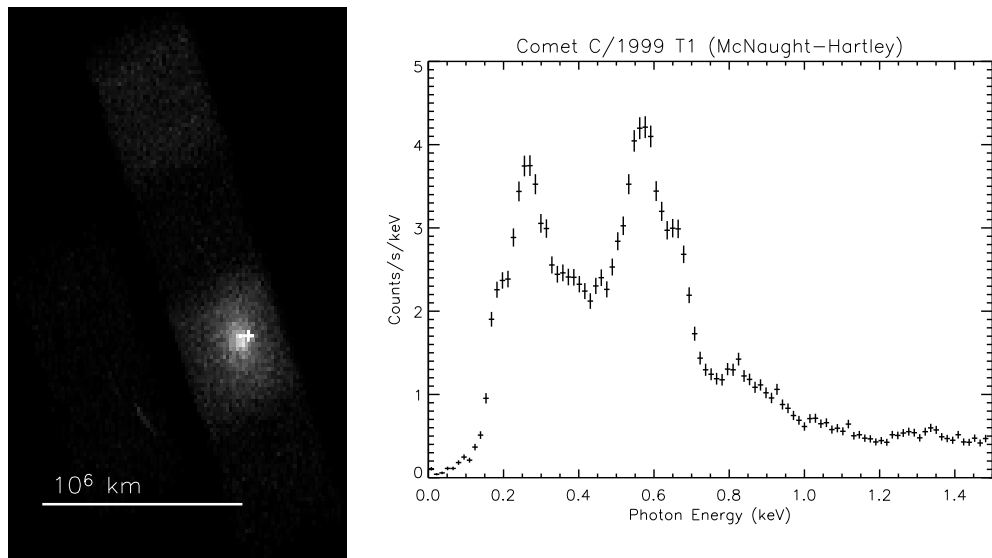


Figure 3.23: The total (over all observing periods) x-ray image and spectrum from the *ACIS* observations of comet C/1999 T1 (McNaught-Hartley).

Again, it appears that the cometary x-rays were constrained to the *S3* chip to a large extent. This is supported by a lack of structure in the morphology on the *S1* CCD (figure 3.24), and by a comparison between the spectra from both of the back illuminated chips (figure 3.25).

Comet C/1999 T1 (McNaught–Hartley)

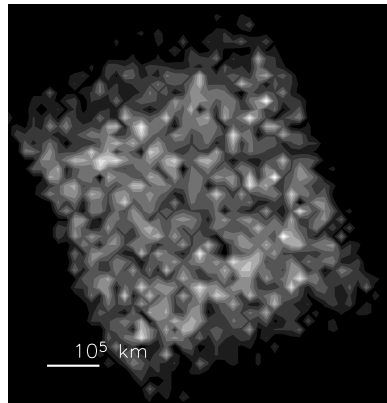


Figure 3.24: The x-ray image of comet C/1999 T1 (McNaught–Hartley) on the ACIS-S1 CCD.

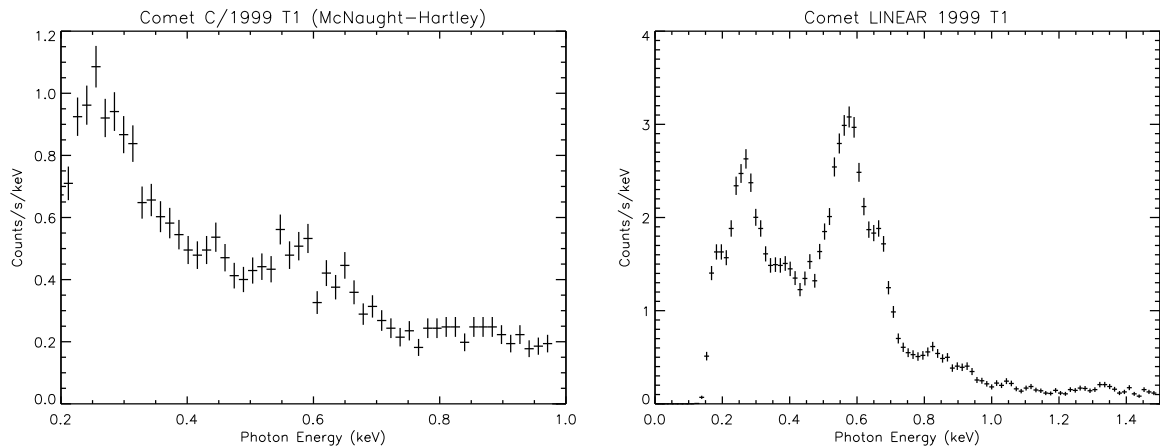


Figure 3.25: A comparison of the total emission spectra from the S1 (left) and S3 (right) chips from observations of comet C/1999 T1 (McNaught–Hartley).

The emission varied with each observing period. Figure 3.26 shows the morphology on each occasion, along with a superposition of the images. The dated images are scaled to the maximum count rate on January 8, and only detections on the S3 chip are shown. In each image, the comet–Sun vector points from the nucleus to the lower-left corner of the image. In each case, the emission brightness centre is offset from the nucleus toward the sun, and the emission is almost symmetrical around the comet–Sun axis. The average position of the brightest point from the three brightest observing periods is 38,000 km.

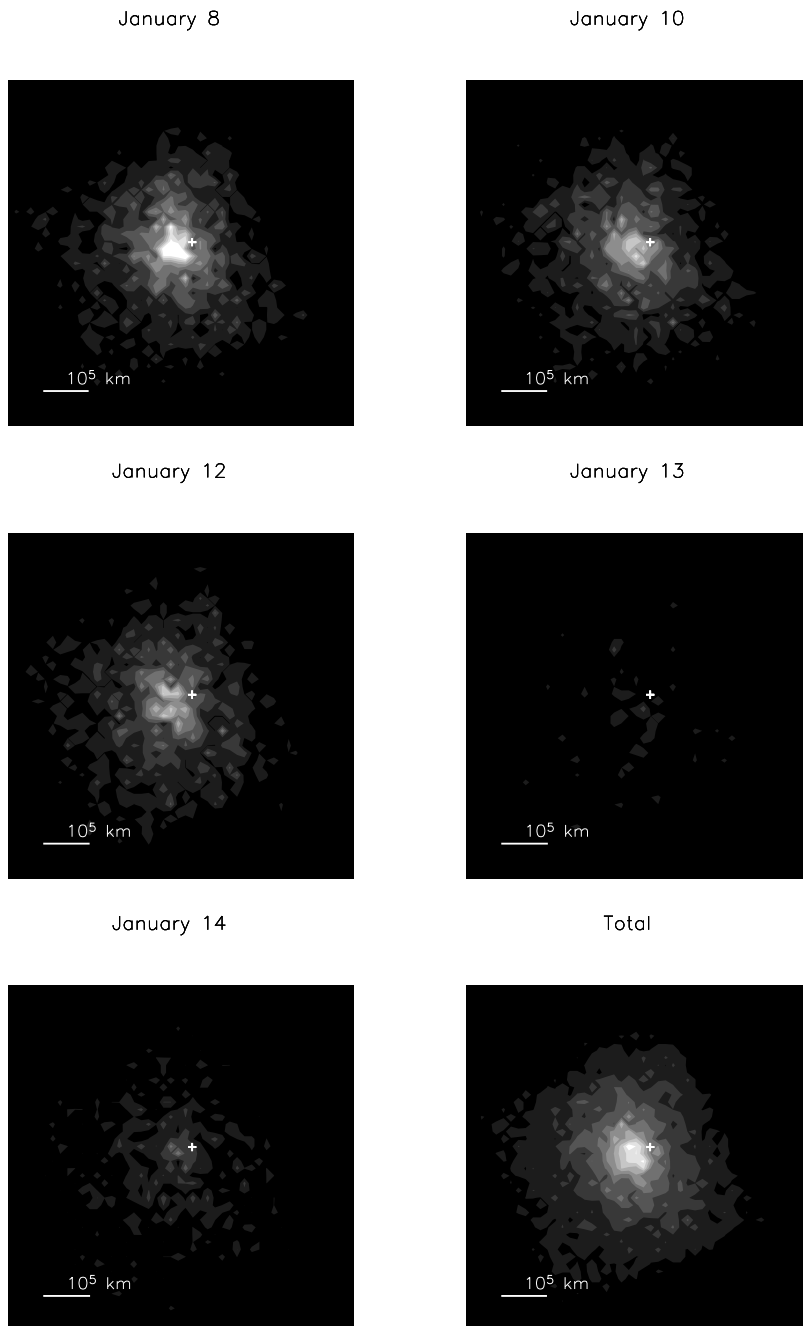


Figure 3.26: The morphology of each observation of comet *C/1999 T1* (McNaught-Hartley) and the combined morphology. All of the images are from the *ACIS-S3* chip, and the energy range of each is 0.2–1.0 keV.

In a similar fashion, the *S3* x-ray spectra from each observing period are shown in figure 3.27, as is the aggregate *S3* spectrum.

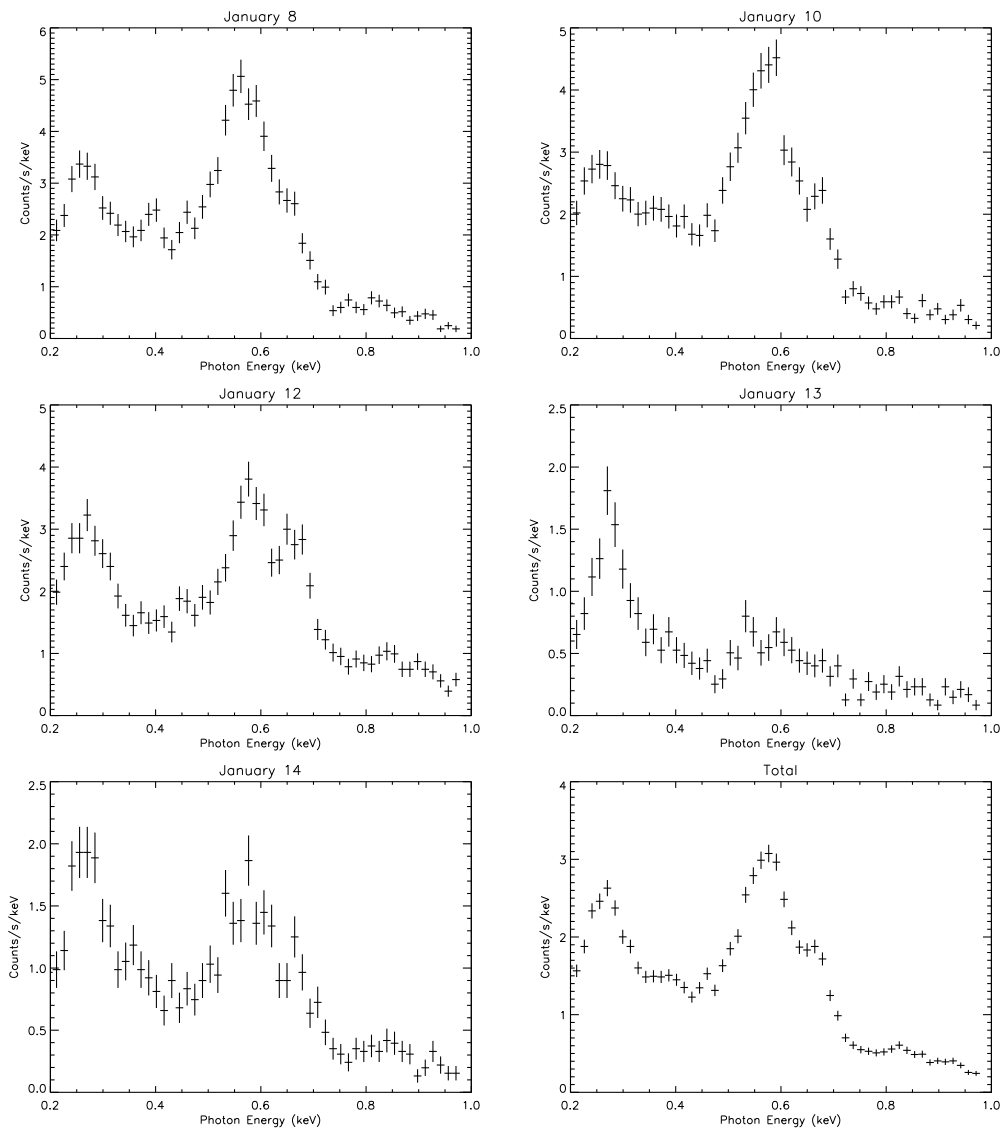


Figure 3.27: The x-ray spectra from each observation of comet C/1999 T1 (McNaught-Hartley), and the combined spectrum. Only detections by the *ACIS-S3* chip are considered.

There are a number of differences in the spectra, indicating that the emitting plasma is variable over the timescale of one day.

A structured morphology is observed in the energy range 0.2–1.0 keV (the energy range used in figure 3.26). The emission maps for the energy ranges 0.2–0.3 keV and 0.8–1.0 keV are shown in figure 3.28. The data are a composite of each observing period.

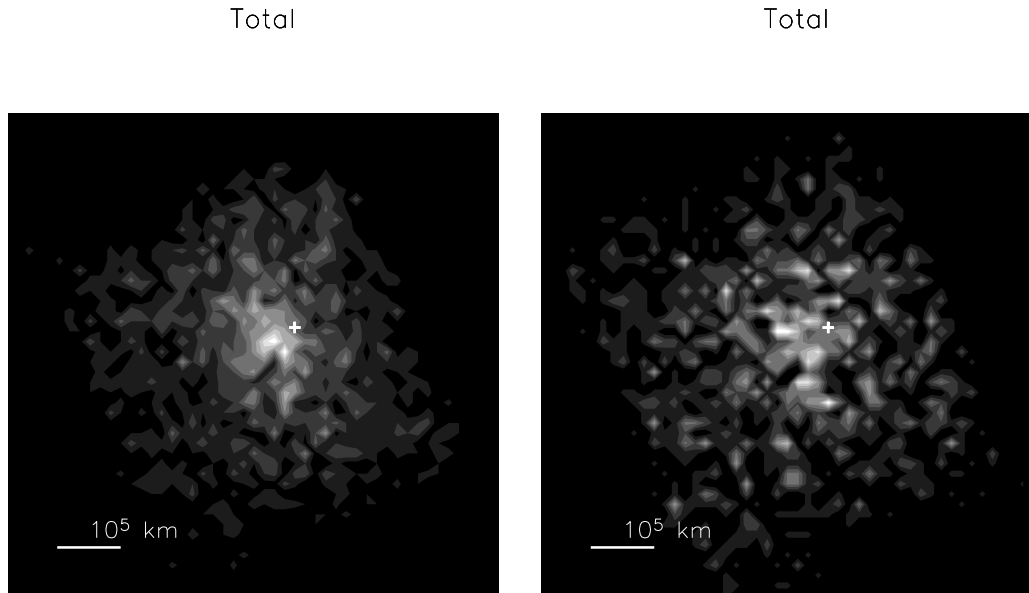


Figure 3.28: Narrow-band emission profiles for comet C/1999 T1 (McNaught-Hartley). The figures show emission in the ranges 0.2–0.3 keV (left) and 0.8–1.0 keV (right).

Figure 3.28 demonstrates that most of the emission between 0.2 and 0.3 keV is attributable to the cometary atmosphere rather than the background. This is also true, though to a lesser extent, of emission between 0.8 and 1.0 keV.

The light curves for each observation are shown in figure 3.29, and are fairly constant over the course of each one hour exposure, although there is variation from observation to observation (day to day). Each exposure was too short to show any significant variation in the x-ray flux.

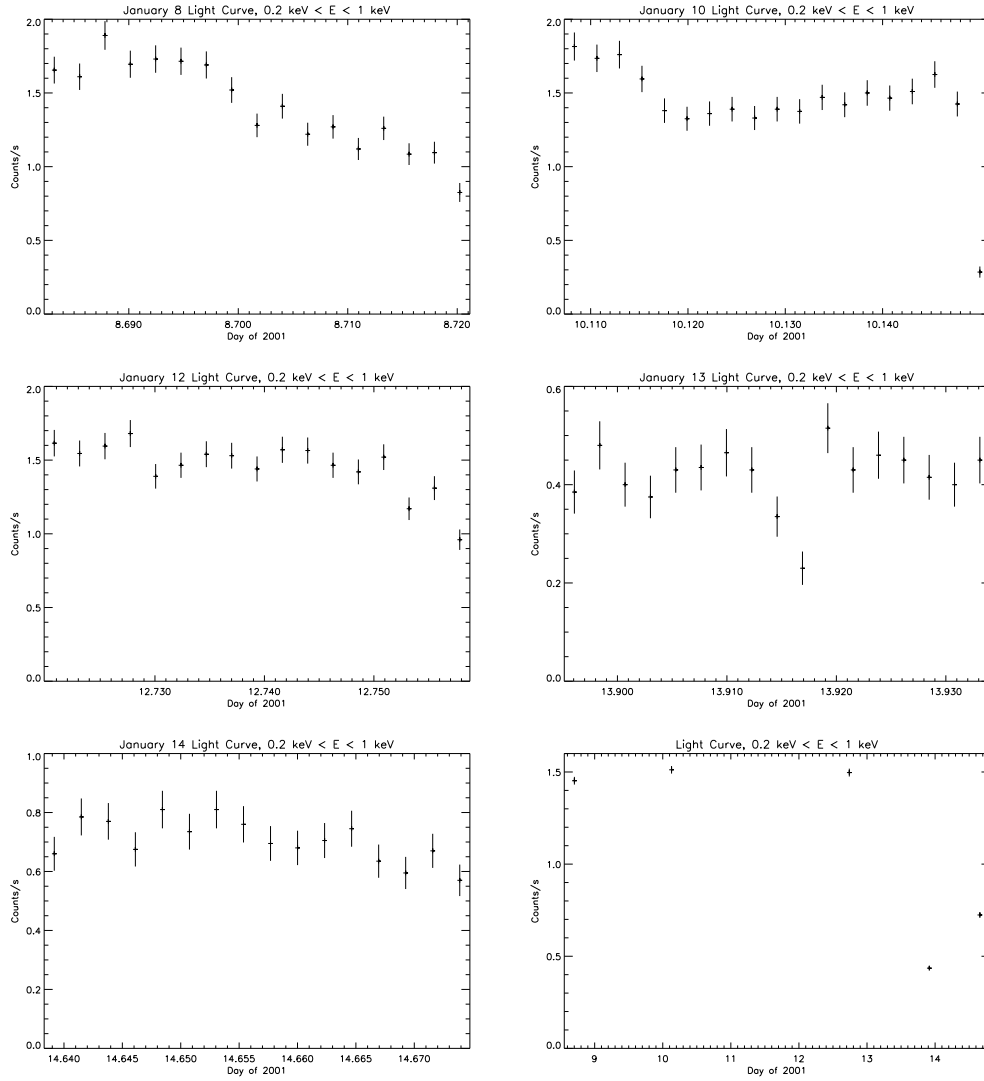


Figure 3.29: The light curves from each observation of comet C/1999 T1 (McNaught-Hartley).

The variability of these observations dictates that a treatment of the combined data — although it may be informative — is not appropriate for a comprehensive analysis as the plasma conditions in each case are not necessarily comparable.

In the analysis presented in chapter 5, data from the observation on January 8th are used. In this exposure, the luminosity detected by the *S3* and *S1* CCDs are  $P_x = 3.5 \times 10^{16} \text{ erg s}^{-1}$  and  $P_x = 9.8 \times 10^{15} \text{ erg s}^{-1}$  respectively.

Making a direct comparison of the light curve to the solar wind parameters is hampered by gaps in the *ACE* data. Measurements from *ACE-SWEPAM* are shown in figure 3.30. In the following plots, the line-shaded region shows the period of the observation, while the dot-shaded region shows this period minus a shift of 4.8 days, representing the time difference between the solar wind conditions travelling from the *ACE* to the region of the comet. Bodewits *et al* (2007) suggest a value of 6.63 days. It is difficult to assign a value from the data due to gaps in the data from *ACE-SWEPAM*.

The possible correlation can be made between periods of high solar wind and x-ray fluxes with a delay of approximately seven days, although such a comparison should not be relied on. The measured magnetic field from the same period is shown in figure 3.31. *ACE-SWICS* data are plotted in figures 3.32 and 3.33.

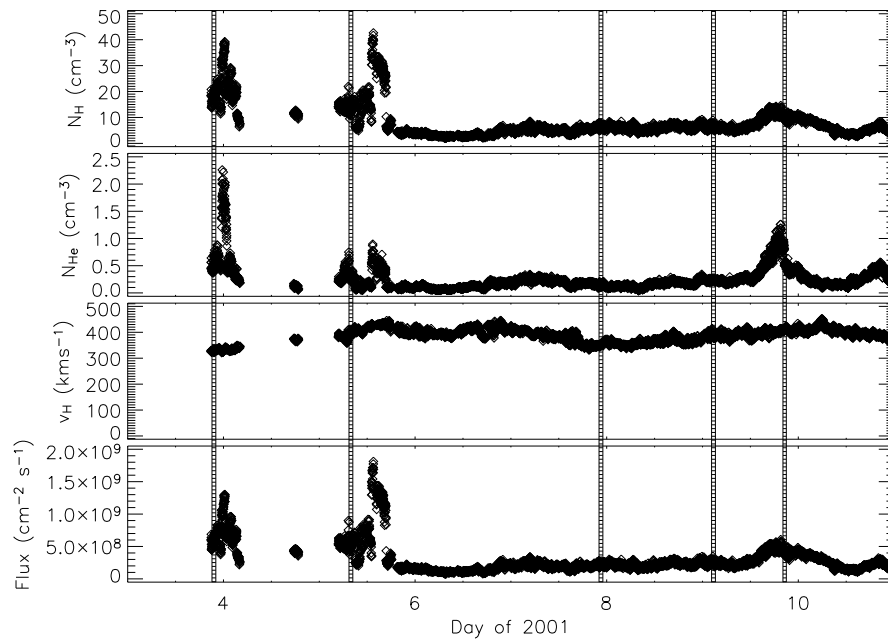


Figure 3.30: *ACE-SWEPAM* measurements of the solar wind parameters around the observation of comet C/1999 T1 (McNaught-Hartley). The *Chandra* observations took place between days 8 and 14 of the year 2001.

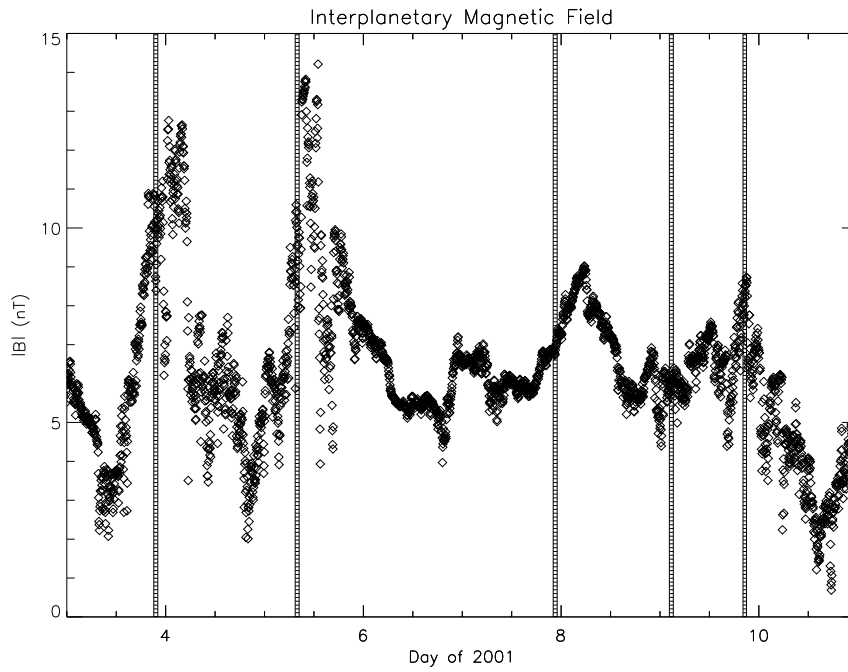


Figure 3.31: *ACE-MAG* measurements of the interstellar magnetic field around the observation of comet *C/1999 T1* (McNaught-Hartley). The *Chandra* observation took place between days 8 and 14 of the year 2001.

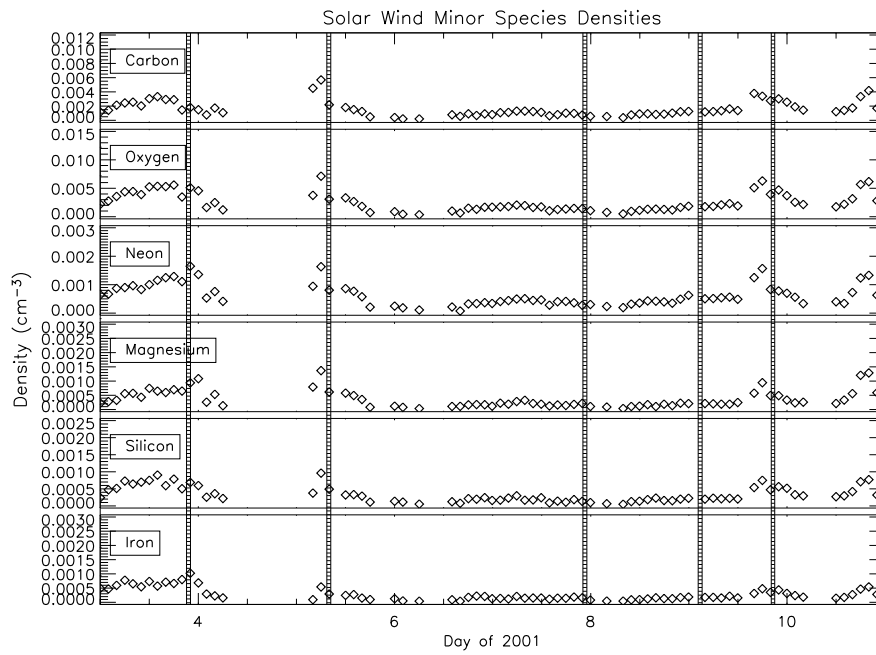


Figure 3.32: *ACE-SWICS* measurements of the solar wind minor species densities in the period of the observation of comet *C/1999 T1* (McNaught-Hartley). The *Chandra* observations took place between days 8 and 14 of the year 2001.

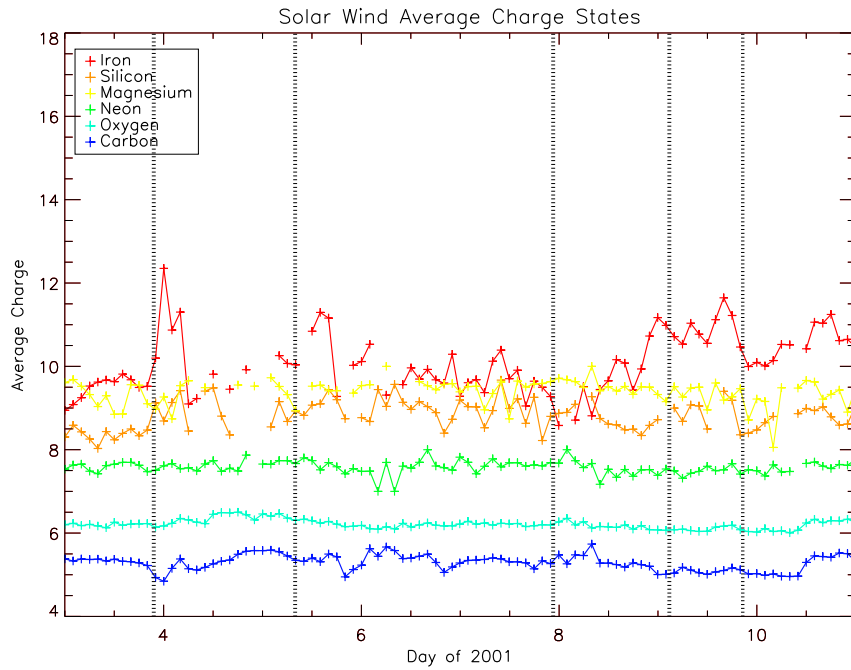


Figure 3.33: *ACE-SWICS* measurements of the average charge of the solar wind minor species in the period of the observation of comet C/1999 T1 (McNaught-Hartley). The *Chandra* observations took place between days 8 and 14 of the year 2001.

### 3.4.4 Comet C/2002 C1 (Ikeya-Zhang)

The *Chandra* observation with the most counts to date is that of comet C/2002 C1 (Ikeya-Zhang) (Dennerl, 2001), also designated 153P/Ikeya-Zhang (the former is used here). The position of the comet was similar to that of comet C/1999 S4 (LINEAR) (see section 3.4.1), with  $R = 0.799$  AU and  $\Delta = 0.457$  AU. Two exposures were taken on the 15th April 2002: one commencing at 1:30 am, the other at 11 pm. Each observing period recorded 3:15 hours of good time. Overall, in the range 0.2–1.5 keV, 425,000 detections were made by six of the *ACIS* CCDs.

The observation was planned in a different manner than the other *Chandra* observations. Rather than periodically re-point the satellite to track the motion of the comet, the pointing direction was fixed and the comet passed through the field of view. This approach has its disadvantages. The period of an observation is limited by the speed of the comet, and as the observed line of sight through the comet is dynamic, it is not possible to construct a light curve. There is one advantage, although its presence is coincidental. In this case, the emitting plasma was large enough to fill a single CCD chip. By allowing the comet to fly through the field of view, a wider exposure of the atmosphere was taken.

The complete aggregate *ACIS* image of the observation is shown in figure 3.34, along with the combined spectrum.

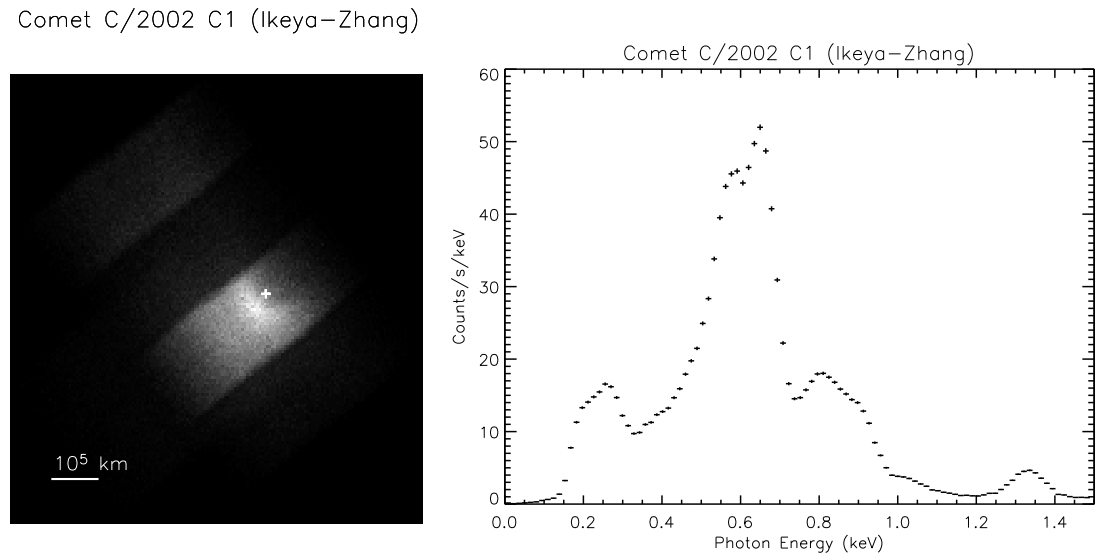


Figure 3.34: The full *ACIS* image and spectrum from the first *Chandra* observation of comet C/2002 C1 (Ikeya-Zhang).

Unlike previous observations, significant source (rather than background) detections were made by chips other than *S3*. The images and spectra from the *ACIS-I*, *S1*, *S2*, *S3* and *S4* chips are shown in figures 3.35 to 3.39.

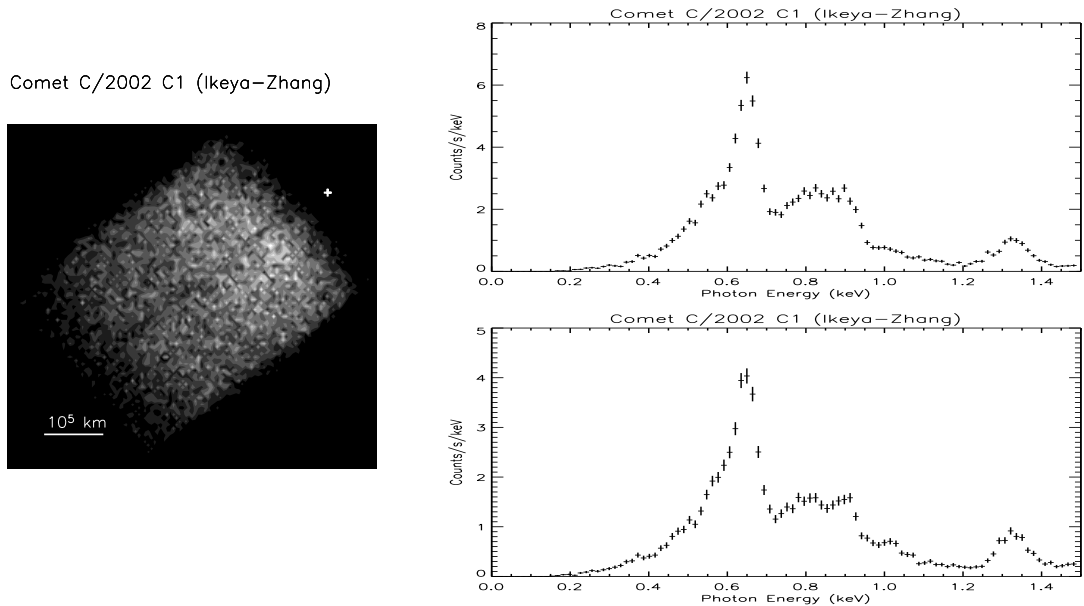


Figure 3.35: The x-ray image and spectrum of comet C/2002 C1 (Ikeya-Zhang) from the *ACIS-I* array. The top spectrum is from the first observing period, and the lower spectrum is from the second observing period.

The *ACIS-I* data are the least significant of the observation. The emission brightness decreases with distance from the nucleus (apart from at the extremities of the chip where the effective area is lower). Spectrally, the signal is weak below 500 eV because the quantum efficiency of the front illuminated chips is low in this energy range. The data from *ACIS-I* CCDs are not considered in the modelling presented in chapter 5.

The data from the secondary back illuminated chip, *S1*, are shown via an image and spectrum in figure 3.36. The position of the cometary nucleus is outside the range of the figure, to the lower right of the image. The gradual reduction of the x-ray brightness confirms that main source of x-rays is the comet rather than the background (compare with *S1* images of comet C/1999 S4 (LINEAR) in figure 3.10).

Comet C/2002 C1 (Ikeya-Zhang)

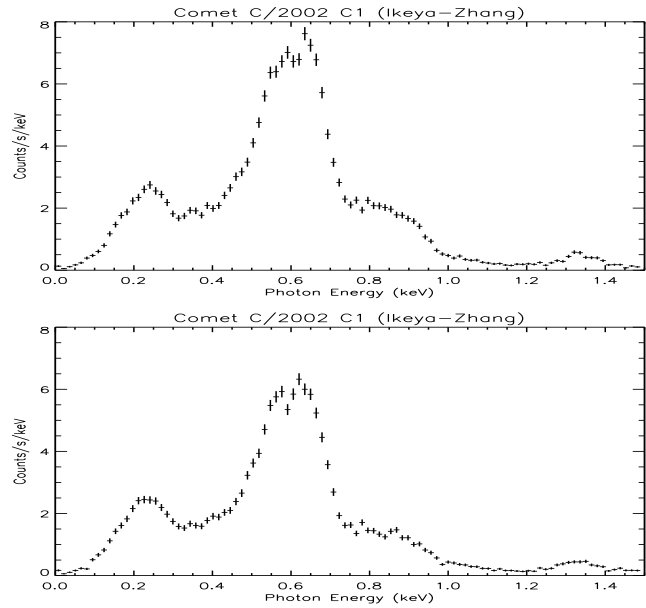
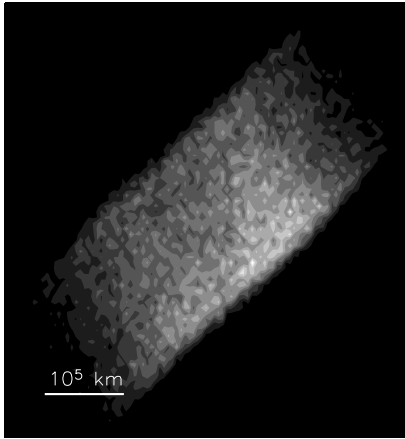


Figure 3.36: The x-ray image and spectrum of comet C/2002 C1 (Ikeya-Zhang) from the ACIS-S1 chip. The nucleus is located off of the image to the lower-right.

Comet C/2002 C1 (Ikeya-Zhang)

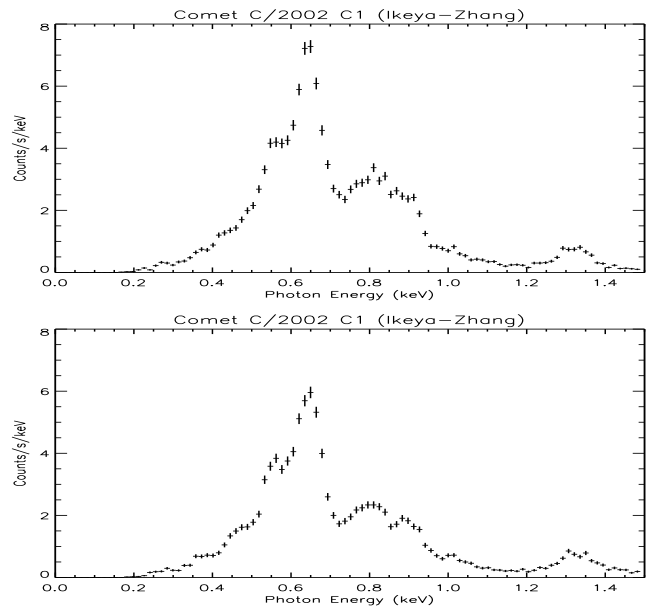
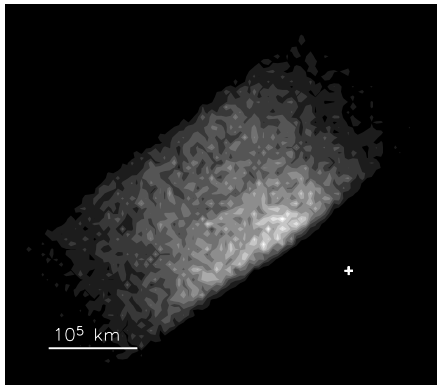


Figure 3.37: The x-ray image and spectrum of comet C/2002 C1 (Ikeya-Zhang) from the ACIS-S2 chip.

The luminosities detected from each observing period are  $P_x = 8.5 \times 10^{15} \text{ erg s}^{-1}$  and  $P_x = 7.2 \times 10^{15} \text{ erg s}^{-1}$ .

The *S2* chip data are interesting in this observation. This is the first comet to be detected with the front illuminated chips *S2* and *S4*. Although these chips suffer from poor quantum efficiency at energies lower than around 500 eV, the resolving power is slightly greater than that of the back illuminated chips. Data from the *S2* chip are shown in figure 3.37. The detected luminosities are  $P_x = 1.8 \times 10^{16} \text{ erg s}^{-1}$  and  $P_x = 1.5 \times 10^{15} \text{ erg s}^{-1}$ .

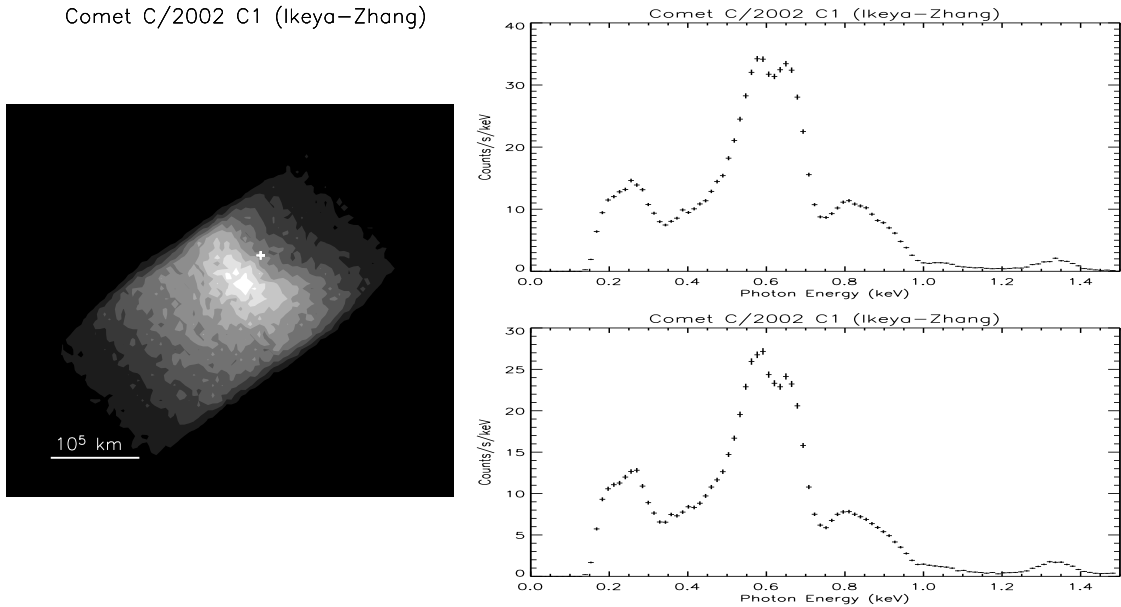


Figure 3.38: The x-ray image and spectrum of comet *C/2002 C1* (Ikeya-Zhang) from the *ACIS-S3* chip.

As with the other *Chandra* observations the comet nucleus was centred on the most sensitive array, *S3*, and so this chip was exposed to the most counts. The *S3* data are shown in figure 3.38. The detected luminosities are  $P_x = 3.1 \times 10^{16} \text{ erg s}^{-1}$  and  $P_x = 2.5 \times 10^{15} \text{ erg s}^{-1}$ . The average point of maximum brightness is 36,000 km from the nucleus.

The *S4* data, shown in figure 3.39 are similar in terms of morphology and the detected spectrum to the *S2* data. The detected luminosities are  $P_x = 1.6 \times 10^{16} \text{ erg s}^{-1}$  and  $P_x = 1.2 \times 10^{15} \text{ erg s}^{-1}$ .

The spectra from each CCD demonstrate that the x-ray emitting atmosphere was large enough to fill the solid angle projected by the *ACIS* array. As a result, it is not possible to designate a background region.

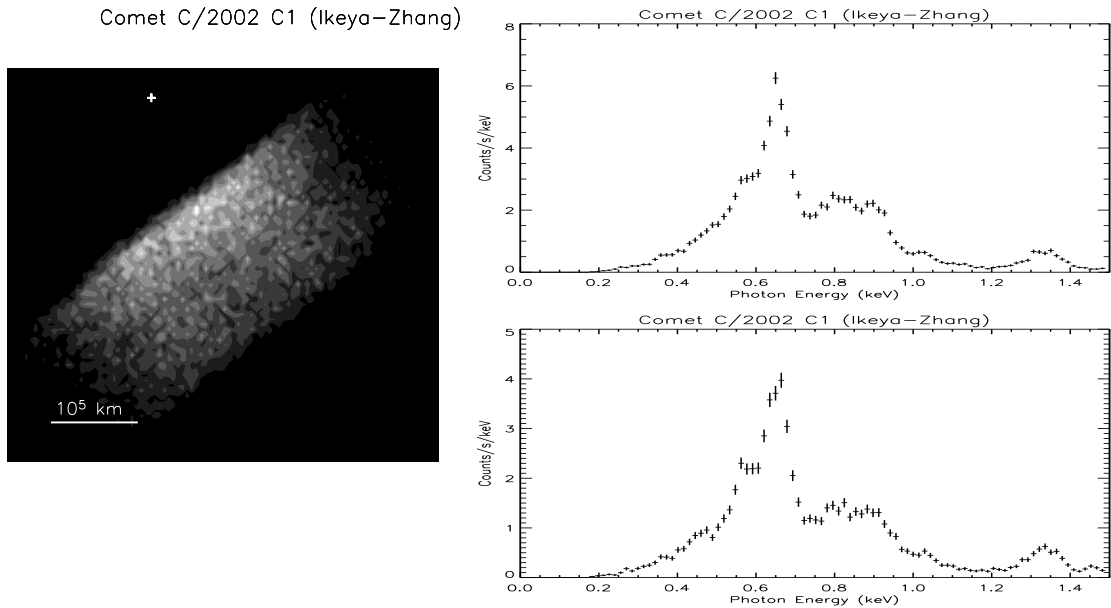


Figure 3.39: The x-ray image and spectrum of comet C/2002 C1 (Ikeya-Zhang) from the *ACIS-S4* chip.

*ACE* data from the period around the observation are shown in figures 3.40 to 3.43. In these figures, the line-shaded region shows the period of the observation, while the dot-shaded region shows this period plus a shift of 4.5 days, representing the time difference between the solar wind conditions travelling from the *ACE* to the region of the comet. Bodewits *et al* (2007) suggest a value of  $-0.73$  days. However, the model used to predict the delay only considers the difference in the ecliptic longitudes of the Earth and the comet. During the observation, this difference was only  $0.5^\circ$ . The relatively large latitude of the comet,  $26^\circ$  is not considered. As a result, the model significantly underestimates the delay between equivalent solar wind conditions being present at the comet and the Earth. The value used here is derived from results of modelling the x-ray spectra. Significant line emission from  $\text{Fe}^{16}$  ions is detected. Figure 3.43 shows that the average charge of iron increased significantly on day 109 of 2002, suggesting a minimum value for the delay. As there are no light curves from the observation, it is difficult to specify the delay with more accuracy.

Figure 3.40 shows measurements from *ACE-SWEPAM*. The magnetic field from the same period is plotted in figure 3.41. The density of each of the minor species and their average ion charges are shown in figures 3.42 and 3.43 respectively.

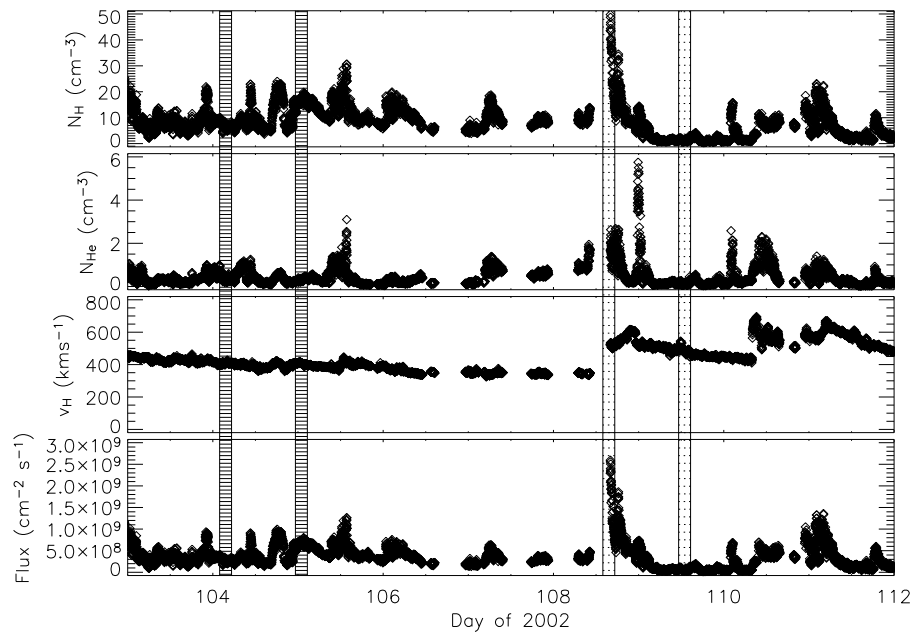


Figure 3.40: *ACE-SWEPAM* measurements of the solar wind parameters around the observation of comet C/2002 C1 (Ikeya-Zhang). The *Chandra* observation took place during day 103 of the year 2002.

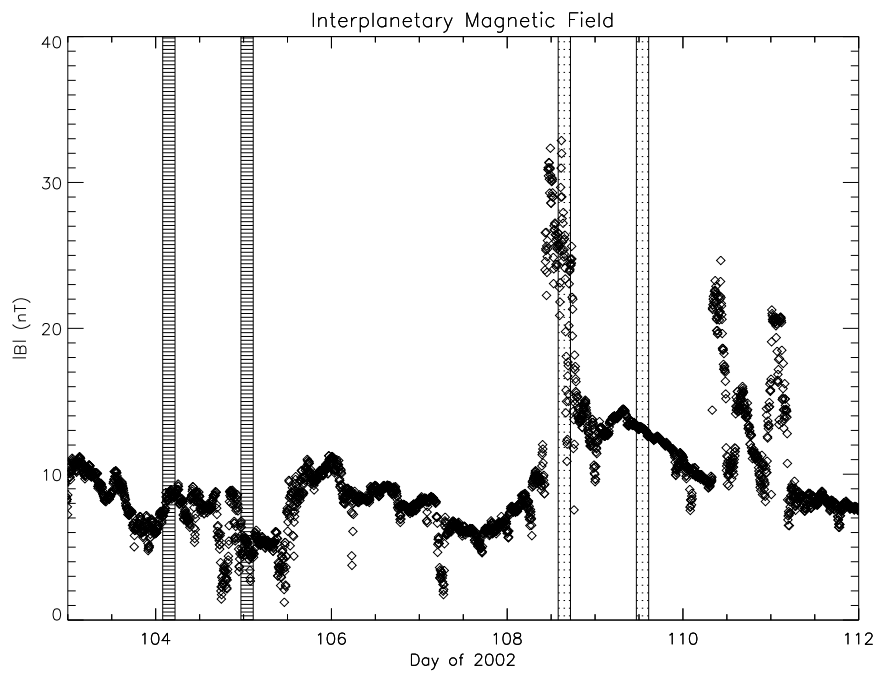


Figure 3.41: *ACE-MAG* measurements of the interstellar magnetic field around the observation of comet C/2002 C1 (Ikeya-Zhang). The *Chandra* observation took place during day 103 of the year 2002.

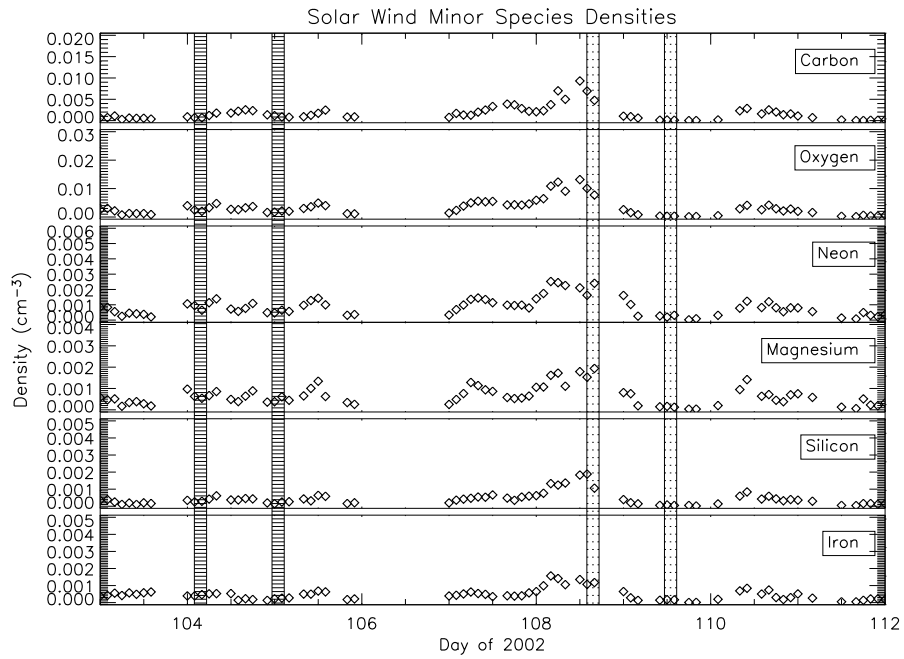


Figure 3.42: *ACE-SWICS* measurements of the solar wind minor species densities in the period of the observation of comet C/2002 C1 (Ikeya-Zhang). The *Chandra* observation took place during day 103 of the year 2002.

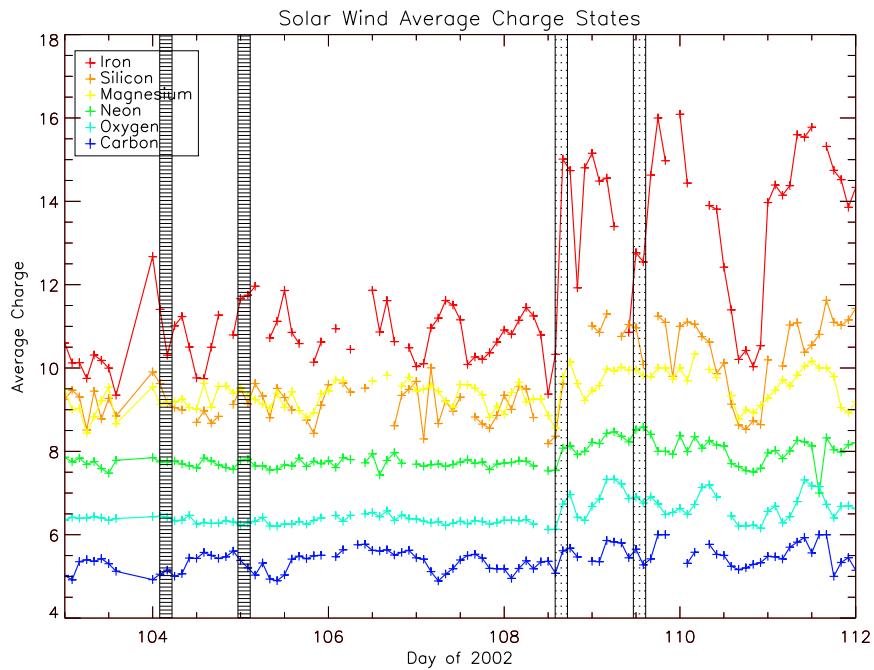


Figure 3.43: *ACE-SWICS* measurements of the average charge of the solar wind minor species in the period of the observation of comet C/2002 C1 (Ikeya-Zhang). The *Chandra* observation took place during day 103 of the year 2002.

### 3.4.5 Comet 2P/Encke (2003)

Comet 2P/Encke is the only comet to be observed in two separate orbits. The first observation with ROSAT (Lisse *et al*, 1999b) is discussed in chapter 2. The second observation is presented in Lisse *et al*, (2005), and an analysis is made here.

The *Chandra* observation of 2P/Encke took place on the 24th of November 2003, when the comet had a heliocentric distance of  $R = 0.891$  AU and a geocentric distance of  $\Delta = 0.275$  AU. The comet was continuously tracked for over 15 hours, resulting in a good time interval of 44,000 seconds. The *ACIS-S3* CCD counted 8795 x-rays in the range 0.2–0.8 keV.

The complete *ACIS* image and spectrum are shown in figure 3.44.

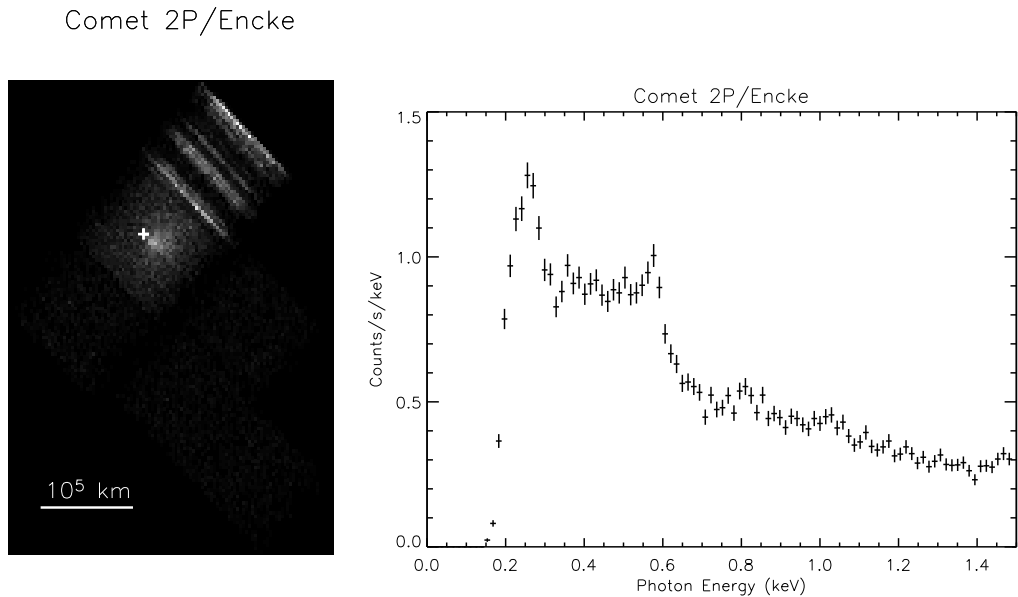


Figure 3.44: The total x-ray image and spectrum from the *ACIS* observation of comet 2P/Encke.

Note the unusual chip configuration for this observation, with the front illuminated *I0* chip being mistakenly activated rather than back illuminated *S1*.

The image and spectrum from the *ACIS-S3* CCD are shown in figure 3.45. The luminosity detected by the *S3* CCD is  $P_x = 2.8 \times 10^{14}$  erg  $s^{-1}$ . The point of maximum x-ray brightness is 9,000 km from the position of the nucleus.

The light curve is plotted in figure 3.46.

Comet 2P/Encke

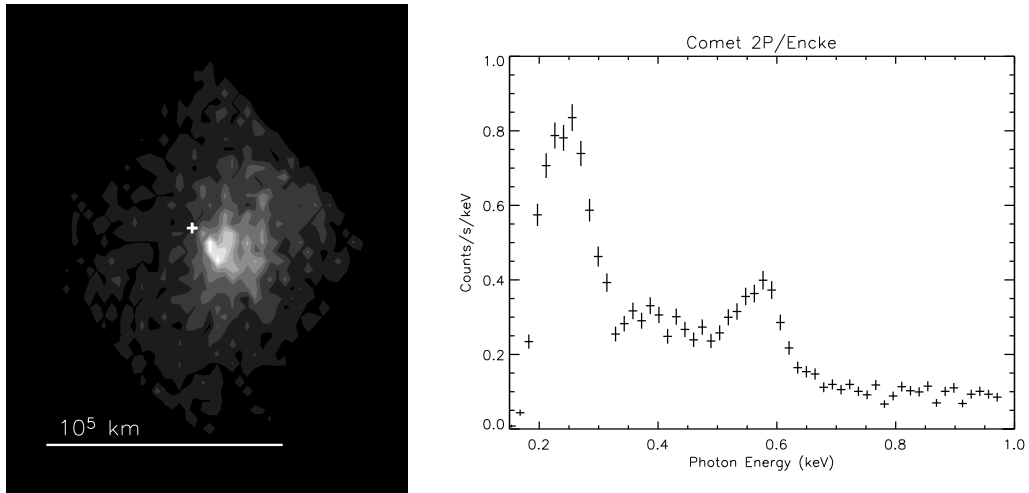


Figure 3.45: The x-ray image and spectrum from the *ACIS-S3* observation of comet 2P/Encke.

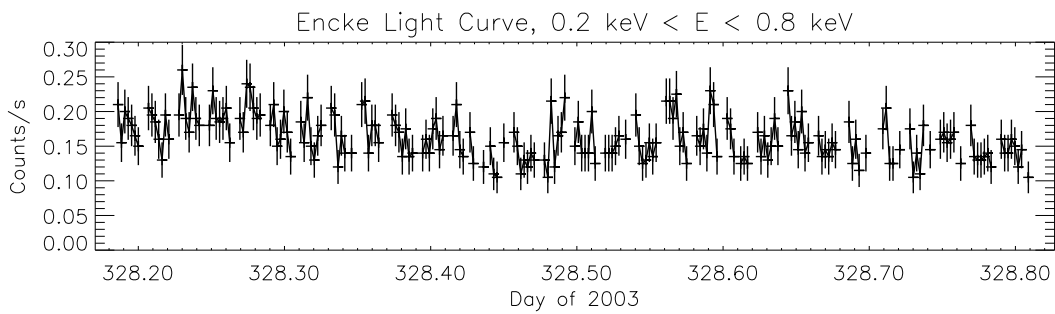


Figure 3.46: The light curve from comet 2P/Encke 2003.

*ACE* data from the period of the observation are shown in figures 3.47 to 3.50. In these figures, the line-shaded region shows the period of the observation, while the dot-shaded region shows this period plus a shift of 0.95 days, representing the time difference between the solar wind conditions travelling from the *ACE* to the region of the comet. This compares well to the value of 1.09 suggested by Bodewits *et al* (2007). Measurements from *ACE-SWEPAM* are shown in figure 3.47. Note that the observation took place four days too late to coincide with a short period of higher solar wind flux. Had the observation occurred at this time, a significantly higher x-ray flux would be expected.

Data from *ACE-MAG* from the same period are shown in figure 3.48. The minor species' densities and averaged charges are plotted in figures 3.49 and 3.50.

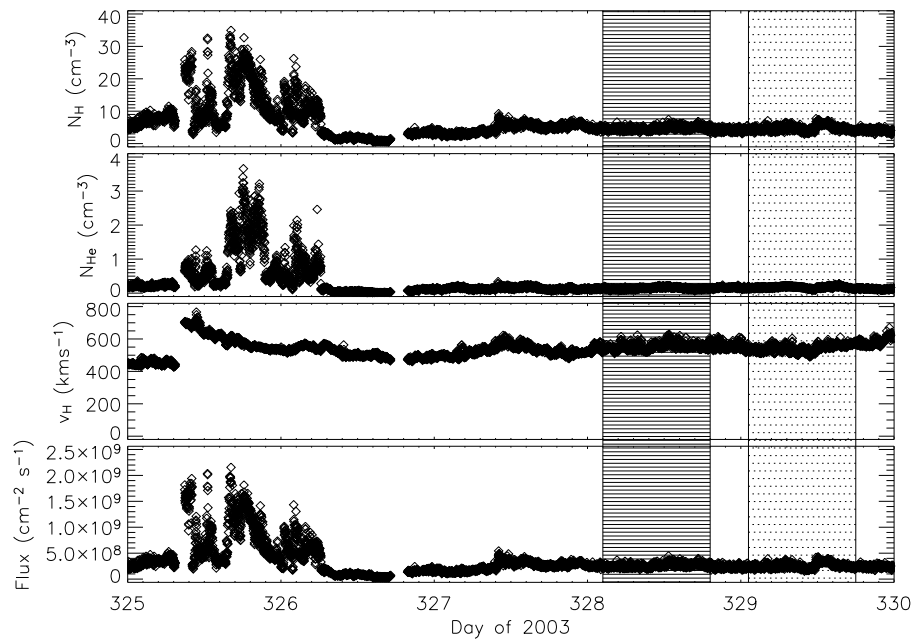


Figure 3.47: *ACE-SWEPAM* measurements of the solar wind parameters around the observation of comet 2P/Encke. The *Chandra* observation took place during day 328 of the year 2003.

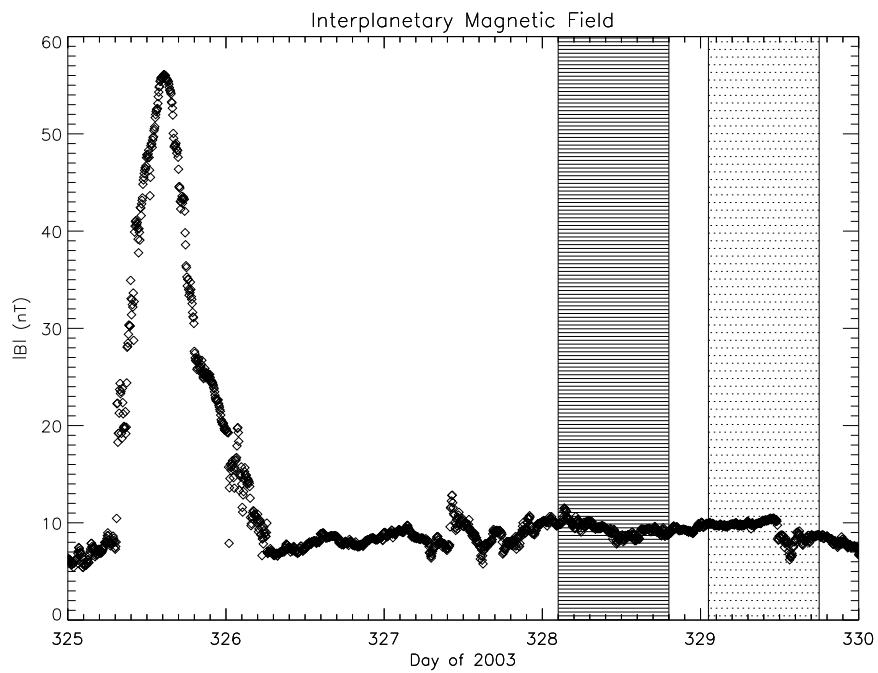


Figure 3.48: *ACE-MAG* measurements of the interstellar magnetic field around the observation of comet 2P/Encke. The *Chandra* observation took place during day 328 of the year 2003.

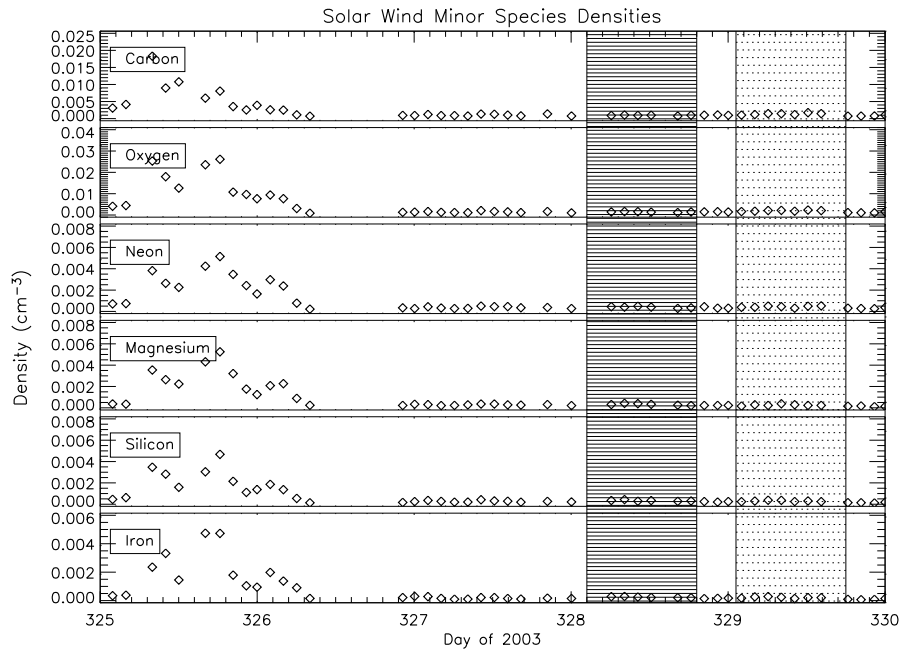


Figure 3.49: *ACE-SWICS* measurements of the solar wind minor species densities in the period of the observation of comet 2P/Encke. The *Chandra* observation took place during day 328 of the year 2003.

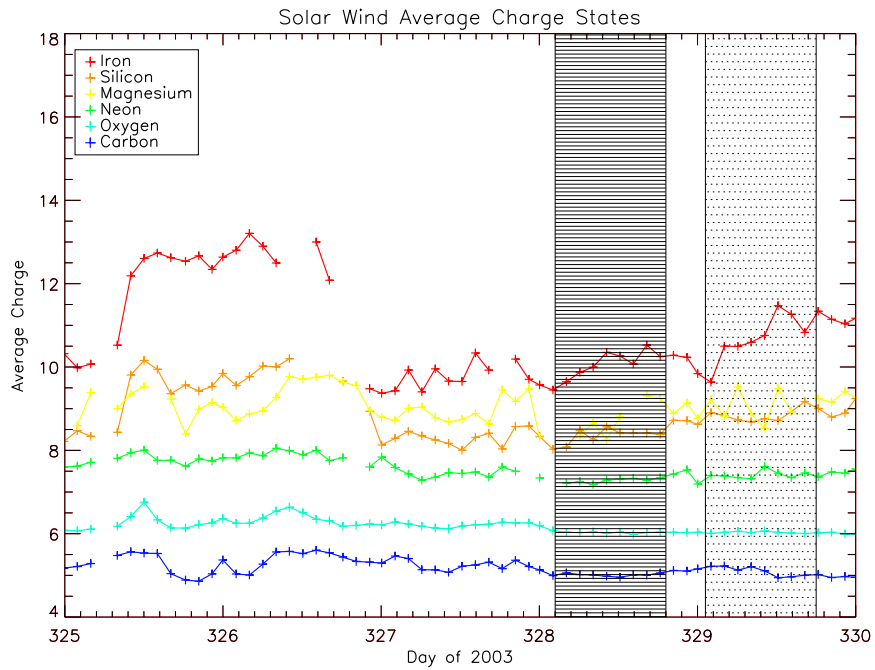


Figure 3.50: *ACE-SWICS* measurements of the average charge of the solar wind minor species in the period of the observation of comet 2P/Encke. The *Chandra* observation took place during day 328 of the year 2003.

### 3.4.6 Comet C/2001 Q4 (NEAT)

A short observation of comet C/2001 Q4 (NEAT) was made on May 12 2004, when the geocentric and heliocentric distances were  $\Delta = 0.362$  AU and  $R = 0.964$  AU respectively. From 3 pointings, the good time interval was 10.3 ks. The *ACIS-S3* chip detected 8764 x-rays in between 0.2 and 0.8 keV.

Comet C/2001 Q4 (NEAT)

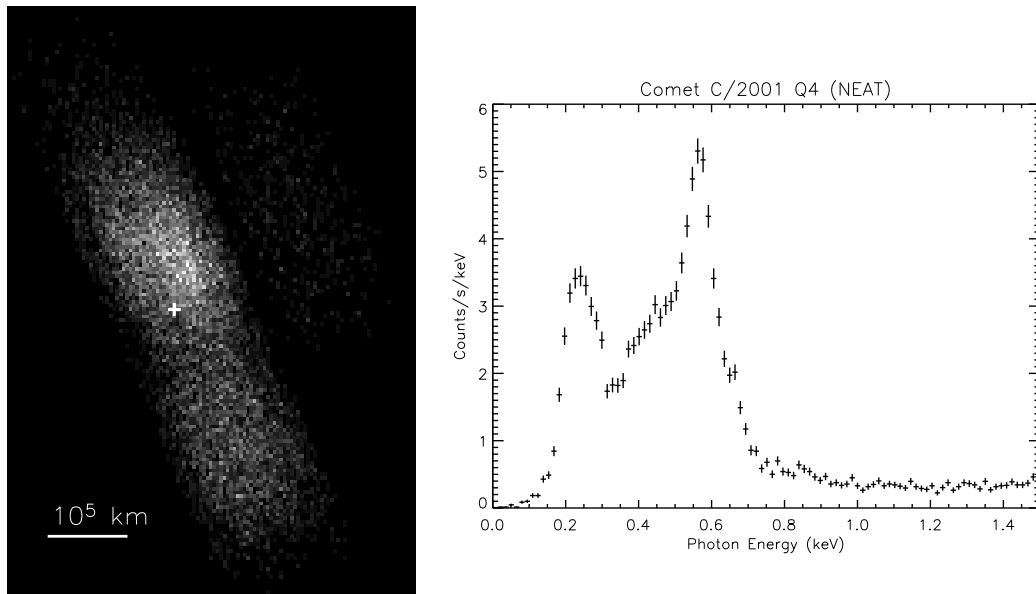


Figure 3.51: The total x-ray image and spectrum from the *ACIS* observation of comet C/2001 Q4 (NEAT).

Data from *ACIS-S3* and *ACIS-S1* are shown in figures 3.52 and 3.53 respectively. The luminosity detected by each CCD is  $P_x = 6.7 \times 10^{15}$  erg s<sup>-1</sup> and  $P_x = 4.4 \times 10^{15}$  erg s<sup>-1</sup>.

Comet C/2001 Q4 (NEAT)

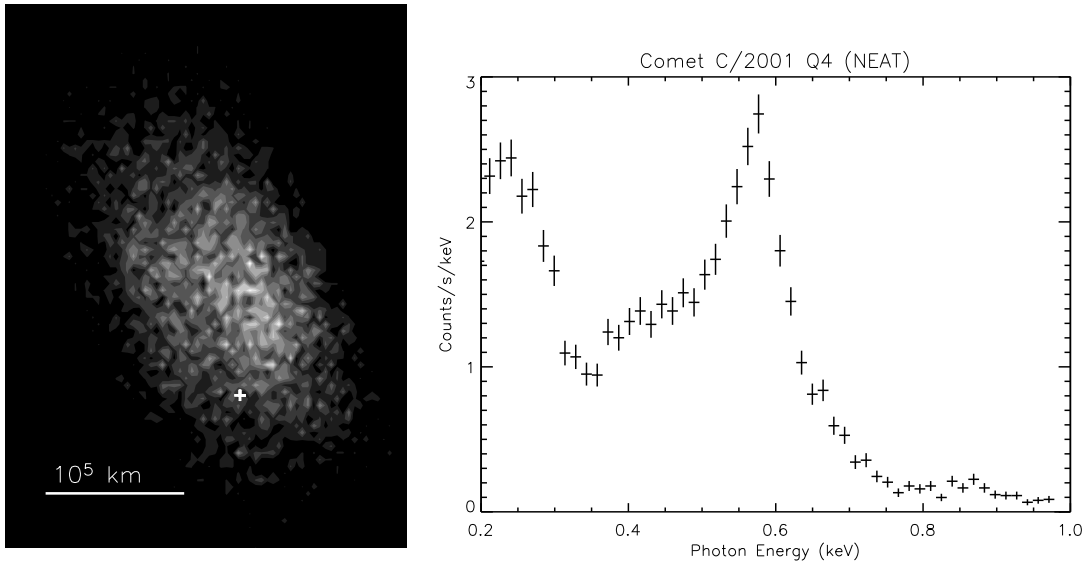


Figure 3.52: The x-ray image and spectrum from the *ACIS-S3* observation of comet C/2001 Q4 (NEAT).

Comet C/2001 Q4 (NEAT)

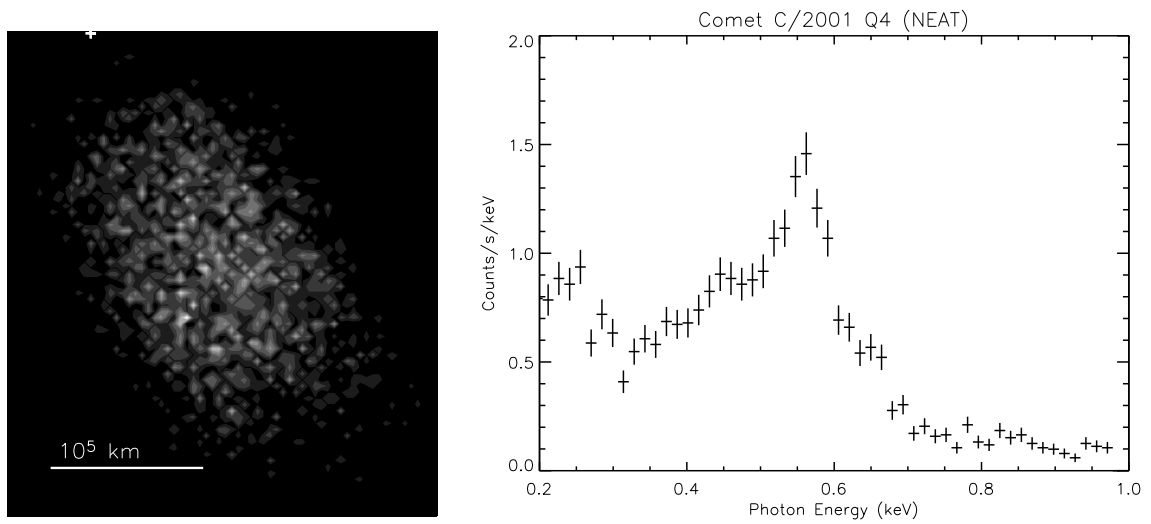


Figure 3.53: The x-ray image and spectrum from the *ACIS-S1* observation of comet C/2001 Q4 (NEAT).

The *ACIS-S3* light curve for the photons in the energy range  $0.2 < E < 0.8$  keV is plotted in figure 3.54.

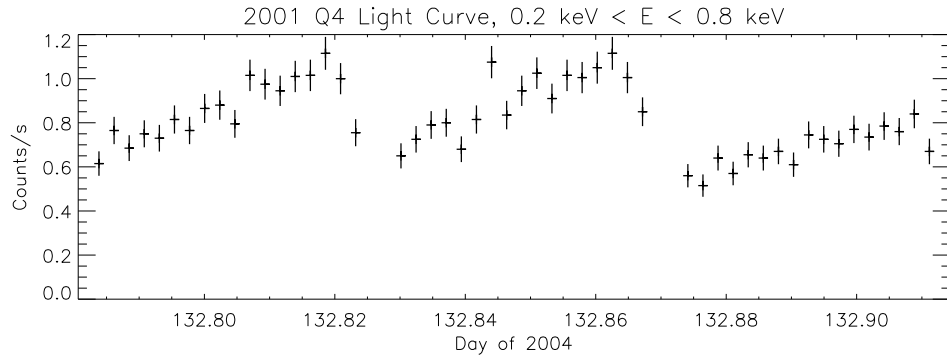


Figure 3.54: The light curve from comet C/2001 Q4 (NEAT).

*ACE* data from the period of the observation are shown in figures 3.55 to 3.58. In these figures, the line-shaded region shows the period of the observation, while the dot-shaded region shows this period plus a shift of 0.95 days (from Bodewits *et al*, 2007). *ACE-SWEPAM* data plotted in figure 3.55. Measurements of the magnetic field from the same period are shown in figure 3.56. The densities and average charges of minor species ions, from *ACE-SWICS*, are shown in figures 3.57 and 3.58.

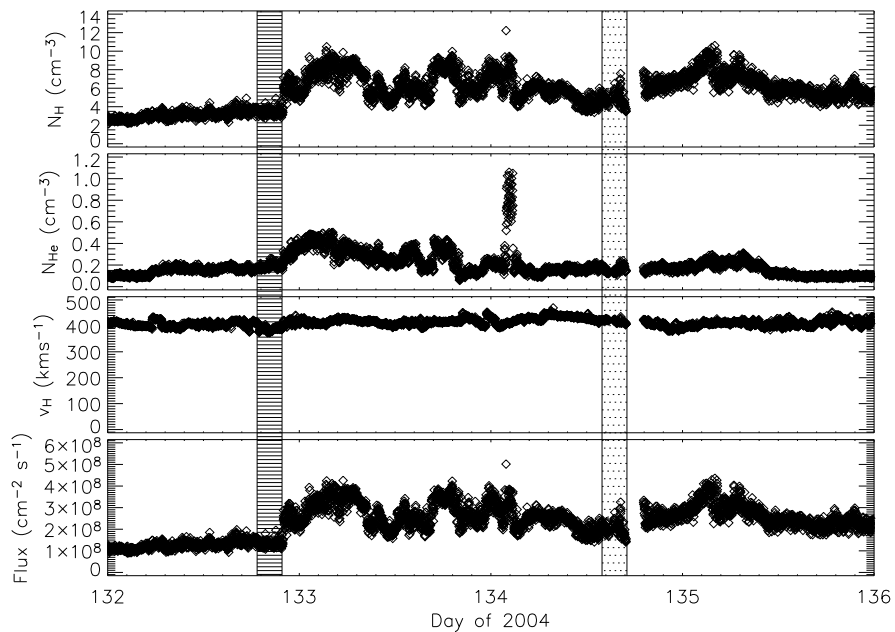


Figure 3.55: *ACE-SWEPAM* measurements of the solar wind parameters around the observation of comet C/2001 Q4 (NEAT). The *Chandra* observation took place during day 132 of the year 2004.

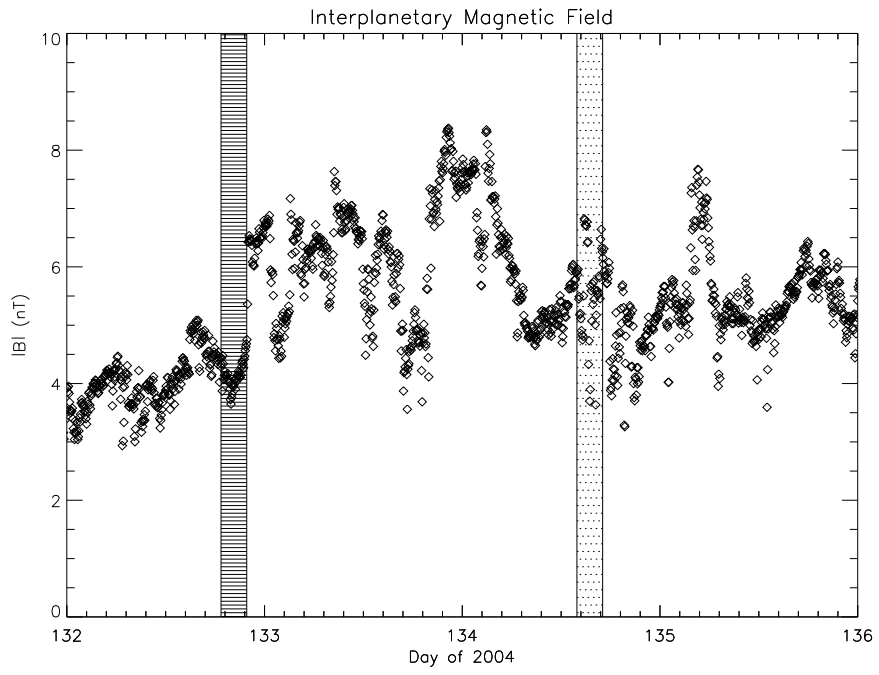


Figure 3.56: *ACE-MAG* measurements of the interstellar magnetic field around the observation of comet *C/2001 Q4* (NEAT). The *Chandra* observation took place during day 132 of the year 2004.

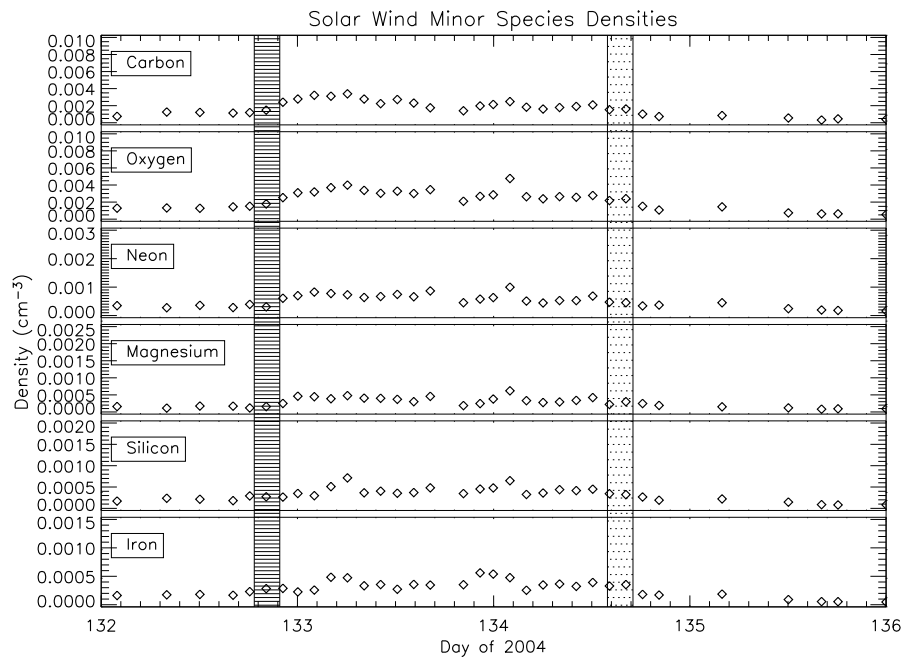


Figure 3.57: *ACE-SWICS* measurements of the solar wind minor species densities in the period of the observation of comet *C/2001 Q4* (NEAT). The *Chandra* observation took place during day 132 of the year 2004.

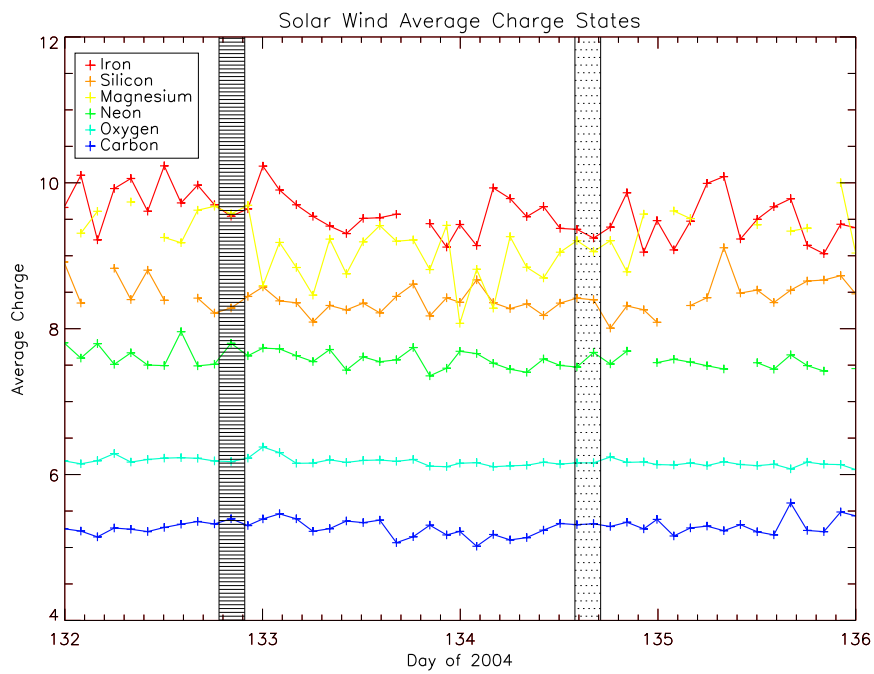


Figure 3.58: *ACE-SWICS* measurements of the average charge of the solar wind minor species in the period of the observation of comet C/2001 Q4 (NEAT). The *Chandra* observation took place during day 132 of the year 2004.

### 3.4.7 Comet 9P/Tempel 1

Comet 9P/Tempel 1 was the target for NASA's Deep Impact mission in July 2005. This mission involved crashing a 300 kg impactor into the surface of the comet and studying the ejected plume. The comet was observed by *Chandra* before, during and after the impact on July 4th 2005 for a total observing period of 293 ks.

A total of 7 separate pointing were performed between June 30 and July 24, with individual exposures ranging from 33 ks to 61 ks. Over the course of the mission, the heliocentric and geocentric distances of the comet changed from  $R = 1.507$  AU and  $\Delta = 0.872$  AU to  $R = 1.518$  AU and  $\Delta = 1.01$  AU.

The *ACIS-S3* x-ray images from each exposure are shown in figure 3.59. The contour scale from the June 8th exposure is used in all of the images to show the intensity relative to the brightest observing period. The point of maximum brightness is 13,000 km from the nucleus for the brightest observation. The x-ray spectrum obtained in each observing period is shown in figure 3.60, and the corresponding light curves, plus a broader light curve encompassing the total observation, are shown in figures 3.61 and 3.62.

Data from the brightest observing period are considered further in chapter 5. In this exposure, the luminosities detected by the *S3* and *S1* CCDs is  $P_x = 1.7 \times 10^{16}$  erg s<sup>-1</sup> and  $P_x = 9.9 \times 10^{15}$  erg s<sup>-1</sup> respectively.

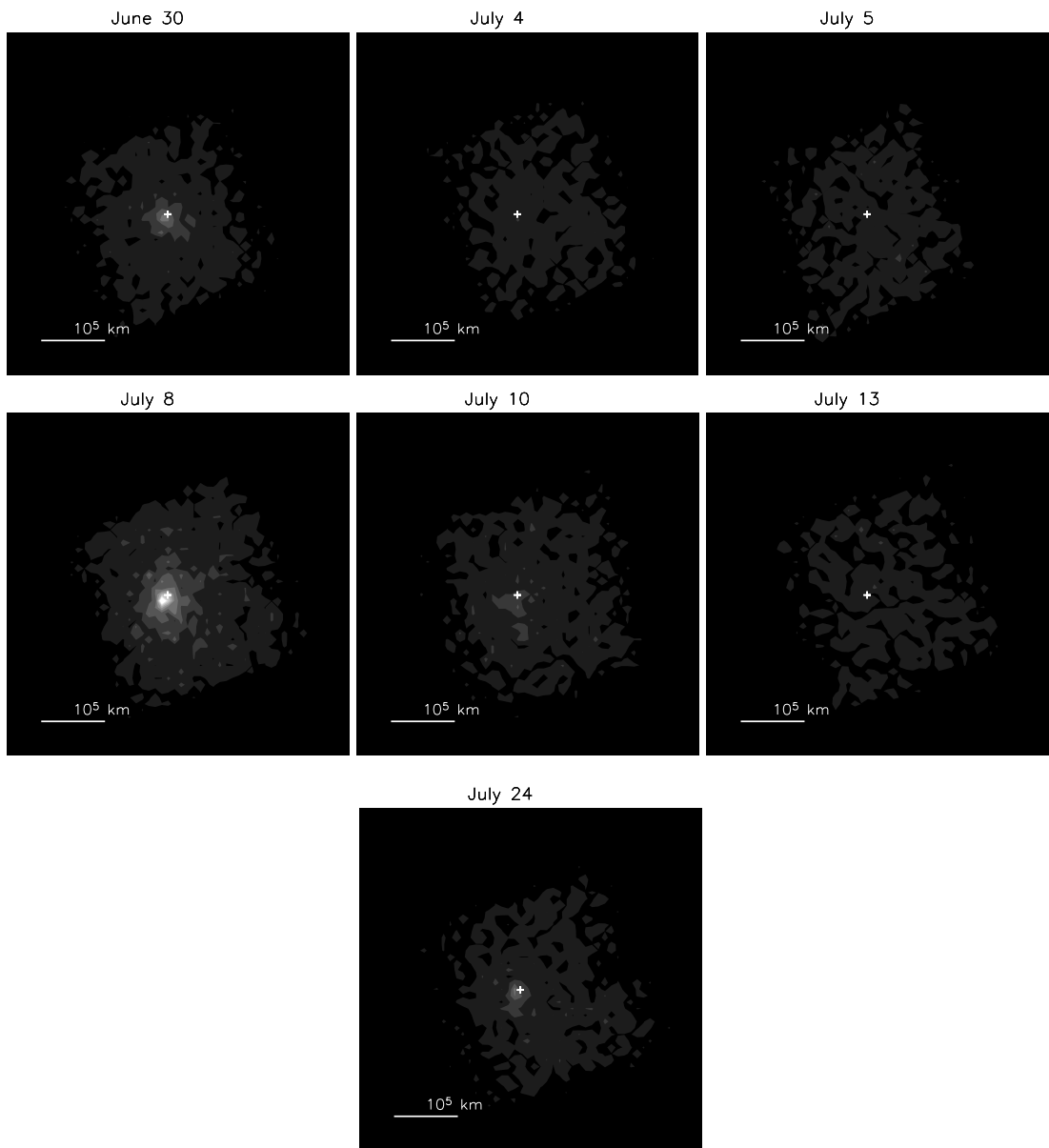


Figure 3.59: The morphology of each observing period of comet 9P/Tempel 1. All of the images are from the *ACIS-S3* chip. Each image is scaled to the brightest exposure (July 8th).

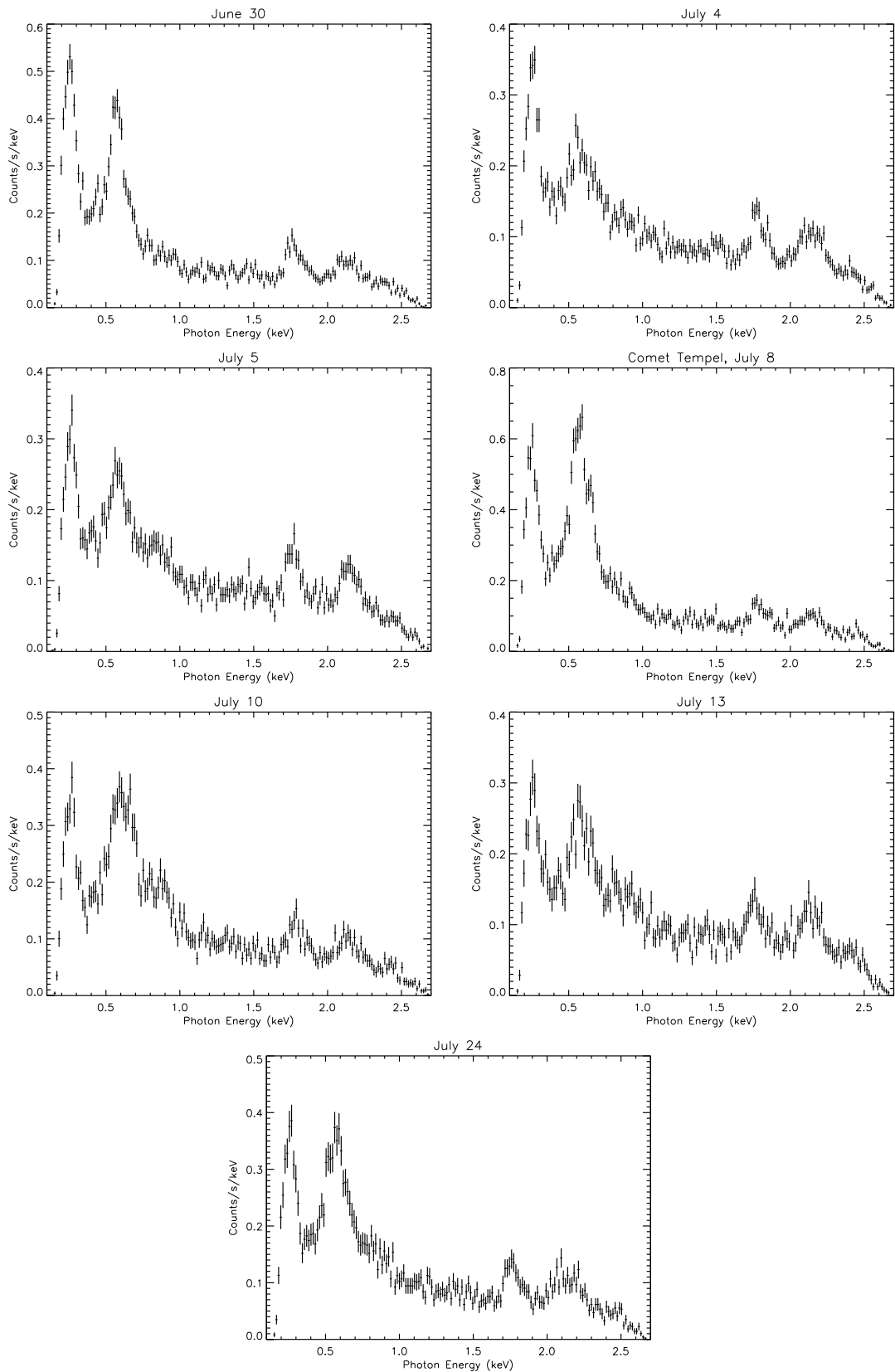


Figure 3.60: The spectrum of each observing period of comet 9P/Tempel 1. All of the data are from the *ACIS-S3* chip.

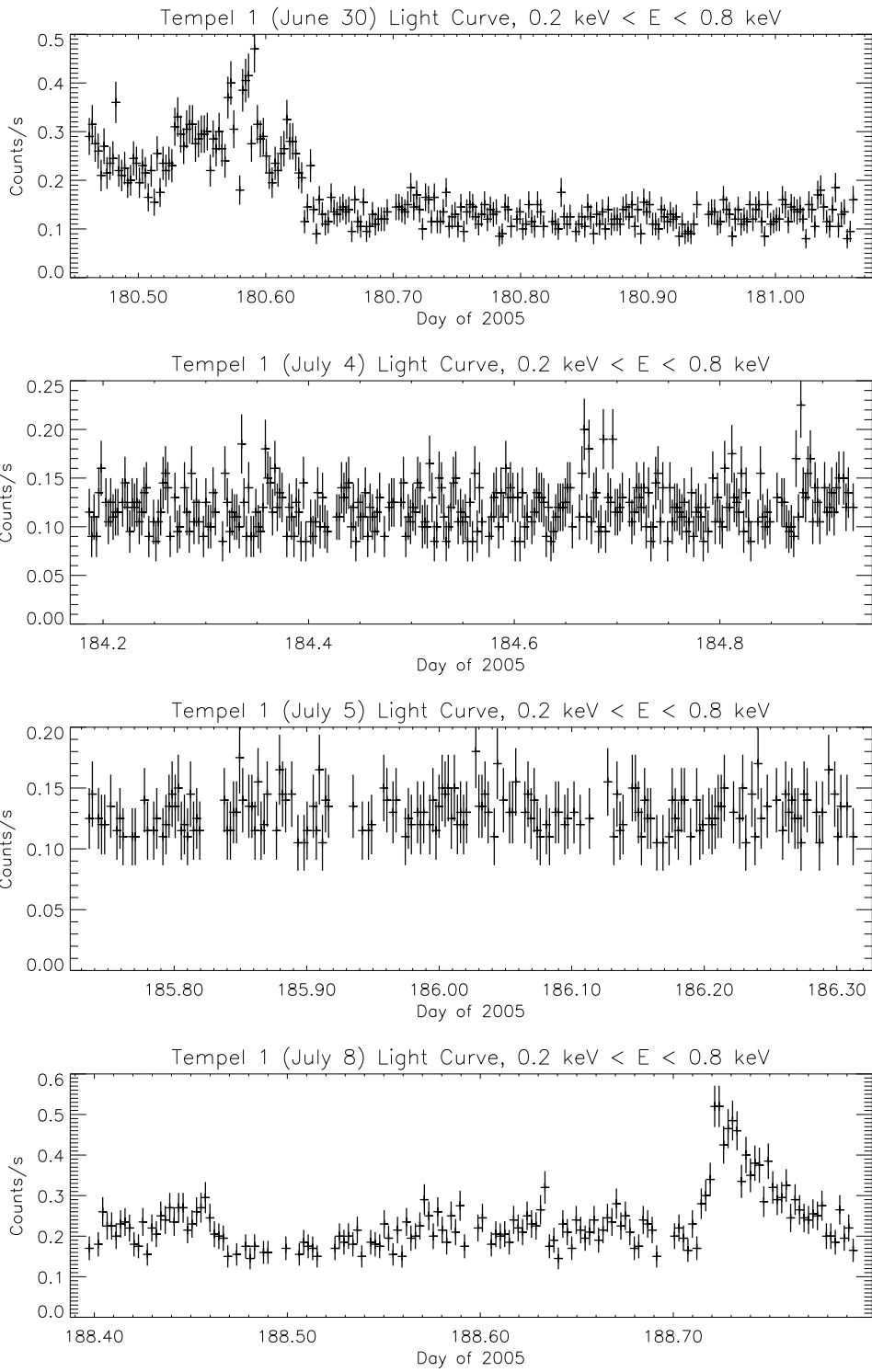


Figure 3.61: The x-ray light curves for comet 9P/Tempel 1.

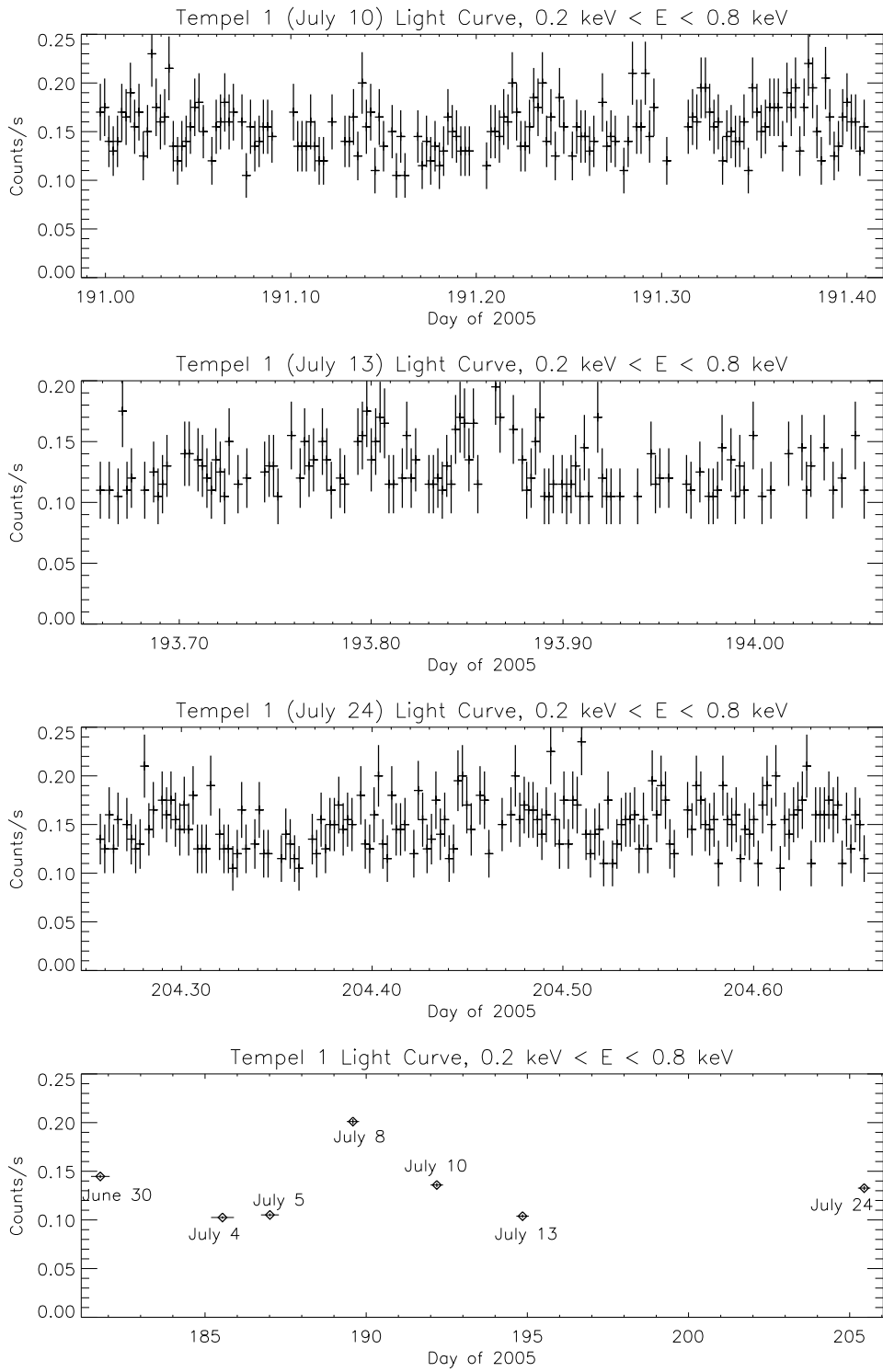


Figure 3.62: The x-ray light curves for comet 9P/Tempel 1.

*ACE* data from the period of the observation are shown in figures 3.63 to 3.66. In these figures, the line-shaded region shows the period of the observation, while the dot-shaded region shows this period plus a shift of 0.38 days (from Bodewits *et al*, 2007). Parameters of the solar wind from the observing period, captured by *ACE-SWEPAM*, are shown in figure 3.63. The light curves suggest that a delay of  $\sim 3$  days provide a better correlation with the measures x-ray flux. With this delay, the observations on June 30, July 8 and July 24 coincide with periods of increase solar wind flux.

The measured magnetic field strength from the same period is plotted in figure 3.64. The densities of the minor species and their average charges are shown in figures 3.65 and 3.66.

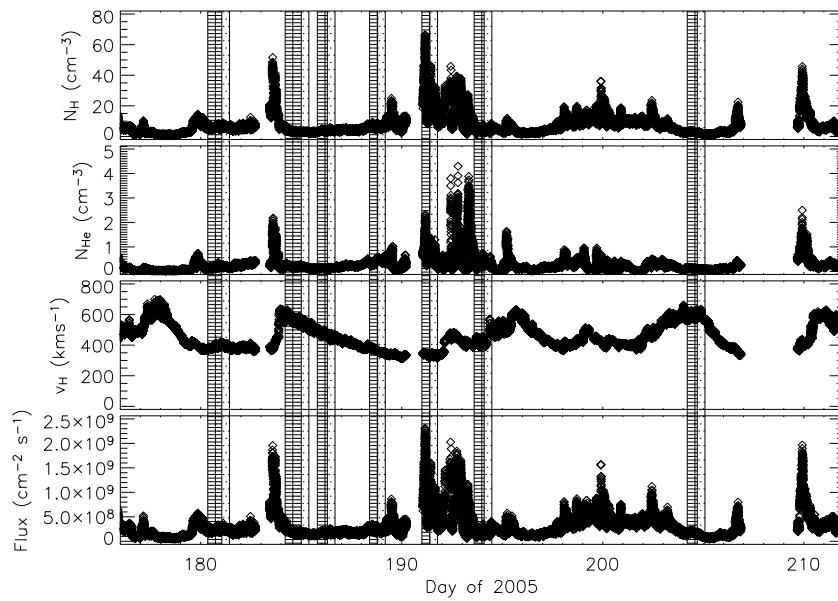


Figure 3.63: *ACE-SWEPAM* measurements of the solar wind parameters around the observation of comet 9P/Tempel 1. The *Chandra* observations took place between days 180 and 204 of the year 2005.

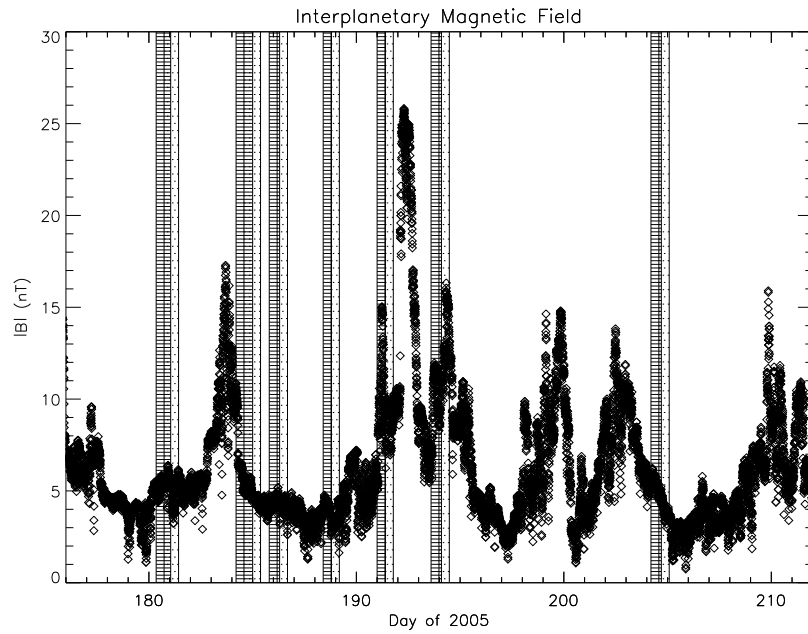


Figure 3.64: *ACE-MAG* measurements of the interstellar magnetic field around the observation of comet 9P/Tempel. The *Chandra* observation took place between days 180 and 204 of the year 2005.

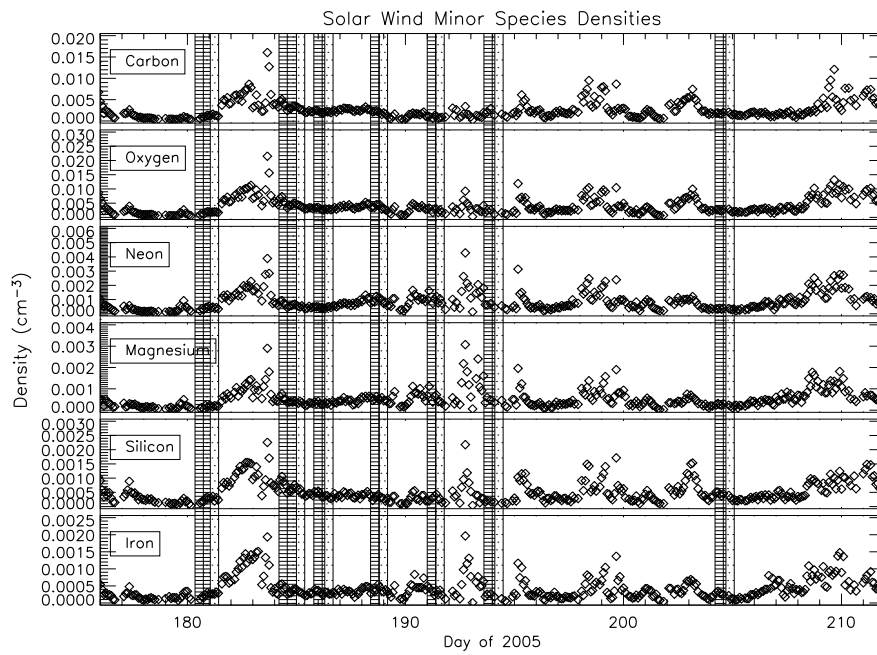


Figure 3.65: *ACE-SWICS* measurements of the solar wind minor species densities in the period of the observation of comet 9P/Tempel 1. The *Chandra* observation took place between days 180 and 204 of the year 2005.

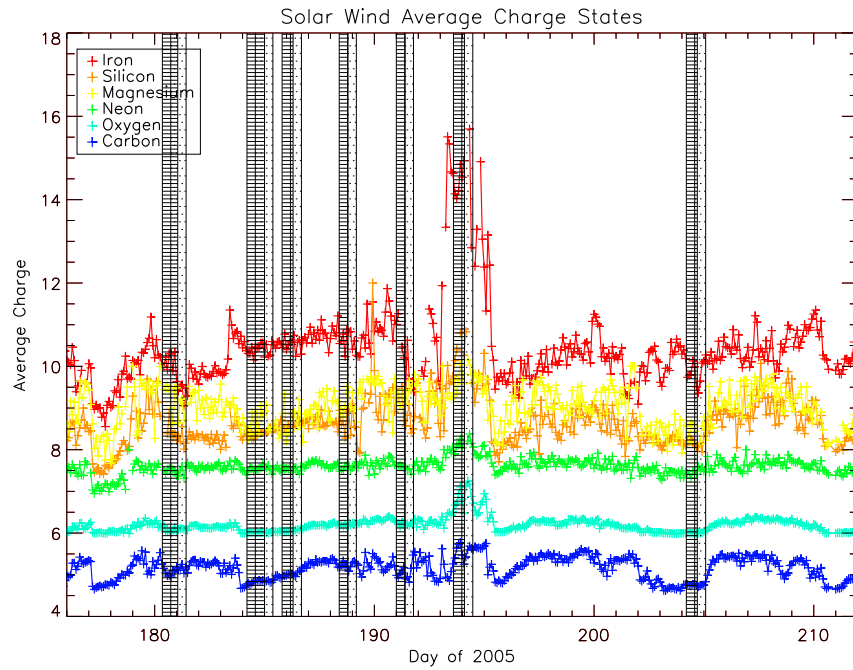


Figure 3.66: *ACE-SWICS* measurements of the average charge of the solar wind minor species in the period of the observation of comet 9P/Tempel 1. The *Chandra* observation took place between days 180 and 204 of the year 2005.

### 3.4.8 Comet 73P/Schwassmann-Wachmann 3B

The most recent observation is that of comet 73P/Schwassmann-Wachmann 3B. The comet passed close to the Earth ( $\Delta = 0.106$  AU,  $R = 0.965$  AU) in May 2006, and a 20.6 ks exposure was made with *Chandra ACIS*. The comet was also observed by *SWIFT*, *XMM-Newton* and *Suzaku*. Results from these observations are still unpublished and are not in the public domain.

During the comet's previous pass in 1995, it began to disintegrate into five large pieces. In the 2006 orbit, eight pieces were visible, each of which appears to be disintegrating further. The *Hubble Space Telescope* observed dozens of fragments steaming from fragments B and G<sup>6</sup>. One of these fragments, designated Comet 73P/Schwassmann-Wachmann 3B, was observed by *Chandra*. The complete image and spectrum from the *ACIS* array are shown in figure 3.67.

Comet 73P/Schwassman–Wachmann 3B

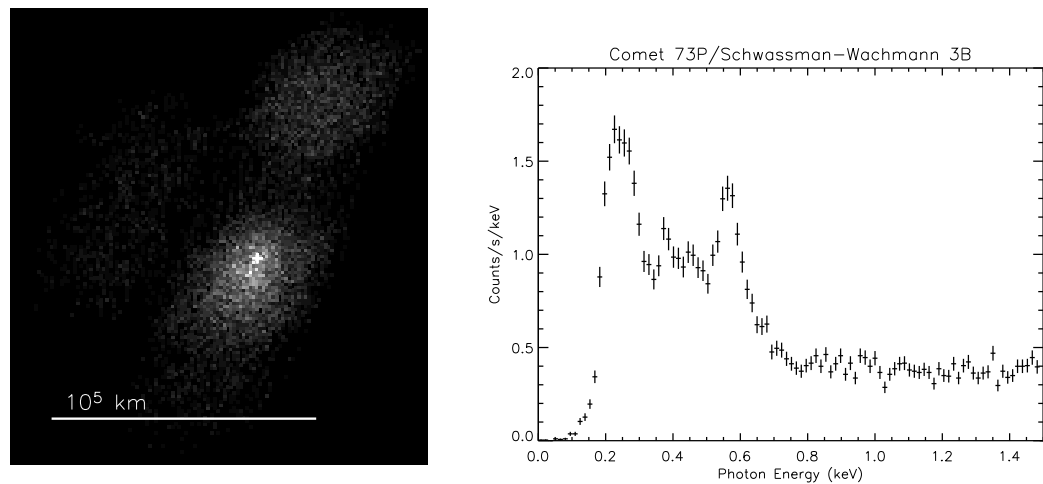


Figure 3.67: The total x-ray image and spectrum from the *ACIS* observation of comet 73P/Schwassmann-Wachmann 3B.

Data from the *S3* and *S1* CCDs are shown in figures 3.68 and 3.69 respectively. The detected luminosities from these CCDs are  $P_x = 3.6 \times 10^{14}$  erg s<sup>-1</sup> and  $P_x = 2.0 \times 10^{14}$  erg s<sup>-1</sup>. The brightest point on the *S3* CCD is located 1,600 km from the nucleus.

The x-ray light curve is shown in figure 3.70.

---

<sup>6</sup>See the press release at <http://hubblesite.org/newscenter/archive/releases/2006/18/>

Comet 73P/Schwassman–Wachmann 3B

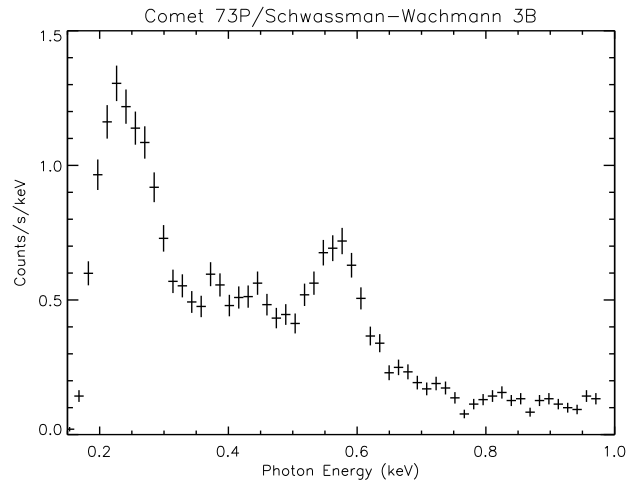
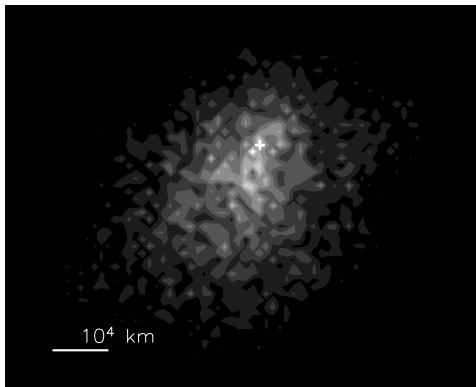


Figure 3.68: The x-ray image and spectrum from the *ACIS-S3* observation of comet 73P/Schwassmann-Wachmann 3B.

Comet 73P/Schwassman–Wachmann 3B

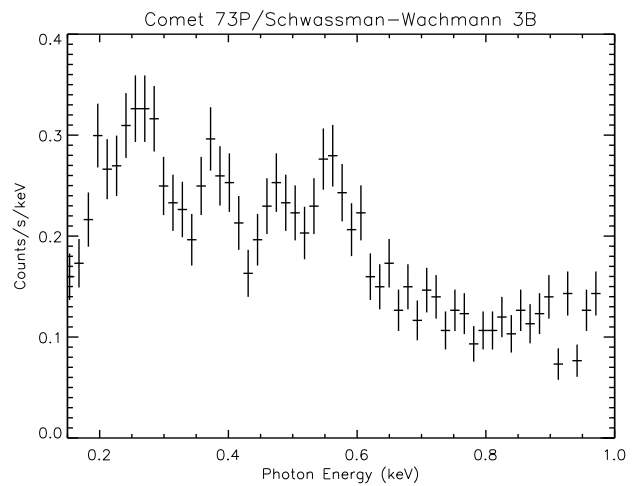
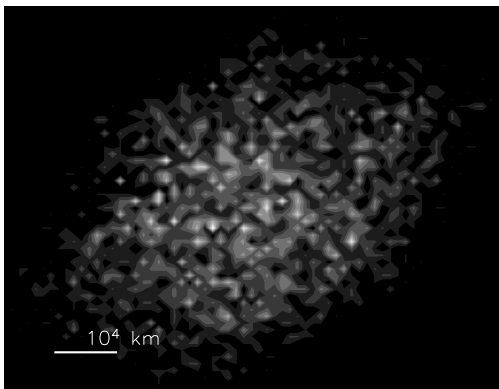


Figure 3.69: The x-ray image and spectrum from the *ACIS-S1* observation of comet 73P/Schwassmann-Wachmann 3B.

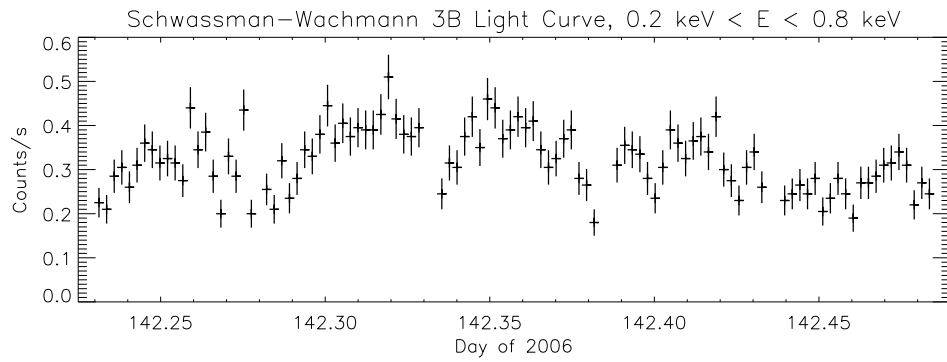


Figure 3.70: The light curve from comet 73P/Schwassmann-Wachmann 3B. The short periods of no counts represent the time taken to re-point the satellite in order to track the movement of the comet.

*ACE* data from the period of the observation are shown in figures 3.71 to 3.74. In these figures, the line-shaded region shows the period of the observation, while the dot-shaded region shows this period minus a shift of 0.2 days (from Bodewits *et al.*, 2007). Parameters of the solar wind from the observing period, captured by *ACE-SWEPAM*, are shown in figure 3.71. Note that like the observation of 2P/Encke, this observation missed a period of increased solar flux by three days. The measured magnetic field strength from the same period is plotted in figure 3.72. The densities of the minor species and their average charges are shown in figures 3.73 and 3.74.

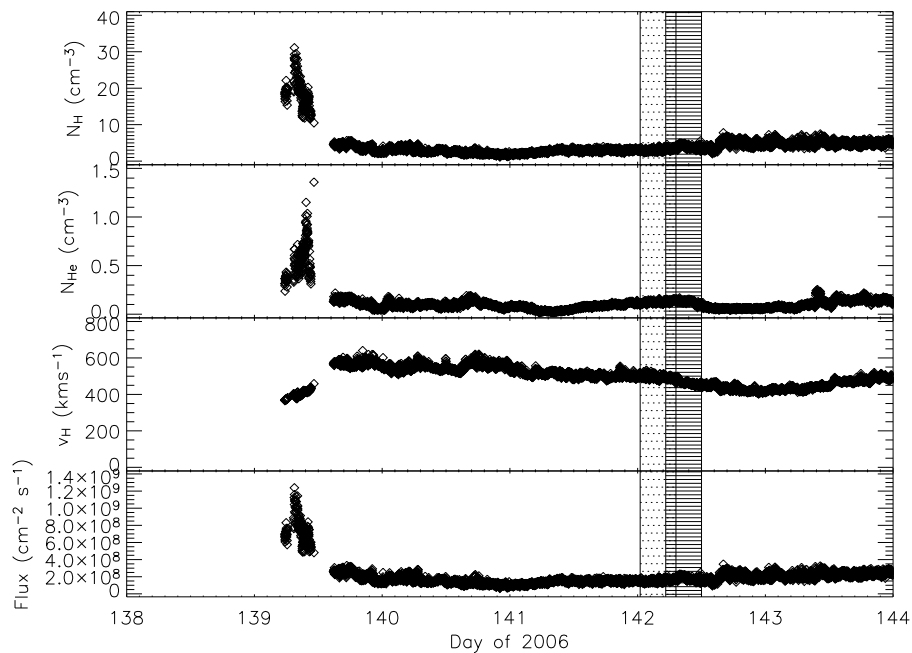


Figure 3.71: *ACE-SWEPAM* measurements of the solar wind parameters around the observation of comet 73P/Schwassmann-Wachmann 3B. The *Chandra* observation took place on day 144 of the year 2006.

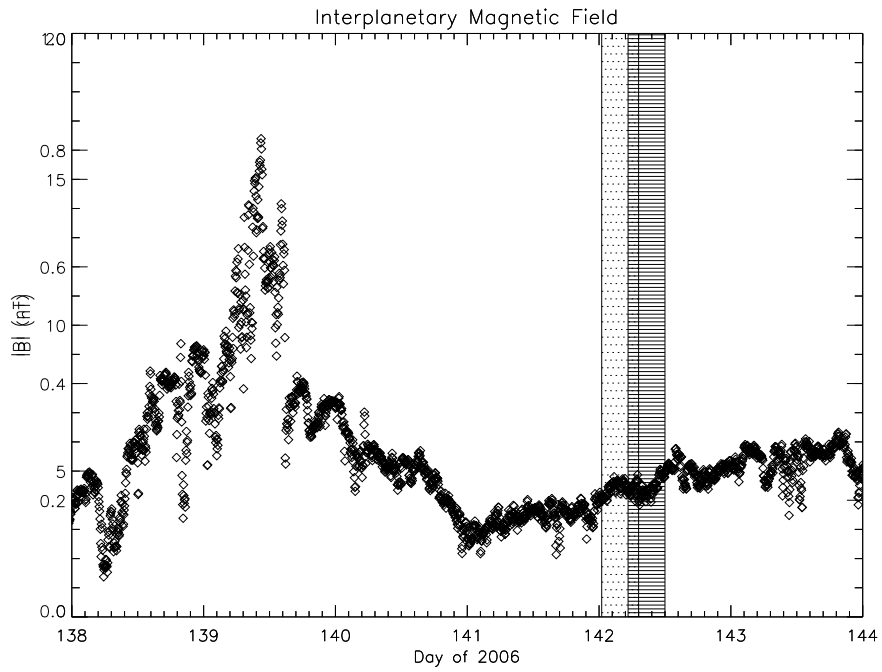


Figure 3.72: *ACE-MAG* measurements of the interstellar magnetic field around the observation of comet 73P/Schwassmann-Wachmann 3B. The *Chandra* observation took place on day 144 of the year 2006.

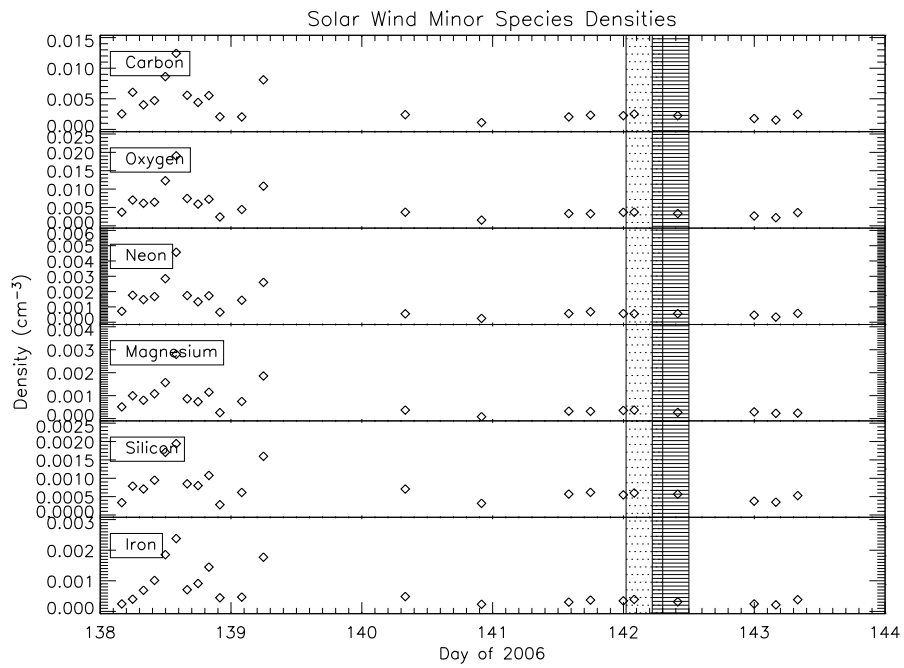


Figure 3.73: *ACE-SWICS* measurements of the solar wind minor species densities in the period of the observation of comet 73P/Schwassmann-Wachmann 3B. The *Chandra* observation took place on day 144 of the year 2006.

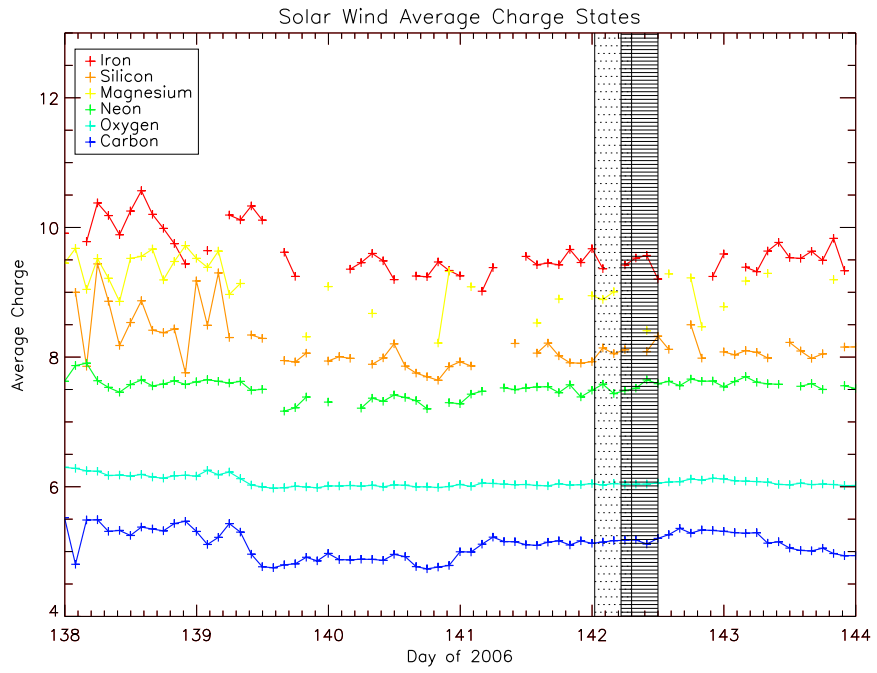


Figure 3.74: *ACE-SWICS* measurements of the average charge of the solar wind minor species in the period of the observation of comet 73P/Schwassmann-Wachmann 3B. The *Chandra* observation took place on day 144 of the year 2006.

### 3.4.9 High Resolution Spectroscopy

Attempts have been made to utilise the high resolution capabilities of *Chandra*. Comet 2001 A2 was observed by Vestrand in July 2001 using the *High Resolution Camera* on *Chandra*. Both the imaging and spectroscopy (with the Low-Energy Transmission Grating) arrays were used. No structured emission is present in the images, and the count rate was too low for the spectra to be statistically significant.

In December 2001, *ACIS* with the *LETG* was used to observe comet 2001 WM1. The extent of the emitting atmosphere and the low count rate resulted in no grating spectra being available. Although it is possible to examine the spectra from the pulse-height generated by the detections (as is the case with all ungrated data), there may be severe deficiencies in some energy ranges. Furthermore, no morphological data may be extracted.

The practise of using gratings on extended sources is developing through experience (see “Analysis Guide for *Chandra* High Resolution Spectroscopy” by Huenemoerder<sup>7</sup>). However, the low x-ray flux from comets suggests that high resolution spectroscopy with *Chandra* will not be possible.

---

<sup>7</sup><http://space.mit.edu/CXC/analysis/AGfCHRS/AGfCHRS.html#purpose>

### 3.4.10 Collective Results

#### Instrument Responses

The difference between the weighted redistribution matrices is small from observation to observation. This is because the *ACIS* calibration does not consider the change in the spectral resolution over the lifetime of *Chandra*. The degradation of the device is solely represented by the gradual reduction of the effective area function. The effective area functions for several of the comet observations are shown in figure 3.75.

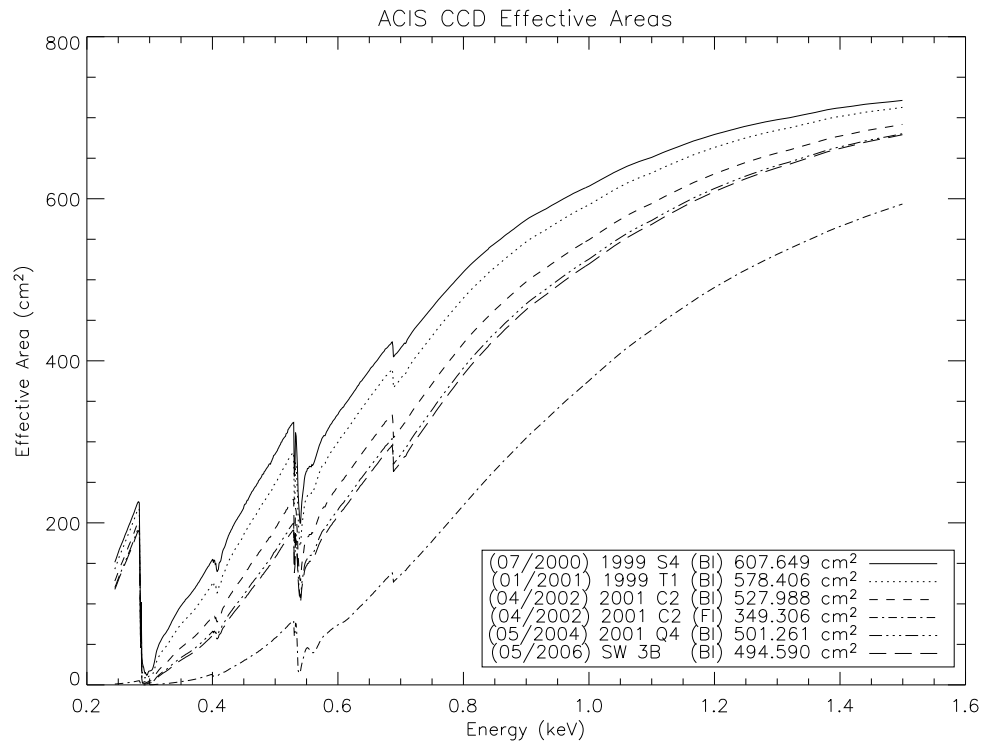


Figure 3.75: Calculated effective areas as a function of photon energy for selected observations. The gradual degradation of the back illuminated *ACIS-S3* CCD can be seen.

#### Morphologies

The morphologies of comet C/1999 S4 (LINEAR), C/1999 T1 (McNaught-Hartley), C/2002 C1 (Ikeya-Zhang), 9P/Tempel 1 are similar to the common morphology observed in comets C/1996 B2 (Hyakutake) (Lisse *et al*, 1996), C/1990 K1 (Levy) (Dennerl *et al*, 1997), C/2000 WM1 (LINEAR) (Dennerl *et al*, 2003; Wegmann *et al*, 2004). That is, a semi-spherical shell on the dayside of the comet, almost symmetrical around the Sun-comet axis. For comet 2P/Encke, there is a disagreement between the position of the nucleus of the comet presented here and that of Lisse *et al* (2005), who position the nucleus at the brightest point of the x-ray emission. In either case, the morphology

forms a sphere, similar to the optical coma morphology rather than following the more common crescent shape.

In the cases of comet C/2001 Q4 (NEAT) and 73P/Schwassmann-Wachmann 3B, it is difficult to qualify the morphologies. From a comparison between the *S3* and *S1* spectra, it appears that the extent of the emission region from comet C/2002 C1 (NEAT) was larger than the area projected by *ACIS*. This, coupled with the low count rate, results in a dilute emission map with no clear structure. 73P/Schwassmann-Wachmann appears to form a crescent shape, although there is no clear displacement between the nucleus and the x-ray emitting region.

## **Spectra**

The x-ray spectra are discussed in chapter 5, as various emission models are compared to the data.

## 3.5 Future Missions and Observations

### 3.5.1 *ASTRO-E2 (Suzaku)*

The Japanese satellite *ASTRO-E2*, later known as *Suzaku*, was launched in July 2005. The main instrument was the *X-ray Spectrometer*, which was an x-ray calorimeter. A calorimeter retains the large effective collecting area of a CCD array, but has a significantly higher energy resolution. In August 2005, a malfunction resulted in all of the liquid helium escaping, rendering the device useless. *Suzaku* is also equipped with the *X-ray Imaging Spectrometer*, a CCD array that is similar to the *Chandra ACIS* device. The energy resolution is approximately twice as high as the *ACIS* array. The format of *XIS* datafiles is identical to the *ACIS* format, so a large proportion of the *Chandra Interactive Analysis of Observations* package will be retained for use with *Suzaku*, meaning that the analysis techniques are already familiar to x-ray astronomers.

*XIS* was used to observe comet 73P/Schwassmann-Wachmann 3B in May 2006, though no results have been published or released to the public domain to date.

### 3.5.2 Sounding Rockets

It has been proposed that a device identical to *ASTRO-E2*'s *XRS* could be deployed on a sounding rocket (Porter, *Private Communication* 2005). The observing time of a mission like this would be around 6 minutes, so a significant increase in the effective area is required (compared to *Chandra ACIS*). A sounding rocket observation would cost  $\sim$  \$1 million. Recent proposals have been made, and have been rejected. Although, as the effective area of detectors increases, the case for a sounding rocket observation grows stronger.

### 3.5.3 Constellation X

The next scheduled large-scale x-ray mission is the NASA project *Constellation X*. This array of 4 identical satellites promises effective areas a factor of 25–100 times the current generation of satellites (as shown in figure 3.76), and spectral resolutions of the order of several eV. A simulation of the resolving power is shown in figure 3.77.

Unfortunately, the current status of the project is “Delayed Indefinitely”, with 2017 being the earliest possibility for launch. This depends on whether *Constellation X*, *LISA* or *JDEM* is chosen to be NASA’s next major astrophysics observatory following the *James Webb Space Telescope*.

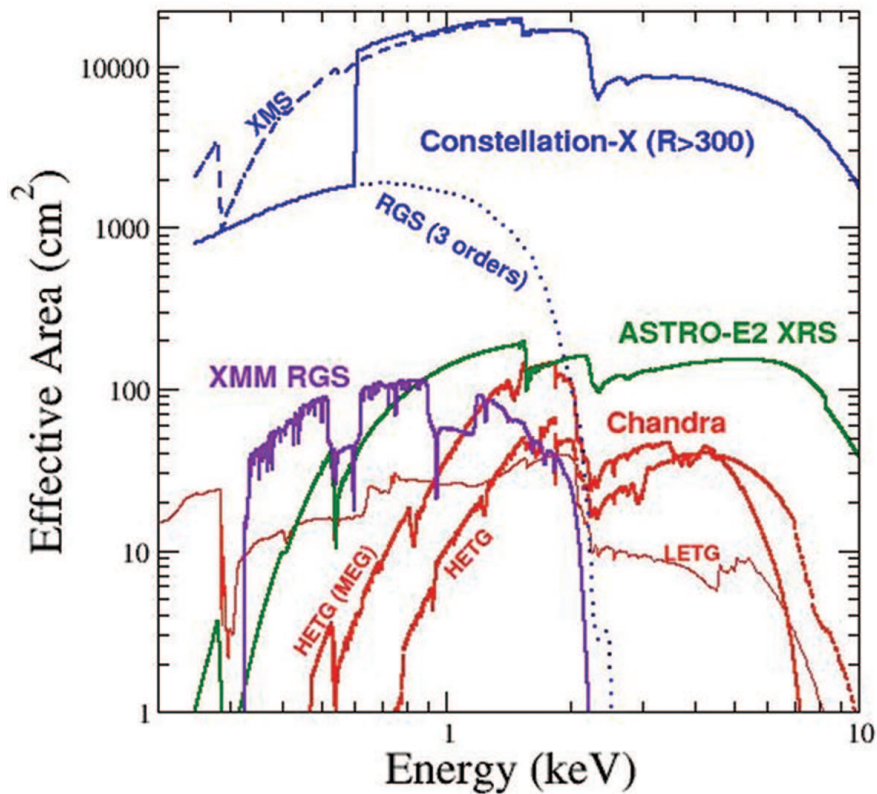


Figure 3.76: The effective areas of current x-ray observatories and Constellation X (blue).

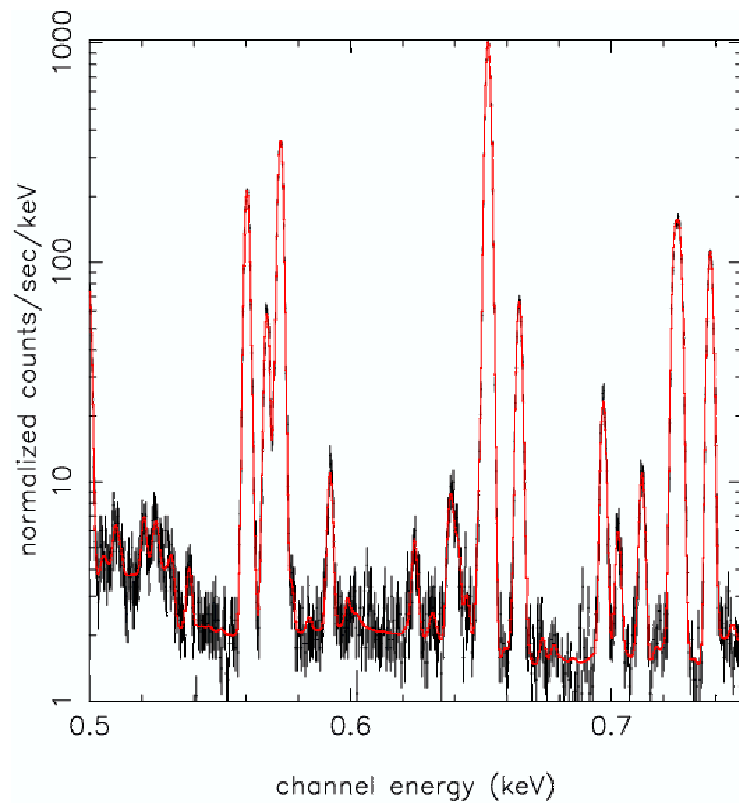


Figure 3.77: A simulation demonstrating the resolving power of *Constellation X*. The spin-forbidden (561 eV) and dipole (574 eV)  $n = 2 \rightarrow n = 1$  lines in O VII are clearly resolved.

## Chapter 4

# Modelling the X-ray Emission from Cometary Atmospheres

Previous studies into the atomic physics of cometary x-rays have focused on one of two areas: charge exchange (Cravens, 1997, Wegmann *et al.*, 1998) or energetic electron collisions (Bingham *et al.*, 1997, Shapiro *et al.*, 1998, 1999). Both of these models are considered in detail here. Firstly, aspects of the interaction between the solar wind and the outgassing cometary atmosphere are discussed in section 4.1. The focus is on the transfer of energy from solar wind ions to the free electrons in the system via a turbulent electric field.

For both the charge exchange and energetic electron models, a general approach to modelling the emission from an ion in a plasma is taken, working within a collisional-radiative framework. The atomic processes and the data describing them are discussed in section 4.2. By way of illustration, data for helium-like oxygen, one of the solar wind's predominant minor species, are presented. By comparing the effectiveness of these reactions in a low density plasma, the collisional-radiative approach can be simplified by removing contributions from weak processes. The collisional-radiative model (Bates *et al.*, 1962, Burgess and Summers 1969), without terms that are negligible in the cometary case, is described in section 4.3. This approach assumes quasi-static equilibrium to determine excited level populations (from which emissivities can be derived) and ion fractional abundances.

Two relevant applications of collisional radiative modelling are shown in section 4.4. Namely, the ionisation balance of the solar wind (as a function of electron temperature and density) is found and the emission from ionic species in the comet-solar wind plasma are modelled.

## 4.1 Electron Energisation

The process that generates electrons, as observed in the coma of comet 1P/Halley (see section 2.2.3) is described. There are two components to the mechanism: firstly, a streaming instability induces the growth of electrostatic waves; the energy of the waves is transferred to the free electrons in the system. These aspects of the model are described in sections 4.1.1 and 4.1.2.

### 4.1.1 The Modified Two-Stream Instability

The development of the cometary atmosphere and the mass loading of the solar wind is discussed briefly in section 2.4. The generation of lower-hybrid waves in the cometary atmosphere (as proposed by Bingham *et al*, 1991 and developed by Bingham *et al*, 1997, 2002; Dawson *et al*, 1997; and Shapiro *et al*, 1998, 1999) is described here.

Following the ionisation of a cometary neutral, the ion is influenced by the solar magnetic field. In the reference frame of the solar wind, the cometary photoions form a ring distribution in velocity space such that the initial cometary ion distribution function can be written as

$$f_i(\mathbf{u}) = \delta(v_\perp - u_\perp)\delta(v_\parallel + u_\parallel)/2\pi u_\parallel. \quad (4.1)$$

where  $u_\perp$  and  $u_\parallel$  are the solar wind velocities perpendicular and parallel to the magnetic field vector. The solar wind ions and free electrons are assumed to have Maxwellian distributions with temperatures  $T_i$  and  $T_e$ ,

$$f_\alpha = \left(\frac{m_\alpha}{2\pi T_\alpha}\right)^{3/2} \exp\left(-\frac{m_\alpha \mathbf{v}^2}{2T_\alpha}\right) \quad (4.2)$$

where  $\alpha$  is used to denote the solar wind ions and electrons.

For electrostatic perturbations, the plasma dispersion relation for a magnetised plasma is (Davidson 1983)

$$1 + \sum_\alpha \frac{\omega_{p\alpha}^2}{k^2} \sum_{n=-\infty}^{\infty} \int d\mathbf{v} \frac{J_n^2(b_\alpha)}{(\omega - n\omega_{c\alpha} - k_\parallel v_\parallel)} \left( k_\parallel \frac{\partial f_\alpha}{\partial v_\parallel} + \frac{n\omega_{c\alpha}}{v_\perp} \frac{\partial f_\alpha}{\partial v_\perp} \right) = 0 \quad (4.3)$$

where

$$\omega_{p\alpha} = \left( \frac{4\pi n_\alpha Z_\alpha^2 e^2}{m_\alpha} \right)^{1/2} \quad (4.4)$$

is the plasma frequency for the particle species  $\alpha$ ,  $\omega$  is the wave frequency, and is composed of both real and imaginary parts,  $\mathbf{k}$  is the wave-vector such that  $k^2 = k_\parallel^2 + k_\perp^2$ ,

$J_n(b)$  is the Bessel function of the first kind, order  $n$ ,  $b_\alpha = k_\perp v_\perp / \omega_{c\alpha}$ , and

$$\omega_{c\alpha} = \frac{Z_\alpha e B}{m_\alpha c} \quad (4.5)$$

is the gyrofrequency.

The solutions of interest lie between the ion and electron gyrofrequencies, and on such a timescale the ions may be treated as unmagnetised particles. That is

$$\omega_{ce} \gg \omega \gg \omega_{ci}. \quad (4.6)$$

Under these conditions, the susceptibility for ions simplifies to

$$\chi_i = \frac{\omega_{pi}^2}{k^2} \int d^3\mathbf{v} \frac{\mathbf{k} \cdot \partial f_i / \partial \mathbf{v}}{\omega - \mathbf{k} \cdot \mathbf{v}} \quad (4.7)$$

At this point, we use subscript  $r$  and  $b$  to denote ring and background (solar wind) ion respectively. As the background ions are assumed to form a Maxwellian distribution, the susceptibility is

$$\chi_b = -\frac{\omega_{pb}}{\omega - k^2 v_{tb}^2}. \quad (4.8)$$

For the ring distribution ions, the susceptibility is

$$\chi_r = -\frac{\omega_{pr}^2 \omega}{(\omega^2 - k_\perp^2 u_\perp^2)^{3/2}} \quad (4.9)$$

and the susceptibility for a Maxwellian distribution of magnetised electrons is

$$\chi_e = \frac{\omega_{pe}^2}{\omega_{ce}^2} - \frac{k_\parallel^2 \omega_{pe}^2}{k^2 \omega^2}. \quad (4.10)$$

The complete dispersion relation can then be written as

$$1 + \frac{\omega_{pe}^2}{\omega^2} - \frac{\omega_{pe}^2 k_\parallel^2}{\omega^2 k^2} - \frac{\omega_{pb}^2}{\omega^2} - \frac{\omega_{pr}^2 \omega}{(\omega^2 - k_\perp^2 u_\perp^2)^{3/2}} = 0. \quad (4.11)$$

Equation 4.11 (or a similar equation based on different assumptions in the particle susceptibilities) has been analysed in detail by McBride *et al* (1972), Akimoto *et al* (1985), Lakhina (1987), Shapiro *et al* (1999). In each study, the instability causes the growth of electrostatic waves near the lower-hybrid frequency, with wave vectors almost perpendicular to the magnetic field. This agrees with the *in situ* detection of low frequency waves in comet Halley by the Vega probes (Klimov *et al*, 1986; see section 2.2.4).

## 4.1.2 Landau Damping of Electrostatic Waves

Electrostatic waves are in resonance with particles when their velocity components coincide. In the case of the lower-hybrid waves generated in the cometary atmosphere, the parallel (with respect to the magnetic field) velocity components of the waves ( $\omega/k_{\perp}$ ) can coincide with free electrons velocities. The waves are Landau damped if the gradient of the electron distribution around the resonant region is negative. This is described by the Fokker-Plank equation,

$$\left(\frac{\partial f_e}{\partial t}\right) = \frac{\partial}{\partial v_{\parallel}} \left( G(v_{\parallel}) \frac{\partial f_e}{\partial v_{\parallel}} \right) \quad (4.12)$$

where  $G(v_{\parallel})$  is a normalised wave diffusion operator. Dendy *et al* (1995) solved equation 4.12 for the case of a Gaussian wave packet transferring energy to a Maxwellian distribution of electrons. In this case, the diffusion operator is

$$G(v_{\parallel}) = \sqrt{\pi} \omega \nu_{ei} \left| \frac{eE}{mv_{th}} \right|^2 \frac{v_{\parallel}}{\Delta} \exp \left[ -\frac{(v_{\parallel} - v_0)^2}{\Delta^2} \right] \quad (4.13)$$

where  $\omega$  is the wave frequency,  $\nu_{ei}$  is the electron-ion collision frequency,  $v_{th}$  is the electron thermal velocity,  $v_0$  is the parallel component of the wave velocity and  $\Delta$  is the half-width of the wave.

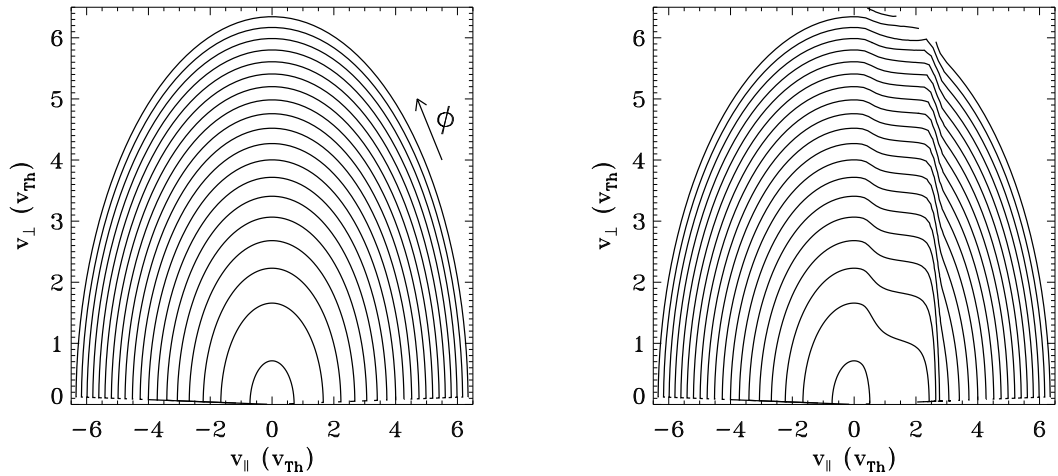


Figure 4.1: The electron distribution before Landau damping ( $t = 0$ ) and after  $t = 3$  ms of electron-wave resonance. In this case, electron temperature is 1 keV, the electron density is  $10 \text{ cm}^{-3}$  and the wave field is  $40 \text{ mV m}^{-1}$ . The resonant velocity is  $1.5 v_{th}$ , with a half-width of  $0.5 v_{th}$ .  $\phi$  is angle from the magnetic field vector.

Results are shown in figure 4.1. The left hand figure shows the electron distribution at  $t = 0$ , and the right hand figure shows the distribution after  $t = 3$  ms. The parameters are given in the figure caption.

The effect of the wave-particle resonance is to accelerate electrons in the parallel direction. The evolution of this high energy tail is shown in figure 4.2.

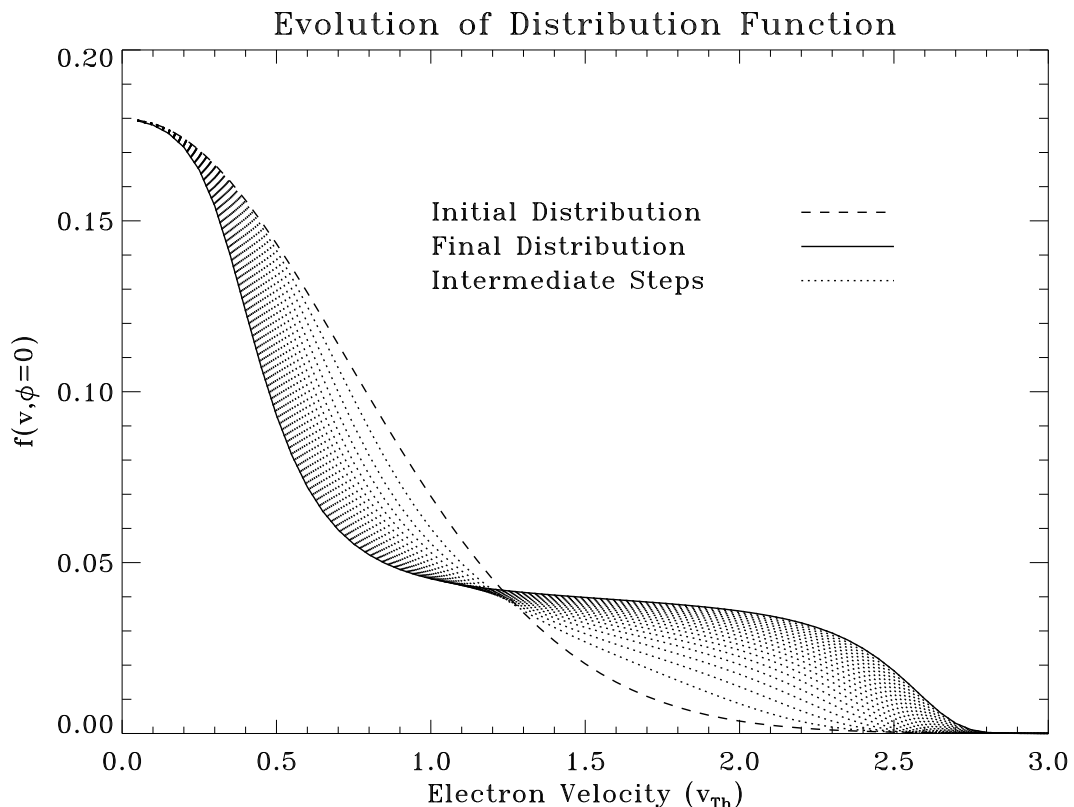


Figure 4.2: The evolution of  $f_e(v_{th})$ . The parameters are the same as those used in figure 4.1.

As electrons are accelerated, a high energy plateau is developed. As the gradient of the distribution function approaches zero, the transfer of energy is stopped. Electron distributions of this kind, families of distribution functions produced with various wave spectra, or any electron distribution function can be accommodated in the atomic modelling techniques presented in sections 2.2.4, 4.3 and 4.4 (Bryans *et al*, 2007).

Particle in a cell simulations can describe the transfer of energy from streaming ion species to free electrons (Su *et al*, 1990; McClements *et al*, 1993; Bingham *et al*, 2002), and a similar model is believed to be responsible for emission from the expanding shell of supernova remnant 1209-52 (Bingham *et al*, 2004).

### 4.1.3 Emission from Energetic Electrons

One of the key features of the emission caused by energetic electrons is a bremsstrahlung continuum (see section 4.2.5). This was due to the nature of early emission spectra, which could be modelled by a bremsstrahlung signature (Dennerl *et al*, 1997; Owens *et al*, 1998). Uchida *et al* (1998) and Shapiro *et al* (1999) sug-

gested that the continuum emission would be accompanied by neutral fluorescence from cometary neutrals as the electrons excite or ionise inner-shell electrons. The resultant x-ray emission lines would include 277 eV from neutral carbon and 525 eV from neutral oxygen. In this scenario, measurement of the x-ray lines would reveal the atomic constitution of the cometary gas.

However, the x-ray spectrum from the *Chandra* observation of comet C/1999 S4 (LINEAR) (Lisse *et al.*, 2001) demonstrated that these neutral lines were not dominant features of the emission. The best fit to the spectrum (from an arbitrary line model) included emission at 560 eV and 670 eV (Lisse *et al.*, 2001) (the latest results for this observation, presented in section 5.5.1, has these lines at 571 eV and 653 eV) indicates emission from O VII (with an emission feature in the range 561 – 574 eV) and O VIII (with an x-ray transition of 654 eV) are present.

Initially, the possibility of the energetic electrons ionising the cometary atmosphere to this extent was explored. The timescale required in this low density plasma is too great to make this viable. Furthermore, it was found that for a cometary composition, the ratio of line emission to continuum emission was too high when compared to the emission from C/1999 S4 (LINEAR).

A new interpretation of the interaction between energetic electrons and the comet-solar wind atmosphere is presented here. By examination of the observed data, it is possible that the energetic electrons cause x-rays by exciting minor species in the solar wind. The emitting ions are already present in the solar wind, so no ionisation reactions are necessary. An accompanying bremsstrahlung continuum is emitted by free-free collisions with solar wind protons and alpha particles, and neutral originating from the comet. As the fractional abundance of line emitting ions (solar wind minor species) to the continuum emitting species listed above is reduced, the ratio of line emission to continuum emission is also reduced, resulting in a closer match with the observation of C/1999 S4 (LINEAR). In this approach there is also the potential for fluorescent line emission from cometary neutrals, although observations indicate that if this emission is present, it is faint compared to emission from solar wind ions. Detectors with higher spectral resolution (for example, *Constellation-X*, see figure 3.77) are required to determine the contribution of fluorescence to the overall x-ray flux.

## 4.2 Atomic Data

The methods used to generate and organise atomic data are presented here. To illustrate, data for helium-like oxygen are presented. Where broad plasma parameters are required to determine the relevance of a process, *in situ* results from Halley are used (see section 2.2). The values are of the order  $n_e \sim 10 \text{ cm}^{-3}$ ,  $n_p \sim 10 \text{ cm}^{-3}$ ,  $T_e^{\text{cold}} \sim 50 \text{ eV}$ ,  $T_e^{\text{hot}} \sim 1000 \text{ eV}$ . The comet-Sun distance is taken as 1 AU, which dictates the solar wind conditions.

### 4.2.1 Atomic Structure

Energy levels may be calculated using, for example, AUTOSTRUCTURE (Badnell 1997). However, more accurate results are delivered by experiment. The NIST<sup>1</sup> database lists accurate energy levels for a large number of ions and atoms.

Spontaneous emission is the relaxation of an excited  $z$ -times ionised ion  $A^{+z}$  in the state  $j$  to the state  $i$ , where the ionisation potential of  $i$ ,  $I_i$  is lower than that of  $j$ ,  $I_j$ ,

$$A^{+z}(j) \rightarrow A^{+z}(i) + h\tilde{\nu}. \quad (4.14)$$

The emitted photon has an energy  $h\tilde{\nu} = I_j - I_i$ . As with energy levels, radiative rates are calculated by AUTOSTRUCTURE (Badnell 1997), and are also archived in the NIST database. It is common practise to adjust calculated energy levels and radiative rates, to better fit tabulated NIST data.

An excited state may also decay to a lower energy state by the emission of two photons,

$$A^{+z}(j) \rightarrow A^{+z}(i) + h\tilde{\nu}_1 + h\tilde{\nu}_2. \quad (4.15)$$

The sum of the photon energies is  $h\tilde{\nu}_1 + h\tilde{\nu}_2 = I_j - I_i$ . Emission rates and continuum profiles for two-photon decays in hydrogenic ions are given by Goldman *et al* (1981), and profiles for helium-like ions are given by Drake *et al* (1969). In He-like ions, there are potentially two radiative decays by two-photon emission:  $1s2s \ ^3S \rightarrow 1s^2 \ ^1S$  and  $1s2s \ ^1S \rightarrow 1s^2 \ ^1S$ . In He-like oxygen, the rates for these transitions are  $2.54 \times 10^{-1} \text{ s}^{-1}$  and  $2.31 \times 10^6 \text{ s}^{-1}$  respectively. The triplet to singlet transition competes with a single-photon spin forbidden transition, which has a decay rate of  $1.04 \times 10^3 \text{ s}^{-1}$ . As a result, the triplet side two-photon transition may be neglected. The alternative single photon decay from  $1s2s \ ^1S \rightarrow 1s^2 \ ^1S$  is an electric monopole transition, and so has a negligible radiative rate. As a result, this two-photon transition competes with collisional processes. This is discussed further in section 4.2.2. The normalised

---

<sup>1</sup>See <http://physics.nist.gov/PhysRefData/ASD/index.html>

continuum from this transition, given by Drake *et al* (1969), is shown in figure 4.3.

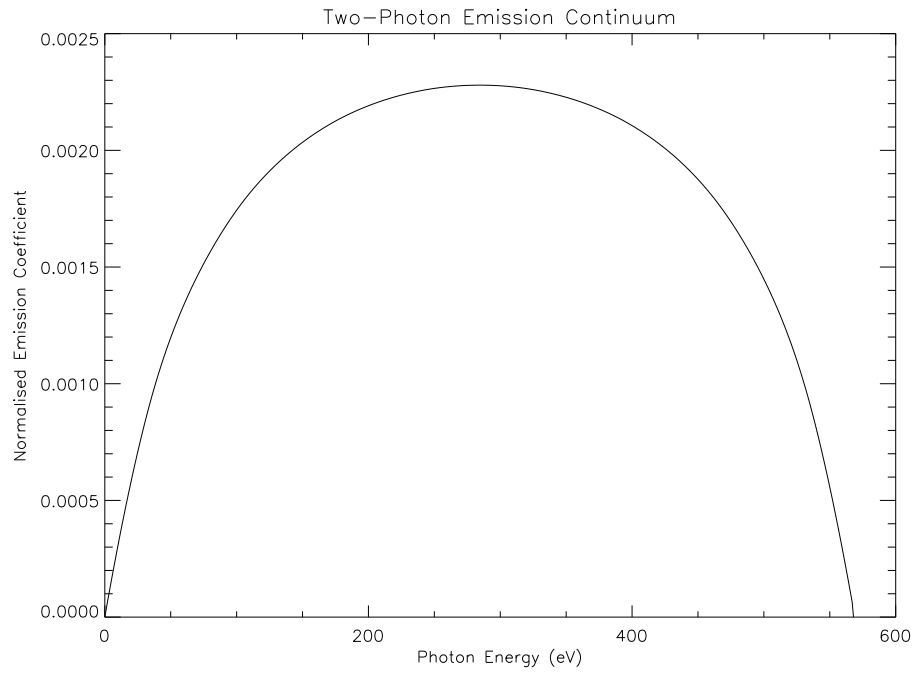


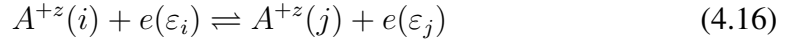
Figure 4.3: The normalised emission coefficient continuum for the two-photon transition  $1s2s\ ^1S \rightarrow 1s^2\ ^1S$  in  $O^{6+}$ .

By multiplying this continuum by the photon emissivity coefficient, a direct comparison to other radiative sources can be made when constructing a theoretical emission spectrum.

## 4.2.2 Excitation/De-excitation Processes

### Electron Collisional Excitation/De-excitation

The processes of excitation/de-excitation by collisions between the ion  $A^{+z}$  and an electron with incident energy  $\varepsilon_i$



where  $\varepsilon_j = \varepsilon_i - I_i + I_j$ , have associated cross-sections  $\sigma_{i \rightarrow j}(\varepsilon_i)$  and  $\sigma_{j \rightarrow i}(\varepsilon_j)$ , such that there are  $N_e N_{A^{+z}} v \sigma(v)$  transitions  $\text{cm}^{-3} \text{s}^{-1}$ , where  $N_e$  is the electron density,  $N_{A^{+z}}$  is the density of  $A^{+z}$ , and the electrons are travelling at a speed  $v$ .

Baseline quality excitation/de-excitation data can be quickly calculated using a Born approximation via AUTOSTRUCTURE (Badnell, 1997) or the Cowan code (Cowan, 1981). More sophisticated results are returned by  $R$ -Matrix methods (Burke and Berrington, 1993), in particular  $R$ -Matrix with pseudo-states (Bartschat *et al.*, 1996). However, as this method is computationally intensive, only baseline data are available for many ions.

Rather than return collision cross-sections, the output of the routines mentioned above are collision strengths,  $\Omega_{ij}$ , which are related to the cross-sections such that

$$\Omega_{ij}(\varepsilon) = \omega_i \frac{\varepsilon_i}{I_H} \frac{\sigma_{i \rightarrow j}(\varepsilon_i)}{\pi a_0^2} = \omega_j \frac{\varepsilon_j}{I_H} \frac{\sigma_{j \rightarrow i}(\varepsilon_j)}{\pi a_0^2}. \quad (4.17)$$

where  $\omega_{i,j}$  are the statistical weights of the levels  $i$  and  $j$ ,  $I_H = 13.606 \text{ eV}$  is the Rydberg energy and  $a_0 = 5.2918 \times 10^{-9} \text{ cm}$  is the Bohr radius. The collision strength is tabulated over electron energy, and it is common for thousands of points to be tabulated for each transition, especially in  $R$ -Matrix calculations. A more practical quantity to tabulate is a distribution averaged collision strength. In the case of a Maxwellian distribution of electrons (and only in this case) with temperature  $T_e$ , the averaged collision strength,  $\Upsilon_{ij}$ , is symmetric with respect to excitation and de-excitation, and is given by

$$\Upsilon_{ij}(T_e) = \int_0^\infty \Omega_{ij} e^{\varepsilon/kT_e} d\left(\frac{\varepsilon}{kT_e}\right). \quad (4.18)$$

where  $k$  is the Boltzmann constant. From this, the excitation and de-excitation rates are

$$q_{i \rightarrow j}(T_e) = 2\sqrt{\pi} \alpha c a_0^2 \frac{1}{\omega_i} \left(\frac{I_H}{kT_e}\right)^{1/2} e^{-(\varepsilon_j - \varepsilon_i)/kT_e} \Upsilon_{ij}(T_e) \quad (4.19)$$

and

$$q_{j \rightarrow i}(T_e) = 2\sqrt{\pi}\alpha c a_0^2 \frac{1}{\omega_j} \left( \frac{I_H}{kT_e} \right)^{1/2} \Upsilon_{ij}(T_e) \quad (4.20)$$

respectively. In the above equations,  $\alpha = 1/137.04$  is the fine structure constant and  $c = 2.9979 \times 10^{10} \text{ cm s}^{-1}$  is the speed of light in vacuum. A study into emission driven by non-Maxwellian electrons is presented by Bryans (2005). The effect of non-Maxwellian distributions is too subtle to be detected by instruments such as *Chandra*, so thermal electrons are used throughout this study. However, as x-ray instrumentation improves, line ratios could be used to diagnose distributions of electrons in an x-ray emitting plasma.

The Maxwell-averaged collision strength is a typically smooth varying function, and may be tabulated over a wide temperature range in relatively few points.

In the case of  $\text{O}^{6+}$  (and every He-like ion from  $\text{C}^{4+}$  to  $\text{Kr}^{34+}$ ) ions, *R*-Matrix calculations have been performed by Whiteford (2006, *private communication*). Comparisons of the Maxwell-averaged collision strengths from *R*-Matrix and Cowan code calculations are shown below. Figure 4.4 shows the averaged collision strength between the terms  $1s^2 \ ^1S$  and  $1s2s \ ^3S$ .

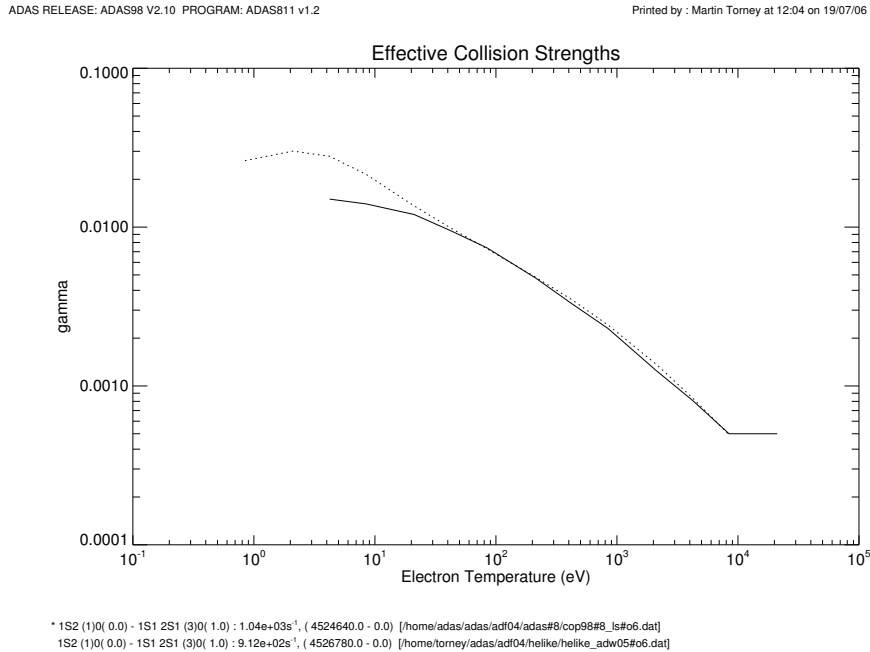


Figure 4.4: Cowan (solid line) and *R*-Matrix (dots) calculation of the Maxwell-averaged collision strength for the  $1s^2 \ ^1S$  and  $1s2s \ ^3S$  transition in  $\text{O}^{6+}$ . Note that “gamma” is referring to  $\Upsilon$  in equation 4.18.

There is reasonable agreement between the two curves above 50 eV. At lower temperatures, a discrepancy is present due to the inclusion of resonances in the *R*-Matrix calculation. The collision rate for this reaction at 50 eV is of the order  $10^{-17} \text{ cm}^3 \text{ s}^{-1}$ , with the rate decreasing rapidly with the electron energy. Compare this to the rate for

electrons with a temperature of 200 eV of  $10^{-12} \text{ cm}^3 \text{ s}^{-1}$ . Even a small population of energetic electrons results in the effect of cooler electrons becoming negligible.

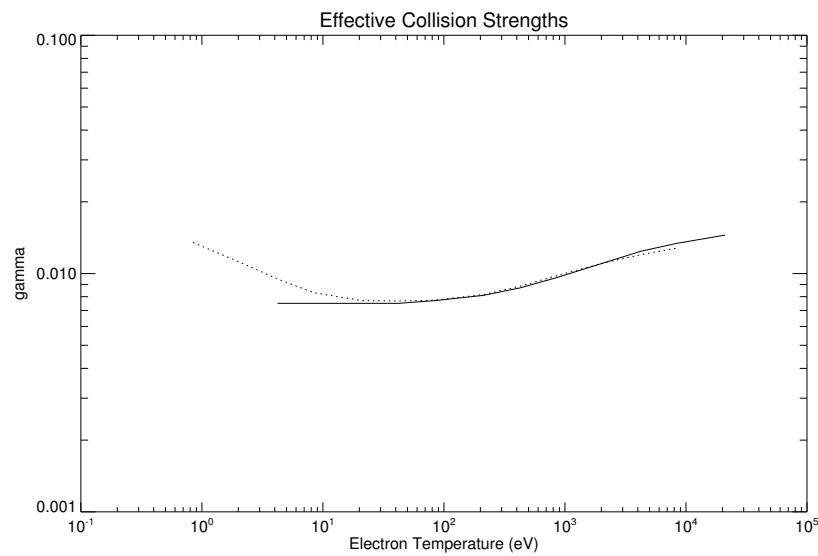
The collision strength between the transition  $1s^2 \ ^1S$  and  $1s2s \ ^1S$  is shown in figure 4.5, and that for  $1s^2 \ ^1S$  and  $1s2s \ ^1P$  is shown in figure 4.6.

For  $1s^2 \ ^1S$  and  $1s2s \ ^1S$ , again there is a good agreement between the methods above 50 eV, with diverging results below this energy. This discrepancy can be discounted with arguments given above. The comparison for the  $1s^2 \ ^1S$  and  $1s2s \ ^1P$  is reasonable at all of the tabulated energies.

Larger discrepancies are present in other transitions, such as between the terms  $1s^2 \ ^1S$  and  $1s3d \ ^1D$ . However, as there is good agreement between the strongest transitions, using Cowan data where *R*-Matrix data is not available is not ideal, but reasonable.

ADAS RELEASE: ADAS98 V2.10 PROGRAM: ADAS811 v1.2

Printed by : Martin Torney at 12:05 on 19/07/06



\* 1S2 (1)0 (0.0) - 1S1 2S1 (1)0 (0.0) : 1.00e-30s<sup>-1</sup>, ( 4588380.0 - 0.0) [/home/adas/adas/adf04/adas#9/cop98#8\_1s#o6.dat]  
 1S2 (1)0 (0.0) - 1S1 2S1 (1)0 (0.0) : 1.00e-30s<sup>-1</sup>, ( 4594784.0 - 0.0) [/home/torney/adas/adf04/helike/helike\_adw05#o6.dat]

Figure 4.5: Cowan (solid line) and *R*-Matrix (dots) calculation of the Maxwell-averaged collision strength between the terms  $1s^2 \ ^1S$  and  $1s2s \ ^1S$  in  $O^{6+}$ . Note that “gamma” is referring to  $\Upsilon$  in equation 4.18.

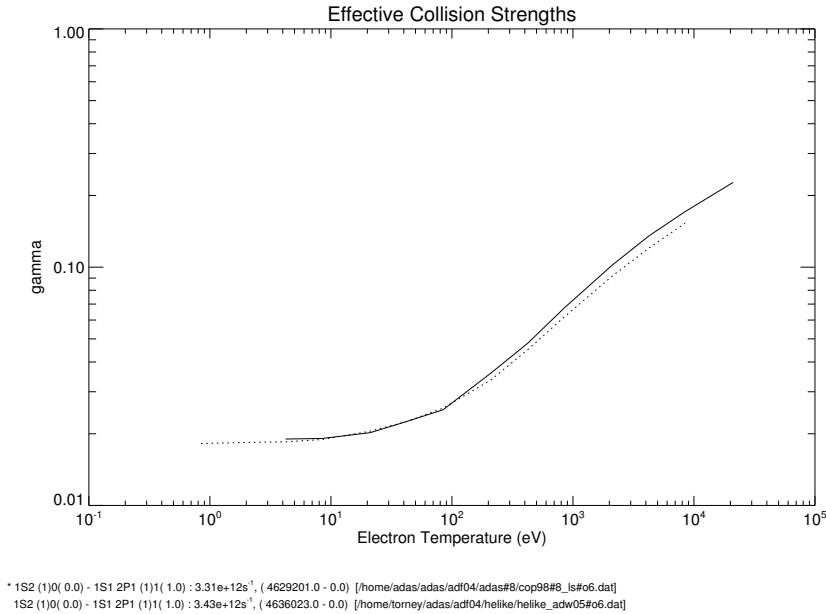


Figure 4.6: Cowan (solid line) and  $R$ -Matrix (dots) calculation of the Maxwell-averaged collision strength between the terms  $1s^2\ ^1S$  and  $1s2p\ ^1P$  in  $O^{6+}$ . Note that “gamma” is referring to  $\Upsilon$  in equation 4.18.

### Electron Impact Redistribution of Excited States

To assess the importance of collisional process from excited states, the collisional excitation and de-excitation rates must be compared to radiative transitions. Consider up to  $n = 2$  excited states in  $O^{6+}$ . Radiative rates from from these states are listed in table 4.1. Note that transitions from  $1s2p\ ^1P$  with comparatively small branching ratios are omitted, and the values in brackets are the radiative rates for two-photon decay. For each of the higher energy excited states ( $n \geq 3$ ), the sum of the radiative rates from a level is always greater than  $10^{10}\ s^{-1}$ .

Transition	A ( $s^{-1}$ )
$1s2s\ ^3S \rightarrow 1s^2\ ^1S$	$1.04 \times 10^3$ ( $2.54 \times 10^{-1}$ )
$1s2p\ ^3P \rightarrow 1s^2\ ^1S$	$7.94 \times 10^7$
$1s2p\ ^3P \rightarrow 1s2s\ ^3S$	$1.54 \times 10^8$
$1s2s\ ^1S \rightarrow 1s^2\ ^1S$	0.00 ( $2.31 \times 10^6$ )
$1s2p\ ^1P \rightarrow 1s^2\ ^1S$	$3.31 \times 10^{12}$

Table 4.1: Radiative rates between the lowest terms in the He-like oxygen system. Values in brackets are the rates for two-photon decay (Drake, 1986, Drake *et al*, 1969).

The total loss rate from a level  $i$  may be written as the sum of all the radiative and collisional transition rates from  $i \rightarrow j$ :

$$\sum_{j<i} A_{i\rightarrow j} + N_e \sum_{i\neq j} q_{i\rightarrow j}(T_e). \quad (4.21)$$

At each temperature, there will be an electron density at which the radiative and collisional loss rates are comparable. Denote this density, or effective density, as  $n'_e(T_e)$ , such that

$$n'_e(T_e) = \frac{\sum_{j<i} A_{i\rightarrow j}}{\sum_{j\neq i} q_{i\rightarrow j}(T_e)}. \quad (4.22)$$

This has been evaluated for the term  $1s2s\ ^3S$ , with the results shown in figure 4.7. Also shown are the effective densities at which radiative transitions compete with all excitation processes only, and excitations to  $1s2p\ ^3P$ .

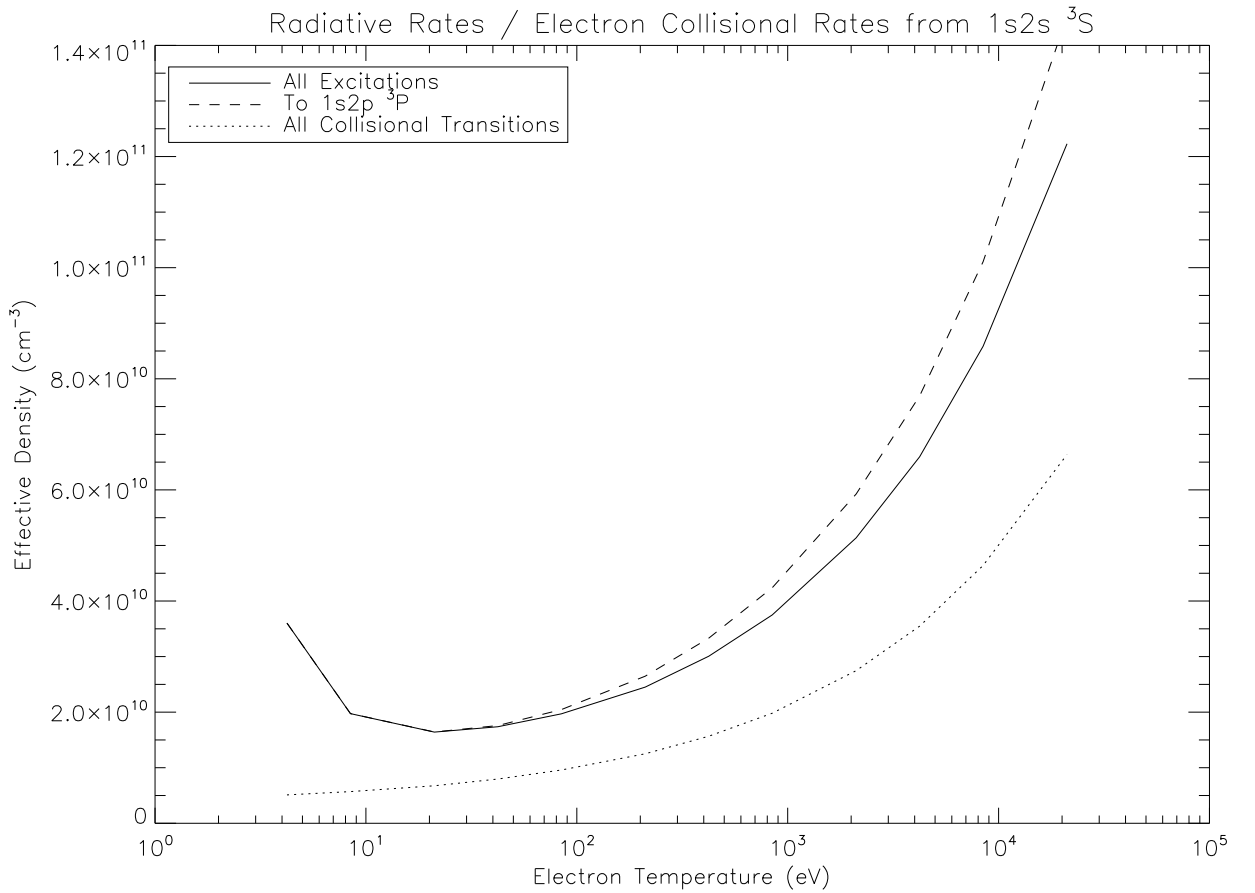


Figure 4.7: The effective density (defined in equation 4.22) for transitions from the  $1s2s\ ^3S$  term in He-like oxygen. The solid line is for all excitations to higher energy states, the dashed line is for excitations to  $1s2p\ ^1P$ , and the dotted line is for all collisional excitations and de-excitations. These lines indicate the density required for collisional processes to occur on the same timescale as radiative processes.

Despite the low radiative rate, electron densities of the order  $10^9\ \text{cm}^{-3}$  are required

for collisional processes to be significant. The effective densities are even higher for other levels as they are more inclined to radiatively decay.

As a result, it is safe to exclude electron-impact driven redistribution of excited populations.

### Proton Collision Excitation/De-excitation

The collision strengths for proton excitation and de-excitation can be large in comparison to electron collisions when the initial and final states are degenerate or almost degenerate. As a result, proton impacts have the potential to be effective in the redistribution of  $l$ -shell populations for a given  $n$ . Pengelly and Seaton (1964) developed redistribution rates in order to bridge the gap between the treatment of recombining ions in low and high density plasmas. The focus was on electron and proton collisions in hydrogenic ions, with degenerate levels  $nl, nl'$ , but their approach was general enough to apply to nearly degenerate levels. The approach of Pengelly and Seaton (1964) was to introduce an effective cut-off to the impact parameter  $R_c$  in order to avoid the problem of collision cross-sections approaching infinity as the transition energy nears zero. This is set such that

$$\bar{R}_c^2 = \text{smallest of } \begin{cases} 8.91 \times 10^{10} T_p \frac{m_e}{m} \tau^2 \\ 5.05 \times 10^{-22} T_p \left(\frac{m_e}{m}\right) \left(\frac{I_H}{\Delta E}\right)^2 \\ 47.9 \frac{T_e}{N_e} \end{cases} \quad (4.23)$$

where  $T_p$  is the proton temperature,  $m_e$  is the electron mass,  $m$  is the proton mass,  $\tau$  is the radiative lifetime of the target ion and  $\Delta E$  is the energy between the levels. The first expression in equation 4.23 is derived based on the impact parameter being close to  $v\tau$ . The second is the usual expression for non degenerate levels. When both of these terms are large, the Debye length (the third expression) is used.

This work was extended to include the non-hydrogenic case, that is for transitions  $nlLS \rightarrow nl'L'S$ , by Summers (1977) and Spence and Summers (1986). The collision rate given by Spence and Summers (1986) is

$$q_{i \rightarrow j} = 9.22 \times 10^{-8} \left(\frac{m}{m_e}\right)^{1/2} \frac{8}{3} Z^2 \frac{S_{ij}}{\omega_i} \frac{1}{\sqrt{T}} \cdot \left[ 15.6 + \log_{10} \left(\frac{m_e T}{m D_{nl}}\right) + 2 \log_{10} \bar{R}_c \right] \text{ cm}^3 \text{ s}^{-1} \quad (4.24)$$

where  $S_{ij}$  is the line strength,  $Z$  is the ion charge,  $\omega_i$  is the statistical weight of  $i$ , and  $T$  is the temperature of the colliding particles in eV. The term  $D_{nl}$  is defined as (Pengelly and Seaton, 1964)

$$D_{nl} = Z^2 6n^2 (n^2 - l^2 - l - 1). \quad (4.25)$$

Using this expression, Spence and Summers (1986) generated proton collisional excitation and de-excitation rates for large  $n$ -shells (up to  $n = 10$ ) for  $O^{7+}$ . The range of  $n$  was chosen to match levels populated by charge exchange recombination. Equation 4.22 (for both proton and electron collisions) was used, and it was found that for temperatures of  $T_{e,p} = 10^7$  K, and densities  $N_{e,p} = 5 \times 10^{13} \text{ cm}^{-3}$  redistribution of angular momentum states is significant for proton collisions only. However, the effective densities required ranged from  $10^{12}$  to  $10^{14} \text{ cm}^{-3}$ . From equation 4.24, the collision rate varies with the logarithm of the incident particle density. It is reasonable to assume that decreasing the proton density by several orders of magnitude will have little effect on the collision rate, or on the required effective density. Therefore, in the cometary environment, proton impact redistribution of excited states is negligible.

### Photo-absorption

Consider the dipole excitation from  $1s^2 \ ^1S$  to  $1s2s \ ^1P$  in  $O^{6+}$ . The energy difference between these states is 573.9 eV, and the oscillator strength  $f_{ij}$  is 0.6945. The energy density of the solar radiation field at a distance of 1 AU is shown in figure 4.8. At the energy required to excite  $O^{6+}$  from the ground state, the energy density is insignificant.

The absorption coefficient is

$$B_{ij} = \frac{4\pi^2 e^2}{m_e h \tilde{\nu} c} f_{ij} \quad (4.26)$$

where  $e$  is the electron charge. The photo-excitation rate is then

$$R_{ij} = u_{\tilde{\nu}} B_{ij} = W \frac{32\pi^3 e^2 \tilde{\nu}^2}{m_e c^4 (e^{h\tilde{\nu}/kT} - 1)} f_{ij} \sim 10^{-175} \text{ s}^{-1} \quad (4.27)$$

where  $u_{\tilde{\nu}}$  is the energy density of the radiation field and  $W$  is the dilution factor. Although other ions and low-energy transitions are more susceptible to photo-excitation, x-ray emission is not a consequence of these transitions. Further, photoionisation of this and similar ions will be even more infrequent. The radiation field can safely be disregarded in the treatment of x-ray emitting solar wind minor species ions.

Of more significance is the effect of the radiation field on the outgassing cometary neutrals. These atoms and molecules have similar ionisation potentials, and so a global ionisation rate can be found. Following ionisation, these particles are influenced by the magnetic field, and are incorporated into the solar wind via mass-loading. This means that the photo-ionisation rate contributes to the neutral loss and the solar wind gain rates.

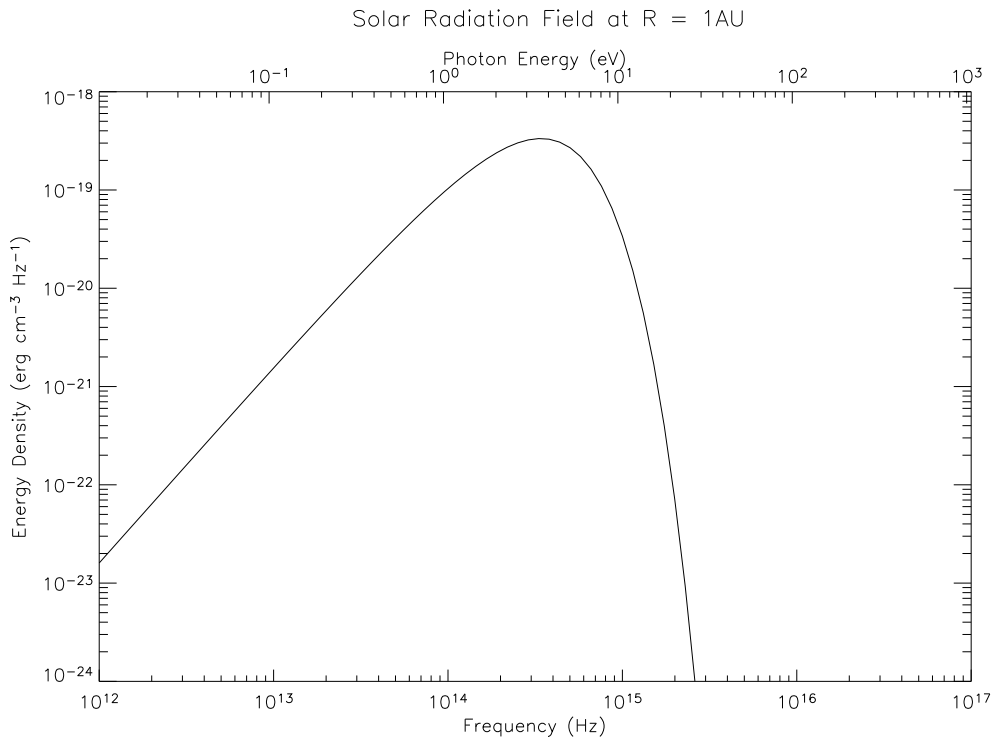
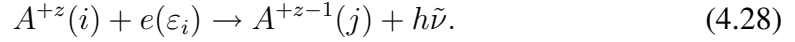


Figure 4.8: The energy density of the solar radiation field at a distance of 1 AU from the Sun.

## 4.2.3 Recombination Processes

### Radiative Recombination

Radiative recombination is the capture of a free-electron by an ion, accompanied by the emission of a photon.



An electron may radiatively recombine into any state,  $j$ . If the ionisation energy of  $j$  is  $I_j$  ( $I_j < 0$ ), the energy of the emitted photon is  $h\tilde{\nu} = \varepsilon_i + I_j$ .

Radiative recombination has an associated capture cross-section  $Q_c(\tilde{\nu})$ , such that for a free electron distribution  $f(v)$  and incident speeds between  $v$  and  $v + dv$ , there are  $N_+ N_e v f(v) Q_c(\tilde{\nu}) dv$  captures  $\text{cm}^{-3} \text{s}^{-1}$ .

Badnell (2006) has calculated partial final-state resolved radiative recombination rates for all of the ionic species present in the solar wind and more. The data from this study is utilised here, and are available online<sup>2</sup>. The total radiative recombination rate coefficient to  $\text{O}^{6+}$  from the ground state of  $\text{O}^{7+}$  is shown in figure 4.9, along with the recombination rates into the levels  $n \leq 5$  (used in collisional radiative model) and  $n \leq 8$  (tabulated in the online datafile).

There is an associated radiative recombination continuum. The emissivity for recombination into the state  $A^{+z-1}(j)$  is (Summers and Hooper, 1983)

$$\epsilon_{\text{RR}} = N_e N_i^{+z} 8 \left( \frac{\pi a_0^2 I_H}{k T_e} \right)^{3/2} \frac{8 \alpha^4 c}{3 \sqrt{3} \pi a_0^2 \nu^3} g^{\text{II}} e^{I_j/k T_e} e^{-h\tilde{\nu}/k T_e} \quad (4.29)$$

where  $\nu$  is the effective principle quantum number of the recombined electron,  $I_j$  is the ionisation potential of the level  $j$ , and  $g^{\text{II}}$  is the free-bound Gaunt factor (Gaunt, 1930; Karzas and Latter, 1960; Burgess and Summers, 1987).

---

<sup>2</sup>See <http://amdpp.phys.strath.ac.uk/tamoc/RR/>

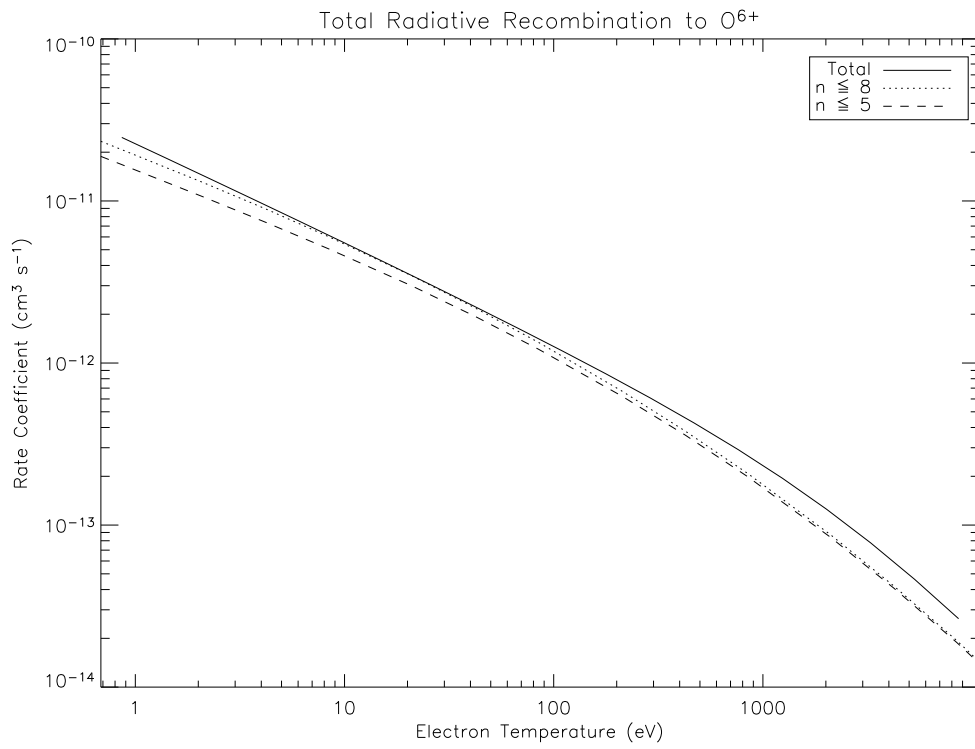
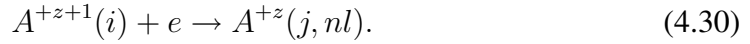


Figure 4.9: The total radiative recombination rate coefficient to  $O^{6+}$  from  $O^{7+}$  ( $1s$ ). The solid line is total recombination rate, the dotted line is the rate into all levels up to and including  $n = 8$ , and the dashed line is the rate into levels up to and including  $n = 5$ .

## Dielectronic Recombination

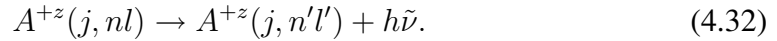
Dielectronic recombination is a two step process, the first of which is resonance capture,



The doubly excited ion  $A^{+z}(j, nl)$  then has two possible paths to a lower energy state. The first, and most likely reaction, is the inverse of equation 4.30, Auger breakup. Alternatively, the excited ion may radiate via a relaxation of the excited core



or the captured electron,

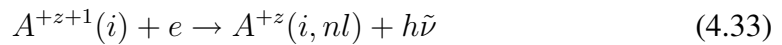


The emitted photon is known as a satellite line. If a radiative transition occurs, the electron has successfully recombined and is still in an excited state, possibly prompting further transitions.

Dielectronic recombination rate coefficients can be calculated by AUTOSTRUC-TURE and ADAS-DR. The rate coefficients for final capture into a recombined, excited state have the same units as radiative recombination rates, and as a result a superposition of the two may be tabulated. The recombination rates for capture into  $O^{6+} 1s2p \ ^1P$  from  $O^{7+} (1s)$  are shown in figure 4.10.

This shows the importance of dielectronic recombination over a wide range of electron temperatures.

The drawback of this approach is the modelling of satellite lines, or rather the archiving of data for these transitions. Retaining data for intermediate states would require hundreds of Gigabytes; making, and including this volume of data in an emission model is not practical. The tabulated dielectronic recombination rate is for the net reaction



but no data on the emitted photon is retained.

To illustrate, consider dielectronic capture by H-like oxygen. After resonance capture, the ion will be in the state  $(nl, n'l')$ . A fraction of the ions in this state will successfully recombine, making the transition to  $(1s, n'l')$  and emitting the corresponding x-ray photon. In this case, one may assume that every successful dielectronic recombination by  $O^{+7}$ , as described by equation 4.33 is accompanied by a photon in the range

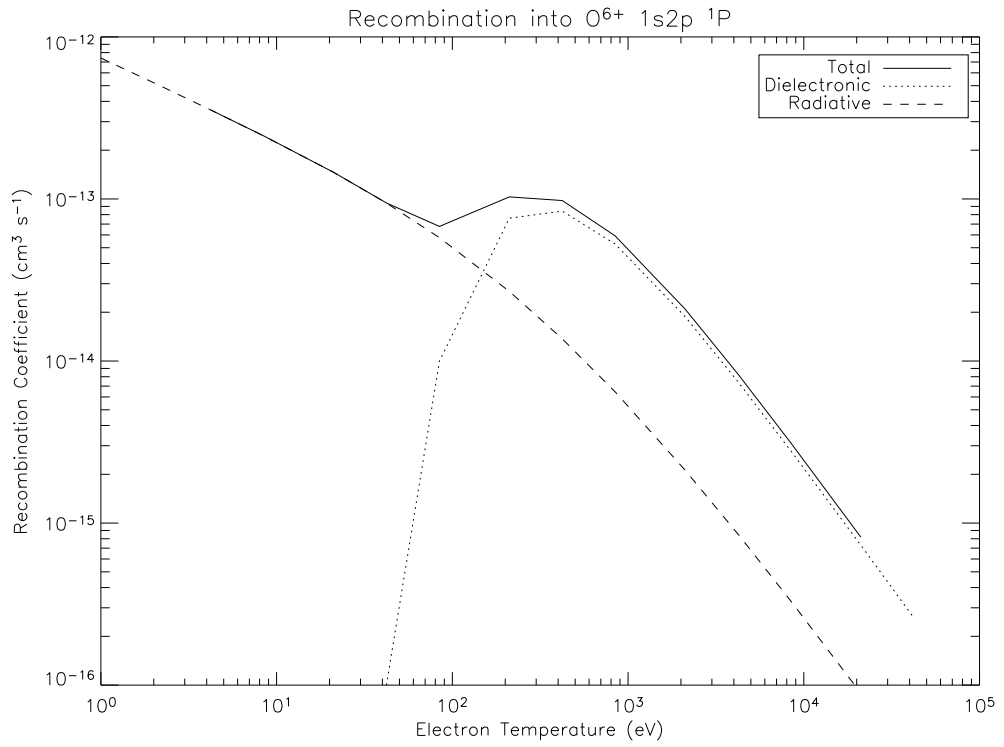
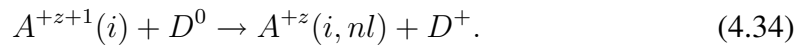


Figure 4.10: The radiative (dashes) and dielectronic (dots) recombination rate coefficients into  $O^{6+} 1s2p \ ^1P$  from  $O^{7+} 1s$ .

of cometary x-ray emission that is not accounted for in the tabulated datafile. The same is true for capture by He-like ions, as  $n > 2$  to  $n = 1$  satellite lines will again be omitted.

## Charge Exchange

Charge exchange is the capture of one or more electrons by ion from a neutral atom donor,



Strictly, there is no requirement that the donor is neutral, though the ion-ion charge exchange cross-section is greatly reduced by electrostatic repulsion. The captured electron is typically in a highly excited state.

The receiver elements considered here are carbon, nitrogen and oxygen. In the solar wind, these elements exist in their fully-stripped, H-like and He-like ions. The charge exchange reactions of interest involve the bare nuclei and hydrogenic ions only, as charge capture by the He-like ions does not drive x-ray emission. In this study the charge exchange reaction is restricted to the transfer of a single electron, although Ali *et al* (2005) have demonstrated that the transfer of multiple electrons is common for donor species more complex than neutral helium, and that the emission spectrum is significantly altered by the transfer of more than one electron.

The charge exchange data used here are detailed below before being summarised in table 4.2.

### *Data for Bare Nucleus Collisions with Neutral Hydrogen*

Fritsch and Lin (1984) calculated  $nl$  resolved cross-sections for collisions between hydrogen atoms and the bare nuclei of several light elements, including carbon, nitrogen and oxygen, using an atomic orbital expansion (AO+) model (Fritsch and Lin, 1983).

### *Data for H-like Collisions with Neutral Hydrogen*

Shimakura *et al* (1992) have presented  $nlS$  resolved cross-sections for H-like carbon collisions with hydrogen. A semi-classical molecular orbital close-coupling model was used for collisions relevant to this study, and a quantum-mechanical close-coupling approach was used for lower energies.

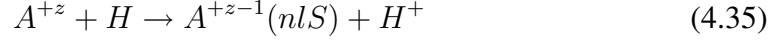
In addition to this,  $nl$  resolved data for H-like oxygen with hydrogen have been posted on the ORNL/UGA Charge Transfer Database for Astrophysics<sup>3</sup>. The data in this archive are generated by a classical trajectory Monte Carlo (CTMC) model.

Resolved data for other ions of interest are not available. However approximate cross-sections can be derived. Consider the case when data are available for the reac-

---

<sup>3</sup>Located at <http://cfadc.phy.ornl.gov/astro/ps/data/home.html>

tion



and data for the collision



are required. Denote the cross-sections for 4.35 as  $\sigma$ , and the cross-sections for 4.36 as  $\sigma'$ . The total charge transfer cross-section for 4.36,  $\sigma'_T(v)$  must be known. The classical over the barrier model (see, for example, Hoekstra, 1990; Ostrovsky, 1995) for charge exchange predicts that for such collisions, the most probable  $n$ -shell of the ion after the collision will be

$$n_z^* = \frac{z}{\sqrt{1 + \frac{z-1}{2\sqrt{z+1}}}}. \quad (4.37)$$

From the most probable  $n$ -shell for each of the above reactions, define the following:

$$dn^* = n_y^* - n_z^* \quad (4.38)$$

$$f = dn^* \pmod{1} \quad (4.39)$$

$$\Delta n^* = dn^* - f + 1. \quad (4.40)$$

The variable  $f$  is introduced to accommodate cases where  $dn^* > 1$ . The normalised (to the total cross-section) cross-sections  $\bar{\sigma}'_{nlS}(v)$  for reaction 4.35 are given by

$$\bar{\sigma}_{nlS}(v) = \frac{\sigma_{nlS}(v)}{\sum_{(nlS)'} \sigma_{(nlS)'}(v)}. \quad (4.41)$$

The normalised cross-sections for 4.36 are then given by

$$\bar{\sigma}'_{nlS}(v) \simeq (1-f)\sigma + f\bar{\sigma}_{n-\Delta n^*, l-\Delta l^*, S} \quad (4.42)$$

where  $\Delta l^* = 0$  or  $\Delta l^* = \Delta n^*$ . At low impact speeds (i.e. in the regime of the solar wind speed), the tendency is for low angular momentum states to be overpopulated with respect to statistical values. As a result,  $\Delta l^* = 0$  is a more appropriate choice for the purposes of this study.

Approximate state-selective charge exchange cross-sections are then given by

$$\sigma'_{nlS}(v) = \bar{\sigma}'_{nlS}(v)\sigma'_T(v). \quad (4.43)$$

Data for H-like nitrogen charge capture from neutral hydrogen and generated in this manner from the resolved  $C^{5+}$  capture cross sections from Shimakura *et al* (1992) and the total  $N^{6+}$  capture cross sections from Meyer *et al* (1985).

### Summary of Charge Exchange Data

The data charge exchange data used in this study are summarised in table 4.2.

Receiver	Resolution	Source
$C^{6+}$	<i>nl</i>	Fritsch and Lin, 1984
$N^{7+}$	<i>nl</i>	Fritsch and Lin, 1984
$O^{8+}$	<i>nl</i>	Fritsch and Lin, 1984
$N^{6+}$	Total	Meyer <i>et al</i> , 1985
$C^{5+}$	<i>nlS</i>	Shimakura <i>et al</i> , 1992
$N^{6+}$	<i>nlS</i>	Derived from Shimakura <i>et al</i> , 1992
$O^{7+}$	<i>nl</i>	ORNL Database

Table 4.2: Charge exchange data sources used in this study. In all cases, the H is the donor. Data for  $N^{6+}$  are derived from  $C^{5+}$  (Shimakura *et al.*, 1992) using the method described above and the total cross sections from Meyer *et al* (1985). A statistical distribution is assumed to obtain the spin-system resolved cross sections of  $O^{7+}$ .

Alternative cross sections for some of these species are presented by Shipsey *et al* (1983), Kimura *et al* (1987), Janev *et al* (1985, 1993), Richter and Solov'ev (1993) and Caillat *et al* (2001).

### Data Requirements

The charge exchange data requirements for cometary x-ray emission were discussed by Stancil *et al* (2002). They suggest the investigation of a large number of reactions through orbital close-coupling methods, be they with quantum-mechanical or semi-classical approaches and atomic or molecular orbitals. Liu *et al* (2005) demonstrated a hyper-spherical close-coupling (HSCC) method that results in a closer agreement with experimental values for non-dominant *n*-shells at low to moderate energies.

Calculations with any of the above methods would represent a significant improvement in the quality of available charge transfer data. The reactions of interest involve the ions prevalent in the solar wind with  $H_2O$ ,  $CO$ ,  $CO_2$ ,  $OH$ ,  $O$  and  $H$  donors. This represents a large volume of research, much of which is computational and labour intensive. Several authors have published more recent cross section calculations and/or

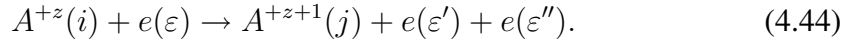
measurements (for example, Greenwood *et al*, 2000, 2001; Hasan *et al*, 2001; Errea *et al*, 2005; Bodewits *et al*, 2006; Otranto *et al*, 2006, Stancil *private communication*, 2006), with many of these studies being performed with the aim of fulfilling the charge exchange requirements of cometary x-rays.

### Other Recombination Processes

Three-body recombination may be neglected as the rate depends on the square of the electron density. Stimulated recombination is not included due to the low product of the electron density and the energy density of the radiation field.

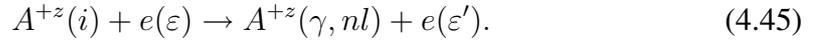
#### 4.2.4 Ionisation

The inverse to three-body recombination is direct electron impact ionisation,

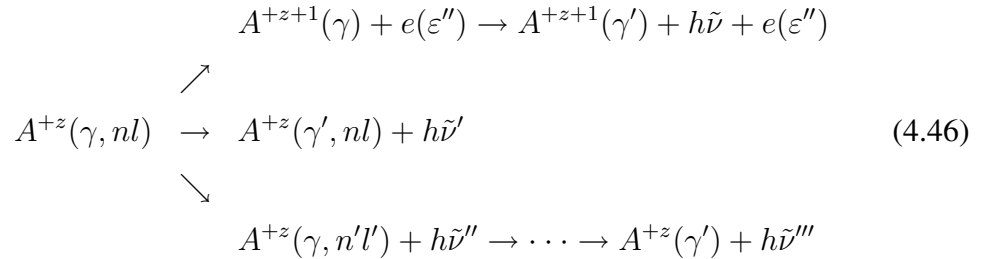


Ionisation in this manner is non-resonant, and the cross-section,  $\sigma_{i \rightarrow +}$  is a smoothly varying function of incident electron energy  $\varepsilon$ .

An alternative route to ionisation is through excitation-autoionisation. The first step of this process is the excitation of an inner-shell electron,



In this notation,  $\gamma$  represents the core electrons, with a vacancy caused by one electron being excited to the state  $nl$ . As with excitation of valence electrons, resonances exist, corresponding to excited states of the  $A^{+z-1}$  system. The excited ion  $A^{+z}(\gamma, nl)$  may relax via several routes:



The first reaction route in equation 4.47 is autoionisation of the  $nl$  electron. Following this step, the ion is still in an excited state with an inner-shell vacancy, and the ion may relax by emitting a photon or undergoing further autoionisations if there is sufficient energy in the system. This step is characterised by an autoionisation (or

Auger) rate  $A_a$ . The second process is a radiative relaxation of the excited core. The third processes is a radiative transition of the  $nl$  electron. The  $nl$  electron will cascade back to the vacancy in the electron core. The second and third processes depend on radiative rates,  $A_r$ . Fluorescence (the radiative relaxation of the excited core) and Auger rates are calculated by Kaastra and Mewe (1993) and revised by Gorczyca *et al* (2003).

With regard to this study, the following aspects of these ionisation processes are relevant. Total ionisation rates, that is the sum of resonant and non-resonant ionisation processes, are required to establish the ionisation balance of a plasma (see section 4.3). Since it is assumed in both the charge exchange and modified energetic electron models that the source of highly charged ions is the solar wind, the radiation associated with ionisation processes is irrelevant.

Within the cometary atmosphere, neutrals are ionised through electron collisions, charge exchange and photoionisation. Resonant ionisation processes are a possible source of x-ray emission, although this x-ray mechanism is not included in this study as preliminary fits to *Chandra* data indicate that fluorescence lines are not necessary (as discussed in sections 4.1.3 and 5.5.1). However, it is possible that neutral fluorescence could contribute a detectable and distinguishable amount of radiation when more advanced satellites such as *Constellation-X* are employed. The total ionisation rate of neutrals represents the loss rate of particles from the solar wind, and is required to model the interaction of the atmosphere with the solar wind (see section 2.4)

Several methods may be used to calculate ionisation cross-sections. The semi-empirical cross-sections of Burgess and Chidichimo (1983) include excitation-autoionisation effects. More sophisticated approaches such as distorted-wave (see for example, Loch *et al*, 2002) or *R*-Matrix with pseudostates (Bartschat *et al*, 1996) may also be used. As with collisional excitation, it is more practical to tabulate ionisation rates  $q_{i \rightarrow +}$  rather than cross-sections. The reaction rates are generated by integrating the product of the cross-section and a Maxwellian distribution of electrons.

## 4.2.5 Bremsstrahlung

The average bremsstrahlung power radiated as a function of photon frequency  $\tilde{\nu}$ ,  $\langle W(\tilde{\nu}) \rangle$  between the frequency interval  $\tilde{\nu}$  and  $\tilde{\nu} + d\tilde{\nu}$  from a Maxwellian distribution of electrons with temperature  $T_e$  is (Karzas and Latter, 1960)

$$\langle W(\tilde{\nu}) \rangle d\tilde{\nu} = \frac{2^5 \pi e^6}{4 h m c^3} Z^2 n_e \left( \frac{2 \pi k_B T_e}{3 m} \right)^{1/2} d \left( \frac{h \tilde{\nu}}{k_B T_e} \right) e^{-h \tilde{\nu} / k_B T_e} \left\langle g^{\text{III}} \left( \frac{h \tilde{\nu}}{k_B T_e}, \frac{Z^2 I_H}{k_B T_e} \right) \right\rangle \quad (4.47)$$

where  $Z$  is the average charge of the ions in the plasma, and  $g^{\text{III}}$  is the temperature

averaged free-free Gaunt factor (Gaunt, 1930; Karzas and Latter, 1960; Burgess and Summers, 1987).

#### **4.2.6 Summary**

Ion or atom energy levels and radiative rates are tabulated, along with *R*-Matrix Maxwell-averaged electron collision strengths where available; otherwise, Cowan code calculations are used. These data are appended with combined radiative and dielectronic recombination coefficients, and electron impact ionisation rates. The above data are in the central ADAS archive. The transition rates are altered to include two-photon transition rates, and charge exchange recombination rates from Fritsch and Lin (1983), the ORNL archive, Shimakura *et al* (1992), or an extrapolation from Shimakura *et al* (1992) complete the datasets.

It has been demonstrated that the solar radiation field and proton impact transitions have a negligible effect on excited state populations or ion charge states and are therefore not included in this analysis.

### 4.3 Collisional Radiative Modelling

From the reaction rates described in section 4.2, the time dependence of the population of the excited state  $N_i$  is given by

$$\begin{aligned} & \sum_{j>i} [A_{j\rightarrow i} + N_e q_{j\rightarrow i}^e] N_j + \sum_{k<i} N_e q_{k\rightarrow i}^e N_k \\ & + N_e N_+ \alpha_i^{\text{rr}} + N_e N_+ \alpha_i^{\text{dr}} + N_H N_+ q_i^{\text{CX}} \\ & = \left\{ \sum_{j>i} N_e q_{i\rightarrow j}^e + \sum_{k<i} [A_{i\rightarrow k} + N_e q_{i\rightarrow k}^e] + N_e q_{i\rightarrow +} \right\} N_i + \frac{dN_i}{dt}. \end{aligned}$$

In this notation, the left-hand side of equation 4.48 represents processes populating the level  $i$  from all of the other levels and recombination, and the right-hand side terms are the losses from  $i$ . Also, the dummy variable  $j$  is used for levels with energies greater than the energy of  $i$ , and the levels  $k$  have energies lower than  $i$ . The superscripts  $e$ , rr, dr and CX denote electron collisions, radiative recombination, dielectronic recombination and charge exchange respectively. The electron impact ionisation rate is  $q_{i\rightarrow +}$ . Processes driven by radiation fields and proton collisions are neglected, as discussed in section 4.2.

To solve this set of simultaneous equations, define the collisional radiative matrix  $C$ , such that the diagonal elements are the total loss rates from each level,

$$C_{ii} = \sum_{j<i} A_{i\rightarrow j} + N_e \sum_{j\neq i} q_{i\rightarrow j}^e + N_e q_{i\rightarrow +} \quad (4.48)$$

and the remaining elements represent processes populating the level  $i$  directly from  $j$ ,

$$C_{ij} = -A_{j\rightarrow i} - N_e q_{j\rightarrow i}^e \quad i \neq j. \quad (4.49)$$

Also, let  $N_e N_+ r_i$  be the sum of the radiative and dielectronic recombination rates to  $i$ . Equation 4.48 may now be written as

$$\sum_j C_{ij} N_j = N_e N_+ r_i + N_H N_+ q_i^{\text{CX}} - \frac{dN_i}{dt}. \quad (4.50)$$

In equilibrium, this becomes

$$\sum_j C_{ij} N_j^{\text{eq}} = N_e N_+ r_i + N_H N_+ q_i^{\text{CX}}. \quad (4.51)$$

At this point, a distinction between levels can be made according to level lifetimes, which are a function of the plasma parameters. In this study, the set of long-lived

metastable levels comprises of the ground state only, with every excited state categorised as a short-lived (or ordinary) level. This is justified by the comparison of collisional and radiative rates in section 4.2.2: collision rates are too small to compete with radiative transitions from even the longest-lived levels. In other parameter regimes (that is, higher density plasmas), the contribution of excitation from metastables on the overall population structure may be significant. This extension to a Generalised Collisional-Radiative model is described by Summers and Hooper (1983) and Summers *et al* (2006).

Ordinary excited levels may be assumed to have reached statistical equilibrium, and so equation 4.51 ( $i \neq 1$ ) applies. Adding to this the dynamic ground state population,

$$\sum_j C_{1j} N_j = N_e N_+ r_1 + N_H N_+ q_1^{\text{CX}} - \frac{dN_1}{dt} \quad (4.52)$$

gives

$$\left( C_{11} - \sum_{j \neq 1} C_{1j} \sum_{k \neq 1} C_{jk}^{-1} C_{k1} \right) N_1 = N_e N_+ r_1 + N_e N_+ \sum_{j \neq 1} C_{1j} \sum_{k \neq 1} C_{jk}^{-1} r_k + \quad (4.53)$$

$$N_H N_+ q_1^{\text{CX}} + N_H N_+ \sum_{j \neq 1} C_{1j} \sum_{k \neq 1} C_{jk}^{-1} q_k^{\text{CX}} - \frac{dN_1}{dt}. \quad (4.54)$$

Equation 4.54 is often written without charge exchange recombination, which allows the definition of “collisional-radiative” ionisation,  $S_{cr}$ , and recombination,  $\alpha_{cr}$  coefficients (Bates *et al*, 1962), such that

$$S_{cr} = (C_{11} - \sum_{j \neq 1} C_{1j} \sum_{k \neq 1} C_{jk}^{-1} C_{k1}) / N_e \quad (4.55)$$

and

$$\alpha_{cr} = r_1 - \sum_{j \neq 1} C_{1j} \sum_{k \neq 1} C_{jk}^{-1} r_k. \quad (4.56)$$

In a similar manner, we can define the collisional-radiative charge exchange recombination coefficient as

$$C_{cr} = q_1^{\text{CX}} - \sum_{j \neq 1} C_{1j} \sum_{k \neq 1} C_{jk}^{-1} q_k^{\text{CX}}. \quad (4.57)$$

## Excited Level Populations

Rearranging equation 4.54 gives the excited level populations,

$$\begin{aligned}
 N_j &= - \sum_{i \neq 1} C_{ji}^{-1} C_{i1} N_1 + \sum_{i \neq 1} C_{ji}^{-1} N_e N_+ r_i + \sum_{i \neq 1} C_{ji}^{-1} N_H N_+ q_i^{\text{CX}} \\
 &= \mathcal{F}_j^{(\text{exc})} N_e N_1 + \mathcal{F}_j^{(\text{rec})} N_e N_+ + \mathcal{F}_j^{(\text{CX})} N_H N_+
 \end{aligned} \tag{4.58}$$

where the  $\mathcal{F}_j^{(\text{exc})}$ ,  $\mathcal{F}_j^{(\text{rec})}$ , and  $\mathcal{F}_j^{(\text{CX})}$  are the effective contributions to the excited populations by excitations from the ground, recombination and charge exchange respectively. From these values, the photon emissivity coefficients can be defined as

$$\mathcal{P}\mathcal{E}\mathcal{C}_{j \rightarrow k}^{(\text{exc})} = A_{j \rightarrow k} \mathcal{F}_j^{(\text{exc})} \tag{4.59}$$

$$\mathcal{P}\mathcal{E}\mathcal{C}_{j \rightarrow k}^{(\text{rec})} = A_{j \rightarrow k} \mathcal{F}_j^{(\text{rec})} \tag{4.60}$$

$$\mathcal{P}\mathcal{E}\mathcal{C}_{j \rightarrow k}^{(\text{CX})} = A_{j \rightarrow k} \mathcal{F}_j^{(\text{CX})}. \tag{4.61}$$

Photon emissivity coefficients are then used to construct line emission spectra. Note that for two-photon emission, the  $\mathcal{P}\mathcal{E}\mathcal{C}$  represents the integral over all possible photon energies. Bremsstrahlung and radiative recombination continua must be added separately to the  $\mathcal{P}\mathcal{E}\mathcal{C}$  spectrum.

## Ionisation Balance

The population of an ionisation stage  $N^z$  may be found by balancing ionisation and recombination rates to and from the stage  $N^z$ ,

$$\begin{aligned}
 \frac{dN^z}{dt} &= N_e S_{cr}^{z-1 \rightarrow z} N^{z-1} \\
 &\quad - \left( N_e S_{cr}^{z \rightarrow z+1} + N_e \alpha_{cr}^{z \rightarrow z-1} + N_H C_{cr}^{z \rightarrow z-1} \right) N^z \\
 &\quad + \left( N_e \alpha_{cr}^{z+1 \rightarrow z} + N_H C_{cr}^{z+1 \rightarrow z} \right) N^{z+1}
 \end{aligned} \tag{4.62}$$

where  $S_{cr}$ ,  $\alpha_{cr}$  and  $C_{cr}$  are the collisional-radiative ionisation, recombination and charge exchange coefficients as defined in section 4.3. In equilibrium, the stage populations can be found from the set of simultaneous equations

$$N_e \begin{bmatrix} -S_{cr}^{0 \rightarrow 1} & \alpha_{cr}^{1 \rightarrow 0} + (N_H/N_e)C_{cr}^{1 \rightarrow 0} & \cdots & 0 \\ S_{cr}^{0 \rightarrow 1} & -(S_{cr}^{1 \rightarrow 2} + \alpha_{cr}^{1 \rightarrow 0} + (N_H/N_e)C_{cr}^{1 \rightarrow 0}) & \cdots & 0 \\ 0 & S_{cr}^{1 \rightarrow 2} & \cdots & 0 \\ \vdots & \vdots & \ddots & \vdots \\ 0 & 0 & \cdots & -(\alpha_{cr}^{z_0 \rightarrow z_0-1} + (N_H/N_e)C_{cr}^{z_0 \rightarrow z_0-1}) \end{bmatrix} \begin{bmatrix} N^0 \\ N^1 \\ N^2 \\ \vdots \\ N^{z_0} \end{bmatrix} = 0, \quad (4.63)$$

normalised such that

$$N_{\text{tot}} = \sum_{z=0}^{z_0} N^z, \quad (4.64)$$

where  $N_{\text{tot}}$  is the density of the element in question.

Again, this method may be expanded to include metastables in a generalised collisional radiative framework (Summers and Hooper, 1983, Summers *et al*, 2006).

## 4.4 Application of Collisional Radiative Modelling

### 4.4.1 The Solar Wind

The x-ray emitting species in the cometary plasma are the heavy ions in the solar wind. These ions are formed in the solar corona, a low density plasma with a temperature of the order 100 eV and electron density  $10^8 \text{ cm}^{-3}$ . The level populations of ion species are not of consequence, as emission from the corona is not being examined here. Only the fractional abundance of each ion of an element is important. The ionisation balance can be found from equation 4.63. Due to the high temperature of the corona, the neutral hydrogen density will be negligible, and so the contribution from charge exchange recombination does not need to be considered.

For illustration, the ionisation fractions for oxygen as a function of temperature are shown in figure 4.11. In this case, the electron density is  $10^8 \text{ cm}^{-3}$ .

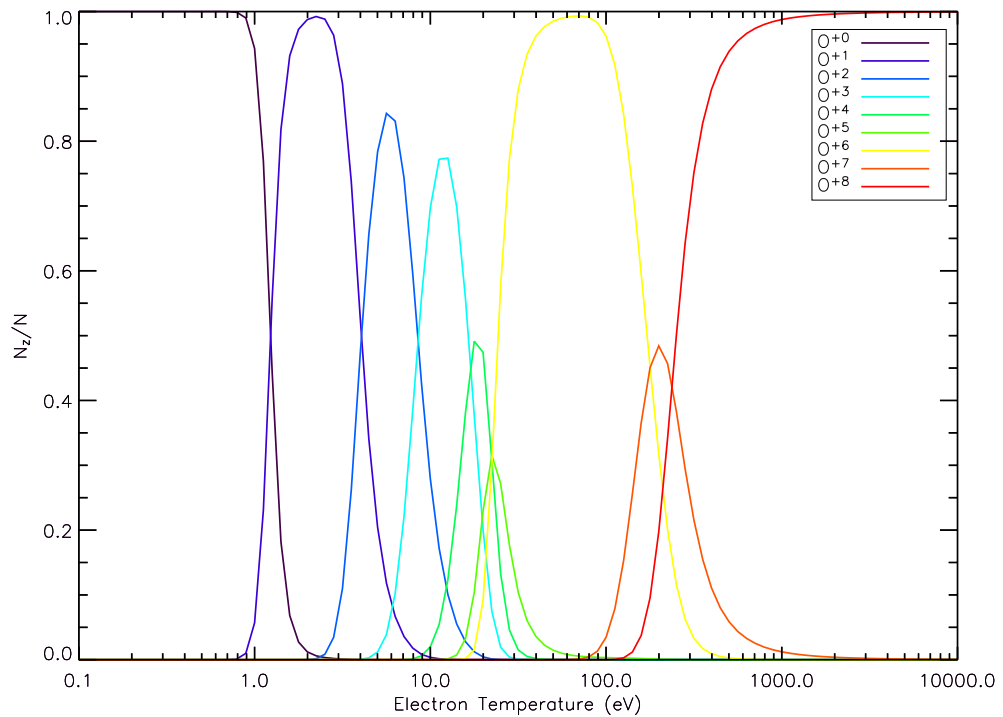


Figure 4.11: The ionisation stages of oxygen as a function of electron temperature for a plasma with electron density  $N_e = 10^8 \text{ cm}^{-3}$ .

In the temperature region of the corona,  $T_e \sim 100 \text{ eV}$ , the main oxygen ions are  $\text{O}^{6+}$ ,  $\text{O}^{7+}$  and  $\text{O}^{8+}$ . Summers (1972) demonstrated that although the fractional abundances of neutral and near-neutral particles are density dependent at low temperatures, the fractional abundances of highly charged ions are constant in the coronal limit (up to a density of  $\sim 10^{12} \text{ cm}^{-3}$ ).

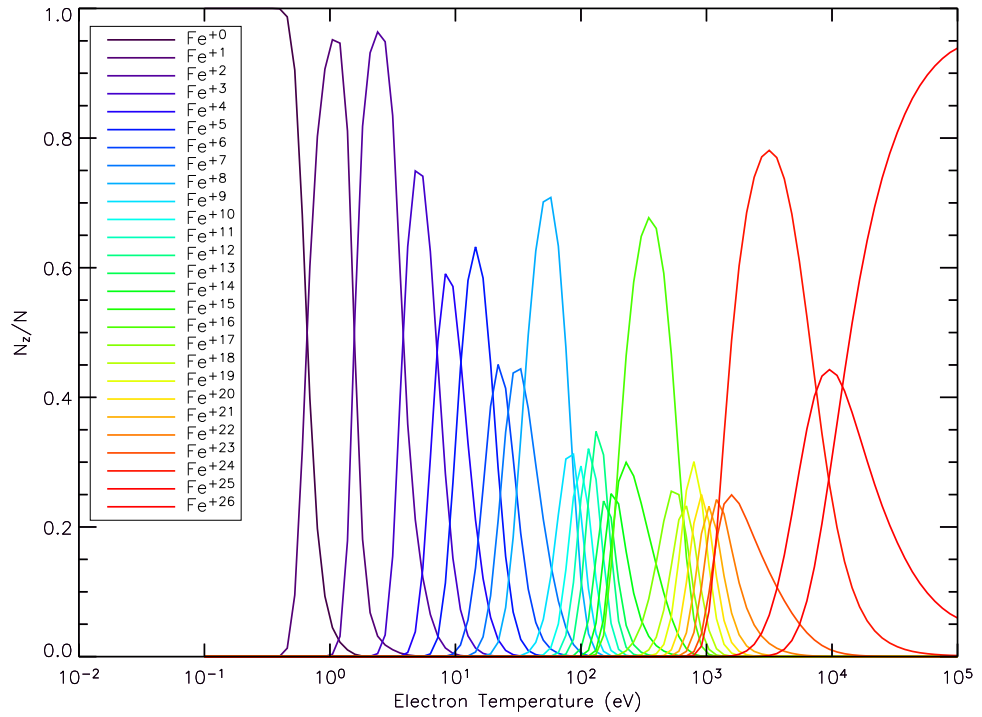


Figure 4.12: The ionisation stages of iron as a function of electron temperature for a plasma with electron density  $N_e = 10^8 \text{cm}^{-3}$ .

The ion fractions for iron at the same density are shown in figure 4.12.

The other minor elements of significance in the solar wind are He (although it does not emit x-ray lines), C, N, Ne, Mg, Si and S. The population of each ion is preserved to a large extent as the solar wind streams from the corona due to the long recombination timescale.

## 4.4.2 Modelling Emission Spectra

Theoretical spectra are created using photon emissivity coefficients (equations 4.59 – 4.61). For example, the emissivity of the transition  $i$  to  $j$  from a plasma element with volume  $dV$  is

$$\begin{aligned} \epsilon_{i \rightarrow j} = N_i^z ( & N_e \mathcal{P} \mathcal{E} \mathcal{C}_{i \rightarrow j}^{(\text{exc})}(N_e, T_e) + \\ & N_e \mathcal{P} \mathcal{E} \mathcal{C}_{i \rightarrow j}^{(\text{rec})}(N_e, T_e) + \\ & N_H \mathcal{P} \mathcal{E} \mathcal{C}_{i \rightarrow j}^{(\text{cx})}(N_e, T_e, v) ) dV \end{aligned} \quad (4.65)$$

where  $N_i^z$ ,  $N_e$ , and  $N_H$  are the ion, electron and hydrogen densities in the volume element,  $T_e$  is the electron temperature and  $v$  is the impact speed of the charge exchange reactions. It has been demonstrated that in this parameter regime the radiative rates from metastable levels are larger than the collisional rates, and so metastable levels may be treated as ordinary excited levels. As a result, the coefficients are density independent, and the charge exchange  $\mathcal{P} \mathcal{E} \mathcal{C}$  does not depend on the free electron temperature. This simplifies the emissivity to

$$\begin{aligned} \epsilon_{i \rightarrow j} = N_i^z ( & N_e \mathcal{P} \mathcal{E} \mathcal{C}_{i \rightarrow j}^{(\text{exc})}(T_e) + \\ & N_e \mathcal{P} \mathcal{E} \mathcal{C}_{i \rightarrow j}^{(\text{rec})}(T_e) + \\ & N_H \mathcal{P} \mathcal{E} \mathcal{C}_{i \rightarrow j}^{(\text{cx})}(v) ) dV. \end{aligned} \quad (4.66)$$

Photon emissivity coefficients of each type are tabulated against their relevant independent variables. An emission spectrum can be developed by adding  $\epsilon_{i \rightarrow j}$  to a spectral array at the corresponding bin, and repeating the process for every observable transition in each of ions present. The exception to this is when the coefficients describe two-photon decay (see section 4.2.1).

The spectrum is completed by including bremsstrahlung (equation 4.47) and radiative recombination continua (equation 4.29) using the same plasma parameters.

## Electron Driven Emission

By way of illustration, the photon emissivity coefficient spectrum from He-like oxygen driven by electrons with temperature  $T_e = 200$  eV is shown in figure 4.13.

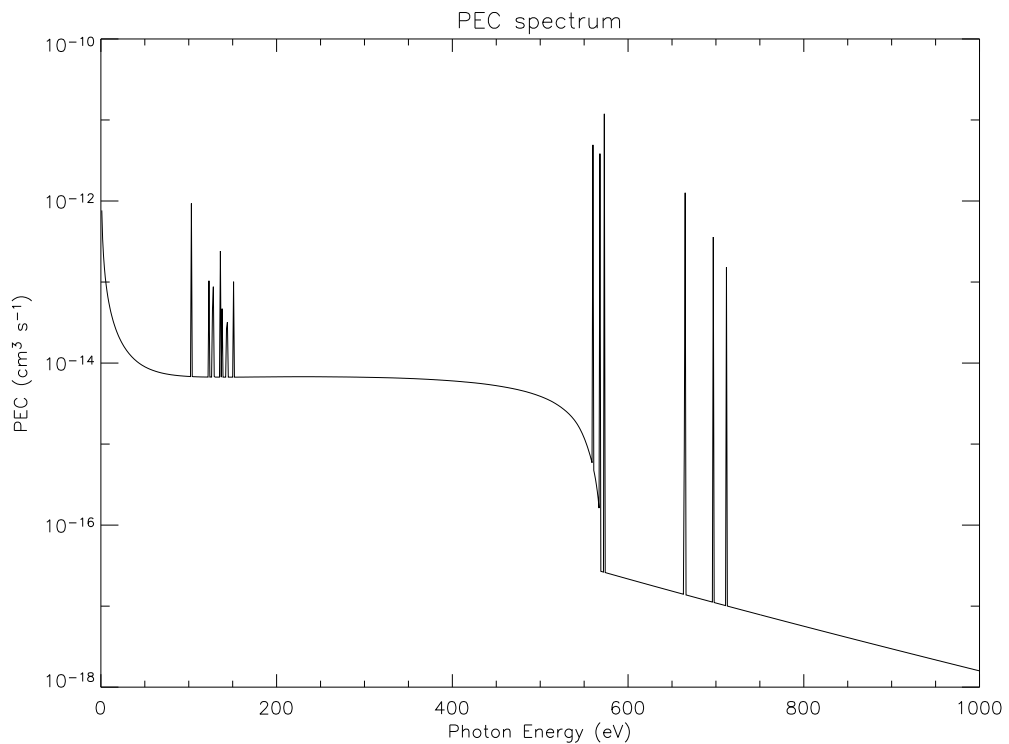


Figure 4.13: The zero density electron excitation driven photon emissivity coefficient spectrum for O VII with  $T_e = 200$  eV.

Note that the emission from bremsstrahlung and two-photon transitions is small compared to line emission. This is the case for all of the x-ray emitting ions in the solar wind. Consequently, if a significant bremsstrahlung continuum is present in observed spectra, the most probable source is hydrogen and helium ions. These ions are the most abundant, and do not emit x-ray lines.

The strongest O VII lines are listed in table 4.3. The variation of these photon emissivity coefficients with electron temperature is shown in figure 4.14.

At low electron temperatures, the coefficient is composed of the contribution from radiative recombination. At higher temperatures, the coefficient is dominated by the contribution from electron impact excitation from the ground state, although the effects from both radiative recombination and dielectronic recombination are included. Again note that the emission of satellite lines in dielectronic recombination is not accounted for in this approach.

Transitions with lower photon emissivity coefficients are not shown in figure 4.14, nor are transitions that are below the detection range of the ACIS device on Chandra, ( $E < 240$  eV).

Transition	Line Energy (eV)	$\mathcal{PEC}^{(\text{exc})}$ ( $\text{cm}^3 \text{s}^{-1}$ )
$1s2p \ ^1P \rightarrow 1s^2 \ ^1S$	574.0	$1.19 \times 10^{-11}$
$1s2s \ ^3S \rightarrow 1s^2 \ ^1S$	561.0	$4.93 \times 10^{-12}$
$1s2p \ ^3P \rightarrow 1s^2 \ ^1S$	568.6	$3.84 \times 10^{-12}$
$1s3p \ ^1P \rightarrow 1s^2 \ ^1S$	665.6	$1.26 \times 10^{-12}$
$1s4p \ ^1P \rightarrow 1s^2 \ ^1S$	697.8	$3.59 \times 10^{-13}$
$1s5p \ ^1P \rightarrow 1s^2 \ ^1S$	712.7	$1.52 \times 10^{-13}$

Table 4.3: The most prominent transitions in the electron excitation  $\mathcal{PEC}$  spectrum for  $T_e = 200$  eV.

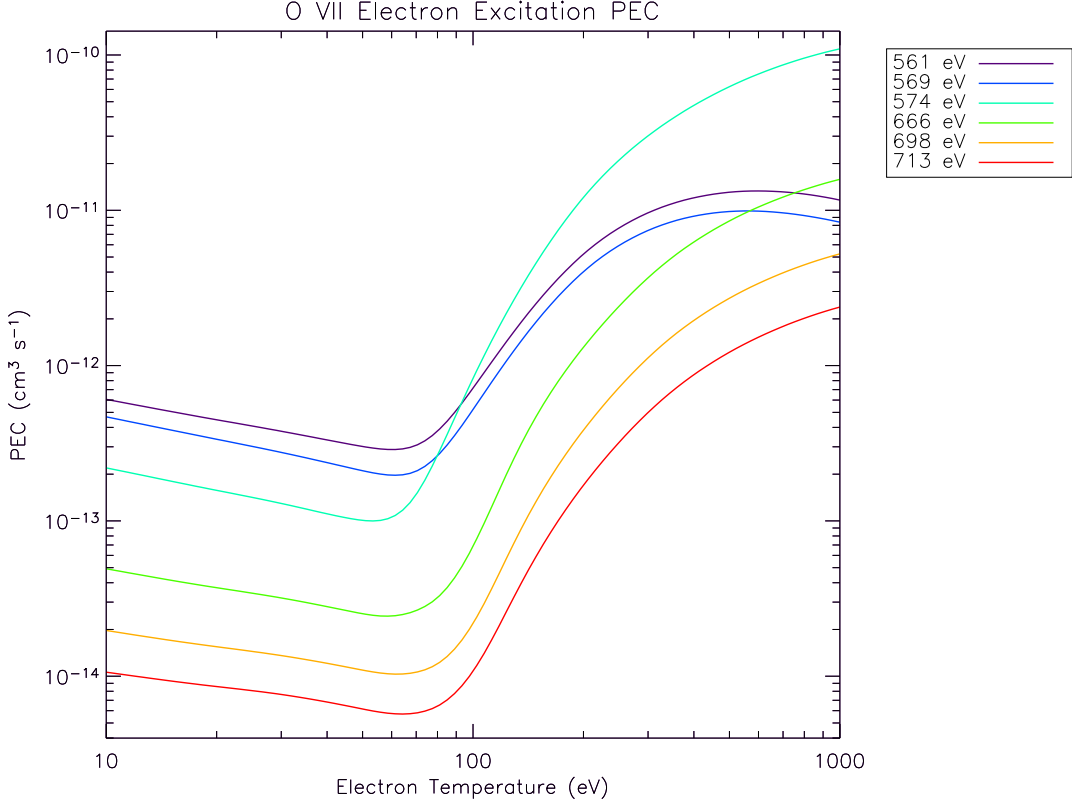


Figure 4.14: The zero density electron driven photon emissivity coefficient for O VII as a function of electron temperature.

The recombination spectrum for the same parameters has a similar form, although the coefficients are approximately 3% of those of the excitation spectrum. Again, the recombination and two-photon continua are much smaller than the line emission emissivities.

Data are available to construct similar figures for many other ions. A summary of the most prominent emission lines from ADAS is given in table 4.4. The data are arranged by emitting ion, and the lines are ordered by photon emissivity coefficient for an electron temperature of 300 eV. This value is used as it is representative of the

electron temperature suggested by various fits to cometary x-ray spectra (see Dennerl *et al*, 1997; Owens *et al*, 1998; Lisse *et al*, 2001).

Ion	Energy (eV)	Transition	Ion	Energy (eV)	Transition	
C <sup>4+</sup>	308	1s2p <sup>1</sup> P → 1s <sup>2</sup> <sup>1</sup> S	S <sup>10+</sup>	317	1s <sup>2</sup> 2s <sup>2</sup> 2p3d <sup>3</sup> D → 1s <sup>2</sup> 2s <sup>2</sup> 2p <sup>2</sup> <sup>3</sup> P	
	299	1s2s <sup>3</sup> S → 1s <sup>2</sup> <sup>1</sup> S		314	1s <sup>2</sup> 2s <sup>2</sup> 2p3d <sup>1</sup> F → 1s <sup>2</sup> 2s <sup>2</sup> 2p <sup>2</sup> <sup>3</sup> P	
	304	1s2p <sup>3</sup> P → 1s <sup>2</sup> <sup>1</sup> S		318	1s <sup>2</sup> 2s <sup>2</sup> 2p3d <sup>3</sup> P → 1s <sup>2</sup> 2s <sup>2</sup> 2p <sup>2</sup> <sup>3</sup> P	
	354	1s3p <sup>1</sup> P → 1s <sup>2</sup> <sup>1</sup> S				
C <sup>5+</sup>	368	2p → 1s	S <sup>11+</sup>	343	1s <sup>2</sup> 2s <sup>2</sup> 3d <sup>2</sup> D → 1s <sup>2</sup> 2s <sup>2</sup> 2p <sup>2</sup> <sup>2</sup> P	
	436	3p → 1s	S <sup>12+</sup>	385	1s <sup>2</sup> 2s3p <sup>1</sup> P → 1s <sup>2</sup> 2s <sup>2</sup> <sup>1</sup> S	
N <sup>5+</sup>	431	1s2p <sup>1</sup> P → 1s <sup>2</sup> <sup>1</sup> S	S <sup>13+</sup>	408	1s <sup>2</sup> 3p <sup>2</sup> P → 1s <sup>2</sup> 2s <sup>2</sup> <sup>2</sup> S	
	426	1s2p <sup>3</sup> P → 1s <sup>2</sup> <sup>1</sup> S	S <sup>14+</sup>	450	1s3p <sup>3</sup> P → 1s2s <sup>3</sup> S	
	498	1s3p <sup>1</sup> P → 1s <sup>2</sup> <sup>1</sup> S		435	1s3d <sup>3</sup> D → 1s2p <sup>3</sup> P	
N <sup>6+</sup>	500	2p → 1s	Ar <sup>9+</sup>	331	1s <sup>2</sup> 2s <sup>2</sup> 2p <sup>4</sup> 3d <sup>2</sup> P → 1s <sup>2</sup> 2s <sup>2</sup> 2p <sup>5</sup> <sup>2</sup> P	
	593	3p → 1s		323	1s <sup>2</sup> 2s <sup>2</sup> 2p <sup>4</sup> 3d <sup>2</sup> D → 1s <sup>2</sup> 2s <sup>2</sup> 2p <sup>5</sup> <sup>2</sup> P	
O <sup>6+</sup>	574	1s2p <sup>1</sup> P → 1s <sup>2</sup> <sup>1</sup> S	Ar <sup>10+</sup>	362	1s <sup>2</sup> 2s <sup>2</sup> 2p <sup>3</sup> 3d <sup>3</sup> P → 1s <sup>2</sup> 2s <sup>2</sup> 2p <sup>4</sup> <sup>3</sup> P	
	561	1s2s <sup>3</sup> S → 1s <sup>2</sup> <sup>1</sup> S				
	569	1s2p <sup>3</sup> P → 1s <sup>2</sup> <sup>1</sup> S		363	1s <sup>2</sup> 2s <sup>2</sup> 2p <sup>3</sup> 3d <sup>1</sup> F → 1s <sup>2</sup> 2s <sup>2</sup> 2p <sup>4</sup> <sup>1</sup> D	
	666	1s3p <sup>1</sup> P → 1s <sup>2</sup> <sup>1</sup> S		360	1s <sup>2</sup> 2s <sup>2</sup> 2p <sup>3</sup> 3d <sup>3</sup> S → 1s <sup>2</sup> 2s <sup>2</sup> 2p <sup>4</sup> <sup>3</sup> P	
O <sup>7+</sup>	654	2p → 1s				
	775	3p → 1s				
	817	4p → 1s				
	837	5p → 1s				
Ne <sup>8+</sup>	915	1s2p <sup>3</sup> P → 1s <sup>2</sup> <sup>1</sup> S	Ar <sup>11+</sup>	396	1s <sup>2</sup> 2s <sup>2</sup> 2p <sup>2</sup> 3d <sup>4</sup> P → 1s <sup>2</sup> 2s <sup>2</sup> 2p <sup>3</sup> <sup>4</sup> S	
	922	1s2p <sup>1</sup> P → 1s <sup>2</sup> <sup>1</sup> S		394	1s <sup>2</sup> 2s <sup>2</sup> 2p <sup>2</sup> 3d <sup>4</sup> D → 1s <sup>2</sup> 2s <sup>2</sup> 2p <sup>3</sup> <sup>4</sup> S	
	1074	1s3p <sup>1</sup> P → 1s <sup>2</sup> <sup>1</sup> S			1s <sup>2</sup> 2s <sup>2</sup> 2p <sup>2</sup> 3d <sup>2</sup> F → 1s <sup>2</sup> 2s <sup>2</sup> 2p <sup>3</sup> <sup>2</sup> F	
Ne <sup>9+</sup>	1022	2p → 1s	Ar <sup>12+</sup>	424	1s <sup>2</sup> 2s <sup>2</sup> 2p3d <sup>3</sup> D → 1s <sup>2</sup> 2s <sup>2</sup> 2p <sup>2</sup> <sup>3</sup> P	
	1211	3p → 1s		421	1s <sup>2</sup> 2s <sup>2</sup> 2p3d <sup>1</sup> F → 1s <sup>2</sup> 2s <sup>2</sup> 2p <sup>2</sup> <sup>1</sup> F	
	255	4s → 2p		426	1s <sup>2</sup> 2s <sup>2</sup> 2p3d <sup>3</sup> P → 1s <sup>2</sup> 2s <sup>2</sup> 2p <sup>2</sup> <sup>3</sup> P	
		4d → 2p	Ar <sup>13+</sup>	453	1s <sup>2</sup> 2s <sup>2</sup> 3d <sup>2</sup> D → 1s <sup>2</sup> 2s <sup>2</sup> 2p <sup>2</sup> <sup>2</sup> P	
Mg <sup>8+</sup>	254	1s <sup>2</sup> 2s4p <sup>1</sup> P → 1s <sup>2</sup> 2s <sup>2</sup> <sup>1</sup> S	Ar <sup>14+</sup>	502	1s <sup>2</sup> 2s3p <sup>1</sup> P → 1s <sup>2</sup> 2s <sup>2</sup> <sup>1</sup> S	
Mg <sup>9+</sup>	263	1s <sup>2</sup> 4d <sup>2</sup> D → 1s <sup>2</sup> 2p <sup>2</sup> <sup>2</sup> P		500	1s <sup>2</sup> 2s3p <sup>3</sup> P → 1s <sup>2</sup> 2s <sup>2</sup> <sup>1</sup> S	
	282	1s <sup>2</sup> 4p <sup>2</sup> P → 1s <sup>2</sup> 2s <sup>2</sup> <sup>2</sup> S		403	1s <sup>2</sup> 2s3p <sup>1</sup> P → 1s <sup>2</sup> 2p <sup>2</sup> <sup>1</sup> S	
Mg <sup>10+</sup>	1351	1s2s <sup>1</sup> S → 1s <sup>2</sup> <sup>1</sup> S	Ar <sup>15+</sup>	528	1s <sup>2</sup> 3p <sup>2</sup> P → 1s <sup>2</sup> 2s <sup>2</sup> <sup>2</sup> S	
	1344	1s2p <sup>3</sup> P → 1s <sup>2</sup> <sup>1</sup> S	Ar <sup>16+</sup>	558	1s3d <sup>3</sup> D → 1s2p <sup>3</sup> P	
	246	1s3p <sup>3</sup> P → 1s2s <sup>3</sup> S				
	235	1s3d <sup>3</sup> D → 1s2p <sup>3</sup> P				
Si <sup>10+</sup>	284	1s <sup>2</sup> 2s3p <sup>1</sup> P → 1s <sup>2</sup> 2s <sup>2</sup> <sup>2</sup> S	Fe <sup>14+</sup>	235	1s <sup>2</sup> 2s <sup>2</sup> 2p <sup>6</sup> 3s4p <sup>1</sup> P → 1s <sup>2</sup> 2s <sup>2</sup> 2p <sup>6</sup> 3s <sup>2</sup> <sup>1</sup> S	
	282	1s <sup>2</sup> 2s3p <sup>3</sup> P → 1s <sup>2</sup> 2s <sup>2</sup> <sup>2</sup> S		Fe <sup>15+</sup>	246	1s <sup>2</sup> 2s <sup>2</sup> 2p <sup>6</sup> 4p <sup>2</sup> P → 1s <sup>2</sup> 2s <sup>2</sup> 2p <sup>6</sup> 3s <sup>2</sup> S
Si <sup>11+</sup>	304	1s <sup>2</sup> 3p <sup>2</sup> P → 1s <sup>2</sup> 2s <sup>2</sup> <sup>2</sup> S		310	1s <sup>2</sup> 2s <sup>2</sup> 2p <sup>6</sup> 5d <sup>2</sup> D → 1s <sup>2</sup> 2s <sup>2</sup> 2p <sup>6</sup> 3p <sup>2</sup> P	
Si <sup>12+</sup>	340	1s3p <sup>3</sup> P → 1s2s <sup>3</sup> S	Fe <sup>16+</sup>	826	1s <sup>2</sup> 2s <sup>2</sup> 2p <sup>5</sup> 3d <sup>1</sup> P → 1s <sup>2</sup> 2s <sup>2</sup> 2p <sup>6</sup> <sup>1</sup> S	
	328	1s3d <sup>3</sup> D → 1s2p <sup>3</sup> P		731	1s <sup>2</sup> 2s <sup>2</sup> 2p <sup>5</sup> 3s <sup>3</sup> P → 1s <sup>2</sup> 2s <sup>2</sup> 2p <sup>6</sup> <sup>1</sup> S	
		1s3d <sup>1</sup> D → 1s2p <sup>3</sup> P		812	1s <sup>2</sup> 2s <sup>2</sup> 2p <sup>5</sup> 3d <sup>3</sup> D → 1s <sup>2</sup> 2s <sup>2</sup> 2p <sup>6</sup> <sup>1</sup> S	
	322	1s3s <sup>3</sup> S → 1s2p <sup>3</sup> P		727	1s <sup>2</sup> 2s <sup>2</sup> 2p <sup>5</sup> 3s <sup>1</sup> S → 1s <sup>2</sup> 2s <sup>2</sup> 2p <sup>6</sup> <sup>1</sup> S	
	318	1s3d <sup>3</sup> D → 1s2p <sup>1</sup> P		Fe <sup>17+</sup>	870	1s <sup>2</sup> 2s <sup>2</sup> 2p <sup>4</sup> 3d <sup>2</sup> D → 1s <sup>2</sup> 2s <sup>2</sup> 2p <sup>5</sup> <sup>2</sup> P
		1s3d <sup>1</sup> D → 1s2p <sup>1</sup> P			869	1s <sup>2</sup> 2s <sup>2</sup> 2p <sup>4</sup> 3d <sup>2</sup> P → 1s <sup>2</sup> 2s <sup>2</sup> 2p <sup>5</sup> <sup>2</sup> P
	1s3s <sup>1</sup> S → 1s2p <sup>1</sup> P	885	1s <sup>2</sup> 2s <sup>2</sup> 2p <sup>4</sup> 3d <sup>2</sup> D → 1s <sup>2</sup> 2s <sup>2</sup> 2p <sup>5</sup> <sup>2</sup> P			
316	1s3s <sup>1</sup> S → 1s2p <sup>1</sup> P	789	1s <sup>2</sup> 2s <sup>2</sup> 2p <sup>4</sup> 3s <sup>2</sup> D → 1s <sup>2</sup> 2s <sup>2</sup> 2p <sup>5</sup> <sup>2</sup> P			
Si <sup>13+</sup>	371	2p → 1s		775	1s <sup>2</sup> 2s <sup>2</sup> 2p <sup>4</sup> 3s <sup>2</sup> P → 1s <sup>2</sup> 2s <sup>2</sup> 2p <sup>5</sup> <sup>2</sup> P	
	501	3p → 1s		857	1s <sup>2</sup> 2s <sup>2</sup> 2p <sup>4</sup> 3d <sup>2</sup> D → 1s <sup>2</sup> 2s <sup>2</sup> 2p <sup>5</sup> <sup>2</sup> P	
S <sup>8+</sup>	262	1s <sup>2</sup> 2s <sup>2</sup> 2p <sup>3</sup> 3d <sup>3</sup> P → 1s <sup>2</sup> 2s <sup>2</sup> 2p <sup>4</sup> <sup>3</sup> P		865	1s <sup>2</sup> 2s <sup>2</sup> 2p <sup>4</sup> 3d <sup>2</sup> F → 1s <sup>2</sup> 2s <sup>2</sup> 2p <sup>5</sup> <sup>2</sup> P	
		1s <sup>2</sup> 2s <sup>2</sup> 2p <sup>3</sup> 3d <sup>1</sup> D → 1s <sup>2</sup> 2s <sup>2</sup> 2p <sup>4</sup> <sup>1</sup> D				
	261	1s <sup>2</sup> 2s <sup>2</sup> 2p <sup>3</sup> 3d <sup>3</sup> D → 1s <sup>2</sup> 2s <sup>2</sup> 2p <sup>4</sup> <sup>3</sup> P				
		1s <sup>2</sup> 2s <sup>2</sup> 2p <sup>3</sup> 3d <sup>1</sup> P → 1s <sup>2</sup> 2s <sup>2</sup> 2p <sup>4</sup> <sup>3</sup> P				
	1s <sup>2</sup> 2s <sup>2</sup> 2p <sup>3</sup> 3d <sup>3</sup> P → 1s <sup>2</sup> 2s <sup>2</sup> 2p <sup>4</sup> <sup>1</sup> D					
	1s <sup>2</sup> 2s <sup>2</sup> 2p <sup>3</sup> 3d <sup>3</sup> S → 1s <sup>2</sup> 2s <sup>2</sup> 2p <sup>4</sup> <sup>3</sup> P					
	1s <sup>2</sup> 2s <sup>2</sup> 2p <sup>3</sup> 3d <sup>1</sup> F → 1s <sup>2</sup> 2s <sup>2</sup> 2p <sup>4</sup> <sup>1</sup> D					
S <sup>9+</sup>	294	1s <sup>2</sup> 2s <sup>2</sup> 2p <sup>2</sup> 3d <sup>2</sup> D → 1s <sup>2</sup> 2s <sup>2</sup> 2p <sup>3</sup> <sup>2</sup> P		865	1s <sup>2</sup> 2s <sup>2</sup> 2p <sup>4</sup> 3d <sup>2</sup> S → 1s <sup>2</sup> 2s <sup>2</sup> 2p <sup>5</sup> <sup>2</sup> P	
		1s <sup>2</sup> 2s <sup>2</sup> 2p <sup>2</sup> 3d <sup>2</sup> F → 1s <sup>2</sup> 2s <sup>2</sup> 2p <sup>3</sup> <sup>2</sup> D				

Table 4.4: Prominent electron collision driven transitions in the soft x-ray regime. Emission lines from each ion species are arranged by photon emissivity coefficient for an electron temperature of 300 eV.

## Charge Exchange Driven Emission

In a similar manner, a charge exchange driven photon emissivity coefficient spectrum for the same ion is presented in figure 4.15. In this case, the collision speed is  $v_H = 800$  eV/amu.

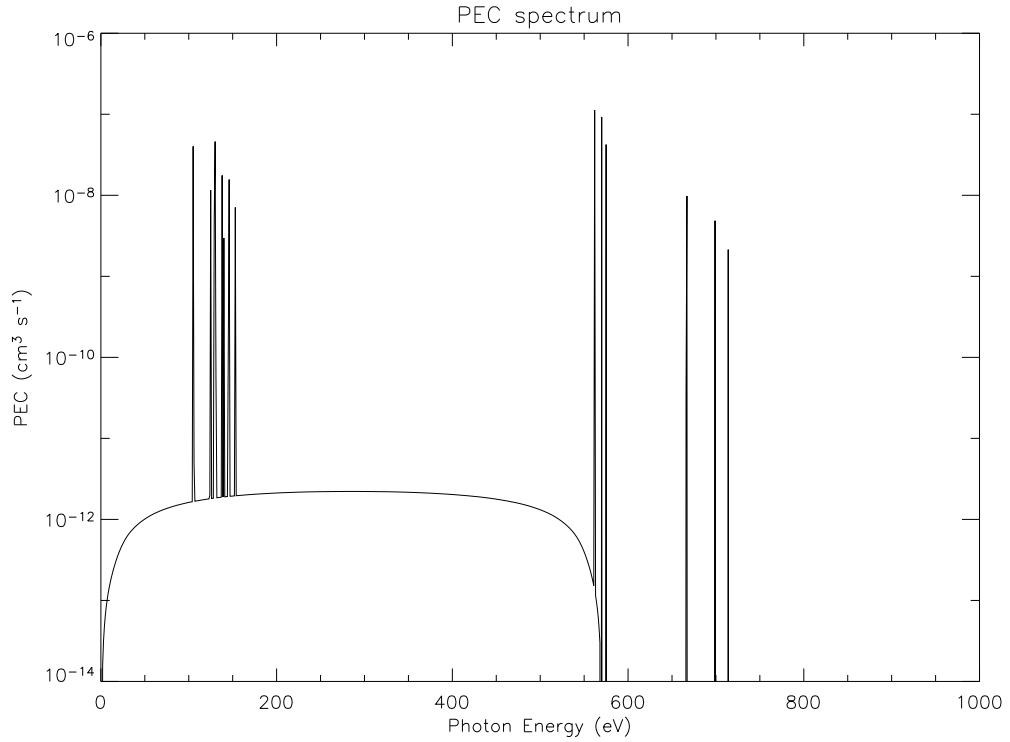


Figure 4.15: The zero density charge exchange driven photon emissivity coefficient spectrum for O VII with  $v_H = 800$  eV/amu.

The only continuum emission driven by charge exchange is from two-photon decay. The most prominent O VII transitions are listed in table 4.5.

Transition	Line Energy (eV)	$\mathcal{PEC}^{(cx)}$ ( $\text{cm}^3 \text{s}^{-1}$ )
$1s2s \ ^3S \rightarrow 1s^2 \ ^1S$	561.0	$1.12 \times 10^{-7}$
$1s2p \ ^3P \rightarrow 1s^2 \ ^1S$	568.6	$9.27 \times 10^{-8}$
$1s2p \ ^1P \rightarrow 1s^2 \ ^1S$	574.0	$4.23 \times 10^{-8}$
$1s3p \ ^1P \rightarrow 1s^2 \ ^1P$	665.6	$9.77 \times 10^{-9}$
$1s4p \ ^1P \rightarrow 1s^2 \ ^1S$	697.8	$4.83 \times 10^{-9}$

Table 4.5: The most prominent transitions in the charge exchange  $\mathcal{PEC}$  spectrum for  $v_H = 800$  eV/amu.

The variation of the emissivity coefficients with collision speed for O VII is shown in figure 4.16.

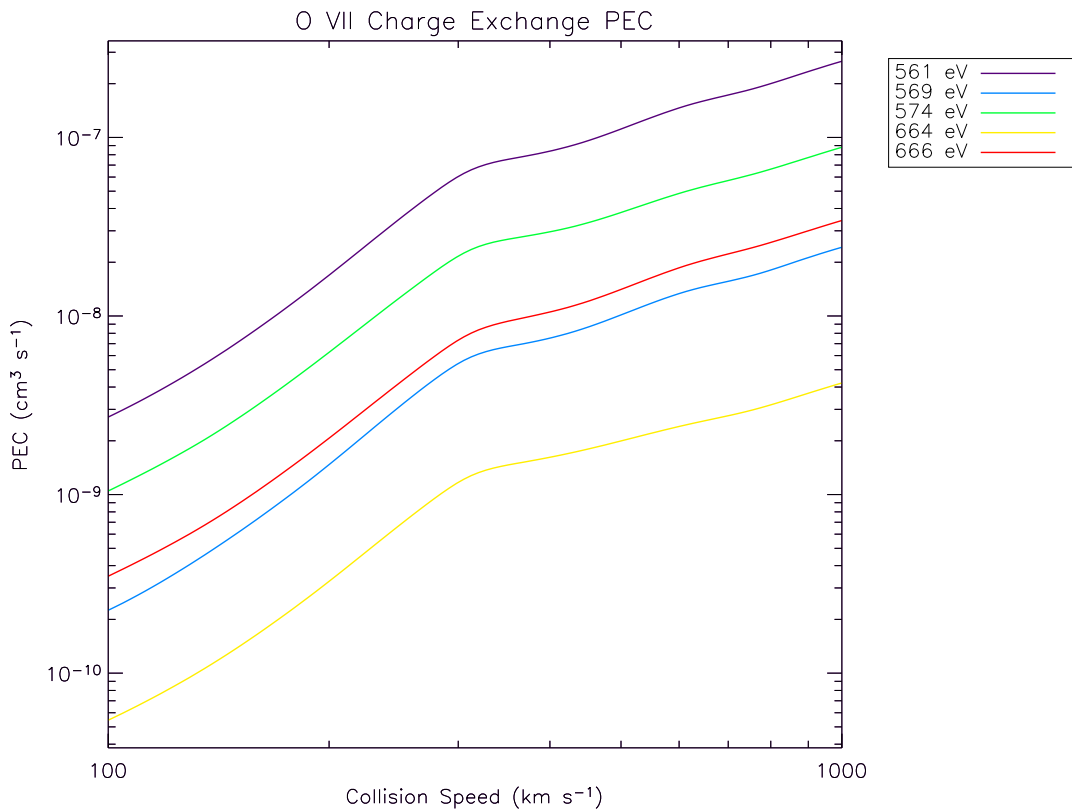


Figure 4.16: The zero density charge exchange driven photon emissivity coefficient for O VII as a function of collision speed.

### Total Emission Spectra

The emission from a plasma can be simulated by superimposing the emissivities from every observable transition of the present ions. The emission is a function of electron temperature and density, the charge exchange collision speed, and the abundances of the ions.

### Distinguishable Differences Between Models

There are two distinguishable differences between the models that will be resolved by sufficiently advanced detectors. The first difference is the presence or absence of a bremsstrahlung continuum. Although the bremsstrahlung emission from collisions between energetic free electrons and highly charged ions such as O<sup>6+</sup> is low compared to the accompanying line emission, the composite emission from the cometary plasma may include a significant free-free continuum contribution from ionised hydrogen (the most abundant ion in the solar wind) and hydrogen-like species created by ionisation of cometary neutrals. Charge exchange driven emission will feature no significant continuum emission.

The second feature is the ratio of the  $1s2s\ ^3S \rightarrow 1s^2\ ^1S$  and  $1s2p\ ^1P \rightarrow 1s^2\ ^1S$  emission lines from He-like ions. Electron collisions result in a lower fraction of ions being excited into triplet states than singlet states due to the nature of the collision strengths, as demonstrated by figures 4.4 and 4.6. As a result, the dipole transition is the strongest. Charge exchange collisions on the other hand will populate the singlet and triplet systems almost statistically. A large proportion of the triplet ions will radiatively cascade to  $1s2s\ ^3S$  (or  $1s2p\ ^3P$ , from which there is a two-photon continuum rather than an emission line) from which they will radiate to the ground state. As a result, the spin-forbidden transition is the strongest.

The spectral resolution of the *ACIS* device on *Chandra* is not sufficient to resolve either the presence of a continuum or the emission lines from the  $1s2l \rightarrow 1s^2$  emission feature in He-like ions. The *Suzaku*'s *XRS* may have been able to distinguish between the models from both of the above features (see an example of the resolving power in figure 2.19). Unfortunately, the device is inoperable. *Constellation-X* will be capable of distinguishing continuum and line emission, and will be able to measure accurate line ratios (an example of the resolving power is shown in figure 3.77).

# Chapter 5

## Fitting

Data from the *Chandra* catalogue presented in chapter 3 are used to evaluate several non-physical and physical x-ray emission models. The non-physical models are used to establish the basic form of the emission spectrum, and the charge exchange and energetic electron models developed in chapter 4 are compared to the data to test the plausibility of the model, and to gain an understanding of the conditions of the emitting plasma if the model accurately represents the conditions of the cometary atmosphere. In order to compare the results of a model to the observed data, a theoretical emission spectrum must be convolved with the instrument response as described in section 5.1. The parameter values are systematically and iteratively altered to obtain the closest fit to the data. The fitting algorithm is detailed in section 5.2.

It is important, whenever possible, to represent the background signal in the observed data. The samples selected to represent the background are shown in section 5.3, and the source data are specified in section 5.4. The models and the best fits to the data are presented in section 5.5. In section 5.6, the results are summarised, compared and discussed.

### 5.1 Convolution of Theoretical Spectra

As mentioned in section 3.2, in order to compare a theoretical model,  $M(E)$  (in units of photons  $\text{cm}^{-2} \text{s}^{-1}$ ), to the observed binned data,  $C(I)$ , the model spectrum must be convolved with the appropriate instrument response. In the case of non-grating data from the *Chandra* ACIS array, the response function has two components: the effective area  $A(E)$  and the normalised redistribution matrix  $R(I, E)$ . The effective area reflects the quantum efficiency of the detector, that is, the amount of radiation that is not absorbed by the detector window. The redistribution matrix shows the probability of the detection of a photon with energy  $E$  resulting in a signal being detected in bin  $I$ , and is normalised such that

$$\sum_i R(I, E) = 1 \quad (5.1)$$

In addition to being functions of photon energy, these quantities also vary with each pixel on the CCD array. This means that they are functions of the morphology of the emission, and that a weighted effective area and a weighted redistribution matrix must be calculated for each observation.

From these functions, the convolved model,  $S$ , is constructed such that

$$S(I) = R(I, E)A(E)M(E) \quad (5.2)$$

This spectrum can be directly compared to the observed data.

### 5.1.1 Verification of Convolution Process

One of the most common tools employed in the analysis of astrophysical x-rays is XSPEC, which incorporates a large number of emission models of varying complexity. Models are convolved with response functions, and are fitted to data. XSPEC is not used in this analysis. The reasons for this are:

- An independent source of atomic data (ADAS) is used,
- The models used (charge exchange and non-thermal plasma) are not part of XSPEC.

As a result, the convolution process used here must be verified before it may be deemed credible. To test the convolution process, compare the response generated by a simple delta function. Figure 5.1 shows the spectrum generated by folding a delta function centred at 571 eV with 1 eV through an *ACIS* response file using XSPEC and the software developed and used here.

The favourable comparison is sufficient to demonstrate the equivalence in the approach used here to that of *XSPEC* in regard to convolution of theoretical models.

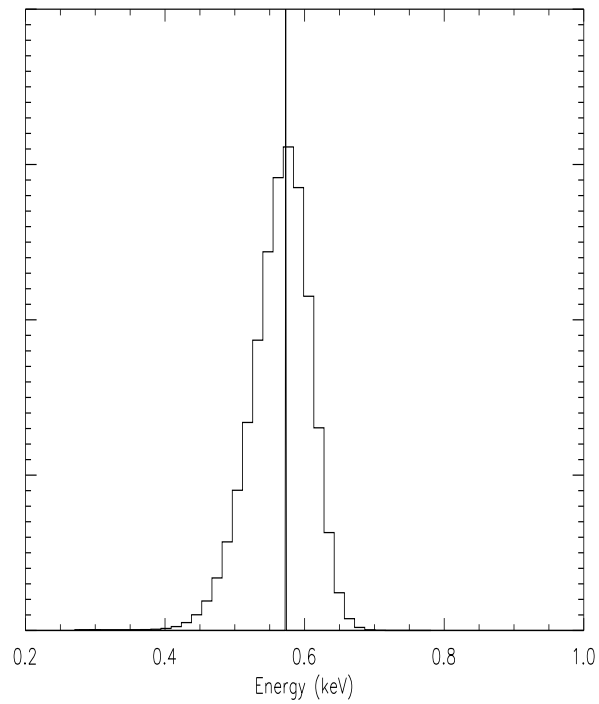
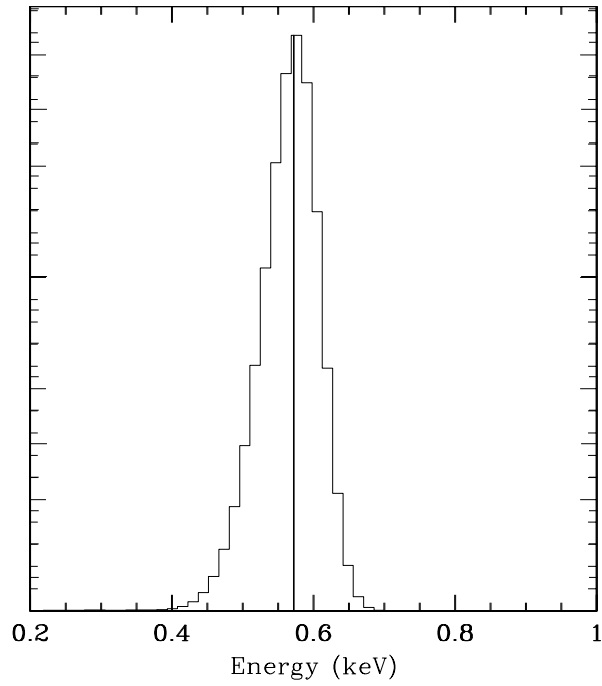


Figure 5.1: Convolution of an x-ray line with energy  $E = 0.571$  keV by XSPEC (top) and by the independent convolution routine used here (bottom). The units of the y-axis are arbitrary as both folded and unfolded models are being compared in the same view.

## 5.2 Fitting Algorithm

A modification of the Levenberg-Marquardt algorithm (Levenberg, 1944; Marquardt, 1963) is used to advance parameters of non-linear models to their least squares values when compared to the *Chandra* emission spectra.

The data are a set of  $N$  points,  $y_n$ , with uncertainties  $\Delta y_n$ . From the uncertainties, each point is assigned a weight  $w_n$  such that

$$w_n = \frac{1}{\Delta y_n^2} \quad (5.3)$$

The model has a set of free parameters  $\mathbf{p}$ , and is convolved to give the points  $f_n$ , which can be directly compared to  $y_n$ . In turn, each of the parameters  $p_i$  is adjusted by  $\delta p_i$  to give the set of points  $f'_n$ . From these, the partial derivatives

$$\frac{\partial f_n}{\partial p_i} = \frac{f'_n - f_n}{\delta p_i} \quad (5.4)$$

are found, and the matrix  $M$  and the vector  $\mathbf{b}$  can be constructed as

$$M_{ij} = \sum_{n=1}^N \frac{\partial f_n}{\partial p_i} \frac{\partial f_n}{\partial p_j} w_n \quad (5.5)$$

$$b_i = - \sum_{n=1}^N \frac{\partial f_n}{\partial p_i} (f_n - y_n) w_n \quad (5.6)$$

The linear change in parameter space,  $\Delta \mathbf{p}$ , to advance  $f_n$  to  $y_n$  is then

$$\Delta \mathbf{p} = M^{-1} \mathbf{b}. \quad (5.7)$$

This is the form of the Gauss-Newton algorithm. In the Levenberg-Marquardt algorithm, the matrix  $M$  is replaced by a damped matrix,  $M + I\lambda$ . The value of the damping parameter  $\lambda$  can be adjusted with each iteration, with  $\lambda$  decreasing (but always remaining positive) as the solution tends toward the least squares solution.

The quality of the fit is assessed by evaluating

$$\chi^2 = \sum_{n=1}^N w_n (f_n - y_n)^2 / (N - P) \quad (5.8)$$

where  $P$  is the number of variable parameters in the model (i.e.  $N - P$  is the number of degrees of freedom).

This process, from evaluating the Jacobian to assessing the fit parameter  $\chi^2$ , is repeated until the difference between successive values of  $\chi^2$  is less than a set tolerance value. Each successive value of  $\chi^2$  will be lower than the previous.

When the minimum  $\chi^2$  has been found, the covariance matrix  $C$  can be defined as

$$C = M^{-1} \quad (5.9)$$

From this, the normalised covariance matrix

$$C_{ij}^N = \begin{cases} \frac{C_{ij}}{\sqrt{C_{ii}C_{jj}}}, & i \neq j \\ \sqrt{C_{ij}}, & i = j \end{cases} \quad (5.10)$$

is a more useful quantity. The diagonal elements of  $C^N$  are the errors in the parameters  $\mathbf{p}$ , and the off-diagonal elements are the correlations between free parameters.

### 5.3 Background Signals

In previous studies of cometary x-rays (e.g. Krasnopolsky *et al*, 2002; Lisse *et al*, 2005), a background has been subtracted from the source data. A different approach is taken here: the background signal is modelled, and the unfolded model is added to any emission model before it is convolved with the instrument response. This increases the accuracy of the background treatment by removing the assumption that the instrument response is uniform.

An estimate to the background signal is obtained by one of two methods. The more preferable is to use the data sampled by the *ACIS-S1* CCD. The advantages of this background signal are that the *S1* and *S3* CCDs are almost identical and operate in a similar manner, the projected solid angles of the chips are close enough to assume that the cosmic backgrounds are similar, and far enough apart to significantly reduce the cometary flux incident on *S1* in some cases.

If *S1* is not activated (as was the case for the observation of comet 2P/Encke), a background may be extracted from the *S3* chip. This can be achieved by assigning a circular source region centred on the comet, and an annular background region around the source. A major disadvantage of this approach is that care must be taken to avoid removing a significant fraction of source detections.

If neither of these methods are available or reliable, then no treatment of the background is made. It is noted, however, that a blank-sky dataset could be used. This approach assumes that the cosmic background signal is uniform or almost uniform, and the blank-sky dataset must be manipulated to match the source observation. As the level 1 event files for these observations are not available, the blank-sky data can't be processed using the same calibration (that is, the most up-to-date version) as the comet observations. Since the blank-sky data are essentially arbitrary, the background emission from any of the cometary observations is as valid a sample as that from the

blank-sky datasets. The variation of the backgrounds presented in this section demonstrate that using a “typical” background sample is not appropriate.

A further possibility, although it has not been explored to date, is to sample the projected position of the comet a short time before the planned exposure. This will provide a clean instance of the local background being sampled by the central region on the *S3* CCD: the region that is used to observe the predicted brightest part of the emission.

Fits to the background signals are obtained using a simple line emission model, where the position and intensity of the lines are arbitrary. Analysis of the line energies is not relevant, as the source of the background is not discussed here.

### 5.3.1 Comet C/1999 S4 (LINEAR)

The background signal for comet C/1999 S4 (LINEAR) is taken from the *ACIS-S1* CCD.

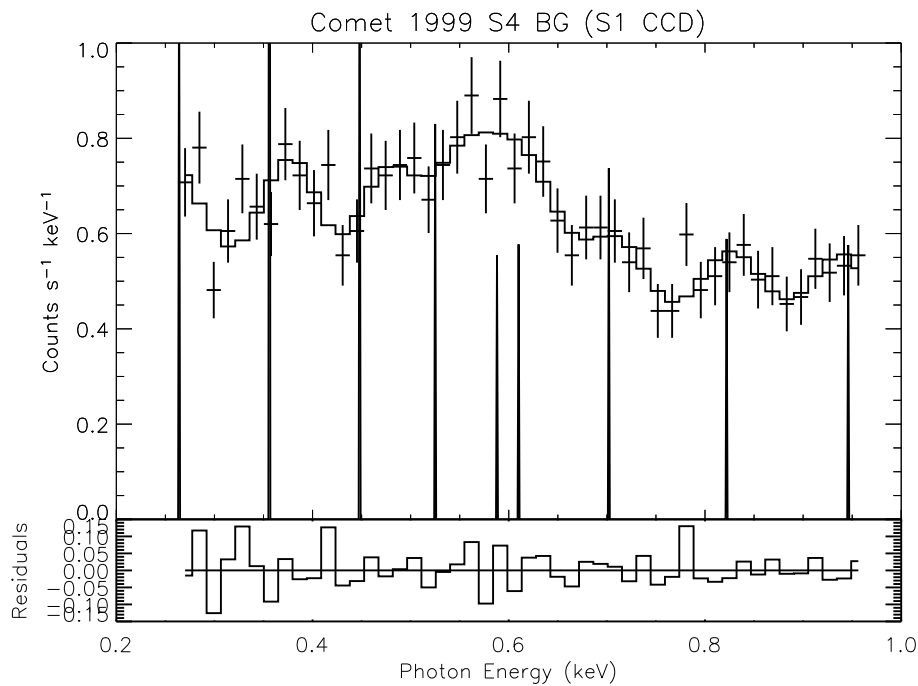


Figure 5.2: The background signal for the first observation of comet C/1999 S4 (LINEAR). The data are taken from the *ACIS-S1* exposure.

### 5.3.2 Comet C/1999 T1 (McNaught-Hartley) (January 8)

The background signal for the January 8 observation of comet C/1999 T1 (McNaught-Hartley) is taken from the *ACIS-S1* CCD.

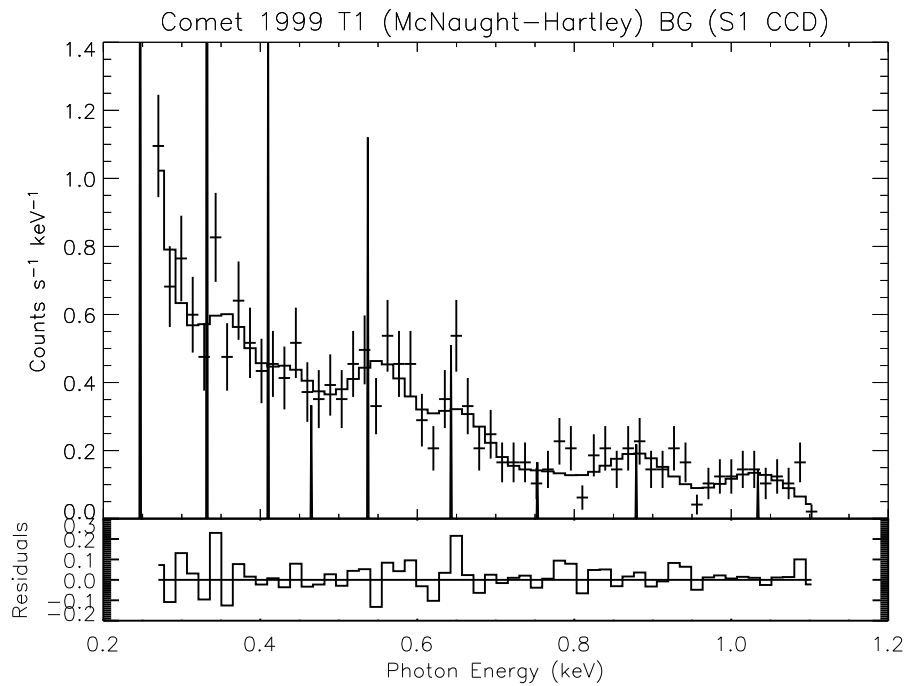


Figure 5.3: The background signal for the January 8 observation of comet C/1999 T1 (McNaught-Hartley). The data are taken from the *ACIS-S1* exposure.

### 5.3.3 Comet C/2002 C1 (Ikeya-Zhang)

As the cometary x-ray atmosphere extended over the full area of the CCD array, it is not possible to extract a background signal from the observation. However, as the detected x-ray flux is much larger than the blank-sky background and all of the other backgrounds presented here, the signal to background ratio is high. In the modelling performed here, no compensation is made for the x-ray background.

### 5.3.4 Comet 2P/Encke

Since the *ACIS-S1* CCD was not activated for the observation of comet 2P/Encke, the preferred source of a contemporary background signal is not available. Instead, a background is extracted from the *ACIS-S3* CCD.

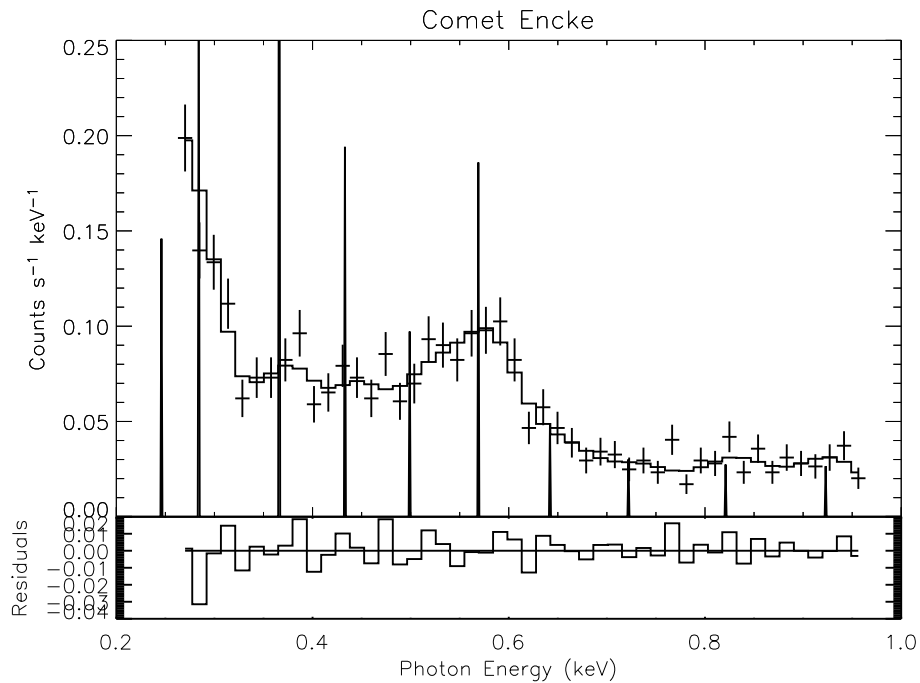


Figure 5.4: The background signal for comet 2P/Encke. The data are from an annular region around the brightness peak of the emission on the *ACIS-S3* CCD.

### 5.3.5 Comet C/2001 Q4 (NEAT)

The signal of comet C/2001 Q4 (NEAT) on the *ACIS-S1* CCD is similar in form to the *S3* signal. This suggests that the majority of the x-ray counts on *S1* are from the comet. As a result, it is not possible to extract a reliable background sample from the observation.

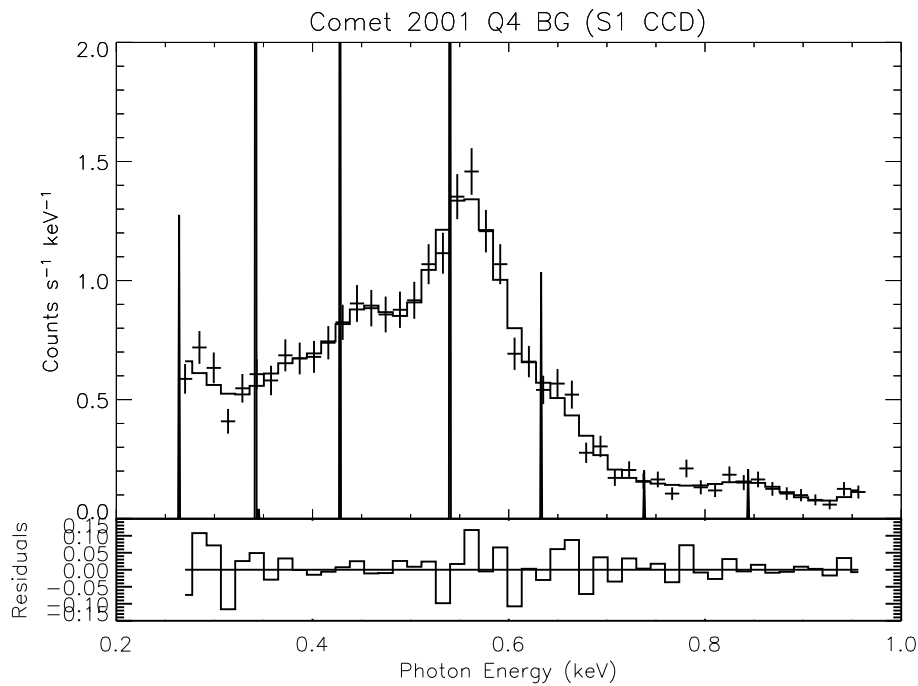


Figure 5.5: The background signal for comet C/2001 Q4 (NEAT). The data are from the *ACIS-S1* CCD.

### 5.3.6 Comet 9P/Tempel 1 (July 8)

The *ACIS-S1* data provide the background for the July 8 observation of comet 9P/Tempel 1. The background has a structure similar to the *ACIS-S3* signal, and so the background signal may contain a significant flux from the comet. As a result, the fits are applied to the data with this background signal and with no background treatment.

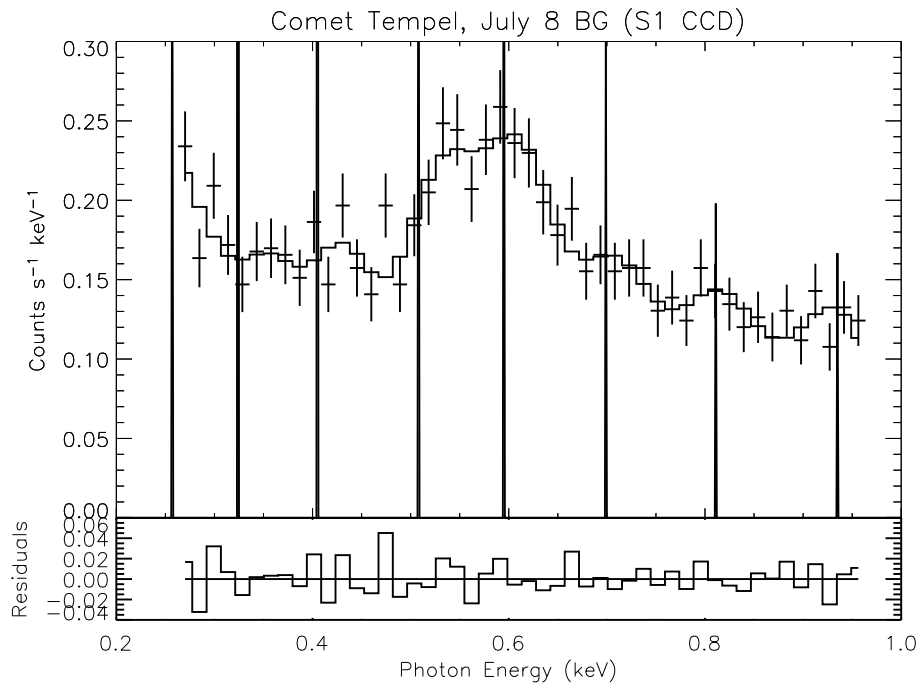


Figure 5.6: The background signal for comet 9P/Tempel 1. The data are from an annular region on the *ACIS-S3* CCD.

### 5.3.7 Comet 73P/Schwassmann-Wachmann 3B

The background signal for comet 73P/Schwassmann-Wachmann 3B is taken from the *ACIS-S1* CCD. As with the observation of comet 9P/Tempel 1, the background signal shown here is similar to the source spectrum. As a result, the data are fitted with and without this background flux included in the model.

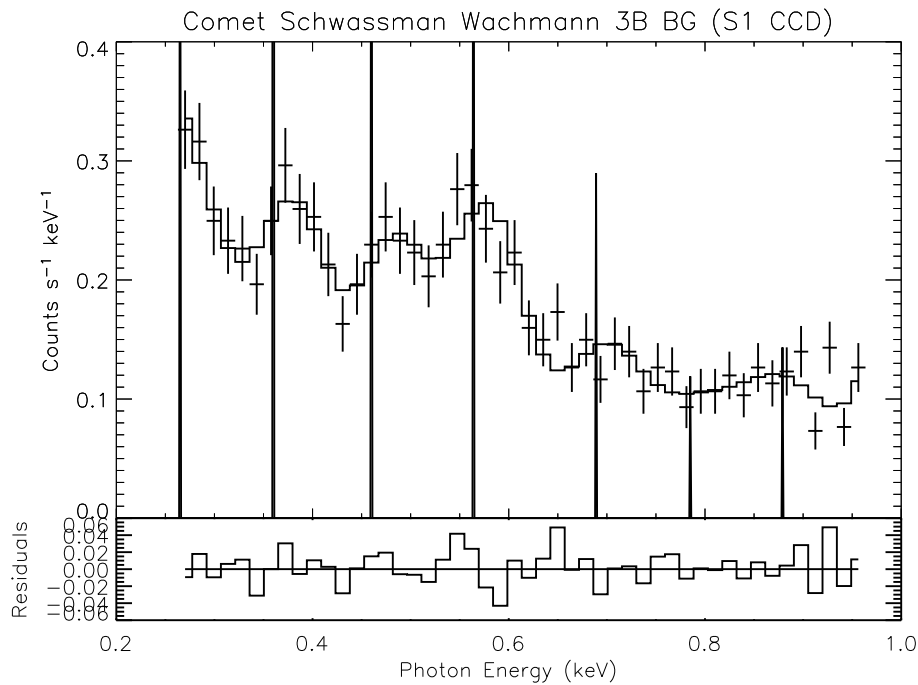


Figure 5.7: The background signal for comet 73/Schwassmann-Wachmann 3B. The data are from the *ACIS-S1* CCD.

## 5.4 Source Data

The source and background data are summarised in table 5.1.

Comet	Source Spectrum	BG Spectrum
1999 S4	Entire <i>ACIS-S3</i>	Entire <i>ACIS-S1</i>
1999 T1 (Jan 8)	Entire <i>ACIS-S3</i>	Entire <i>ACIS-S1</i>
2002 C1 (Both Exp)	Entire <i>ACIS-S1, S2, S3, S4</i>	None
Encke	Region on <i>ACIS-S3</i>	Region on <i>ACIS-S3</i>
2001 Q4	Entire <i>ACIS-S3</i>	None
Tempel (Jul 8)	Entire <i>ACIS-S3</i>	Entire <i>ACIS-S1</i> , None
SW 3B	Entire <i>ACIS-S3</i>	Entire <i>ACIS-S1</i> , None

Table 5.1: Data sources for modelling

For comets C/1999 S4 (LINEAR), C/1999 T1 (McNaught-Hartley), C/2001 Q4 (NEAT), 9P/Tempel 1 and 73P/Schwassmann-Wachmann 3B, data collected by the entire *ACIS-S3* CCD are used as a source, with the background being taken from the *ACIS-S1* CCD. For comet C/2002 C1 (Ikeya-Zhang), the data from *ACIS-S1*, *S2*, *S3* and *S4* are modelled separately. Also, each exposure is modelled independently.

For comet 2P/Encke, the source is taken from a circular region on the *ACIS-S3* CCD. The area projected by these regions at the position of the comets are  $6.36 \times 10^8$  km<sup>2</sup> (318 pixels in radius) and  $6.76 \times 10^9$  km<sup>2</sup> (329 pixels in radius) respectively. The regions are centred at the brightest point of the x-ray emission. The background signals are taken from annular regions immediately surrounding the sources, with equal areas.

For comets C/1999 T1 (McNaught-Hartley) and 9P/Tempel 1, only 1 of the observing periods is modelled. In each case, the brightest exposure is used. For comet C/2002 C1 (Ikeya-Zhang), data from both observing periods are treated as separate observations in this analysis.

## 5.5 Fitting *Chandra* Data

In this section results of several emission models are presented, with non-physical models appearing first. These models are: arbitrary line emission (section 5.5.1, arbitrary bremsstrahlung (section 5.5.2 and a combination of arbitrary line emission and bremsstrahlung (section 5.5.3). Results from physical models are then presented: charge exchange emission (section 5.5.4) and energetic electrons (section 5.5.5).

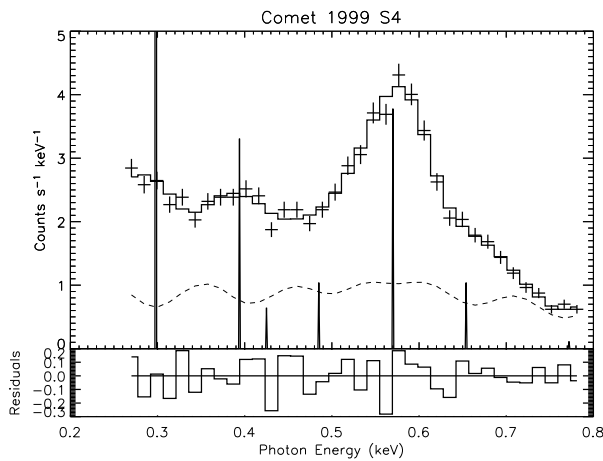
The stated errors are from the normalised covariance matrix  $C^N$  (equation 5.10).

### 5.5.1 Arbitrary Line Emission

This is the most simple modelling approach. A number of emission lines of arbitrary position and magnitude are used to fit the data. Some previous studies have also incorporated lines of varying width. The ions in the cometary atmosphere are too cold to exhibit detectable Doppler broadening, and even if this were the case, the associated temperature would presumably be constant for all ions. Therefore, the alteration of line widths is inappropriate.

Although this model is unphysical, the energy of the required lines gives an indication of which ions are present. Furthermore, this model will reveal the energy ranges that are impossible to model. Results from the model are presented in figures 5.8 to 5.23.

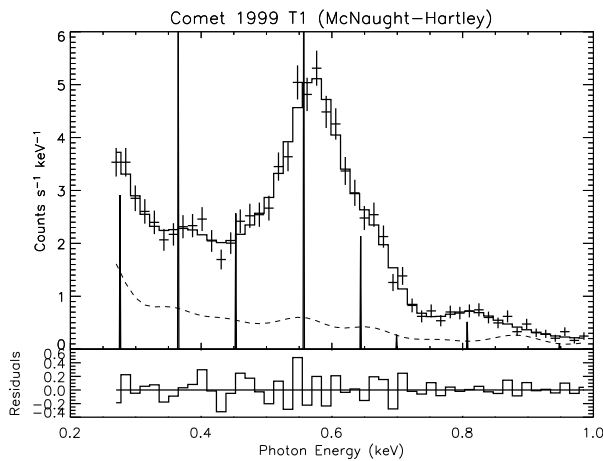
### Comet C/1999 S4 (LINEAR)



Energy (eV)	Magnitude (Arb. Units)
298 ± 2	10.7 ± 2.6
394 ± 16	0.827 ± 0.727
425 ± 98	0.161 ± 0.752
485 ± 16	0.260 ± 0.108
570 ± 2	0.945 ± 0.042
654 ± 5	0.260 ± 0.022
772 ± 36	0.0284 ± 0.0095
$\chi^2$	1.39

Figure 5.8: 8 line fit of comet C/1999 S4 (LINEAR). The dashed line is the convolution of the background model

### Comet C/1999 T1 (McNaught-Hartley) (January 8)



Energy (eV)	Magnitude (Arb. Units)
277 ± 7	0.728 ± 0.075
366 ± 10	1.52 ± 0.23
454 ± 13	0.641 ± 0.108
558 ± 5	1.96 ± 0.14
645 ± 21	0.534 ± 0.148
699 ± 96	0.0687 ± 0.216
808 ± 10	0.129 ± 0.021
948 ± 19	0.0270 ± 0.00679
$\chi^2$	0.920

Figure 5.9: 8 line fit of comet C/1999 T1 McNaught-Hartley). The dashed line is the convolution of the background model

## Comet C/2002 C1 (Ikeya-Zhang) - First Observation

The data from the observation of comet C/2002 C1 (Ikeya-Zhang) are partitioned according to observing period (commencing at 01:33:49 and 22:53:32 on April 15th 2002) and CCD array (the *S1*, *S2*, *S3* and *S4* chips).

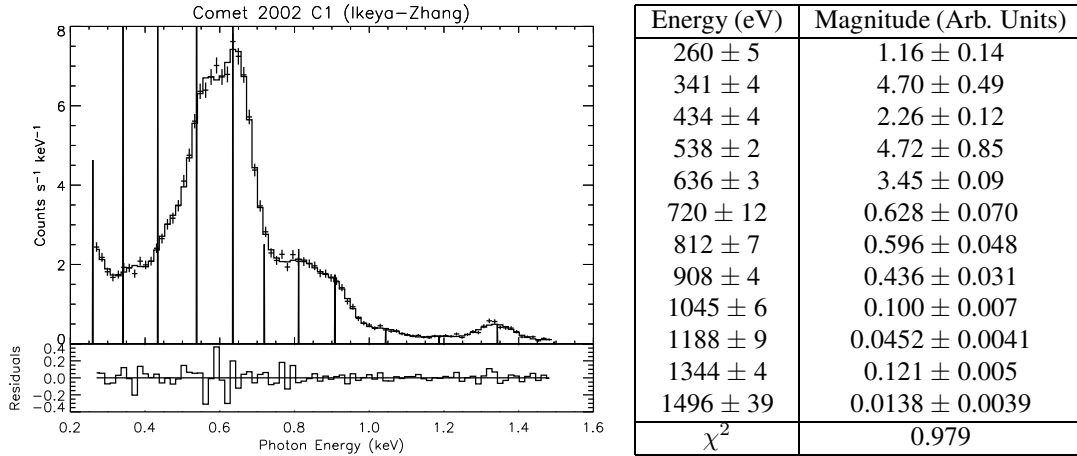


Figure 5.10: 12 line fit of comet C/2002 C1 (Ikeya-Zhang) (*ACIS-S1*) (first observation) on the *ACIS-S1* chip.

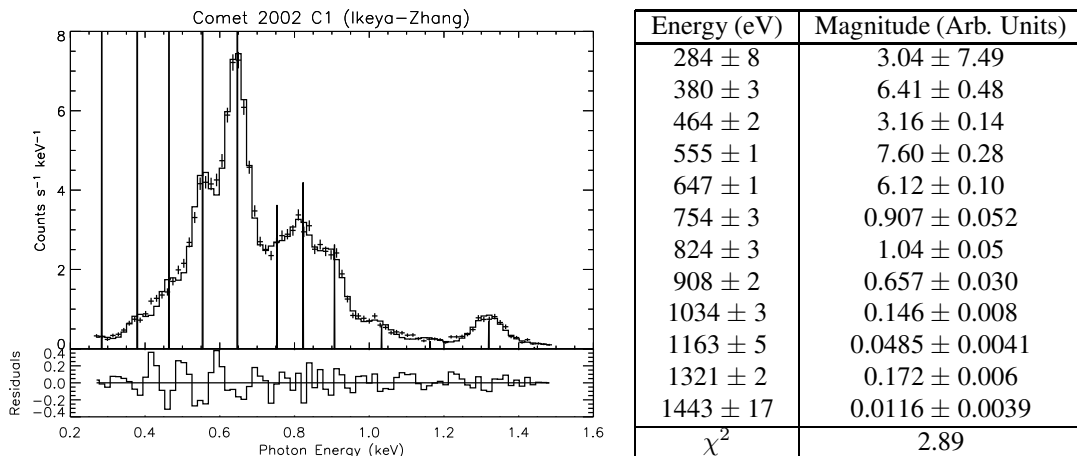
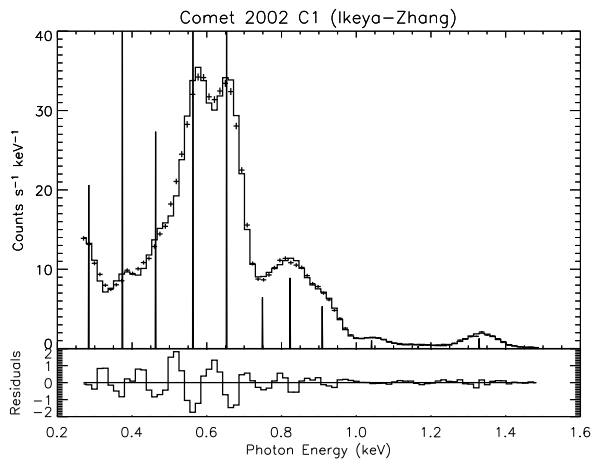
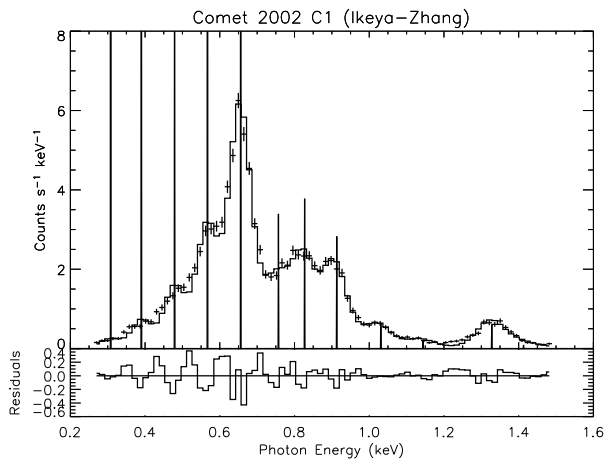


Figure 5.11: 12 line fit of comet C/2002 C1 (Ikeya-Zhang) (*ACIS-S2*) (first observation) on the *ACIS-S2* chip.



Energy (eV)	Magnitude (Arb. Units)
285 ± 1	5.16 ± 2.05
374 ± 1	11.5 ± 0.2
463 ± 1	6.84 ± 0.10
563 ± 1	14.7 ± 0.1
653 ± 1	10.9 ± 0.1
749 ± 3	1.62 ± 0.06
824 ± 2	2.23 ± 0.06
910 ± 1	1.33 ± 0.04
1041 ± 2	0.259 ± 0.008
1166 ± 4	0.0870 ± 0.0044
1329 ± 1	0.321 ± 0.007
1440 ± 12	0.0205 ± 0.0034
$\chi^2$	5.25

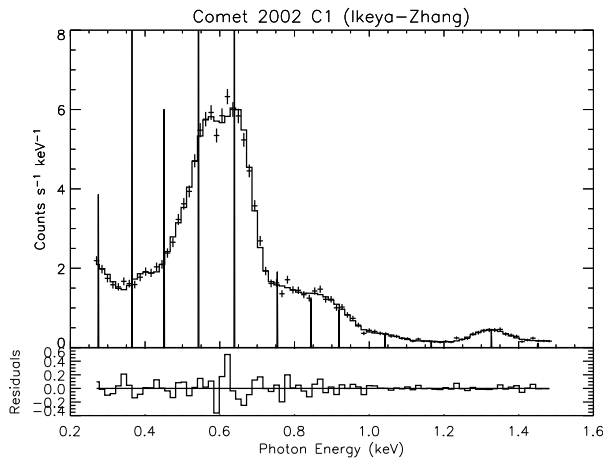
Figure 5.12: 12 line fit of comet C/2002 C1 (Ikeya-Zhang) (ACIS-S3) (first observation) on the ACIS-S3 chip.



Energy (eV)	Magnitude (Arb. Units)
309 ± 4	45.9 ± 29.6
390 ± 2	5.21 ± 0.37
480 ± 2	2.95 ± 0.11
568 ± 1	7.23 ± 0.40
656 ± 1	5.78 ± 0.11
757 ± 3	0.849 ± 0.047
828 ± 3	0.9444 ± 0.043
913 ± 2	0.707 ± 0.026
1032 ± 3	0.156 ± 0.009
1145 ± 5	0.0502 ± 0.0046
1329 ± 3	0.152 ± 0.008
1413 ± 11	0.0231 ± 0.0057
$\chi^2$	3.23

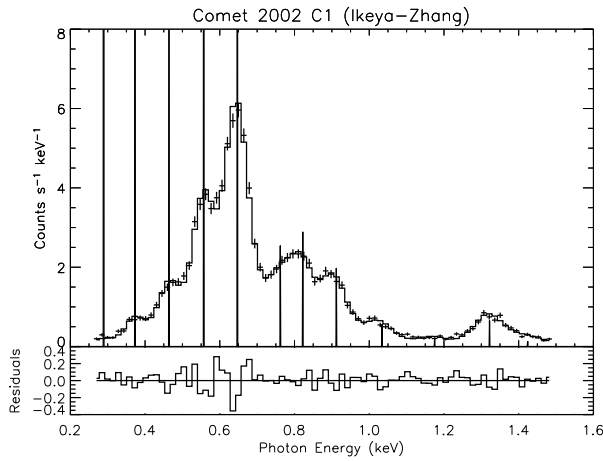
Figure 5.13: 12 line fit of comet C/2002 C1 (Ikeya-Zhang) (ACIS-S4) (first observation) on the ACIS-S4 chip.

## Comet C/2002 C1 (Ikeya-Zhang) - Second Observation



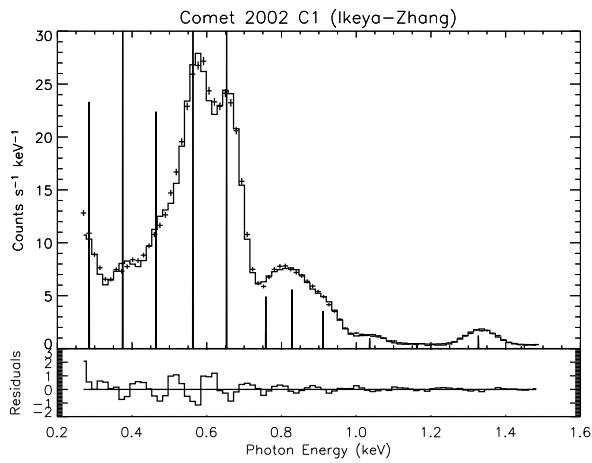
Energy (eV)	Magnitude (Arb. Units)
275 ± 3	0.965 ± 0.056
365 ± 4	3.16 ± 0.18
452 ± 6	1.50 ± 0.12
544 ± 3	4.09 ± 0.42
639 ± 2	2.84 ± 0.07
754 ± 8	0.478 ± 0.037
844 ± 17	0.307 ± 0.042
920 ± 11	0.239 ± 0.061
1043 ± 9	0.0860 ± 0.0090
1167 ± 12	0.0361 ± 0.0052
1328 ± 4	0.110 ± 0.006
1453 ± 14	0.0286 ± 0.0037
$\chi^2$	1.22

Figure 5.14: 12 line fit of comet C/2002 C1 (Ikeya-Zhang) (ACIS-S1) (second observation) on the ACIS-S1 chip.



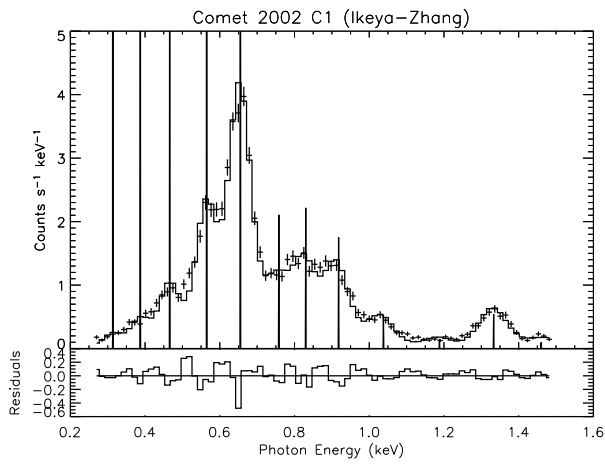
Energy (eV)	Magnitude (Arb. Units)
290 ± 9	53.4 ± 39.5
373 ± 2	7.74 ± 0.47
465 ± 2	3.10 ± 0.13
557 ± 1	7.24 ± 0.34
648 ± 1	5.04 ± 0.10
763 ± 5	0.636 ± 0.068
823 ± 4	0.723 ± 0.068
912 ± 2	0.495 ± 0.022
1035 ± 3	0.140 ± 0.008
1175 ± 5	0.0454 ± 0.0039
1322 ± 2	0.164 ± 0.007
1424 ± 8	0.0340 ± 0.0047
$\chi^2$	1.66

Figure 5.15: 12 line fit of comet C/2002 C1 (Ikeya-Zhang) (ACIS-S2) (second observation) on the ACIS-S2 chip.



Energy (eV)	Magnitude (Arb. Units)
285 ± 3	5.83 ± 9.23
375 ± 1	9.81 ± 0.21
464 ± 1	5.60 ± 0.10
564 ± 1	11.8 ± 0.1
654 ± 1	7.75 ± 0.07
759 ± 3	1.23 ± 0.06
828 ± 3	1.40 ± 0.06
912 ± 2	0.890 ± 0.032
1036 ± 2	0.242 ± 0.008
1164 ± 4	0.0777 ± 0.0041
1327 ± 1	0.305 ± 0.007
1443 ± 6	0.0494 ± 0.0037
$\chi^2$	5.05

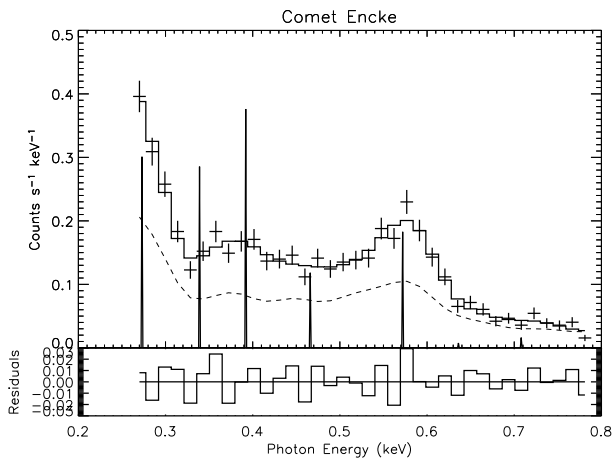
Figure 5.16: 12 line fit of comet C/2002 C1 (Ikeya-Zhang) (*ACIS-S3*) (second observation) on the *ACIS-S3* chip.



Energy (eV)	Magnitude (Arb. Units)
315 ± 4	21.7 ± 6.5
388 ± 4	3.59 ± 0.41
466 ± 2	2.30 ± 0.12
566 ± 1	5.91 ± 0.33
656 ± 1	3.94 ± 0.08
759 ± 4	0.527 ± 0.035
831 ± 3	0.554 ± 0.032
919 ± 2	0.439 ± 0.018
1038 ± 3	0.132 ± 0.007
1189 ± 5	0.0367 ± 0.0033
1333 ± 2	0.136 ± 0.005
1460 ± 9	0.0243 ± 0.0028
$\chi^2$	2.96

Figure 5.17: 12 line fit of comet C/2002 C1 (Ikeya-Zhang) (*ACIS-S4*) (second observation) on the *ACIS-S4* chip.

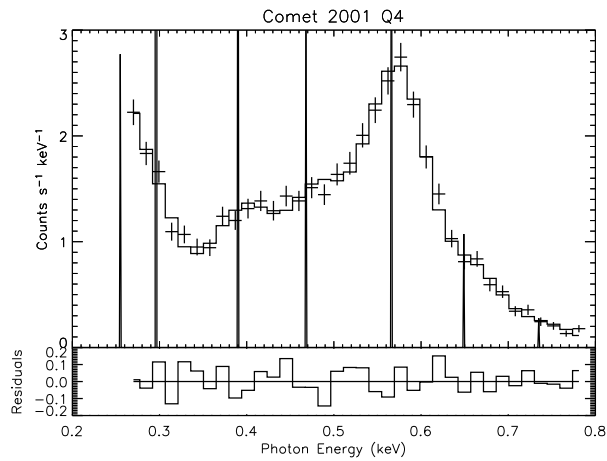
## Comet 2P/Encke



Energy (eV)	Magnitude (Arb. Units)
274 ± 8	0.0784 ± 0.0151
340 ± 54	0.0762 ± 0.0818
393 ± 19	0.0913 ± 0.0591
467 ± 15	0.0297 ± 0.0100
573 ± 9	0.0458 ± 0.0064
637 ± 182	0.00173 ± 0.00555
710 ± 280	0.00411 ± 0.00329
$\chi^2$	1.42

Figure 5.18: 7 line fit of comet 2P/Encke. The dashed line is the convolution of the background model

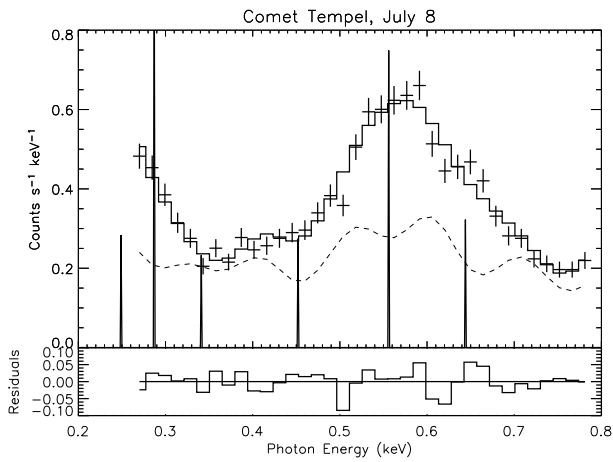
## Comet C/2001 Q4 (NEAT)



Energy (eV)	Magnitude (Arb. Units)
255 ± 32	0.693 ± 0.518
296 ± 9	68.4 ± 100.1
391 ± 4	1.64 ± 0.11
468 ± 4	0.858 ± 0.056
567 ± 2	1.41 ± 0.05
649 ± 5	0.268 ± 0.022
735 ± 8	0.0692 ± 0.0113
$\chi^2$	1.31

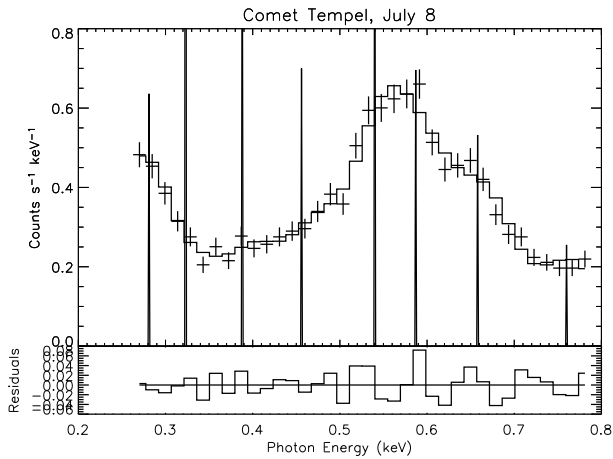
Figure 5.19: 7 line fit of comet C/2001 Q4 (NEAT).

## Comet 9P/Tempel 1



Energy (eV)	Magnitude (Arb. Units)
$250 \pm 234$	$0.0709 \pm 0.4378$
$287 \pm 409$	$0.266 \pm 93.893$
$342 \pm 86$	$0.0582 \pm 0.27647$
$452 \pm 10$	$0.0686 \pm 0.01112$
$556 \pm 4$	$0.187 \pm 0.013$
$644 \pm 5$	$0.0806 \pm 0.0080$
$801 \pm 45$	$0.0201 \pm 0.0154$
$\chi^2$	1.90

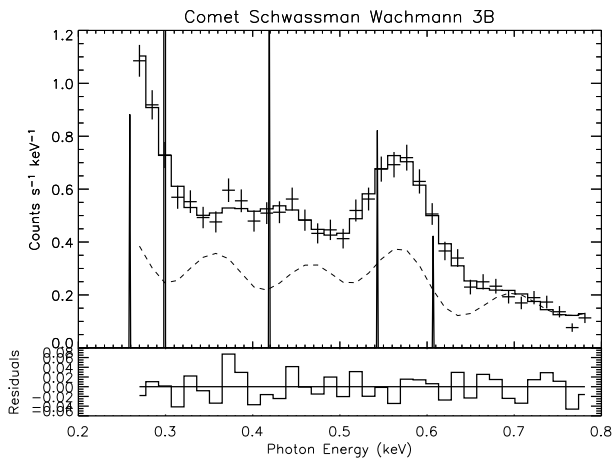
Figure 5.20: 7 line fit of comet 9P/Tempel 1. The dashed line is the convolution of the background model.



Energy (eV)	Magnitude (Arb. Units)
$281 \pm 9$	$0.159 \pm 0.029$
$323 \pm 20$	$0.829 \pm 0.895$
$388 \pm 11$	$0.300 \pm 0.069$
$456 \pm 9$	$0.175 \pm 0.022$
$540 \pm 11$	$0.363 \pm 0.172$
$587 \pm 15$	$0.174 \pm 0.075$
$658 \pm 5$	$0.133 \pm 0.016$
$760 \pm 6$	$0.0638 \pm 0.0037$
$\chi^2$	1.58

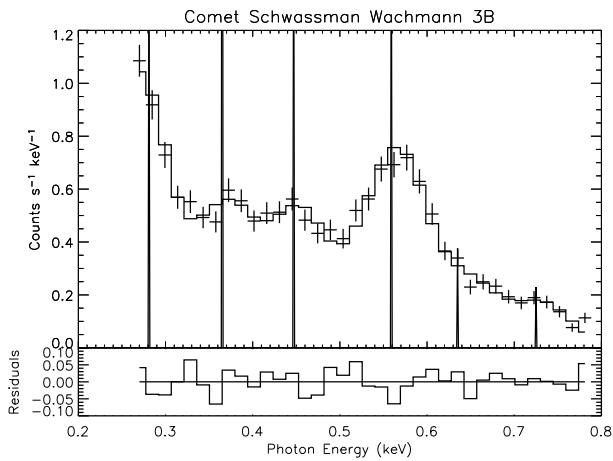
Figure 5.21: 8 line fit of comet 9P/Tempel 1 with no background treatment.

## Comet 73P/Schwassmann-Wachmann 3B



Energy (eV)	Magnitude (Arb. Units)
$259 \pm 31$	$0.221 \pm 0.134$
$299 \pm 8$	$16.6 \pm 17.6$
$419 \pm 4$	$0.388 \pm 0.031$
$543 \pm 7$	$0.206 \pm 0.047$
$607 \pm 6$	$0.106 \pm 0.020$
$\chi^2$	1.02

Figure 5.22: 5 line fit of comet 73P/Schwassmann-Wachmann 3B. The dashed line is the convolution of the background model.



Energy (eV)	Magnitude (Arb. Units)
$281 \pm 3$	$0.405 \pm 0.025$
$366 \pm 4$	$1.11 \pm 0.09$
$447 \pm 3$	$0.453 \pm 0.029$
$560 \pm 2$	$0.437 \pm 0.019$
$637 \pm 7$	$0.0921 \pm 0.0097$
$726 \pm 5$	$0.0569 \pm 0.0062$
$\chi^2$	1.36

Figure 5.23: 6 line fit of comet 73P/Schwassmann-Wachmann 3B with no background treatment.

## Comments on the Arbitrary Line Model

This simple model can provide an indication of which ions are responsible for the observed line emission, although some of the features that are employed in fitting the spectra may correspond to a combination of emission lines. The data are over-fitted in two cases (figures 5.8 and 5.10). The  $\chi^2$  values for fits to comet C/2002 C1 (Ikeya-Zhang) are high (up to 5.25). The high number of counts results in a low statistical error. Errors from the instrument calibration are not included.

There are some emission features that are common to all features. A list of transitions and energies is given in table 4.4. The most prominent of these is in the emission range 538–587 eV, corresponding to three  $O^{6+}$  transitions from  $n = 2 \rightarrow n = 1$  (561, 568 and 571 eV). From the spread in energy of the emission lines, it is not possible to specify which of the three transitions is most likely. Another common feature in all fits other than 73/P Schwassmann-Wachmann 3B (figure 5.23) is a line in the energy range 636–658 eV, explained by emission from  $O^{7+}$  ( $2 \rightarrow 1$ ) (654 eV). In all of the back illuminated fits, a line in the range 250–298 eV is present. This could correspond to neutral carbon fluorescence at 277 eV,  $Mg^{9+}$  (263, 282 eV), or  $Si^{10+}$  (282, 284 eV).

The feature in the range 340–394 eV, may be from neutral nitrogen fluorescence at 392 eV,  $C^{5+}$  (368 eV), or  $Ar^{10+}$  (362, 363, 360 eV). The feature at 433–473 eV does not correspond to any strong transitions in table 4.4 or to any neutral fluorescence transitions.

Comets C/1999 T1 (McNaught-Hartley) (figure 5.9) and C/2002 C1 (Ikeya-Zhang) (figures 5.10 to 5.17) require a line at 808–844 eV, for which  $Fe^{16+}$  (826 eV) is the only strong electron collision excited line. In this region there are also charge exchange driven lines from  $O^{7+}$  (817 and 837 eV).

Comet C/2002 C1 (Ikeya-Zhang) has a unique feature in the energy range 1325–1347 eV, close to lines from  $Mg^{10+}$  (1344 and 1351 eV). The change in the strength of this emission on each chip (S3 requiring a larger flux, and the flux on other chips reducing with distance from the brightness centre) indicates that the emission at this energy is from the comet rather than the background.

## 5.5.2 Arbitrary Bremsstrahlung Emission

The arbitrary bremsstrahlung model is described in section 4.2.5. The data are fitted with a hydrogenic continuum (effective charge of 1), with free parameters of the electron temperature  $T_e$  and a multiplicative constant  $M$ .

A fit to the observation of comet C/1999 S4 (LINEAR) is shown in figure 5.24.

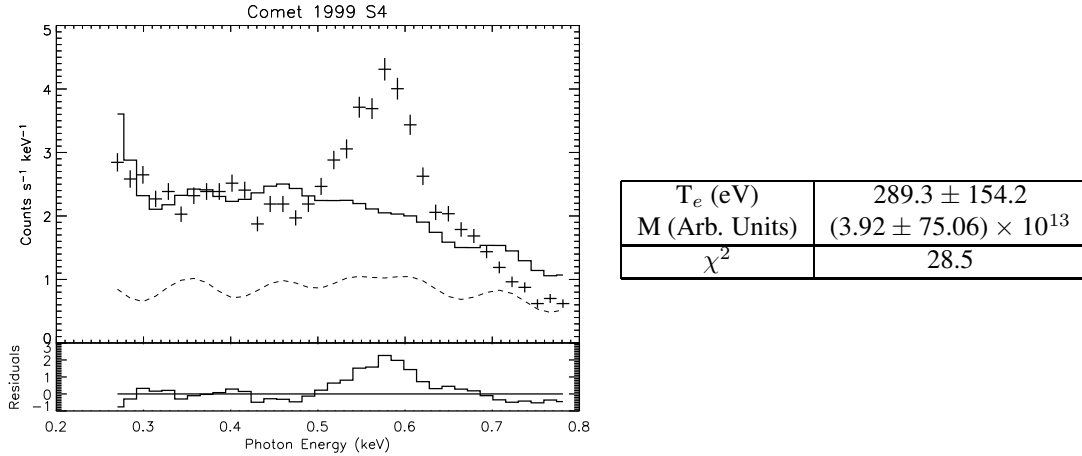


Figure 5.24: A hydrogenic bremsstrahlung fit of comet C/1999 S4 (LINEAR). The dashed line is the convolution of the background model.

The quality of the fit is low, as is the case when the model is applied to the other observations. Consequently, the results for other comets are not shown.

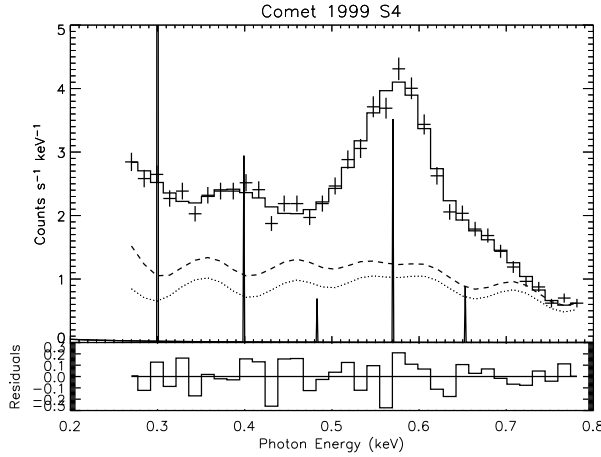
### Comments on the Arbitrary Bremsstrahlung Model

It is clear from the fit to comet C/1999 S4 (LINEAR) (5.24) and every other comet that a bremsstrahlung continuum is not sufficient to explain the emission. However, it remains plausible that bremsstrahlung from electrons with a temperature of several hundred eV may form a component of the emission.

### 5.5.3 Arbitrary Line + Bremsstrahlung Emission

In this model, the previous two approaches are combined. A hydrogenic thermal bremsstrahlung is supplemented by narrow emission lines of arbitrary position and magnitude. The continuum is multiplied by a factor  $M$ .

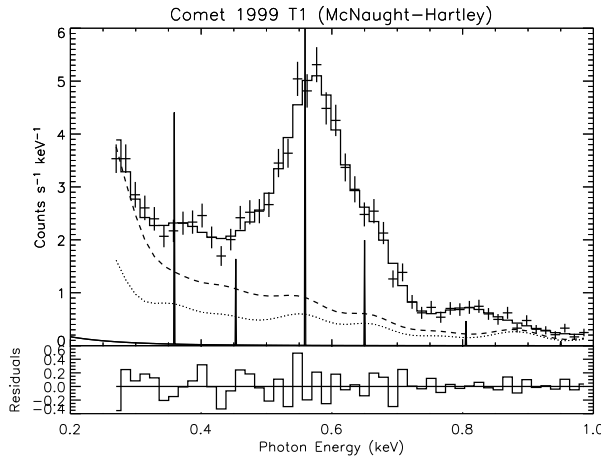
#### Comet C/1999 S4 (LINEAR)



Energy (eV)	Magnitude (Arb. Units)
$301 \pm 4$	$6.87 \pm 1.56$
$399 \pm 4$	$0.733 \pm 0.112$
$483 \pm 13$	$0.172 \pm 0.054$
$570 \pm 3$	$0.879 \pm 0.045$
$653 \pm 5$	$0.222 \pm 0.023$
$T_e$ (eV)	$243 \pm 90$
$M$ (Arb. Units)	$(1.17 \pm 0.98) \times 10^{13}$
$\chi^2$	1.34

Figure 5.25: A bremsstrahlung plus 5 lines fit of comet C/1999 S4 (LINEAR). The dotted line represents the convolved background signal, and the dashed line is the contribution from bremsstrahlung

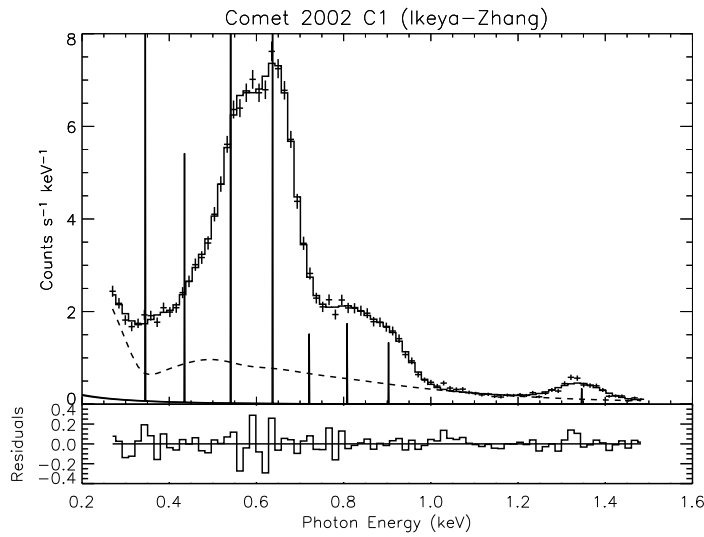
#### Comet C/1999 T1 (McNaught-Hartley)



Energy (eV)	Magnitude (Arb. Units)
$359 \pm 11$	$1.09 \pm 0.25$
$453 \pm 18$	$0.411 \pm 0.176$
$560 \pm 4$	$1.85 \pm 0.16$
$651 \pm 7$	$0.497 \pm 0.078$
$806 \pm 7$	$0.116 \pm 0.035$
$951 \pm 26$	$0.0211 \pm 0.0142$
$T_e$ (eV)	$154 \pm 73$
$M$ (Arb. Units)	$(5.36 \pm 3.20) \times 10^{13}$
$\chi^2$	0.971

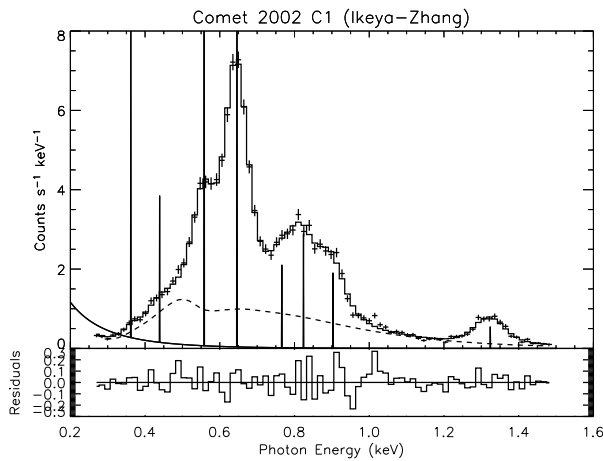
Figure 5.26: A bremsstrahlung plus 6 lines fit of comet C/1999 T1 (McNaught-Hartley). The dotted line represents the convolved background signal, and the dashed line is the contribution from bremsstrahlung

### Comet C/2002 C1 (Ikeya-Zhang) - First Observation



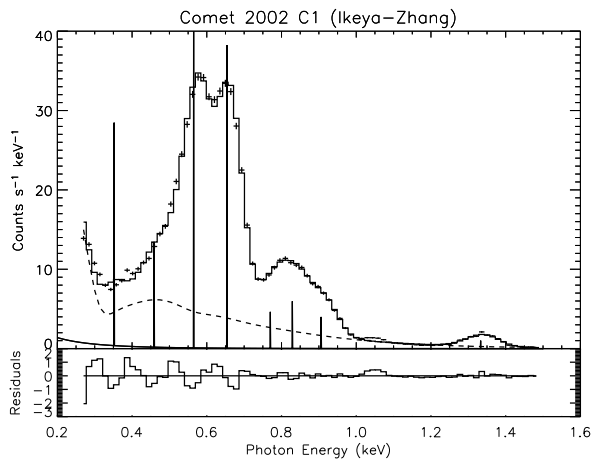
Energy (eV)	Magnitude (Arb. Units)
$346 \pm 5$	$2.74 \pm 0.33$
$435 \pm 6$	$1.34 \pm 0.13$
$541 \pm 3$	$4.69 \pm 0.92$
$638 \pm 3$	$3.09 \pm 0.10$
$721 \pm 23$	$0.378 \pm 0.078$
$809 \pm 12$	$0.435 \pm 0.061$
$904 \pm 6$	$0.332 \pm 0.037$
$1346 \pm 3$	$0.0852 \pm 0.0053$
$T_e$ (eV)	$387 \pm 12$
M (Arb. Units)	$(4.05 \pm 0.25) \times 10^{13}$
$\chi^2$	1.22

Figure 5.27: Bremsstrahlung and 8 lines fit of comet C/2002 C1 (Ikeya-Zhang) (first observation). The dashed line is the contribution from bremsstrahlung



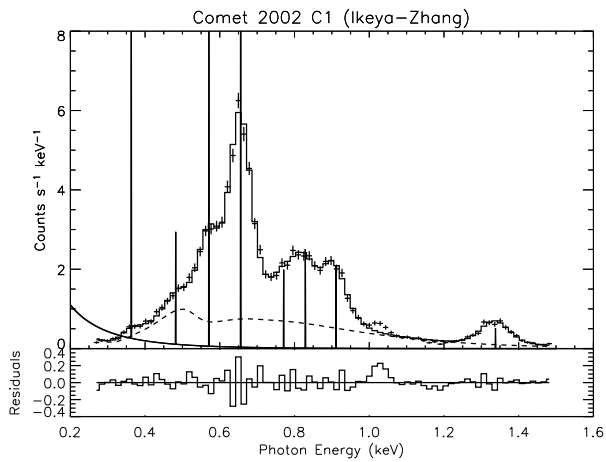
Energy (eV)	Magnitude (Arb. Units)
$441 \pm 9$	$0.902 \pm 0.291$
$364 \pm 11$	$2.01 \pm 0.71$
$558 \pm 2$	$6.09 \pm 0.24$
$647 \pm 1$	$5.18 \pm 0.12$
$767 \pm 7$	$0.530 \pm 0.087$
$825 \pm 6$	$0.717 \pm 0.080$
$904 \pm 3$	$0.472 \pm 0.036$
$1325 \pm 2$	$0.137 \pm 0.006$
$T_e$ (eV)	$234 \pm 6$
M (Arb. Units)	$(2.49 \pm 0.24) \times 10^{14}$
$\chi^2$	1.59

Figure 5.28: Bremsstrahlung and 8 lines fit of comet C/2002 C1 (Ikeya-Zhang) (first observation). The dashed line is the contribution from bremsstrahlung



Energy (eV)	Magnitude (Arb. Units)
$458 \pm 2$	$3.39 \pm 0.12$
$351 \pm 2$	$7.27 \pm 0.36$
$565 \pm 1$	$12.2 \pm 0.1$
$654 \pm 1$	$9.58 \pm 0.09$
$769 \pm 5$	$1.13 \pm 0.11$
$829 \pm 4$	$1.52 \pm 0.10$
$906 \pm 2$	$1.00 \pm 0.05$
$1333 \pm 1$	$0.253 \pm 0.007$
$T_e$ (eV)	$263 \pm 2$
M (Arb. Units)	$(2.89 \pm 0.06) \times 10^{14}$
$\chi^2$	5.87

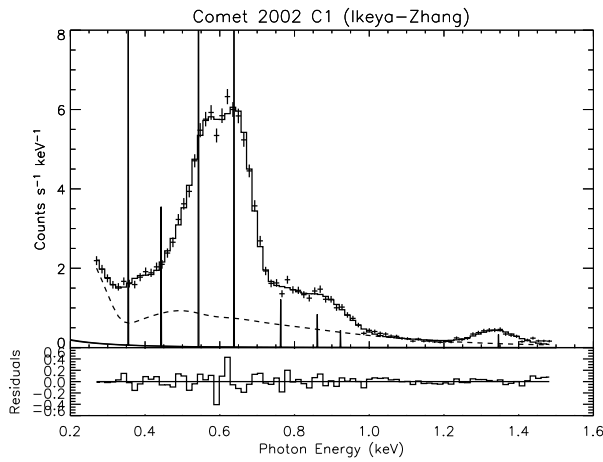
Figure 5.29: Bremsstrahlung and 8 lines fit of comet C/2002 C1 (Ikeya-Zhang) (first observation). The dashed line is the contribution from bremsstrahlung



Energy (eV)	Magnitude (Arb. Units)
$482 \pm 7$	$0.709 \pm 0.185$
$363 \pm 6$	$2.94 \pm 0.70$
$571 \pm 2$	$4.64 \pm 0.29$
$656 \pm 1$	$4.91 \pm 0.126$
$772 \pm 7$	$0.493 \pm 0.076$
$830 \pm 5$	$0.624 \pm 0.071$
$912 \pm 2$	$0.523 \pm 0.030$
$1339 \pm 2$	$0.127 \pm 0.006$
$T_e$ (eV)	$239 \pm 6$
M (Arb. Units)	$(2.54 \pm 0.24) \times 10^{14}$
$\chi^2$	1.65

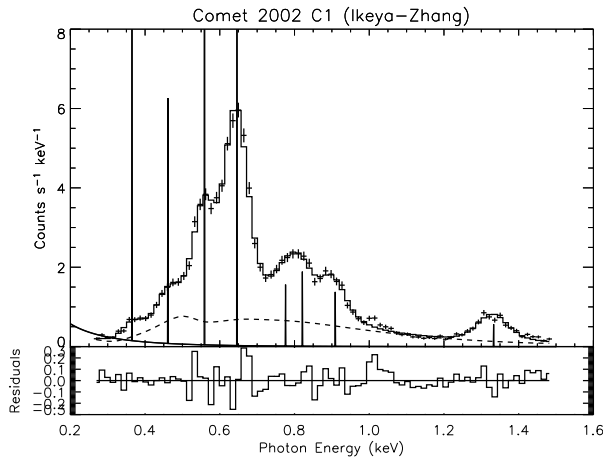
Figure 5.30: Bremsstrahlung and 8 lines fit of comet C/2002 C1 (Ikeya-Zhang) (first observation). The dashed line is the contribution from bremsstrahlung

## Comet C/2002 C1 (Ikeya-Zhang) - Second Observation



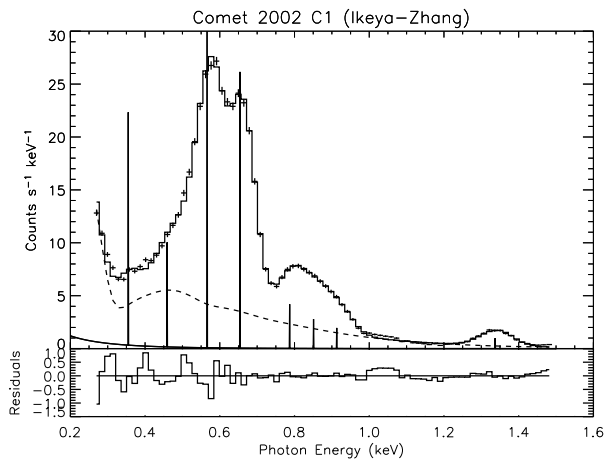
Energy (eV)	Magnitude (Arb. Units)
$443 \pm 9$	$0.878 \pm 0.107$
$356 \pm 5$	$2.23 \pm 0.18$
$544 \pm 3$	$3.45 \pm 0.35$
$639 \pm 2$	$2.52 \pm 0.07$
$764 \pm 11$	$0.302 \pm 0.033$
$923 \pm 25$	$0.108 \pm 0.096$
$861 \pm 25$	$0.209 \pm 0.067$
$1347 \pm 33$	$0.0824 \pm 0.0051$
$T_e$ (eV)	$381 \pm 11$
M (Arb. Units)	$(3.94 \pm 0.21) \times 10^{13}$
$\chi^2$	1.58

Figure 5.31: Bremsstrahlung and 7 lines fit of comet C/2002 C1 (Ikeya-Zhang) (second observation). The dashed line is the contribution from bremsstrahlung



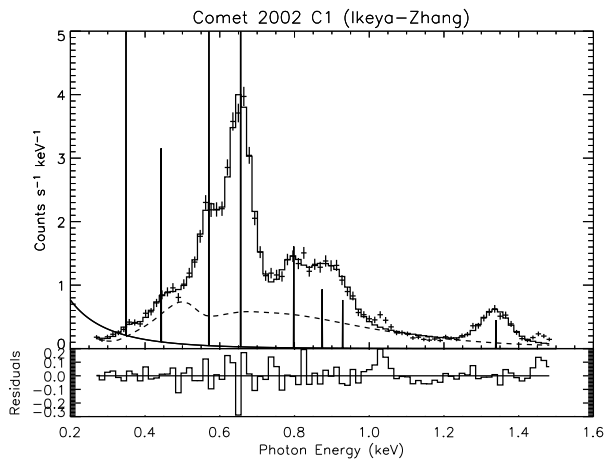
Energy (eV)	Magnitude (Arb. Units)
$462 \pm 4$	$1.55 \pm 0.21$
$366 \pm 4$	$4.47 \pm 0.65$
$559 \pm 2$	$5.98 \pm 0.24$
$647 \pm 1$	$4.41 \pm 0.11$
$777 \pm 13$	$0.387 \pm 0.169$
$822 \pm 10$	$0.470 \pm 0.167$
$909 \pm 3$	$0.343 \pm 0.026$
$1334 \pm 2$	$0.141 \pm 0.006$
$T_e$ (eV)	$285 \pm 13$
M (Arb. Units)	$(1.24 \pm 0.19) \times 10^{14}$
$\chi^2$	1.78

Figure 5.32: Bremsstrahlung and 8 lines fit of comet C/2002 C1 (Ikeya-Zhang) (second observation). The dashed line is the contribution from bremsstrahlung



Energy (eV)	Magnitude (Arb. Units)
$460 \pm 2$	$2.47 \pm 0.11$
$355 \pm 2$	$5.50 \pm 0.27$
$566 \pm 1$	$9.52 \pm 0.11$
$655 \pm 1$	$6.53 \pm 0.08$
$788 \pm 3$	$1.05 \pm 0.09$
$852 \pm 9$	$0.693 \pm 0.063$
$913 \pm 5$	$0.486 \pm 0.082$
$1338 \pm 14$	$0.249 \pm 0.007$
$T_e$ (eV)	$270 \pm 2$
M (Arb. Units)	$(2.67 \pm 0.06) \times 10^{14}$
$\chi^2$	4.12

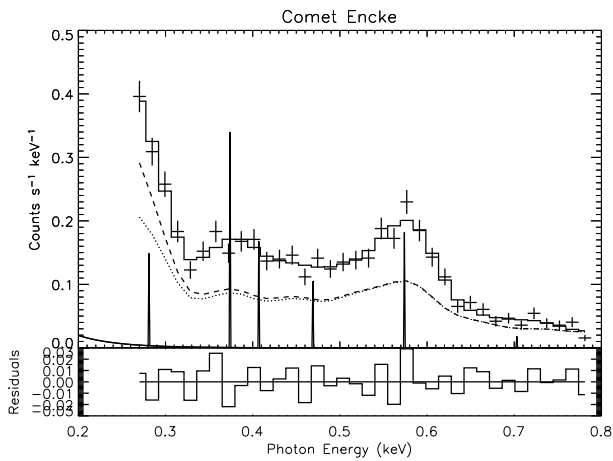
Figure 5.33: Bremsstrahlung and 8 lines fit of comet C/2002 C1 (Ikeya-Zhang) (second observation). The dashed line is the contribution from bremsstrahlung



Energy (eV)	Magnitude (Arb. Units)
$443 \pm 7$	$0.763 \pm 0.218$
$349 \pm 6$	$3.46 \pm 0.86$
$571 \pm 2$	$3.41 \pm 0.24$
$656 \pm 1$	$3.23 \pm 0.10$
$799 \pm 4$	$0.400 \pm 0.034$
$875 \pm 11$	$0.232 \pm 0.043$
$929 \pm 8$	$0.190 \pm 0.050$
$1340 \pm 2$	$0.112 \pm 0.006$
$T_e$ (eV)	$254 \pm 8$
M (Arb. Units)	$(1.72 \pm 0.18) \times 10^{14}$
$\chi^2$	1.83

Figure 5.34: Bremsstrahlung and 8 lines fit of comet C/2002 C1 (Ikeya-Zhang) (second observation). The dashed line is the contribution from bremsstrahlung

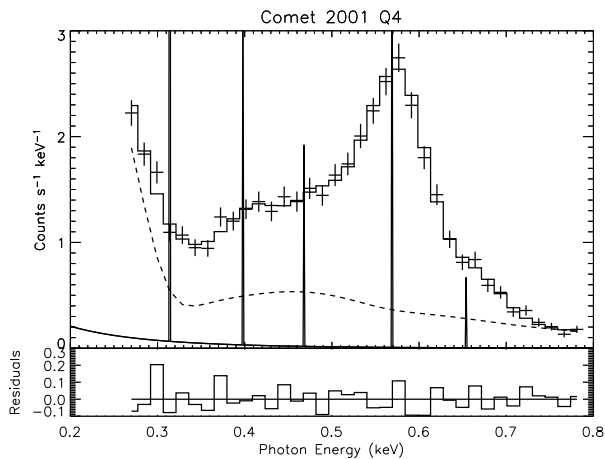
## Comet 2P/Encke



Energy (eV)	Magnitude (Arb. Units)
$281 \pm 25$	$0.0384 \pm 0.0910$
$374 \pm 38$	$0.0900 \pm 0.1206$
$411 \pm 79$	$0.0382 \pm 0.1243$
$470 \pm 32$	$0.0255 \pm 0.0294$
$575 \pm 4$	$0.0455 \pm 0.0108$
$705 \pm 16$	$0.00453 \pm 0.00219$
$T_e$ (eV)	$61.7 \pm 319.2$
M (Arb. Units)	$(3.06 \pm 62.29) \times 10^{13}$
$\chi^2$	1.43

Figure 5.35: A bremsstrahlung plus 6 lines fit of comet 2P/Encke. The dotted line represents the convolved background signal, and the dashed line is the contribution from bremsstrahlung

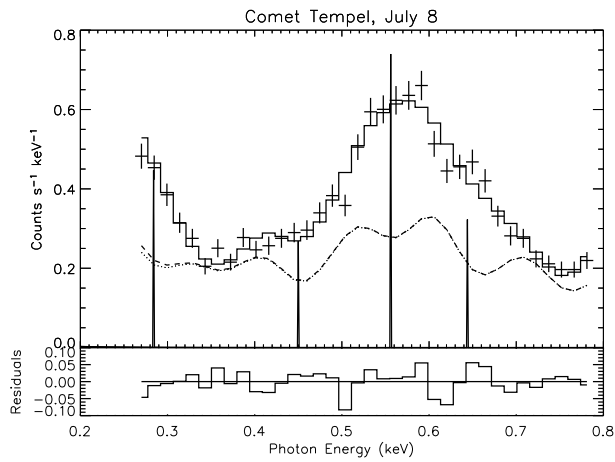
## Comet C/2001 Q4 (NEAT)



Energy (eV)	Magnitude (Arb. Units)
$316 \pm 9$	$3.63 \pm 2.34$
$399 \pm 9$	$0.846 \pm 0.134$
$468 \pm 8$	$0.474 \pm 0.086$
$569 \pm 2$	$1.19 \pm 0.050$
$654 \pm 5$	$0.166 \pm 0.020$
$T_e$ (eV)	$193 \pm 11$
M (Arb. Units)	$(5.65 \pm 0.85) \times 10^{13}$
$\chi^2$	0.928

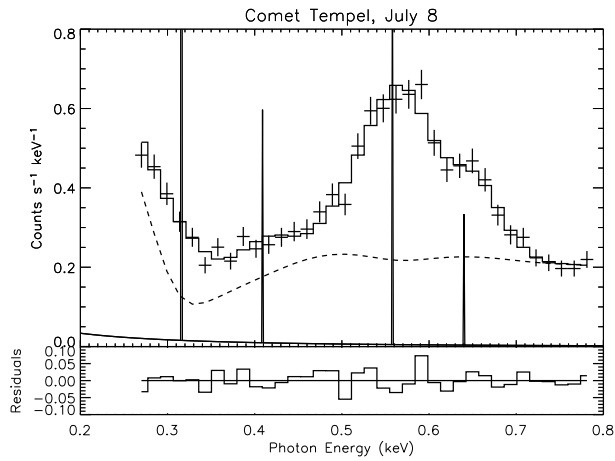
Figure 5.36: A bremsstrahlung plus 5 lines fit of comet C/2001 Q4 (NEAT). The dashed line is the contribution from bremsstrahlung

## Comet 9P/Tempel 1



Energy (eV)	Magnitude (Arb. Units)
$285 \pm 13$	$0.111 \pm 0.400$
$450 \pm 12$	$0.0674 \pm 0.0385$
$556 \pm 4$	$0.185 \pm 0.030$
$644 \pm 5$	$0.0808 \pm 0.0161$
$932 \pm 262$	$0.718 \pm 5.374$
$T_e$ (eV)	$92.3 \pm 2185.2$
$M$ (Arb. Units)	$(1.90 \pm 167.29) \times 10^{12}$
$\chi^2$	1.88

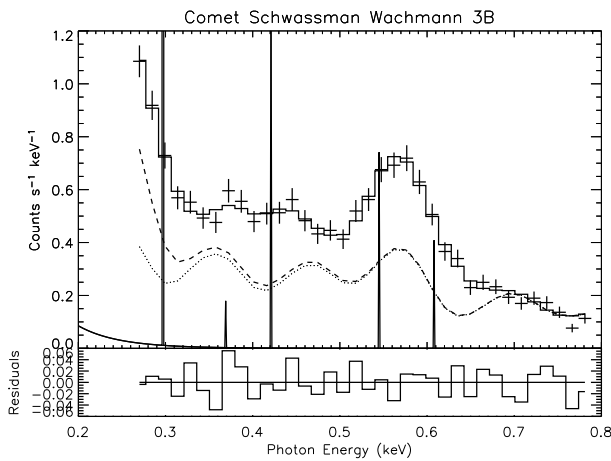
Figure 5.37: A bremsstrahlung plus 5 lines fit of comet 9P/Tempel 1. The dotted line represents the convolved background signal, and the dashed line is the contribution from bremsstrahlung



Energy (eV)	Magnitude (Arb. Units)
$317 \pm 5$	$1.34 \pm 0.45$
$412 \pm 7$	$0.135 \pm 0.033$
$559 \pm 3$	$0.247 \pm 0.016$
$641 \pm 5$	$0.0823 \pm 0.0097$
$T_e$ (eV)	$628 \pm 101$
$M$ (Arb. Units)	$(6.19 \pm 0.63) \times 10^{12}$
$\chi^2$	1.08

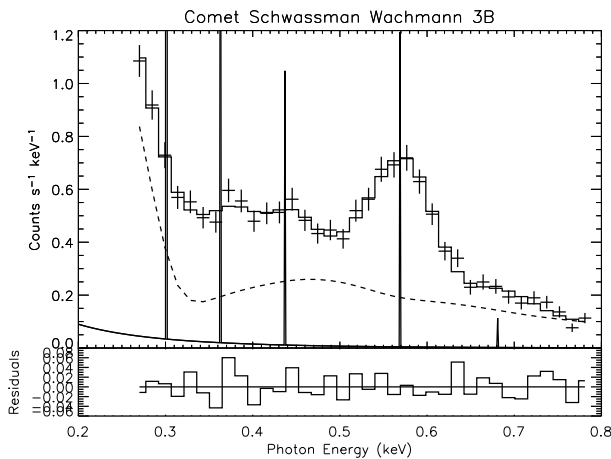
Figure 5.38: A bremsstrahlung plus 4 lines fit of comet 9P/Tempel 1 with no background treatment. The dashed line is the contribution from bremsstrahlung

## Comet 73P/Schwassmann-Wachmann 3B



Energy (eV)	Magnitude (Arb. Units)
$297 \pm 9$	$19.2 \pm 40.9$
$370 \pm 192$	$0.0443 \pm 0.2181$
$422 \pm 12$	$0.333 \pm 0.150$
$545 \pm 9$	$0.185 \pm 0.068$
$608 \pm 7$	$0.102 \pm 0.022$
$T_e$ (eV)	$64.1 \pm 117.0$
M (Arb. Units)	$(1.21 \pm 8.14) \times 10^{14}$
$\chi^2$	1.07

Figure 5.39: A bremsstrahlung plus 5 lines fit of comet 73P/Schwassmann-Wachmann. The dotted line represents the convolved background signal, and the dashed line is the contribution from bremsstrahlung



Energy (eV)	Magnitude (Arb. Units)
$302 \pm 16$	$7.81 \pm 9.12$
$364 \pm 11$	$0.629 \pm 0.219$
$437 \pm 6$	$0.258 \pm 0.052$
$569 \pm 2$	$0.297 \pm 0.021$
$681 \pm 10$	$0.0276 \pm 0.0072$
$T_e$ (eV)	$221 \pm 23$
M (Arb. Units)	$(2.21 \pm 0.59) \times 10^{13}$
$\chi^2$	0.869

Figure 5.40: A bremsstrahlung plus 5 lines fit of comet 73P/Schwassmann-Wachmann. The dashed line is the contribution from bremsstrahlung.

### Comments on the Arbitrary Bremsstrahlung and Line Emission Model

As with the arbitrary line model, this model over-fits the data in several instances. The contribution of a continuum is small in the fits for comet 2P/Encke (figure 5.35), 9P/Tempel 1 (with background) (figure 5.37) and 73P/Schwassmann-Wachmann (with background) (figure 5.40). In the case of comet 9P/Tempel (without background) (figure 5.38), the temperature associated with the continuum is significantly higher than the temperature in every other fit. The other results feature continua with temperatures ranging from 154–381 eV.

The line energies required are similar to those required by the arbitrary line model, as one would expect. The main difference is that in general a significant fraction of

the low energy emission is due to bremsstrahlung rather than emission from neutral carbon fluorescence at 277 eV, Mg<sup>9+</sup> (263, 282 eV), or Si<sup>10+</sup> (282, 284 eV).

#### 5.5.4 Charge Exchange Between Solar Wind Ions and Cometary Neutrals

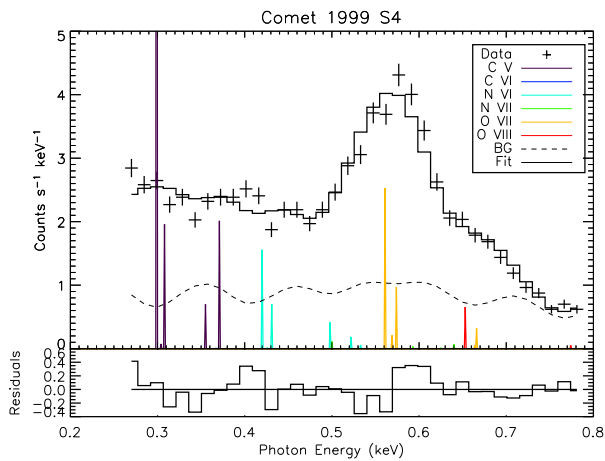
From the charge exchange data and emission modelling described in chapter 4, synthetic spectra can be created. A simple charge exchange model incorporates the relative collision speed,  $v$ , and the abundances of emitting ion in the solar wind, i.e. C<sup>6+,5+</sup>, N<sup>7+,6+</sup>, and O<sup>8+,7+</sup>. There is a temperature associated with each element,  $T_C$ ,  $T_N$  and  $T_O$ . These temperatures represent the equilibrium electron temperature required to obtain the appropriate ionisation balance in a low density plasma.

After the fit is complete, the ion abundances are normalised to unity, and the normalisation factor is given as the emission measure  $M$  such that

$$M = \frac{1}{4\pi\Delta^2} \int N_I N_H dV \quad (5.11)$$

where  $\Delta$  is the geocentric distance of the comet,  $N_I$  is the density of the solar wind minor species ions,  $N_H$  is the neutral hydrogen donor density and  $V$  represents the emitting volume of plasma.

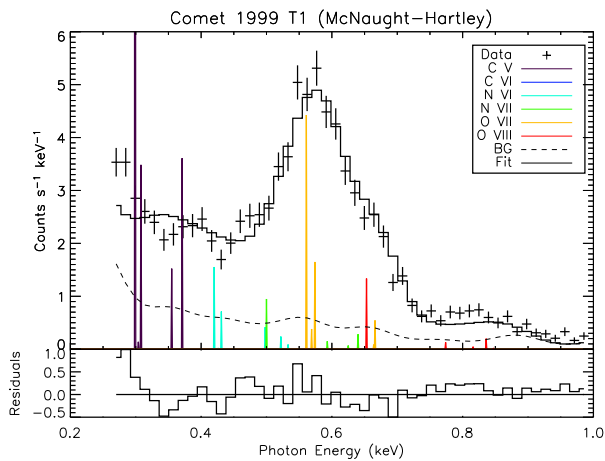
### Comet C/1999 S4 (LINEAR)



$N_C$	$0.947 \pm 23.997$
$T_C$ (eV)	$45.0 \pm 115.1$
$N_N$	$0.0174 \pm 0.0256$
$T_N$ (eV)	$91.0 \pm 11.9$
$N_O$	$0.0355 \pm 0.0352$
$T_O$ (eV)	$178 \pm 30$
$v_{sw}$ (km s <sup>-1</sup> )	$94.0 \pm 58.4$
$M$	$2.13 \times 10^{10}$
$\chi^2$	2.44

Figure 5.41: Charge exchange fit of comet C/1999 S4 (LINEAR). The dashed line is the convolution of the background model

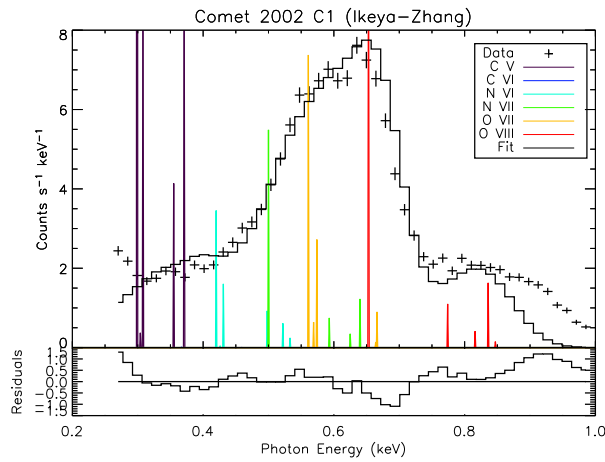
### Comet C/1999 T1 (McNaught-Hartley)



$N_C$	$0.996 \pm 283.753$
$T_C$ (eV)	$38.8 \pm 961.9$
$N_N$	$0.000491 \pm 0.000387$
$T_N$ (eV)	$119 \pm 14$
$N_O$	$0.00340 \pm 0.00199$
$T_O$ (eV)	$163 \pm 3$
$v_{sw}$ (km s <sup>-1</sup> )	$174 \pm 33$
$M$	$9.49 \times 10^{10}$
$\chi^2$	2.52

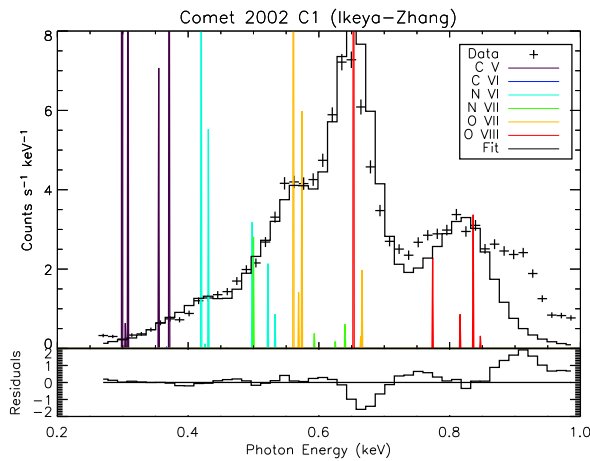
Figure 5.42: Charge exchange fit of comet C/1999 T1 (McNaught-Hartley).

## Comet C/2002 C1 (Ikeya-Zhang) - First Observation



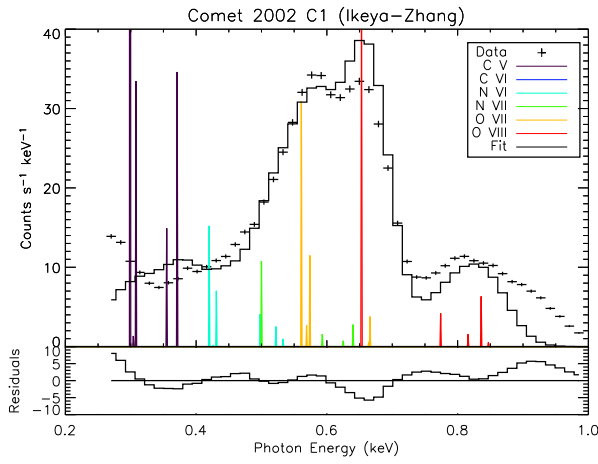
$N_C$	$0.999 \pm 152.217$
$T_C$ (eV)	$37.6 \pm 482.4$
$N_N$	$0.000250 \pm 0.000052$
$T_N$ (eV)	$138 \pm 5$
$N_O$	$0.000951 \pm 0.000214$
$T_O$ (eV)	$216 \pm 3$
$v_{sw}$ (km s <sup>-1</sup> )	$202 \pm 14$
$M$	$2.88 \times 10^{11}$
$\chi^2$	34.2

Figure 5.43: Charge exchange fit of comet C/2002 C1 (Ikeya-Zhang) (first observation) on the ACIS-S1 CCD.



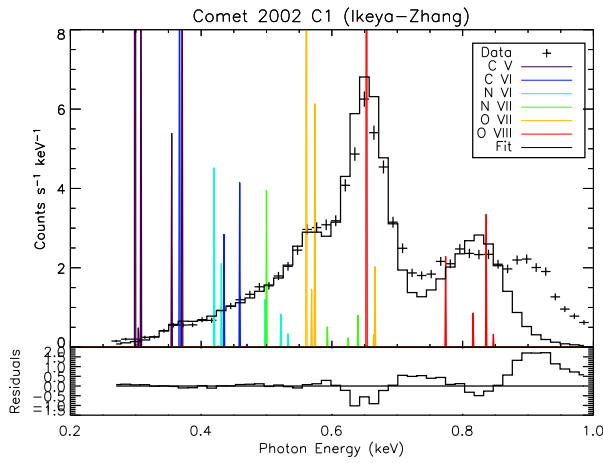
$N_C$	$0.997 \pm 104.381$
$T_C$ (eV)	$38.3 \pm 344.1$
$N_N$	$0.000986 \pm 0.000341$
$T_N$ (eV)	$104 \pm 4$
$N_O$	$0.00152 \pm 0.00070$
$T_O$ (eV)	$214 \pm 5$
$v_{sw}$ (km s <sup>-1</sup> )	$204 \pm 28$
$M$	$3.80 \times 10^{11}$
$\chi^2$	37.3

Figure 5.44: Charge exchange fit of comet C/2002 C1 (Ikeya-Zhang) (first observation) on the ACIS-S2 CCD.



$N_C$	$0.998 \pm 61.849$
$T_C$ (eV)	$37.5 \pm 195.4$
$N_N$	$0.000321 \pm 0.00030$
$T_N$ (eV)	$121 \pm 2$
$N_O$	$0.00119 \pm 0.00011$
$T_O$ (eV)	$212 \pm 1$
$v_{sw}$ (km s <sup>-1</sup> )	$189 \pm 5$
$M$	$1.19 \times 10^{12}$
$\chi^2$	181

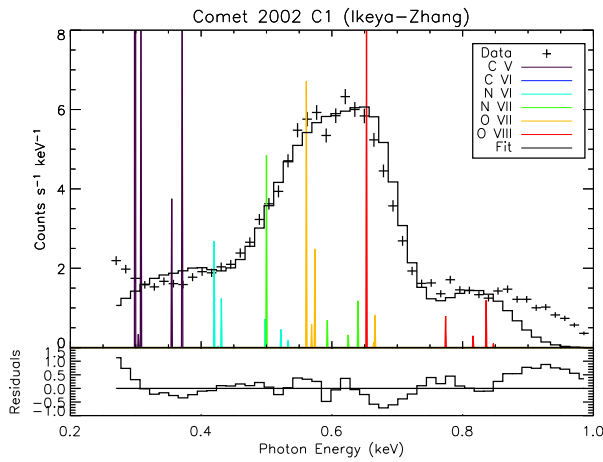
Figure 5.45: Charge exchange fit of comet C/2002 C1 (Ikeya-Zhang) (first observation) on the ACIS-S3 CCD.



$N_C$	$0.753 \pm 0.355$
$T_C$ (eV)	$74.0 \pm 3$
$N_N$	$0.03517 \pm 0.0162$
$T_N$ (eV)	$126 \pm 6$
$N_O$	$0.212 \pm 0.114$
$T_O$ (eV)	$214 \pm 7$
$v_{sw}$ (km s <sup>-1</sup> )	$209 \pm 34$
$M$	$2.61 \times 10^9$
$\chi^2$	38.1

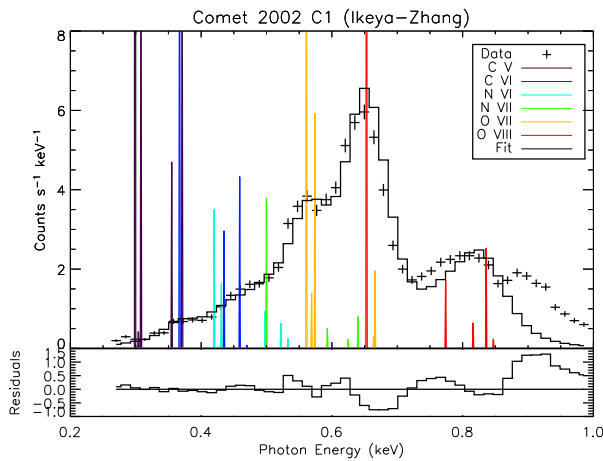
Figure 5.46: Charge exchange fit of comet C/2002 C1 (Ikeya-Zhang) (first observation) on the ACIS-S4 CCD.

### Comet C/2002 C1 (Ikeya-Zhang) - Second Observation



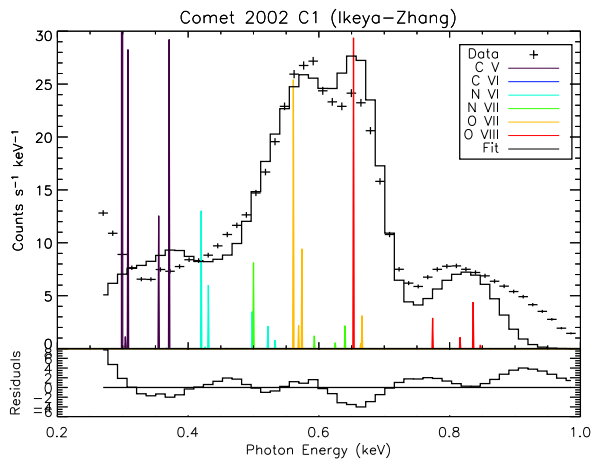
$N_C$	$0.997 \pm 72.012$
$T_C$ (eV)	$40.1 \pm 260.0$
$N_N$	$0.000456 \pm 0.000117$
$T_N$ (eV)	$141 \pm 7$
$N_O$	$0.00216 \pm 0.00044$
$T_O$ (eV)	$206 \pm 2$
$v_{sw}$ (km s <sup>-1</sup> )	$195 \pm 12$
$M$	$1.31 \times 10^{11}$
$\chi^2$	26.0

Figure 5.47: Charge exchange fit of comet C/2002 C1 (Ikeya-Zhang) (second observation) on the ACIS-S1 CCD.



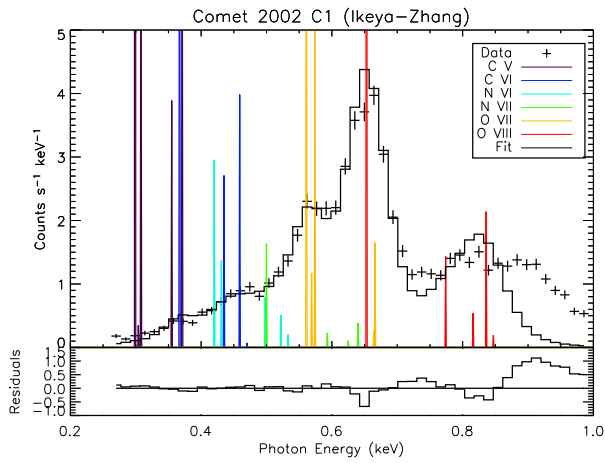
$N_C$	$0.721 \pm 0.338$
$T_C$ (eV)	$75.6 \pm 3.2$
$N_N$	$0.0310 \pm 0.0163$
$T_N$ (eV)	$130 \pm 8$
$N_O$	$0.248 \pm 0.138$
$T_O$ (eV)	$204 \pm 6$
$v_{sw}$ (km s <sup>-1</sup> )	$206 \pm 35$
$M$	$2.30 \times 10^9$
$\chi^2$	28.9

Figure 5.48: Charge exchange fit of comet C/2002 C1 (Ikeya-Zhang) (second observation) on the ACIS-S2 CCD.



$N_C$	$0.996 \pm 21.317$
$T_C$ (eV)	$40.8 \pm 79.7$
$N_N$	$0.000871 \pm 0.000088$
$T_N$ (eV)	$119 \pm 2$
$N_O$	$0.00313 \pm 0.00030$
$T_O$ (eV)	$205 \pm 1$
$v_{sw}$ (km s <sup>-1</sup> )	$186 \pm 6$
$M$	$3.98 \times 10^{11}$
$\chi^2$	140

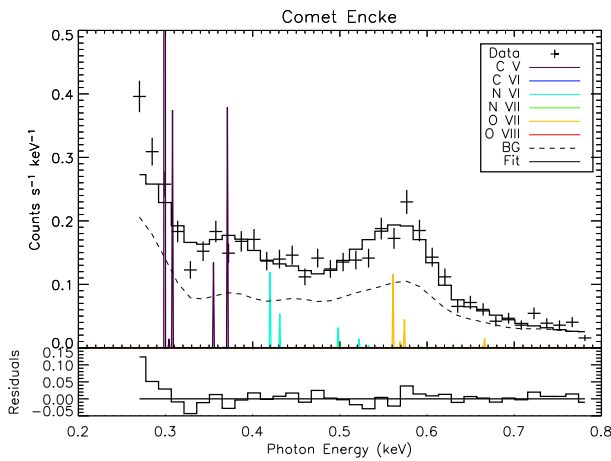
Figure 5.49: Charge exchange fit of comet C/2002 C1 (Ikeya-Zhang) (second observation) on the ACIS-S3 CCD.



$N_C$	$0.698 \pm 0.387$
$T_C$ (eV)	$76.3 \pm 3.6$
$N_N$	$0.0354 \pm 0.0242$
$T_N$ (eV)	$117 \pm 9$
$N_O$	$0.266 \pm 0.176$
$T_O$ (eV)	$203 \pm 5$
$v_{sw}$ (km s <sup>-1</sup> )	$198 \pm 40$
$M$	$2.05 \times 10^9$
$\chi^2$	26.5

Figure 5.50: Charge exchange fit of comet C/2002 C1 (Ikeya-Zhang) (second observation) on the ACIS-S4 CCD.

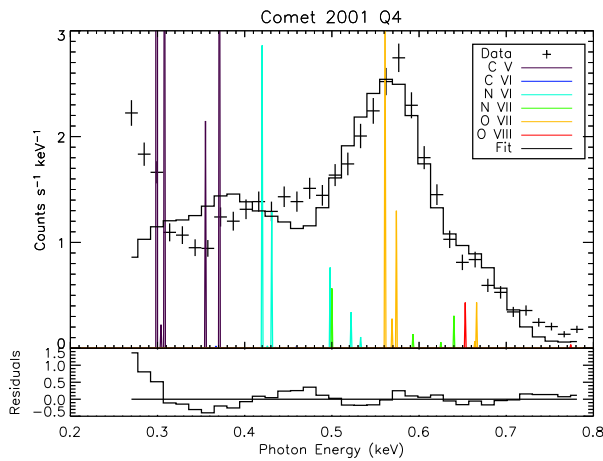
## Comet 2P/Encke



$N_C$	$0.969 \pm 64.865$
$T_C$ (eV)	$42.5 \pm 270.2$
$N_N$	$0.00413 \pm 0.02162$
$T_N$ (eV)	$89.4 \pm 28.7$
$N_O$	$0.0273 \pm 0.4331$
$T_O$ (eV)	$107 \pm 204$
$v_{sw}$ (km s <sup>-1</sup> )	$97.6 \pm 238.7$
$M$	$7.10 \times 10^9$
$\chi^2$	2.86

Figure 5.51: Charge exchange fit of comet 2P/Encke. The dashed line is the convolution of the background model

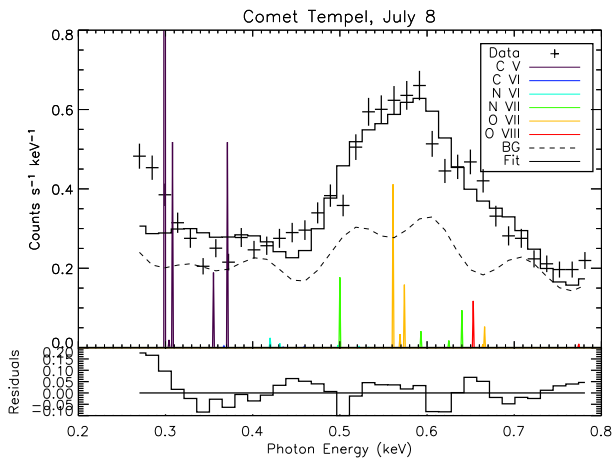
## Comet C/2001 Q4 (NEAT)



$N_C$	$0.983 \pm 21.8306$
$T_C$ (eV)	$43.6 \pm 94.3$
$N_N$	$0.00405 \pm 0.00288$
$T_N$ (eV)	$103 \pm 5$
$N_O$	$0.0125 \pm 0.0063$
$T_O$ (eV)	$156 \pm 8$
$v_{sw}$ (km s <sup>-1</sup> )	$102 \pm 30$
$M$	$8.21 \times 10^{10}$
$\chi^2$	12.8

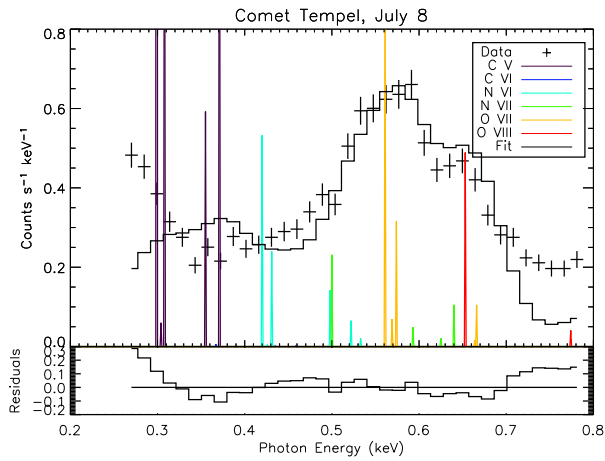
Figure 5.52: Charge exchange fit of comet C/2001 Q4 (NEAT).

## Comet 9P/Tempel 1



$N_C$	$0.948 \pm 13.114$
$T_C$ (eV)	$50.0 \pm 79.8$
$N_N$	$0.00131 \pm 0.00326$
$T_N$ (eV)	$194 \pm 262$
$N_O$	$0.0505 \pm 0.0406$
$T_O$ (eV)	$176 \pm 12.8$
$v_{sw}$ (km s <sup>-1</sup> )	$104 \pm 45$
$M$	$2.03 \times 10^9$
$\chi^2$	6.10

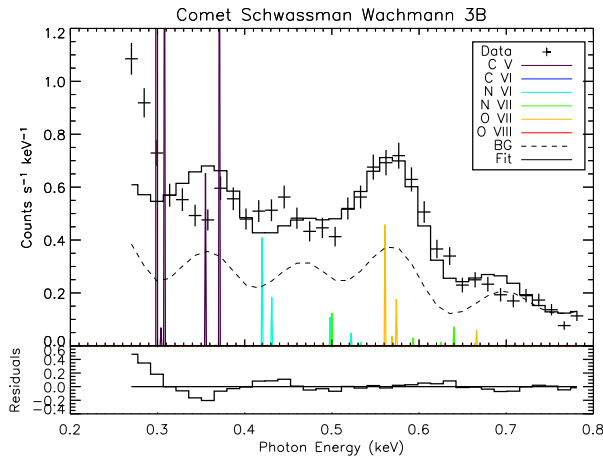
Figure 5.53: Charge exchange fit of comet 9P/Tempel 1. The dashed line is the convolution of the background model.



$N_C$	$0.993 \pm 29.755$
$T_C$ (eV)	$42.6 \pm 121.7$
$N_N$	$0.00143 \pm 0.00072$
$T_N$ (eV)	$115 \pm 6$
$N_O$	$0.00589 \pm 0.00242$
$T_O$ (eV)	$194 \pm 7$
$v_{sw}$ (km s <sup>-1</sup> )	$118 \pm 22$
$M$	$2.48 \times 10^{10}$
$\chi^2$	17.1

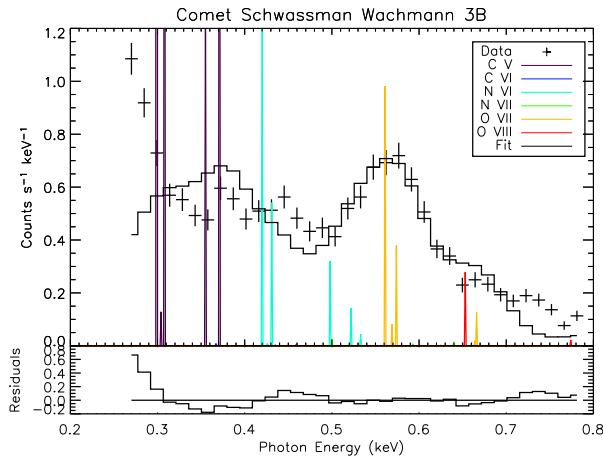
Figure 5.54: Charge exchange fit of comet 9P/Tempel 1.

## Comet 73P/Schwassmann-Wachmann 3B



$N_C$	$0.972 \pm 110.916$
$T_C$ (eV)	$39.8 \pm 403.3$
$N_N$	$0.000621 \pm 0.000997$
$T_N$ (eV)	$109 \pm 12$
$N_O$	$0.0275 \pm 1.4003$
$T_O$ (eV)	$94.5 \pm 549.0$
$v_{sw}$ (km s <sup>-1</sup> )	$97.3 \pm 65.3$
$M$	$7.03 \times 10^{10}$
$\chi^2$	7.67

Figure 5.55: Charge exchange fit of comet 73P/Schwassmann Wachmann 3B. The dashed line is the convolution of the background model



$N_C$	$0.971 \pm 24.609$
$T_C$ (eV)	$42.2 \pm 101.1$
$N_N$	$0.0256 \pm 0.2252$
$T_N$ (eV)	$69.1 \pm 65.6$
$N_O$	$0.00384 \pm 0.00525$
$T_O$ (eV)	$178 \pm 36$
$v_{sw}$ (km s <sup>-1</sup> )	$100 \pm 78$
$M$	$6.81 \times 10^{10}$
$\chi^2$	13.1

Figure 5.56: Charge exchange fit of comet 73P/Schwassmann Wachmann 3B.

### Comments on the Charge Exchange Model

The charge exchange model results in a good fit of points around the main emission feature from  $O^{6+}$ . Fitting of the  $O^{7+}$  emission regions is less successful as several emission lines are present, and the fit shows a compromise between  $n \geq 3 \rightarrow n = 1$  lines fitting a broad range around 800 eV and the prominent (in some observations)  $n = 2 \rightarrow n = 1$  line at 654 eV. This could be resolved with including emission from  $Fe^{16+}$  at 826 eV.

At lower energies, the combination of carbon and nitrogen lines cannot match the observed data below 500 eV. This is despite each ion species having a specific temperature. This effectively allow the abundance of each ion to vary freely, causing the model

to be more adaptable than the solar wind conditions it should represent. This results in a very large abundance of carbon at a low average ion charge. This is because the model needs a large amount of emission from  $C^{5+}$  charge exchange, but a very small amount of emission from  $C^{6+}$  charge exchange. At the plasma temperatures given for carbon ( $\sim 40$  eV), the dominant carbon ion is  $C^{4+}$ , but the ratio of  $C^{5+}$  (0.5%) to  $C^{6+}$  ( $8 \times 10^{-5}\%$ ) is high. Again, this could be resolved by the inclusion of more ions.

From these results, it is impossible that a charge exchange model based on a more extensive set of charge exchange cross sections could not explain the observed x-ray spectra.

### 5.5.5 Energetic Electrons – Excitation of Solar Wind Ions and Bremsstrahlung

The abundance of carbon, nitrogen, oxygen, neon, magnesium, silicon, sulphur, argon, iron and nickel are parameters in this model. In addition to this, the abundance of hydrogen is set to 1.0.

The hydrogen abundance actually represents all of the ions and atoms that do not emit x-ray lines, but still contribute to continuum emission. This includes solar wind protons and  $\alpha$  particles, cometary neutrals and cometary photoions. As a result of this, and the condition that the hydrogen abundance is 1, it is expected that the abundance of the other species is lower than the the ratio of the species density to the H density in the solar wind.

The array of these abundances is then normalised by divided by the sum over all elements. The other parameters are the free electron temperature and the solar corona temperature. Emission lines are observed following collisions between the free electrons and the minor species ions, and a bremsstrahlung continuum is generated by collisions between the electrons and all of the ions. The corona temperature is used to indicate the ionisation balance of each species.

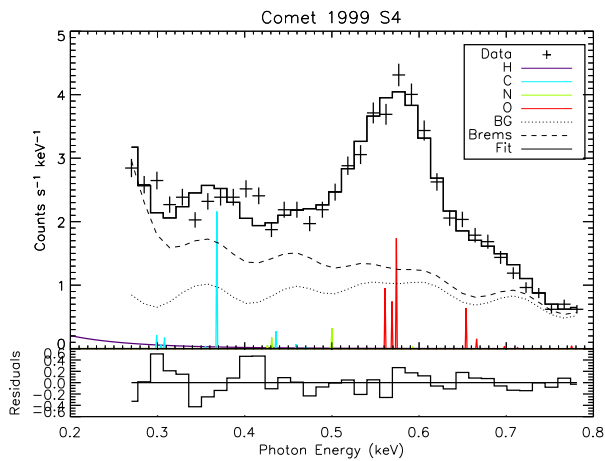
Finally, the photon emissivity coefficient spectrum is multiplied by a factor  $M$ , such that

$$M = \frac{1}{4\pi R^2 \Delta E} \int n_e n_i dV \quad (5.12)$$

where  $R$  is the distance to the comet,  $\Delta E = 14.6eV$  is the width of the *ACIS* energy bins,  $V$  is the emitting plasma volume,  $n_e(V)$  is the electron density, and  $n_i(V)$  is the ion density.

Results are shown in figures 5.57 to 5.72.

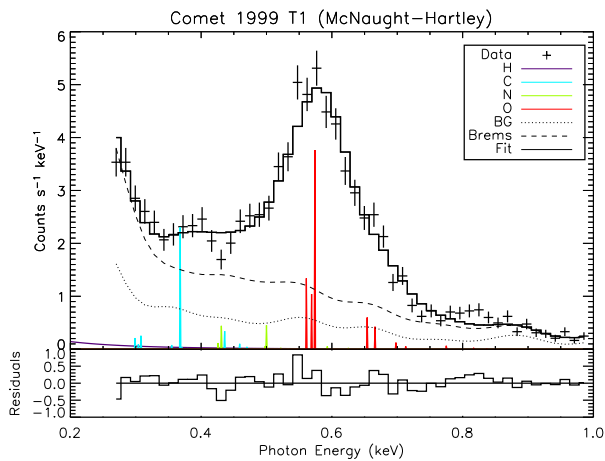
### Comet C/1999 S4 (LINEAR)



C	$(5.06 \pm 2.16) \times 10^{-5}$
N	$(6.55 \pm 4.54) \times 10^{-6}$
O	$(5.70 \pm 2.30) \times 10^{-5}$
$T_e$ (eV)	$131 \pm 15$
$T_i^{\text{COR}}$ (eV)	$167 \pm 11$
M	$(5.31 \pm 1.06) \times 10^{15}$
$\chi^2$	3.01

Figure 5.57: Energetic electron fit of comet C/1999 S4 (LINEAR). The dashed line is the convolution of the background model

### Comet C/1999 T1 (McNaught-Hartley)



C	$(2.07 \pm 0.75) \times 10^{-5}$
N	$(3.57 \pm 1.50) \times 10^{-6}$
O	$(2.70 \pm 0.37) \times 10^{-5}$
$T_e$ (eV)	$249 \pm 16$
$T_i^{\text{COR}}$ (eV)	$138 \pm 8$
M	$(2.24 \pm 0.26) \times 10^{15}$
$\chi^2$	1.60

Figure 5.58: Energetic electron fit of comet C/1999 T1 (McNaught-Hartley). The dashed line is the convolution of the background model

### Comet C/2002 C1 (Ikeya-Zhang) (First Observation)

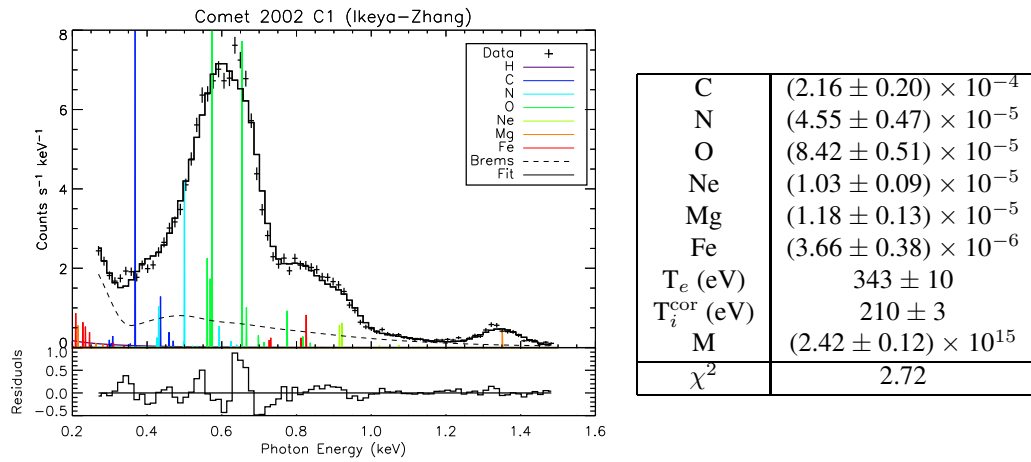


Figure 5.59: Energetic electron fit of comet C/2002 C1 (Ikeya-Zhang) (first observation). The dashed line is the convolution of the background model

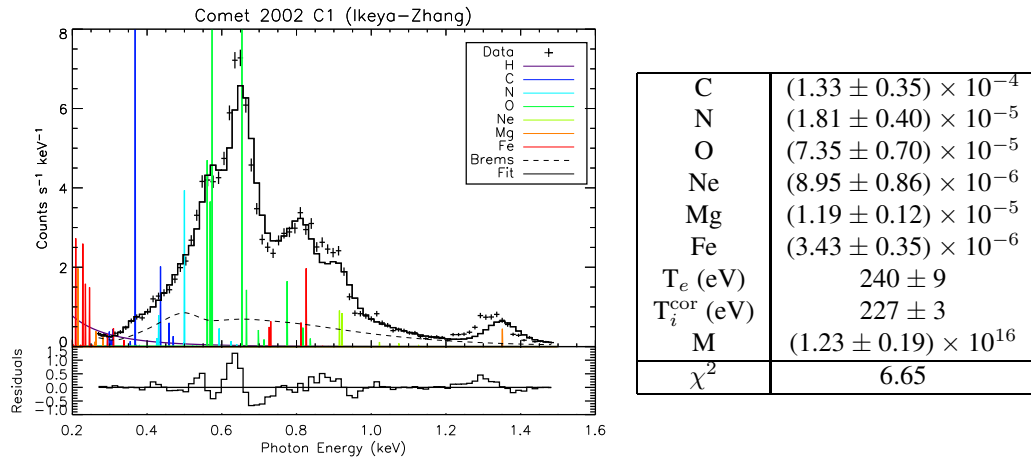
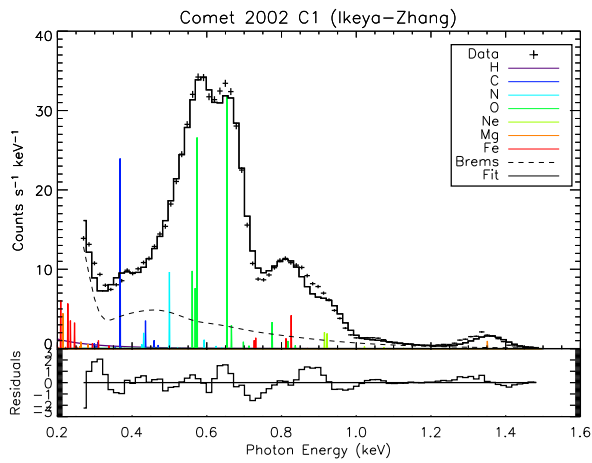
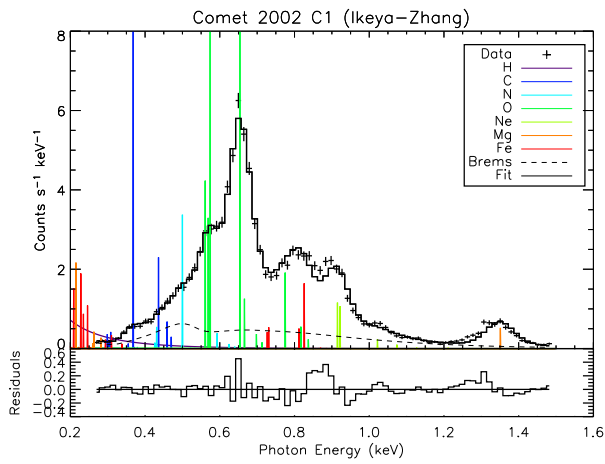


Figure 5.60: Energetic electron fit of comet C/2002 C1 (Ikeya-Zhang) (first observation). The dashed line is the convolution of the background model



C	$(1.47 \pm 0.07) \times 10^{-4}$
N	$(2.82 \pm 0.16) \times 10^{-5}$
O	$(9.62 \pm 0.30) \times 10^{-5}$
Ne	$(1.31 \pm 0.06) \times 10^{-5}$
Mg	$(1.70 \pm 0.10) \times 10^{-5}$
Fe	$(4.80 \pm 0.19) \times 10^{-6}$
$T_e$ (eV)	$238 \pm 2$
$T_i^{\text{COR}}$ (eV)	$226 \pm 1$
M	$(1.94 \pm 0.04) \times 10^{16}$
$\chi^2$	13.4

Figure 5.61: Energetic electron fit of comet C/2002 C1 (Ikeya-Zhang) (first observation). The dashed line is the convolution of the background model



C	$(2.18 \pm 0.57) \times 10^{-4}$
N	$(2.30 \pm 0.59) \times 10^{-5}$
O	$(1.11 \pm 0.12) \times 10^{-4}$
Ne	$(1.46 \pm 0.01) \times 10^{-5}$
Mg	$(1.66 \pm 0.02) \times 10^{-5}$
Fe	$(2.79 \pm 0.01) \times 10^{-6}$
$T_e$ (eV)	$234 \pm 9$
$T_i^{\text{COR}}$ (eV)	$248 \pm 4$
M	$(1.16 \pm 0.20) \times 10^{16}$
$\chi^2$	2.17

Figure 5.62: Energetic electron fit of comet C/2002 C1 (Ikeya-Zhang) (first observation). The dashed line is the convolution of the background model

### Comet C/2002 C1 (Ikeya-Zhang) (Second Observation)

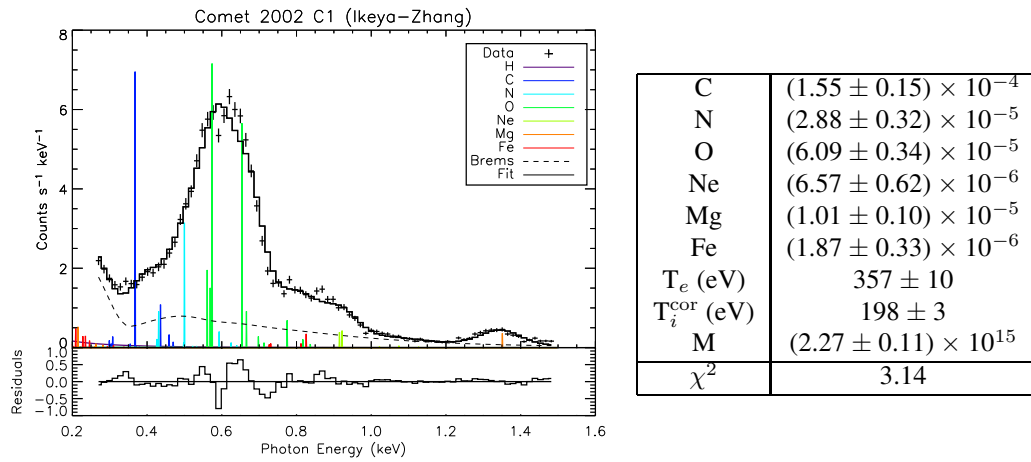


Figure 5.63: Energetic electron fit of comet C/2002 C1 (Ikeya-Zhang) (second observation). The dashed line is the convolution of the background model

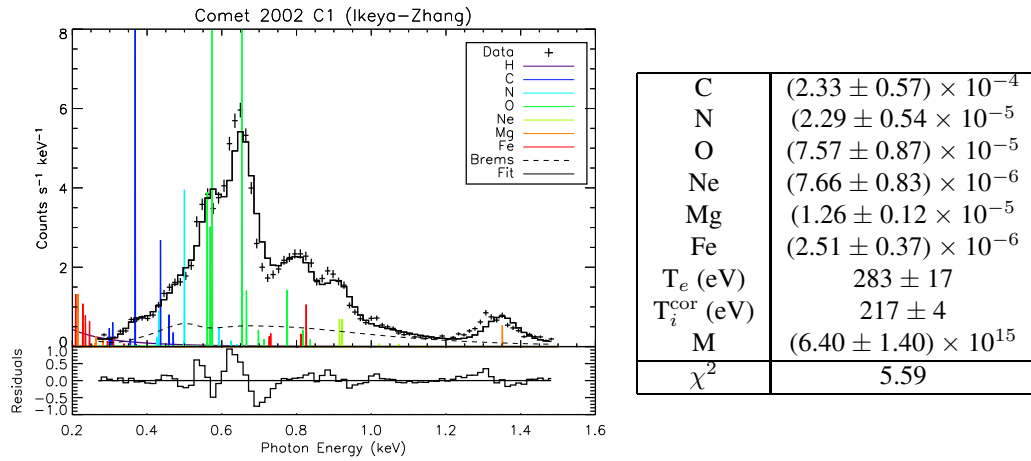
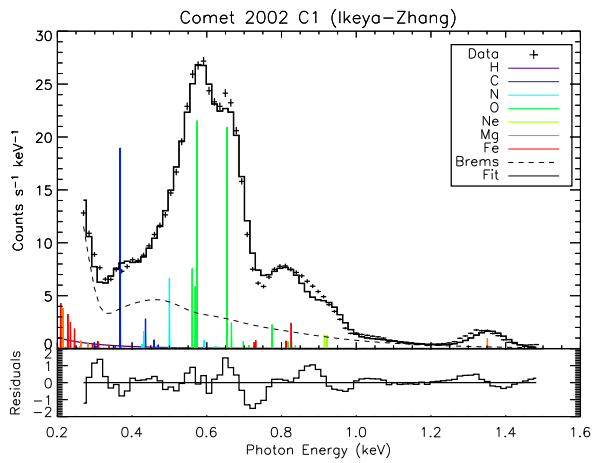
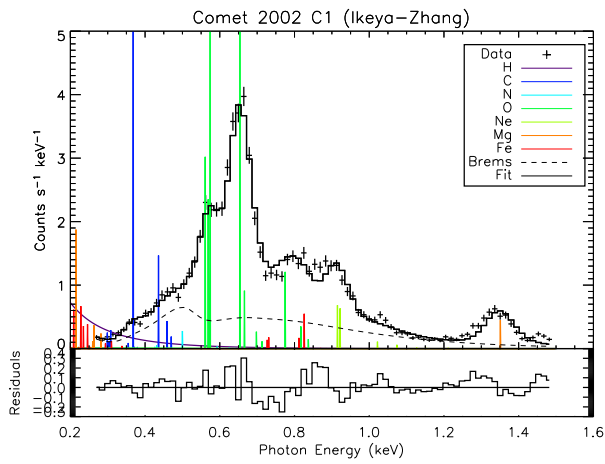


Figure 5.64: Energetic electron fit of comet C/2002 C1 (Ikeya-Zhang) (second observation). The dashed line is the convolution of the background model



C	$(1.03 \pm 0.05) \times 10^{-4}$
N	$(1.67 \pm 0.11) \times 10^{-5}$
O	$(6.04 \pm 0.17) \times 10^{-5}$
Ne	$(7.60 \pm 0.36) \times 10^{-6}$
Mg	$(1.44 \pm 0.08) \times 10^{-5}$
Fe	$(3.17 \pm 0.15) \times 10^{-6}$
$T_e$ (eV)	$254 \pm 3$
$T_i^{\text{COR}}$ (eV)	$213 \pm 1$
M	$(1.65 \pm 0.04) \times 10^{16}$
$\chi^2$	10.4

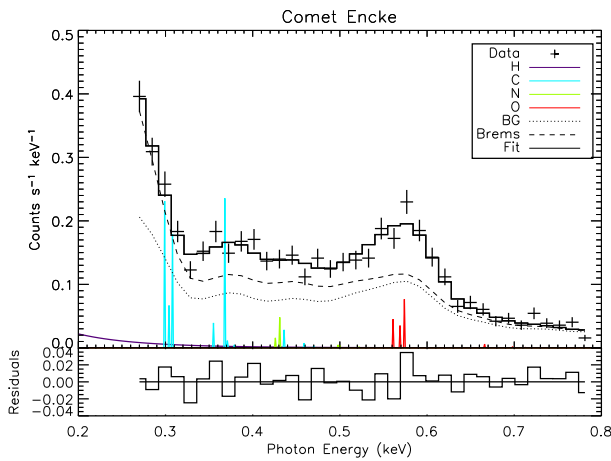
Figure 5.65: Energetic electron fit of comet C/2002 C1 (Ikeya-Zhang) (second observation). The dashed line is the convolution of the background model



C	$(1.19 \pm 0.37) \times 10^{-4}$
N	$(1.58 \pm 0.28) \times 10^{-6}$
O	$(6.20 \pm 0.64) \times 10^{-5}$
Ne	$(7.70 \pm 0.79) \times 10^{-6}$
Mg	$(1.31 \pm 0.14) \times 10^{-5}$
Fe	$(9.54 \pm 1.67) \times 10^{-7}$
$T_e$ (eV)	$238 \pm 9$
$T_i^{\text{COR}}$ (eV)	$237 \pm 4$
M	$(1.16 \pm 0.19) \times 10^{16}$
$\chi^2$	2.76

Figure 5.66: Energetic electron fit of comet C/2002 C1 (Ikeya-Zhang) (second observation). The dashed line is the convolution of the background model

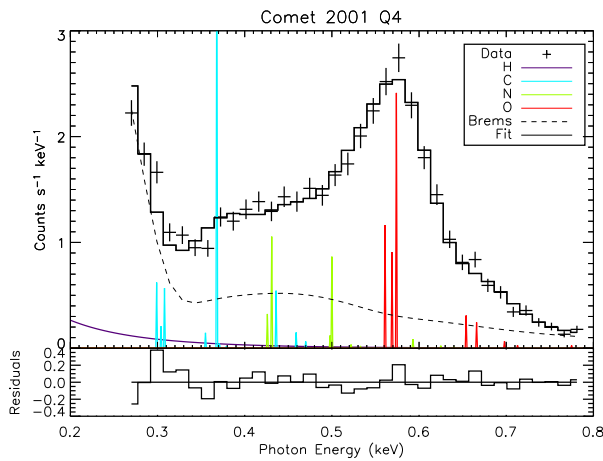
### Comet 2P/Encke



C	$(1.10 \pm 0.43) \times 10^{-5}$
N	$(2.50 \pm 1.80) \times 10^{-6}$
O	$(1.76 \pm 0.68) \times 10^{-5}$
$T_e$ (eV)	$116 \pm 15$
$T_i^{\text{cor}}$ (eV)	$85.2 \pm 49.2$
M	$(7.04 \pm 2.50) \times 10^{14}$
$\chi^2$	1.25

Figure 5.67: Energetic electron fit of comet 2P/Encke. The dashed line is the convolution of the background model

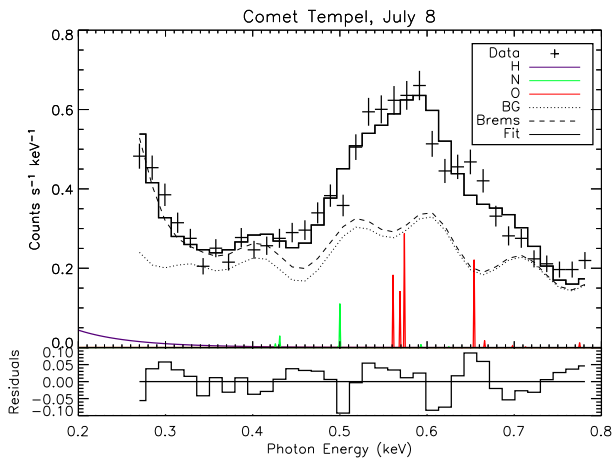
### Comet C/2001 Q4 (NEAT)



C	$(2.55 \pm 0.65) \times 10^{-5}$
N	$(7.43 \pm 1.50) \times 10^{-6}$
O	$(2.34 \pm 0.33) \times 10^{-5}$
$T_e$ (eV)	$160 \pm 8$
$T_i^{\text{cor}}$ (eV)	$132 \pm 6$
M	$(5.61 \pm 0.46) \times 10^{15}$
$\chi^2$	1.62

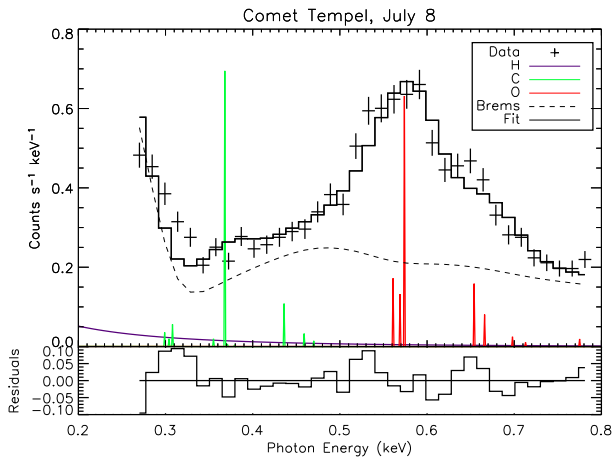
Figure 5.68: Energetic electron fit of comet C/2001 Q4 (NEAT).

## Comet 9P/Tempel 1



N	$(4.35 \pm 4.84) \times 10^{-5}$
O	$(2.59 \pm 2.65) \times 10^{-4}$
$T_e$ (eV)	$102 \pm 20$
$T_i^{\text{cor}}$ (eV)	$221 \pm 25$
M	$(1.62 \pm 0.78) \times 10^{15}$
$\chi^2$	2.92

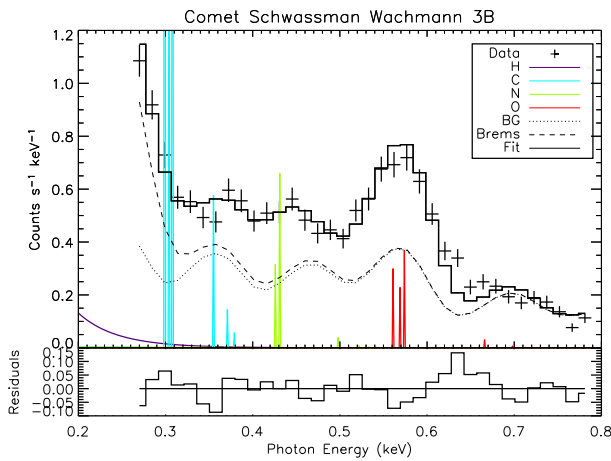
Figure 5.69: Energetic electron fit of comet 9P/Tempel. The dashed line is the convolution of the background model



C	$(1.83 \pm 0.46) \times 10^{-5}$
O	$(8.43 \pm 0.98) \times 10^{-6}$
$T_e$ (eV)	$358 \pm 21$
$T_i^{\text{cor}}$ (eV)	$150 \pm 7$
M	$(7.05 \pm 0.45) \times 10^{14}$
$\chi^2$	2.84

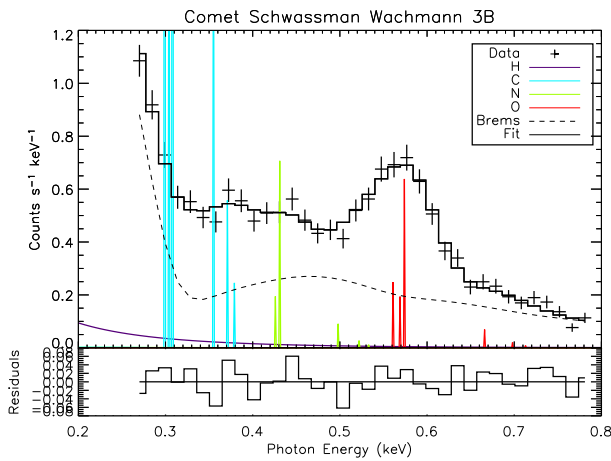
Figure 5.70: Energetic electron fit of comet 9P/Tempel with no background treatment.

### Comet 73P/Schwassmann-Wachmann 3B



C	$(3.63 \pm 2.44) \times 10^{-5}$
N	$(4.62 \pm 5.79) \times 10^{-5}$
O	$(3.96 \pm 12.2) \times 10^{-4}$
$T_e$ (eV)	$60.4 \pm 23.5$
$T_i^{\text{COR}}$ (eV)	$36.3 \pm 420.2$
M	$(1.51 \pm 2.25) \times 10^{16}$
$\chi^2$	2.11

Figure 5.71: Energetic electron fit of comet 73P/Schwassmann-Wachmann. The dashed line is the convolution of the background model



C	$(1.86 \pm 3.85) \times 10^{-5}$
N	$(2.94 \pm 113.98) \times 10^{-6}$
O	$(1.05 \pm 522.00) \times 10^{-5}$
$T_e$ (eV)	$219 \pm 8$
$T_i^{\text{COR}}$ (eV)	$25.9 \pm 4250.0$
M	$(1.57 \pm 0.14) \times 10^{15}$
$\chi^2$	0.857

Figure 5.72: Energetic electron fit of comet 73P/Schwassmann-Wachmann with no background treatment.

### **Comments on the Energetic Electron Model**

In general, this model provides a good fit to the data, including an over-fit of the observation of comet 73P/Schwassmann-Wachmann 3B (without background) (figure 5.72). The only observation in which all of the emission features are not represented is that of comet C/1999 S4 (LINEAR) (figure 5.57). A possible resolution of this is the inclusion of fluorescence from neutral nitrogen at 392 eV. Fluorescence from cometary neutrals is compatible with the energetic electron model.

The fits generated by this model indicate that the spectral resolution below 1 keV of the *ACIS-S* instrument is greater than the resolution predicted by the latest *Chandra* calibration data.

## 5.6 Conclusions

The main aim of this study is to determine which emission mechanism is more probable: charge exchange or energetic electrons. Results of the fits are shown in table 5.2. The arbitrary line and the arbitrary line plus bremsstrahlung models are included for completeness.

Comet	L	L+B	CX	EE
1999 S4	1.39	1.34	2.44	3.01
1999 T1	0.920	0.971	2.52	1.60
2002 C1 (S1) (I)	0.979	1.22	34.2	2.72
2002 C1 (S2) (I)	2.89	1.59	37.3	6.65
2002 C1 (S3) (I)	5.25	5.87	181	13.4
2002 C1 (S4) (I)	3.23	1.65	38.1	2.17
2002 C1 (S1) (II)	1.22	1.58	26.0	3.14
2002 C1 (S2) (II)	1.66	1.78	28.9	5.59
2002 C1 (S3) (II)	5.05	4.12	140	10.4
2002 C1 (S4) (II)	2.96	1.83	26.5	2.76
Encke	1.42	1.43	3.01	1.25
2001 Q4	1.31	0.928	12.8	1.62
Tempel (With BG)	1.90	1.88	6.10	2.92
Tempel (No BG)	1.58	1.08	17.1	2.84
S-W 3B	1.02	1.07	7.67	2.11
S-W 3B (No BG)	1.36	0.869	13.1	0.857

Table 5.2:  $\chi^2$  results for each fit. The listed models are arbitrary line emission (L), arbitrary line emission plus bremsstrahlung (L+B), charge exchange (CX) and energetic electrons (EE).

In almost every case, the energetic electron model results in a significant improvement in  $\chi^2$ . This is due, in part, to the available archive of charge exchange cross sections being incomplete. Incorporating charge exchange lines from magnesium, argon and iron would improve the data, although it is possible to quantify the improvement.

From these results, it is impossible to categorically state that charge exchange emission could not explain the observed emission spectra. However, one can state that the energetic electron model can explain all of the features of the observed emission spectra.

Based on this spectroscopic analysis alone, the energetic electron model is a more likely explanation for cometary x-rays.

# Chapter 6

## Conclusions

In this thesis, a comprehensive catalogue of cometary x-ray observations from *Chandra* is presented (section 3.4). The data are processed using the latest versions of the *Chandra* calibration database (*CALDB* version 3.3.0) and the *CIAO* analysis package (version 3.4).

Two emission models from the literature were considered: charge exchange collisions and energetic electron collisions. The energetic electron model was modified to become more compatible with observations. Early versions of this model predicted bremsstrahlung emission and neutral fluorescence. *Chandra* results from comet C/1999 S4 (LINEAR) (Lisse *et al*, 2001) indicated that the strongest emission lines are from the ions  $O^{6+}$  and  $O^{7+}$ . Preliminary studies on a highly ionised cometary plasma demonstrated that this route was unfeasible due to the required ionisation timescales. Therefore, the main emission lines could not be from cometary constituents.

The new version of the model presented here is as follows. The processes generating energetic electrons remain unchanged from the original model (section 4.1). The difference is in the emitting species. Rather than neutral fluorescence, the emission is from electron impact excitation of solar wind minor species ions. In addition to this, there is a bremsstrahlung continuum from solar wind protons, cometary neutrals and cometary ions. In this approach, there is still the potential for emission from neutral fluorescence, although it appears that if such a component is present, its contribution is relatively small.

Energetic electrons were observed in the atmosphere of comet Halley by *VEGA-2* (Gringauz *et al*, 1987) but not by *Giotto* (Rème *et al*, 1986). It had been proposed that this was due to the energisation process being sporadic in nature, and that the *VEGA-2* transit coincided with such an event. A new explanation is presented here (section 2.2.3). If cometary x-rays are generated by energetic electrons, one would expect energetic electrons to be present only in x-ray active regions. The literature and the *Chandra* catalogue show that typically, x-ray emission is brightest at  $\sim 10,000$  km

from the nucleus on the dayside, falling to almost background levels near the nucleus. The closest approach of *VEGA-2* was  $\sim 9,000$  km; the closest approach of *Giotto* was 600 km. It is possible that *Giotto* passed through comet Halley without entering the active x-ray region (compare figures 2.14 with the cometary x-ray morphologies presented in section 3.4).

Both the charge exchange models and the modified energetic electron models were constructed in a collisional radiative model (section 4.3) using the most advanced data available (see section 4.2). The models were compared to data from the *Chandra* catalogue (section 5.5). The results indicate that the energetic electron model can represent all of the emission features observed in almost every case. In the only exception, the inclusion of a neutral nitrogen fluorescence line could explain the discrepancy.

This model can be advanced by considering the role of energetic electrons in models of the cometary atmosphere. From such an approach, the morphology from the model can be calculated. A further development is to include non-Maxwellian distribution functions rather than rely on Maxwell-averaged representations, although the variation in emission line ratios is too subtle to be detected by current x-ray observatories.

In the case of charge exchange driven emission, it is impossible to conclude that the model can or can not explain the emission. This is due to the low quantity and quality of charge exchange data available. The required charge exchange data have already been specified by Stancil *et al* (2002).

Given the fact that both models have the potential to explain the observed emission spectra, the emission mechanism for cometary x-rays remains unresolved. However, according to the analysis performed here, which demonstrates that the energetic electron model generally produces lower  $\chi^2$  values in fits of the emission spectra and from the explanation of the discrepancy between *VEGA-2* and *Giotto* observations, it has been demonstrated that at this stage the energetic electron emission mechanism is at least as probable as charge exchange.

Diagnosable differences between the charge exchange and energetic electron models are specified (see section 4.4.2). They are: the absence or presence of a bremsstrahlung continuum; and the line ratio of the  $1s2s \ ^3S \rightarrow 1s^2 \ ^1S$  and  $1s2p \ ^1P \rightarrow 1s^2 \ ^1S$  in helium-like systems. The current generation of x-ray observatories are unable to resolve these features. The XRS device on *Suzaku* could resolve these features (see figure 2.19 for an example of the spectral resolution), but unfortunately the device is not operational. A equivalent device could be employed in a sounding rocket observation, although the six minute limit on the exposure is probably too short to collect a statistically significant number of cometary x-rays. An instrument similar to *Constellation-X* could distinguish between the emission models (see figures 3.77 for an example of the predicted spectral resolution). A device with this resolving power

would also be able to detect weak emission from neutral fluorescence.

Until the launch of *Constellation-X* or a similar device, care must be taken to maximise the scientific yield of observations with current observatories. Every new version of the *Chandra* calibration benefits from the continued improvement in the understanding of the instrument. Consequently, all of the *Chandra* data should be reprocessed, and the fitting methods demonstrated here should be reapplied whenever a new version of *CALDB* is released.

Steps can be taken to ensure that the background sample used in the analysis of the data is free from emission from the comet. This can be achieved by including in observation proposals an exposure of the projected position of the comet a short period before the observation. This will provide a clean sample of the local background using the entire *ACIS* array.

Due to the apparent correlation between the solar wind flux and the cometary x-ray flux, future observations should avoid being constricted to one observing period. As the emission mechanism is still uncertain, the aim of observations must be to gain further insight into the emission process rather than a diagnosis of the solar wind. Until cometary x-rays are fully understood, observations with as many source counts as possible are desirable. Partitioning of the exposure increases the probability of an observation coinciding with a period of high solar wind flux, thereby increasing the probability of observing a bright x-ray atmosphere. Only when the emission model has been established should continuous observations can be used as measurements of the short-scale variation of the solar wind.

Potentially, each of these models may provide useful diagnostics of both the solar wind at large geocentric distances and the constituents of the comet. Charge exchange emission could reveal the speed of the shocked solar wind through the cometary atmosphere, the solar wind constituents and the cometary constituents on a molecular level. The energetic electron model could be used to diagnose the solar wind species, the free electron distribution and the cometary atomic abundances if fluorescence can be detected.

## References

- A'Hearn, M. F., Schleicher, D. G., Feldman, P. D., Millis, R. L., Thompson, D. T.  
Comet Bowell 1980b, *Astron. J.*, **89**, 4, 579, 1984
- A'Hearn, M. F., Belton, M. J. S., Delamere, W. A., Kissel, J., Klaasen, K. P., McFadden, L. A., Meech, K. J., Melosh, H. J., Schultz, P. H., Sunshine, J. M., Thomas, P. C., Veverka, J., Yeomans, D. K., Baca, M. W., Busko, I., Crockett, C. J., Collins, S. M., Desnoyer, M., Eberhardy, C. A., Ernst, C. M., Farnham, T. L., Feaga, L., Groussin, O., Hampton, D., Ipatov, S. I., Li, J.-Y., Linder, D., Lisse, C. M., Mastromedios, N., Owen Jr., W. M., Richardson, J. E., Wellnitz, D. D., White, R. L.  
*Deep Impact: Excavating Comet Tempel 1*, *Science*, **310**, 258, 2005
- Akimoto, K., Papadopoulos, K., Winske, D.  
Lower-hybrid instabilities driven by an ion velocity ring, *J. Plasma Phys.*, **34**, 445, 1985
- Ali, R., Neill, P. A., Beiersdorfer, P., Harris, C. L., Raković, M. J., Wang, J. G., Schultz, D. R., Stancil, P. C.  
On the Significance of the Contribution of Multiple-Electron Capture Processes to Cometary X-ray Emission, *Astrophys. J.*, **629**, L125, 2005
- Anderson, K. A.  
Balloon Measurements of X-rays in the Auroral Zone, *Auroral Phenomena*, ed. M. Walt, (Stanford University Press), 1965
- Balsiger, H., Altwegg, K., Bühler, F., Geiss, J., Ghielmetti, A. G., Golstein, B. E., Goldstein, R., Huntress, W. T., Ip, W.-H., Lazarus, A. J., Meier, A., Neugebauer, M., Rettenmund, U., Rosenbauer, H., Schwenn, R., Sharp, R. D., Shelley, E. G., Ungstrup, E., Young, D. T.  
Ion Composition and Dynamics at Comet Halley, *Nature*, **321**, 330, 1986
- Bartschat, K., Hudson, E. T., Scott, M. P., Burke, P. G., Burke, V. M.  
Electron-Atom Scattering at Low and Intermediate Energies Using a Pseudostate/*R*-Matrix Basis, *J. Phys. B*, **29**, 115, 1996
- Bates, D. R., Kingston, A. E., McWhirter, R. W. P.  
Recombination Between Electrons and Atomic Ions. 1. Optically Thin Plasmas, *Proc. Roy. Soc.*, **A267**, 297, 1962
- Beiersdorfer, P., Boyce, K. R., Brown, G. V., Chen, H., Kahn, S. M., Kelley, R. L., May, M., Olson, R. E., Porter, F. S., Stahle, C. K., Tillson, W. A.  
Laboratory Simulation of Charge Exchange-Produced X-ray Emission from Comets, *Science*, **300**, 1558, 2003
- Bingham, R., Shapiro, V. D., Tsyrovich, V. N., de Angelis, U., Gilman, M., Shevchenko, V. I.  
Theory of Wave Activity Occurring in the AMPTE Artificial Comet, *Phys. Fluids*, **3**, 1728, 1991
- Bingham, R., Dawson, J. M., Shapiro, V. D., Mendis, D. A., Kellett, B. J.  
Generation of X-rays from Comet C/Hyakutake 1996 B2, *Science*, **275**, 49, 1997
- Bingham, R., Kellett, B. J., Dawson, J. M., Shapiro, V. D., Mendis, D. A.  
X-Ray Emission from Comets, Cometary Knots and Supernova Remnants, *Astrophys. J. Supp. Series*, **127**, 233, 2000
- Bingham, R., Dawson, J. M., Shapiro, V. D.  
Particle Acceleration by Lower-Hybrid Turbulence, *J. Plasma Phys.*, **68**, 161, 2002
- Bodewits, D., Juhász, J., Hoekstra, R., Tielens, A. G. G. M.  
Catching Some Sun: Probing the Solar Wind with Cometary X-ray and Far-Ultraviolet Emission, *Astrophys. J.*, **606**, L81, 2004
- Bodewits, D., Hoekstra, R., Serezyuk, B., McCullough, R. W., Jones, G. H., Tielens, A. G. G. M.  
Charge Exchange Emission from Solar Wind Helium Ions, *Astrophys. J.*, **642**, 1, 593, 2006
- Bodewits, D., Christian, D. J., Torney, M., Dryer, M., Lisse, C. M., Dennerl, K., Zürbuchen, T. H., Wolk, S. J., Tielens, A. G. G. M., Hoekstra, R.  
Spectral Analysis of the *Chandra* Comet Survey, *In Preparation*, 2007
- Brandes, G., Dorn, E.  
Über die Sichtbarkeit der Röntgenstrahlen, *Annalen der Physik*, **296**, 3, 478, 1896
- Brownlee, D. E., Tsou, P., Clark, B. C., Swanson, P. N., Vellinga, J.  
Comet Coma Sample Return Plus Interstellar Dust, Science and Technical Approach, <http://stardust.jpl.nasa.gov/science/details.html>, 1994
- Bryans, P.  
Ph.D. Thesis, University of Strathclyde, 2005
- Bryans, P., O'Mullane, M. G., Paton, I. D., Summers, H. P., Torney, M. Whiteford, A. D., Bingham, R., Kellett, B. J.  
Ionisation State, Excited Populations and Emission of Impurities in Dynamic Finite Density Plasmas. II. Population Structure of Ions in Non-Maxwellian Plasmas, *Plasma Phys. Controlled Fus.*, *In Preparation*, 2007
- Burgess, A., Summers, H. P.  
The Effects of Electron and Radiation Density on Dielectronic Recombination, *Astrophys. J.*, **157**, 1007, 1969
- Burgess, A., Chidichimo, M.  
Electron Impact Ionization of Complex Ions, *Mon. Not. R. Astron. Soc.*, **203**, 1269, 1983
- Burgess, A., Summers, H. P.  
Radiative Gaunt Factors, *Mon. Not. R. Astr. Soc.*, **226**, 257, 1987
- Burke, P. G. and Berrington, K. A.  
Atomic and Molecular Processes – An *R*-matrix Approach, *Institute of Physics Publishing*, 1993
- Burnight, T. R.  
Soft X-Radiation in the Upper Atmosphere, *Phys. Rev.*, **76**, 165, 1949
- Caillat, J., Dubois, A., Hansen, J. P.  
Recommended Partial Cross Sections for Electron Capture in  $C^{6+} + H(1s)$  Collisions, 2nd (Final) IAEA Research Co-ordination Meeting on "Charge Exchange Cross Section Data for Fusion Plasma Studies", Summary Report, 2001

- Combi, M. R., Delsemme, A. H.  
Neutral Cometary Atmospheres. I. An Average Random Walk Model for Photodissociation in Comets, *Astrophys. J.*, **237**, 633, 1980a
- Combi, M. R., Delsemme, A. H.  
Neutral Cometary Atmospheres. II. The Production of CN in Comets, *Astrophys. J.*, **237**, 641, 1980b
- Combi, M. R.  
Neutral Cometary Atmospheres. III. Acceleration of Cometary CN by Solar Radiation Pressure, *Astrophys. J.*, **241**, 830, 1980
- Combi, M. R.  
The Outflow Speed of the Coma of Halley's Comet, *Icarus*, **81**, 41, 1989
- Cowan, R. D.  
The Theory of Atomic Structure and Spectra (*Berkley: University of California Press*), 1981
- Cravens, T. E.  
Comet Hyakutake X-ray Source: Charge Transfer of Solar Wind Heavy Ions, *Geophys. Res. Lett.*, **24**, 1, 105, 1997
- Cravens, T. E.  
X-ray Emission from Comets, *Science*, **296**, 2002
- Curtis, C. C., Fan, C. Y., Hsieh, K. C., Hunten, D. M., Ip, W.-H., Keppler, E., Richter, A. K., Umlauf, G., Afonin, V. V., D'yachkov, A. V., Erö Jr., J., Somogyi, A. J.  
Comet P/Halley Neutral Gas Density Profile Along the Vega-1 Trajectory Measured by the Neutral Gas Experiment, *Astron. Astrophys.*, **187**, 360, 1987
- Davidson, R. C.  
Kinetic Waves and Instabilities in a Uniform Plasma, *Handbook of Plasma Physics* vol. 1, 1983
- Dawson, J. M., Bingham, R., Shapiro, V. D.  
X-rays from Comet Hyakutake, *Plasma Phys. Control. Fusion*, **39**, A185, 1997
- Delsemme, A. H., Combi, M. R.  
Neutral Cometary Atmospheres. IV. Brightness Profiles in the Inner Coma of Comet Kohoutek 1973 XII, *Astrophys. J.*, **271**, 388, 1983
- Dendy, R. O., Harvey, B. M., O'Brien, M.  
Fokker-Planck Modelling of Auroral Wave-Particle Interactions, *J. Geophys. Res.*, **100**, A11, 1995
- Dennerl, K., Englhauser, J., Trümper, J., Lisse, C. M.  
Comet C/1996 Q1 (Tabur), *IAU Circular*, **6495**, 1996
- Dennerl, K., Englhauser, J., Trümper, J.  
X-ray Emissions from Comets Detected in the Röntgen X-ray Satellite All-Sky Survey, *Science*, **277**, 1625, 1997
- Dennerl, K.  
Spectroscopic Imaging of Charge Exchange X-ray Emission from Comet C/2002 C1, *Chandra Proposal ID #03108076*, 2001
- Dennerl, K., Aschenbach, B., Burwitz, V., Englhauser, J., Lisse, C. M., Rodriguez-Pascual, P. M.  
A Major Step in Understanding the X-ray Generation in Comets: Recent Progress Obtained with XMM-Newton, *Proceedings of the SPIE*, **4851**, 277, 2003
- Divine, N., Fechtig, H., Gombosi, T. I., Hanner, M. S., Keller, H. U., Larson, S. M., Mendis, D. A., Newburn Jr., R. L., Reinhard, R., Sekanina, Z., Yeomans, D. K.  
The Comet Halley Dust and Gas Environment, *Space Sci. Rev.*, **43**, 1, 1986
- Drake, G. W. F., Victor, G. A., Dalgarno, A.  
Two-Photon Decay of the Singlet and Triplet Metastable States of Helium-like Ions, *Phys. Rev.*, **180**, 1, 25, 1969
- Drake, G. W. F.  
Spontaneous Two-Photon Decay Rates in Hydrogenlike and Heliumlike Ions, *Phys. Rev. A*, **34**, 4, 2871, 1986
- Errea, L. F., Illescas, C., Méndez, L., Pons, B., Riera, A., Suárez, J.  
Classical and Semiclassical Treatments of Highly Charged Ions + H(1s) collisions, *Nuc. Inst. Methods Phys. Res. B*, **235**, 315, 2005
- Festou, M. C.  
The Density Distribution of Neutral Compounds in Cometary Atmospheres I. Models and Equations, *Astron. Astrophys.*, **95**, 69, 1981
- Fritsch, W., Lin, C. D.  
Atomic-Orbital Expansions for Describing Charge Transfer in Slow Ion-Atom Collisions, *Physica Scripta*, **T3**, 241, 1983
- Fritsch, W., Lin, C. D.  
Atomic-orbital-expansion Studies of Electron Transfer in Bare-Nucleus  $Z$  ( $Z = 2, 4-8$ ) -Hydrogen-atom Collisions, *Phys. Rev. A*, **29**, 6, 3039, 1984
- Fritsch, W., Lin, C. D.  
The Semiclassical Close-Coupling Description of Atomic Collisions: Recent Developments and Results, *Phys. Rep.*, **202**, 1, 1991
- Fry, C. D., Dryer, D., Smith, Z., Sun, W., Deehr, C. D., Aka-sofu, S. -I.,  
Forecasting Solar Wind Structures and Shock Arrival Times Using an Ensemble of Model, *J. Geophys. Res.*, **108**, A2, 1070, 2003
- Fusilier, S. A., Shelley, E. G., Goldstein, B. E., Goldstein, R., Meugebauer, M., Ip, W.-H., Balsiger, H., Eème, H.  
Observations of Solar Wind Ion Charge Exchange in the Comet Halley Coma, *Astrophys. J.*, **379**, 734, 1991
- Giacconi, R., Gursky, H., Paolini, F. R., Rosso, B. B.  
Evidence for X-rays from Sources Outside the Solar System, *Phys. Rev. Lett.*, **9**, 439, 1962
- Giacconi, R., Gursky, H.  
Observation of X-ray Sources Outside the Solar System, *Space Sci. Rev.*, **4**, 151, 1965
- Giacconi, R., Gursky, H., Kellogg, E., Schreier, E., Tananbaum, T.  
Discovery of Periodic X-ray Pulsations in Centaurus X-3 from *Uhuru*, *Astrophys. J.*, **167**, L67, 1971
- Goldman, S. P., Drake, G. W. F.  
Relativistic Two-Photon Decay Rates of  $2s_{1/2}$  Hydrogenic Ions, *Phys. Rev. A*, **24**, 1, 183, 1981
- Gombosi, T. I., Powell, K. G., De Zeeuw, D. L.  
Axisymmetric Modeling of Cometary Mass Loading on an Adaptively Refined Grid: MHD Results, *J. Geophys. Res.*, **99**, A11, 21,525, 1994

- Gombosi, T. I., De Zeeuw, D. L., Häberli, R. M., Powell, K. G.  
Three-Dimensional Multiscale MHD Model of Cometary Plasma Environments, *J. Geophys. Res.*, **101**, A7, 15,233, 1996
- Gorczyca, T. W., Kodituwakku, C. N., Korista, K. T., Zatsarinny, O., Badnell, N. R., Behar, E., Chen, M. H., Savin, D. W.  
Assessment of the Fluorescence and Auger Database Used in Plasma Modeling, *Astrophys. J.*, **592**, 636, 2003
- Greenwood, J. B., Williams, I. D., Smith, S. J., Chutjian, A.  
Measurement of Charge Exchange and X-ray Emission Cross-Sections for Solar Wind-Comet Interactions, *Ap. J.*, **533**, L175, 2000
- Greenwood, J. B., Williams, I. D., Smith, S. J., Chutjian, A.  
Experimental Investigation of the Processes Determining X-ray Emission Intensities from Charge Exchange Collisions, *Phys. Rev. A*, **63**, 062707, 2001
- Gringauz, K. I., Gombosi, T. I., Remizov, A. P., Apáthy, I., Szemerey, T., Verigin, M. I., Denchikova, L. I., D'yachkov, A. V., Keppler, E., Klimenko, I. N., Richter, A. K., Somogyi, A. J., Szegő, K., Szendro, S., Tatrallyay, M., Varga, A., Vladimirova, G. A.  
First *In Situ* Plasma and Neutral Gas Measurement at Comet Halley, *Nature*, **321**, 282, 1986a
- Gringauz, K. I., Gombosi, T. I., Remizov, A. P., Apáthy, I., Szemerey, T., Denchikova, L. I., D'yachkov, A. V., Keppler, E., Klimenko, I. N., Richter, A. K., Somogyi, A. J., Szegő, K., Szendro, S., Tatrallyay, M., Varga, A., Verigin, M. I., Vladimirova, G. A.  
First *In Situ* Plasma and Neutral-Gas Measurements Near Comet Halley: Preliminary *Vega* Results, *Sov. Astron. Lett.*, **12**, 279, 1986b
- Gringauz, K. I., Remizov, A. P., Verigin, M. I., Richter, A. K., Tatrallyay, M., Skegő, K., Klimenko, I. N., Apáthy, I., Gombosi, T. I., Szemerey, T.  
Analysis of the Electron Measurements from the Plasmag-1 Experiment Onboard *Vega 2* in the Vicinity of Comet P/Halley, *Astron. Astrophys.*, **187**, 287, 1987
- Häberli, R. M., Altwegg, K., Balsiger, H., Geiss, J.  
Heating of Thermal Electrons in the Coma of Comet P/Halley, *J. Geophys. Res.*, **101**, A7, 15,579, 1996
- Häberli, R. M., Gombosi, T. I., De Zeeuw, D. L., Combi, M. R., Powell, K. G.  
Modeling of Cometary X-rays Caused by Solar Wind Minor Ions, *Science*, **276**, 939, 1997
- Hasan, A. A., Eissa, F., Ali, R., Schultz, D. R., Stancil, P. C.  
State-Selective Charge Transfer Studies Relevant to Solar Wind-Comet Interactions, *Astrophys. J. Lett.*, **560**, L201, 2001
- Haser, L.  
Distribution d'intensité dans la tête d'un comète, *Bull. Adac. Roy. Sci. Leège*, **43**, 740, 1957
- Hoekstra, R.  
Ph.D. Thesis, Rijksuniversiteit Groningen, 1990
- Hudson, H. S., Ip, W. -H., Mendis, D. A.  
An *Einstein* Search for X-ray Emission from Comet Bradfield (1979), *Planet. Space Sci.*, **29**, 1373, 1981
- Huebner, W. F., Keady, J. J., Lyon S. P.  
Solar Photorates for Planetary Atmosphere and Atmospheric Pollutants, *Astrophys. and Space Sci.*, **195**, 1, 1992
- Ibadov, S.  
On the Efficiency of X-ray Generation in Impacts of Cometary and Zodiacal Dust Particles, *Icarus*, **86**, 283, 1990
- Ip, W. -H., Mendis, D. A.  
The Generation of Magnetic Fields and Electric Currents in Cometary Plasma Tails, *Icarus*, **29**, 147, 1976
- Ip, W. -H.  
On Charge Exchange Effect in the Vicinity of the Cometopause of Comet Halley, *Astrophys. J.*, **343**, 946, 1989
- Janev, R. K., Winter, H.  
State-selective Electron Capture in Atom-Highly Charged Ion Collisions, *Phys. Rep.*, **117**, 265, 1985
- Janev, R. K., Phaneuf, R. A., Tawara, H., Shirai, T.  
Recommended Cross Sections for State-Selective Electron Capture in Collisions of  $C^{6+}$  and  $O^{8+}$  Ions with Atomic Hydrogen, *Atomic Data and Nuclear Data Tables*, **55**, 201, 1993
- Kaastra, J. S., Mewe, R.  
X-Ray Emission from Thin Plasmas. I. Multiple Auger Ionisation and Fluorescence Processes for Be to Zn, *Astron. Astrophys. Supp. Series*, **97**, 443, 1993
- Karzas, W. J., Latter, R.  
Electron Radiative Transitions in a Coulomb Field, *Astrophys. J.*, Supplement No. 55, **VI**, 167
- Keppler, E., Afonin, V. V., Curtis, C. C., D'yachkov, A. V., Erő, J., Fan, C. Y., Hsieh, K. C., Hunten, D. M., Ip, W. -H., Richter, A. K., Somogyi, A. J., Umlauf, G.  
Neutral Gas Measurements of Comet Halley from *Vega 1*, *Nature*, **321**, 273, 1986
- Kharchenko, V., Dalgarno, A.  
Spectra of Cometary X-rays Induced by Solar Wind Ions, *J. Geophys. Res.*, **105**, 18,351, 2000
- Kharchenko, V., Dalgarno, A.  
Variability of Cometary X-ray Emission Induced by Solar Wind Ions, *Astrophys. J.*, **554**, L99, 2001
- Kharchenko, V., Rigazio, M., Dalgarno, A., Krasnopolsky, V. A.  
Charge Abundances of the Solar Wind Ions Inferred from Cometary X-ray Spectra, *Astrophys. J.*, **585**, L53, 2003
- Kimura, M.  
Theoretical Investigation of Charge Transfer in Collisions of  $C^{6+}$  and  $N^{7+}$  Ions with H and  $H_2$  Targets at Low to Intermediate Energy, *Phys. Rev. A*, **33**, 6, 4440, 1986
- Kimura, M., Kobayashi, N., Ohtani, S., Tawara, H.  
Electron Transfer into Selective Excited States in Collisions of Highly Stripped C, N, O and Ne Ions with H and  $H_2$ , *Nuc. Inst. Meth. Phys. Res. A*, **262**, 19, 1987
- Klimov, S., Savin, S., Aleksevich, Ya., Avanesova, G., Balebanov, V., Balikhin, M., Galeev, A., Gribov, G., Nozdachev, M., Smirnov, 3V., Solokov, A., Vaisberg, O., Oberc, P., Krawczyk, Z., Grzedzielski, S., Juchniewicz, J., Nowak, K., Orłowski, D., Parfianovich, B., Wozniak, D., Zbyszynski, Z., Voita, Ya., Triska, P.  
Extremely-Low-Frequency Plasma Waves in the Environment of Halley, *Nature*, **321**, 292, 1986

- Krankowsky, D., Lammerzahl, P., Herrwerth, I., Woweries, J., Eberhardt, P., Dolder, U., Herrmann, U., Schulte, W., Berthelier, J. J., Illiano, J. M., Hodges, R. R., Hoffman, J. H.  
*In Situ* Gas and Ion Measurements at Comet Halley, *Nature*, **321**, 326, 1986
- Krasnopolsky, V. A.  
 On the Nature of Soft X-ray Radiation in Comets, *Icarus*, **128**, 368, 1997a
- Krasnopolsky, V. A., Mumma, M. J., Abbott, M., Flynn, B. C., Meech, K. J., Yeomans, D. K., Feldman, P. D., Cosmovici, C. B.  
 Detection of Soft X-rays and a Sensitive Search for Noble Gases in Comet Hale-Bopp (C/1995 O1), *Science*, **277**, 1488, 1997b
- Krasnopolsky, V. A.  
 X-Ray Spectroscopy of Comet C/1999 T1, *Chandra* Proposal ID #02100340, 2000
- Krasnopolsky, V. A., Mumma, M. J.  
 Spectroscopy of Comet Hyakutake at 80-700Å: First Detection of Solar Wind Charge Transfer Emissions, *Astrophys. J.*, **549**, 629, 2001
- Krasnopolsky, V. A.  
 Production of Cometary X rays by Electron Impact and Bremsstrahlung Processes, *em J. Geophys. Res.*, **106** A7, 18,741, 2001
- Krasnopolsky, V. A., Christian, D. J., Kharchenko, V., Dalgarno, A., Wolk, S. J., Stern, S. A.  
 X-ray Emission from Comet McNaught-Hartley (C/1999 T1), *Icarus*, **160**, 437, 2002
- Krasnopolsky, V. A.  
 Comparison of X-rays from Comets LINEAR (C/1999 S4) and McNaught-Hartley (C/1999 T1), *Icarus*, **167**, 417, 2004
- Krasnopolsky, V. A., Greenwood, J. B., Stancil, P. C.  
 X-ray and Extreme Ultraviolet Emission from Comets, *Space Sci. Rev.*, **113**, 271, 2004
- Krasnopolsky, V. A.  
 X-ray and Solar Wind Composition in Four Comets Observed with *Chandra X-ray Observatory*, *J. Geophys. Res.*, **111**, A12, 2006
- Lakhina, G. S.  
 Low-Frequency Plasma Turbulence During Solar Wind-Comet Interaction, *Astrophys. Space Sci.*, **133**, 203, 1987
- Levenberg, K.  
 A Method for the Solution of Certain Problems in Least Squares, *Quart. Appl. Math.*, **2**, 164, 1944
- Lewin, W. H. G., Clark, G. W., Smith, W. B.  
 Observation of an X-ray Flare from Sco X-1, *Astrophys. J.*, **152**, L55, 1968
- Lipatov, A. S., Motschmann, U., Bagdonat, T.  
 3D Hybrid Simulations of the Interaction of the Solar Wind with a Weak Comet, *Planet. Space Sci.*, **50**, 403, 2002
- Lisse, C. M., Dennerl, K., Englhauser, J., Harden, M., Marshall, F. E., Mumma, M. J., Petre, R., Pye, J. P., Ricketts, M. J., Schmitt, J., Trümper, J., West, R. G.  
 Discovery of X-ray and Extreme Ultraviolet Emission from Comet C/Hyakutake 1996 B2, *Science*, **274**, 205, 1996
- Lisse, C. M., Dennerl, K., Englhauser, J., Trümper, J., Marshall, F. E., Petre, R., Valinia, A., Kellett, B. J., Bingham, R.  
 X-ray Emission from Comet Hale-Bopp, *Earth, Moon and Planets*, **77**, 283, 1999a
- Lisse, C. M., Christian, D., Dennerl, K., Englhauser, J., Trümper, J., Desch, M., Marshall, F. E., Petre, R., Snowden, S.  
 X-ray and Extreme Ultraviolet Emission from Comet P/Encke 1997, *Icarus*, **141**, 316, 1999b
- Lisse, C. M.  
 AXAF Low Energy Spectroscopy and Photometric Imaging of Cometary X-ray Emission from Comet P/Tempel 2, *Chandra* Proposal ID #01100323, 1999c
- Lisse, C. M., Christian, D. J., Dennerl, K., Meech, K. J., Petre, R., Weaver, H. A., Wolk, S. J.  
 Charge Exchange-Induced X-ray Emission from Comet C/1999 S4 (LINEAR), *Science*, **292**, 5523, 2001
- Lisse, C. M., Cravens, T. E., Dennerl, K.  
 X-ray and Extreme Ultraviolet Emission from Comets, *Comets II*, University of Arizona Press, 2004
- Lisse, C. M., Christian, D. J., Dennerl, K., Wold, S. J., Bode-wits, D., Hoekstra, R., Combi, M. J., Mäkinen, T., Dryer, M., Fry, C. D., Weaver, H.  
*Chandra* Observations of Comet 2P/Encke 2003: First Detection of a Collisionally Thin, Fast Solar Wind Charge Exchange System, *Astrophys. J.*, **635**, 1329, 2005
- Liu, C. N., Cheng, S. C., Le, A. T., Lin, C. D.  
 Charge Transfer in Slow Collisions of C<sup>6+</sup> with H below 1 keV/amu, *Phys. Rev. A*, **72**, 012717, 2005
- Loch, S. D., Pindzola, M. S., Ballance, C. P., Griffin, D. C., Mitnik, D. M., Badnell, N. R., O'Mullane, M. G., Summers, H. P., Whiteford, A. D.  
 Electron-impact Ionization of All Ionization Stages of Krypton, *Phys. Rev. A*, **66**, 2002
- Lubinski, G., Juhász, Z., Morgenstern, R., Hoekstra, R.  
 Low-Energy State-Selective Charge Transfer by Multiply Charged Ions, *Phys. Rev. Lett.*, **86**, 616, 2001
- Marquardt, D.  
 An Algorithm for Least-Squares Estimation of Nonlinear Parameters, *SIAM J. Appl. Math.*, **11**, 431-441, 1963
- McBride, J. B., Ott, E., Boris, J. P., Orens, J. H.  
 Theory and Simulation of Turbulent Heating by the Modified Two-Stream Instability, *Phys. Fluids*, **15**, 2367, 1972
- McClements, K. G., Bingham, R., Su, J. J., Dawson, J. M., Spicer, D. S.  
 Lower Hybrid Resonance Acceleration of Electrons and Ions in Solar Flares and the Associated Microwave Emission, *Astrophys. J.*, **409**, 465, 1993
- Meyer, F. W., Howald, A. M., Havener, C. C., Phaneuf, R. A.  
 Low-energy Total-Electron-Capture Cross Sections for Fully Stripped and H-like Projectiles Incident on H and H<sub>2</sub>, *Phys. Rev. A*, **32**, 3310, 1985
- Milikh, G. M., Sharma, A. S.  
 Generation of X-rays by Suprathermal Electrons at Comets, *EOS Trans. AGU*, **78**(17), S243, 1997

- Moroz, V. I., Combes, M., bibring, J. P., Coron, N., Crovisier, J., Encrenaz, T., Crifo, J. F., Sanko, N., Grigoryev, A. V., Bockelée-Morvam, D., Gispert, R., Nikolsky, Y. V., Emerich, C., Lamarre, J. M., Rocard, F., Krasnopolsky, V. A., Owens, T.  
Detection of Parent Molecules in Comet P/Halley from the *IKS-Vega* Experiment, *Astron. Astrophys.*, **187**, 513, 1987
- Mumma, M. J., Krasnopolsky, V. A., Abbott, M. J.  
Soft X-rays from Four Comets Observed with *EUVE*, *Astrophys. J.*, **491**, L125, 1997
- Northrop, T. G., Lisse, C. M., Mumma, M. J., Desch, M. D.  
A Possible Source of the X-rays from Comet Hyakutake, *Icarus*, **127**, 246, 1997
- Northrop, T. G.  
The Spectrum of X-rays from Comet Hyakutake, *Icarus*, **128**, 480, 1997
- Nousek, J. A.  
Science Instrument (SI) Operations Handbook for the *AXAF CCD Imaging Spectrometer (ACIS)*, [acis.mit.edu/acis/sop01.v265/sop.v265.pdf](http://acis.mit.edu/acis/sop01.v265/sop.v265.pdf), 1997
- Ostrovsky, V. N.  
Rydberg Atom-Ion Collisions: Classical Overbarrier Model for Charge Exchange, *J. Phys. B*, **28**, 3901, 1995
- Otranto, S., Olson, R. E., Beiersdorfer, P.  
X-ray Emission Cross Sections Following Charge Exchange by Multiply Charged Ions of Astrophysical Interest, *Phys. Rev. A*, **73**, 022723-1, 2006
- Owens, A., Parmar, A. N., Oosterbroek, T., Orr, A., Antonelli, L. A., Fiore, F., Schultz, R., Tozzi, G. P., Maccarone, M. C., Piro, L.  
Evidence for Dust-Related X-ray Emission from Comet C/1995 O1 (Hale-Bopp), *Astrophys. J.*, **493**, L47, 1998
- Pengelly, R. M., Seaton, M. J.  
Recombination Spectra. II. Collisional Transition Between States of Degenerate Energy Levels, *Mon. Not. Roy. Ast. Soc.*, **127**, 165, 1964
- Rayman, M. D.  
The Successful Conclusion of the *Deep Space 1* Mission: Important Results Without a Flashy Title, *Space Technology*, **23**, 185, 2003
- Rème, H., Sauvaud, J. A., D'Uston, C., Cotin, F., Cros, A., Anderson, K. A., Carlson, C. W., Curtis, D. W., Lin, R. P., Mendis, D. A., Korth, A., Richter, A. K.  
Comet Halley-Solar Wind Interaction from Electron Measurements Aboard *Giotto*, *Nature*, **321**, 349, 1986
- Rème, H., Mazelle, C., Sauvaud, J. A., D'Uston, C., Froment, F., Lin, R. P., Anderson, K. A., Carlson, C. W., Larson, D. E., Korth, A., Chaizy, P., Mendis, D. A.  
Electron Plasma Environment at Comet Grigg-Skjellerup: General Observations and Comparison with the Environment at Comet Halley, *J. Geophys. Res.*, **98**, A12, 20,965, 1993
- Richter, K. Solov'ev, E. A.  
Application of the Advanced Adiabatic Approach to Charge Exchange in Slow Collisions between H and  $O^{8+}$ , *Phys. Rev. A*, **48**, 1, 432, 1993
- Riedler, W., Schwingenschuh, K., Yeroshenko, Ye. G., Styashkin, V. A., Russell, C. T.  
Magnetic Field Observations in Comet Halley's Coma, *Nature*, **321**, 288, 1986
- Rigazio, M., Kharchenko, V., Dalgarno, A.  
X-ray Emission Spectra Induced by Hydrogenic Ions in Charge Transfer Collisions, *Phys. Rev. A*, **66**, 064701, 2002
- Röntgen, W. C.  
Über eine neue Art von Strahlen, *From the minutes of meeting of the Würzburger Medical-Physics Society*, 1895
- Röntgen, W. C.  
Über eine neue Art von Strahlen, *Annalen der Physik*, **300**, 1, 12, 1898
- Schwadron, N. A., Cravens, T. E.  
Implications of Solar Wind Composition for Cometary X-rays, *Astrophys. J.*, **544**, 558, 2000
- Shapiro, V. D., Bingham, R., Dawson, J. M., Dobe, Z., Kellett, B. J., Manedi, D. A.  
Electron Energization by Lower-Hybrid Waves as a Possible Source for X-ray Emission from Comets, *Physica Scripta*, **T75**, 39, 1998
- Shapiro, V. D., Bingham, R., Dawson, J. M., Dobe, Z., Kellett, B. K., Mendis, D. A.  
Energetic Electrons Produced by Lower Hybrid Waves in the Cometary Environment and Soft X-ray Emission: Bremsstrahlung and K Shell Emission, *J. Geophys. Res.*, **104**, A2, 2537, 1999
- Shelley, E. G., Fuselier, S. A., Balsiger, H., Drake, J. F., Geiss, J., Goldstein, B. E., Goldstein, R., Ip, W.-H., Lazarus, A. J.  
Charge Exchange of Solar Wind Ions in the Coma of Comet P/Halley, *Astron. Astrophys.*, **187**, 304, 1987
- Shimakura, N., Koizumi, S., Suzuki, S., Kimura, M.  
Molecular Treatment of electron Capture in Atomic Collisions in the meV to keV Energy Regime: Collisions of  $C^{5+}$  Ions with H Atoms and the Effect of Core Electrons, *Phys. Rev. A*, **45**, 7876, 1992
- Shipsey, E. J., Green, T. A., Browne, J. C.  
Modified Method of Perturbed Stationary States. V. Electron-Capture Cross Sections for the Reaction  $O^{8+} + H(1s) \rightarrow O^{7+}(n, l) + H^+$ , *Phys. Rev. A*, **27**, 821, 1983
- Spence, J., Summers, H. P.  
The Recombination and Level Populations of Ions III — The Role of Charge Exchange from Neutral Hydrogen, *J. Phys. B*, **19**, 3749, 1986
- Stancil, P. C., Wang, J. G., Raković, M. J., Schultz, D. R., Ali, R.  
Charge Transfer Needs for Cometary X-ray Emission Modeling, *AIP Conf. Proc.*, **636**, 144, 2002
- Su, J. J., Bingham, R., McClements, K. G., Dawson, J. M.  
*Bull. APS*, **35**, 2097, 1990
- Summers, H. P.  
The Density Dependent Ionization Balance of Carbon, Oxygen and Neon in the Solar Atmosphere, *Mon. Not. Roy. Ast. Soc.*, **158**, 255, 1972

- Summers, H. P.  
The Recombination and Level Populations of Ions II. Resolution of Angular Momentum States, *Mon. Not. Roy. Ast. Soc.*, **178**, 101, 1977
- Summers, H. P., Hooper, M. B.  
On Radiative Power From Impurities in Plasmas, *Plasma Physics*, **25**, 12, 1311, 1983
- Summers, H. P.  
The Atomic Data and Analysis Structure (ADAS) User Manual (Version 2.7),  
<http://adas.phys.strath.ac.uk>, 2003
- Summers, H. P., Dickson, W. J., O'Mullane, M. G., Badnell, N. R., Whiteford, A. D., Brooks, D. R., Lang, J., Loch, S. D., Griffin, D. C.  
Ionisation State, Excited Populations and Emission of Impurities in Finite Density Plasmas. I. Overview and the Generalised Collisional-Radiative Model for Light Elements, *Plasma Phys. Controlled. Fus.*, **48**, 2, 263, 2006
- Szegő, K., Glassmeier, K.-H., Bingham, R., Bogdanov, A., Fischer, C., Haerendel, G., Brinca, A., Cravens, T., Dubinin, E., Sauer, K., Fisk, L., Gombisi, T., Schwadron, N., Isenberg, P., Lee, M., Mazelle, C., Möbius, E., Motschmann, U., Shapiro, V. D., Tsurutani, B., Zank, G.  
Physics of Mass Loaded Plasmas, *Space Sci. Rev.*, **94**, 429, 2000
- Uchida, M., Morikawa, M., Kubotani, H., Mouri, H.  
X-ray Spectra of Comets, *Astrophys. J.*, **498**, 863, 1998
- Umbach, R., Jockers, K., Geyer, E. H.  
Spatial Distribution of Neutral and Ionic Constituents in Comet P/Halley, *Astron. Astrophys. Supp. Ser.*, **127**, 479, 1998
- Wegmann, R., Schmidt, H. U., Lisse, C. M., Dennerl, K., Englhauser, J.  
X-rays from Comets Generated by Energetic Solar Wind Particles, *Planet. Space Sci.*, **46**, 603, 1998
- Wegmann, R.  
Large-scale Disturbance of the Solar Wind by a Comet, *Astron. Astrophys.*, **389**, 1039, 2002
- Wegmann, R., Dennerl, K., Lisse, C. M.  
The Morphology of Cometary X-ray Emission, *Astron. Astrophys.*, **428**, 647, 2004
- Wegmann, R., Dennerl, K.  
X-ray Tomography of a Cometary Bow Shock, *Astron. Astrophys.*, **430**, L33, 2005
- Wimmer-Schweingruber, R. F.  
The Composition of the Solar Wind, *Adv. Space Res.*, **30**, 23, 2002
- Yeomans, D.  
Near Earth Object Program,  
<http://neo.jpl.nasa.gov/orbits/>